Combinatorial Synthesis and High-Throughput Analysis of Halide Perovskite Materials for Thin-Film Optoelectronic Devices

---

Dissertation

zur Erlangung des akademischen Grades

doctor rerum naturalium

(Dr. rer. nat.)

im Fach: Physik, Spezialisierung: Experimentalphysik

eingereicht an der

Mathematisch-Naturwissenschaftlichen Fakultät
der Humboldt-Universität zu Berlin

von

M.Sc. Hampus Näsström

Präsident (komm.) der Humboldt-Universität zu Berlin
Prof. Peter A. Frensch, PhD

Dekanin der Mathematisch-Naturwissenschaftlichen Fakultät
Prof. Dr. Caren Tischendorf

Gutachter/innen:	1. Prof. Dr. Emil List-Kratochvil 2. Prof. Dr. Eva Unger 3. Prof. Dr. Udo Bach
Tag der mündlichen Prüfung:	23.6.2022

Abstract

In order to keep up with the increasing need for specialized materials, an acceleration of the materials discovery process is needed. One identified approach for accomplishing this is through parallel, so-called combinatorial, synthesis, and high-throughput screening. An area with increasing demand for novel materials is that of optoelectronics, especially for the use in photovoltaic solar cells. Within this area, metal halide perovskites have proven to be an excellent material class and have achieved impressive performance in photovoltaic devices among other applications. However, the degradation of the frequently employed organic components contributes to limiting the long-term stability of metal halide perovskite devices. Therefore, there is an ongoing effort to replace the organic cations with inorganic cesium, but the effects of this substitution on the structural and optoelectronic properties of the compounds are not yet fully understood.

In this work, accelerated materials discovery is addressed through the development, implementation, and validation of two complementary methods for combinatorial synthesis. Firstly, the solution-based method of combinatorial inkjet printing was further developed by providing a new algorithm for improved ink mixing. To validate the method, printed libraries of the inorganic $CsPb(Br_xI_{1-x})_3$ perovskite were investigated through synchrotron-based micro-spot structural measurements of the local homogeneity. Secondly, the vapor-based synthesis of double-gradient $Cs_yPb_{1-y}(Br_xI_{1-x})_{2-y}$ was implemented by modification and extension of a multi-source co-evaporation chamber.

Combinatorial libraries created via both solution and vapor-based combinatorial methodologies were used for the high-throughput investigation of the structural and optical properties of $Cs_yPb_{1-y}(Br_xI_{1-x})_{2-y}$. This enabled the construction of complete phase diagrams for thin-films of the $CsPb(Br_xI_{1-x})_3$ solid solution, through the application of temperature-dependent X-ray diffraction experiments. The results show that the addition of Br stabilizes the semiconducting perovskite phase and allows for lower processing temperatures. This provides important information for the implementation of this material in optoelectronic devices. By correlating the structural and optical properties it was found that the optical band-gap of $CsPbBr_{0.9}I_{2.1}$ follows the largest pseudo-cubic lattice parameter, c.

Finally, combinatorially co-evaporated $Cs_yPb_{1-y}(Br_xI_{1-x})_{2-y}$ libraries were investigated by means of automized, contact-less, optical mapping measurements, enabling the rapid screening of over 3,400 compositions. For the first time, this enabled the assessment of the photovoltaic potential of $Cs_yPb_{1-y}(Br_xI_{1-x})_{2-y}$ over a very broad composition range. The maximum efficiency potential was found for stoichiometric compositions, with any excess of Pb or Cs causing increased losses by non-radiative recombination. These results provide vital knowledge for further development and optimization of inorganic halide perovskite devices.

German translation (Kurzzusammenfassung)

Um mit dem steigenden Bedarf an neuen Materialien Schritt halten zu können, ist eine Beschleunigung des Prozesses der Materialentwicklung notwendig. Dies kann mit kombinatorischen Synthesemethoden und Hochdurchsatz-Charakterisierung erreicht werden. Neue Materialien werden unter anderem in der Optoelektronik, insbesondere für den Einsatz in Solarzellen, benötigt. Hier haben sich Metallhalogenid-Perowskite als eine hervorragende Materialklasse mit hohen demonstrierten Wirkungsgraden erwiesen. Die Degradation der in Metallhalogenid-Perowskite häufig verwendeten organischen Komponenten bewirkt jedoch eine begrenzte Langzeitstabilität. Daher wird versucht, die organischen Kationen durch anorganisches Cäsium zu ersetzen. Die Auswirkungen dieser Substitution auf die strukturellen und optoelektronischen Eigenschaften der Verbindungen sind jedoch gegenwärtig noch wenig verstanden.

In dieser Arbeit wird die Beschleunigung der Materialentwicklung durch die Entwicklung und Validierung von zwei komplementären Methoden für die kombinatorische Synthese angegangen. Erstens wurde die lösungsbasierte Methode des kombinatorischen Tintenstrahldrucks weiterentwickelt, indem ein neuer Algorithmus für eine verbesserte Tintenmischung bereitgestellt wurde. Zur Validierung der Methode wurden gedruckte $\mathrm{CsPb(Br}_x\mathrm{I}_{1-x})_3$-Perowskit-Bibliotheken durch Synchrotron-basierte Mikrospot-Strukturmessungen der lokalen Homogenität untersucht. Zweitens wurde die Synthese von $\mathrm{Cs}_y\mathrm{Pb}_{1-y}(\mathrm{Br}_x\mathrm{I}_{1-x})_{2-y}$ Doppelgradientenschichten durch Modifizierung und Erweiterung einer Mehrfachquellen-Koverdampfungsanlage implementiert.

Kombinatorische Bibliotheken, die sowohl durch Lösungs- als auch durch Verdampfungs-basierte kombinatorische Methoden erstellt wurden, wurden für die Hochdurchsatzuntersuchung der strukturellen und optischen Eigenschaften von $\mathrm{Cs}_y\mathrm{Pb}_{1-y}(\mathrm{Br}_x\mathrm{I}_{1-x})_{2-y}$ verwendet. Dies ermöglichte die Erstellung vollständiger Phasendiagramme für $\mathrm{CsPb(Br}_x\mathrm{I}_{1-x})_3$-Mischkristallfilme durch temperaturabhängige Röntgenbeugungsexperimente. Die Ergebnisse zeigen, dass die Zugabe von Br die halbleitende Perowskitphase stabilisiert und niedrigere Verarbeitungstemperaturen ermöglicht. Dies liefert wichtige Informationen für den Einsatz dieses Materials in Bauelementen. Desweiteren wurde durch Korrelation der strukturellen und optischen Eigenschaften festgestellt, dass die optische Bandlücke von $\mathrm{CsPbBr}_{0.9}\mathrm{I}_{2.1}$ dem größten pseudokubischen Gitterparameter c folgt.

Schließlich wurden kombinatorisch koverdampfte $\mathrm{Cs}_y\mathrm{Pb}_{1-y}(\mathrm{Br}_x\mathrm{I}_{1-x})_{2-y}$-Bibliotheken mittels automatisierter, kontaktloser optischer Raster-Messungen untersucht, die eine schnelle Sichtung von über 3.400 Zusammensetzungen ermöglichten. Dies ermöglichte zum ersten Mal die Bewertung des photovoltaischen Potenzials von $\mathrm{Cs}_y\mathrm{Pb}_{1-y}(\mathrm{Br}_x\mathrm{I}_{1-x})_{2-y}$ über einen sehr weiten Zusammensetzungsbereich. Das maximale Wirkungsgradpotenzial wurde für stöchiometrische Zusammensetzungen gefunden, wobei jeder Überschuss an Pb oder Cs zu erhöhten Verlusten durch nichtstrahlende Rekombination führte. Diese gewonnenen Ergebnisse liefern wichtige Erkenntnisse für die weitere Entwicklung und Optimierung von anorganischen Metallhalogenid-Perowskite-Bauelementen.

Acknowledgements

I would like to begin by thanking Prof. Dr. Eva Unger for giving me the inspiration and opportunity to perform this work. Without her support and constant ideas for improvement, this thesis would not have been possible. The same can be said for the supervision and help of Dr. Thomas Unold. I am extremely grateful for getting to be a part of his group and for all the scientific discussions we had together. I am also deeply indebted to Prof. Dr. Emil List-Kratochvil for his wise insights and for always supporting me in my ideas.

I am extremely thankful to Prof. Dr. Udo Bach, Prof. Dr. Claudia Draxl, and Prof. Dr. Jan Lüning for agreeing to be part of my doctoral committee and reviewing my work.

I would like to extend my deepest gratitude to Dr. Oleksandra Shargaieva and Dr. Pascal Beblo for their never-ending support. For all the days at the printer and all the nights at the beam-times, Oleksandra. For the long days at the evaporator in Wannsee and the even longer days in the home office coding project Kameleont together, Pascal. Thank you both for everything.

Many thanks to my personal cheering team, Dr. Jose Márquez Prieto, for his constant enthusiasm and scientific input. I would also like to thank Dr. Roland Mainz for introducing me to the metal-jet source and for all his support. Thanks should also go to Dr. Hannes Hempel for being a great teacher and for always making time for helping me.

Thank you to Dr. Florian Mathies for teaching me the ways of the inkjet printer and to Vincent Schröder for testing that my crazy ideas actually work. I also had the great pleasure of working with Dr. Ivo Zizak at the µSpot beam-line and his support with the experiments is greatly appreciated.

Many thanks to Fatima Akhundova and Jinzhao Li for assisting with the measurements. Special thanks to Dr. Leo Choubrac for helping with the database project and to Carola Klimm for the beautiful microscope images. I also very much appreciate the discussions I had with Dr. Amran Al-Ashouri, Dr. Jesper Jacobsson, Max Grischek, Hans Köbler, and Dr. Rowan MacQueen as well as current and former members of the groups of Eva Unger and Thomas Unold. I also wish to thank my father, Dr. Jacques Näsström, for providing a fresh set of eyes on this dissertation.

Especially helpful to me during this time was the X-ray school arranged by Prof. Dr. Susan Schorr, Dr. Michael Tovar, Rene Gunder, and members of their group as well as their continued support with X-ray diffraction analysis. I gratefully acknowledge the assistance of Lars Steinkopf and Thomas Lußky in constructing and maintaining setups as well as Hagen Heinz, Monika Gabernig, and Carola Ferber for keeping the laboratory running like clockwork. Thank you also to Marion Krusche, Antonia Tallerek, and Hagen Heinz for your fantastic help in navigating the German bureaucracy. I would also like to extend my gratitude to the rest of the people working at Helmholtz-Zentrum Berlin as well as the institution itself. I am also grateful to the HyPerCells research school as well as for the allocated beam-times at the µSpot beam-line at BESSY II and acknowledge the funding from the German Ministry of Education and Research (BMBF) for the Young Investigator Group Hybrid Materials Formation and Scaling (HyPerFORME) within the program "NanoMatFutur"(grant no. 03XP0091).

In addition, I would like to acknowledge the importance of all the people who have inspired me to pursue this path and the truly great teachers that have made it possible. Among others, I would like to thank my science teacher from middle school, Dr. Håkan Yildirim. His passion for science remains in my memory until this day and was a contributing factor to the choices that brought me here. Another teacher which has really left a lasting impact is my math and chemistry teacher from high school, Dr. Marc Roddis. I am truly grateful for his burning passion to teach and his instructions on lab report writing have laid the foundations for the writing of this very dissertation.

Finally, I would like to thank my friends and family for all their support. Their encouragement has been a vital component for the completion of this thesis and I could not have done it without them. From the bottom of my heart, thank you.

Contents

List of Abbreviations

CAD	Computer Aided Design
CB	Conduction Band
CCD	Charge Coupled Device
CIGS	Copper Indium Gallium Diselenide
CVD	Chemical Vapor Deposition
DMF	Dimethylformamide
DMSO	Dimethyl Sulfoxide
DOD	Drop-On-Demand
dpi	dots per inch
EQE	External Quantum Efficiency
FA	Formamidinium
FF	Fill Factor
FWHM	Full Width at Half Maximum
GIWAXS	Grazing-Incidence Wide-Angle X-ray Scattering
IUPAC	International Union of Pure and Applied Chemistry
LASER	Light Amplification by Stimulated Emission of Radiation
LED	Light Emitting Diode
MA	Methylammonium
MHP	Metal Halide Perovskite
ML	Machine Learning
MPP	Maximum Power Point
ND	Neutral Density
NIR	Near-Infrared
PCE	Power Conversion Efficiency
PID	Proportional Integral Derivative

PL	Photoluminescence
PLQY	Photoluminescence Quantum Yield
PMT	Photo Multiplier Tube
ppm	parts per million
PTFE	Polytetrafluoroethylene
PV	Photovoltaics
PVD	Physical Vapor Deposition
QCM	Quartz Crystal Microbalance
sCMOS	scientific Complementary Metal–Oxide–Semiconductor
SEM	Scanning Electron Microscopy
SRH	Shockley-Read-Hall recombination
TCSPC	Time-Correlated Single Photon Counting
TMM	Transfer Matrix Method
TRMC	Time-Resolved Microwave Conductivity
TRPL	Time-Resolved Photoluminescence
UV/Vis	Ultraviolet/Visible Reflection and Transmission Spectroscopy
VB	Valence Band
XRD	X-Ray Diffraction
XRF	X-Ray Fluorescence

Chapter 1

Introduction

1.1 Motivation & Aim

In the world we live in, we are constantly surrounded by purposefully designed materials. These materials are often the result of a long research and development process. Historically the materials research cycle has been mostly serial with conceptualization, synthesis of material, characterization, and analysis being performed on a single sample before restarting the cycle for the next one. In order to meet today's fast-growing need for specialized materials, a parallelization of the development process is needed [1].

One proposed solution for parallelization is the so-called combinatorial research. In this type of research, a library of samples is created at once by combining different materials and varying synthesis parameters between samples. These libraries are then characterized by high-throughput experiments with automized or parallel measurements. In this way, high-throughput screening of materials can be performed [2]. This approach has for example proven effective in the field of life science where numerous drugs have been developed by this method [3].

The field of optoelectronics is one area where fast materials discovery is needed, especially within the area of Photovoltaics (PV) and Light Emitting Diodes (LEDs). With more and more countries and individuals looking to reduce their carbon footprint and dependence on fossil fuels, the accelerated development of solar cells and efficient lighting is urgently required.

One example of a material class that is currently under development for various thin-film optoelectronic devices is that of the Metal Halide Perovskites (MHPs). In the last 10 years this material class has been implemented in PV, LEDs, LASERs, detectors, and more [4–7]. Most notably the materials have been used to manufacture solar cells that outperform established thin-film materials like Copper Indium Gallium Diselenide (CIGS) and can be combined with the industry-standard crystalline silicon solar cells to boost their efficiency using tandem device structures.

The main challenge that prevents MHPs from being launched to the market is the observed instability of the devices. One reason for this instability is the thermal and photo-instability of its organic constituents. There is, therefore, an effort to replace these organic compounds with inorganic ones, such as Cs. However, the resulting material is reported to form different crystallographic phases and more work is needed to understand the structure and photovoltaic potential of these materials.

Therefore, the aim of this thesis is to develop, implement and validate methods of combinatorial synthesis and high-throughput analysis in order to identify promising compositions of inorganic $Cs_yPb_{1-y}(Br_xI_{1-x})_{2-y}$ MHP thin films for the use in optoelectronics. This has been done through the development of combinatorial deposition by the two complementary and industrially compatible synthesis methods of co-evaporation and inkjet printing. These methods have been validated and used to prepare thin-film combinatorial libraries with a compositional variation of Cs to Pb and Br to I. For these libraries, the structural and optical properties have been determined using high-throughput experimentation for the understanding of stability and photovoltaic potential as a function of the material composition.

1.2 Outline of Dissertation

Chapter 2 introduces the fundamental knowledge and background needed to understand the results of the thesis with a focus on PV, MHPs and combinatorial research.

Chapter 3 provides a detailed description of the synthesis and characterization setups used within this work as well as the method of their operation.

Chapter 4 is the first of the two chapters presenting the results of this work. In this chapter, the development, implementation, and validation of the two combinatorial synthesis methods are shown.

Section 4.1 contains a description of the development and validation of a new method for combinatorial inkjet printing.

Section 4.2 explains the implementation and modeling of a four source co-evaporation chamber for use in combinatorial research.

Chapter 5 is the second of the two results chapters and presents the structural and optical high-throughput investigation of the printed and evaporated combinatorial libraries of $Cs_yPb_{1-y}(Br_xI_{1-x})_{2-y}$.

Section 5.1 presents the high-throughput study of structural properties of inkjet-printed combinatorial libraries of $CsPb(Br_xI_{1-x})_3$ and the temperature-dependent phase diagram determined from the results.

Section 5.2 shows a detailed example of how a high-throughput screening for a PV material can be performed by contact-less measurements. The photovoltaic potential as function of the composition is determined and discussed for combinatorially evaporated $\mathrm{Cs}_y\mathrm{Pb}_{1-y}(\mathrm{Br}_x\mathrm{I}_{1-x})_{2-y}$ libraries.

Section 5.3 combines the information from the two previous sections and shows a high-throughput study of the temperature-dependent correlation of structural and optical parameters for a sample of interest.

Chapter 6 summarizes the results and discussion from the previous chapters and provides the conclusions and outlook of the dissertation.

Chapter 2

Fundamentals

In this chapter the scientific background, needed to understand the context of the results of this thesis, is presented. The chapter will begin by discussing some key concepts of semiconductor physics, which are useful in the screening of optoelectronic materials. Next, a description of the optoelectronic devices known as solar cells will be given and their limits with regard to material properties discussed. A large section of this chapter will be dedicated to explaining and motivating the choice of Metal Halide Perovskites (MHPs) as the selected material class for showcasing combinatorial synthesis and high-throughput analysis. Finally, the background and most importantly a set of definitions for combinatorial science will be given, together with an introduction to the combinatorial methods used in this work.

2.1 Semiconductor Physics

When considering optoelectronics such as PV or LEDs the material class that comes to mind is semiconductors. Therefore, an understanding of semiconductor physics is crucial when investigating materials for use in optoelectronics. Specifically, this section aims to elaborate on the important processes of absorption of light and recombination of charge carriers. These two complementary processes are important for understanding the results of the material screening performed as one of the main results of this thesis in section 5.2. For a rigorous background on semiconductor physics, please see one of many textbooks such as the book on semiconductor devices by Sze and Lee [8] and the one on the quantum theory of their optoelectronic properties by Haug and Koch [9].

The key feature of semiconductors is the filling and separation of their bands of allowed energetic states. More specifically, at 0 K for an intrinsic semiconductor, the highest occupied band, called the Valence Band (VB), is completely filled and the lowest unoccupied band, called the Conduction Band (CB), is completely empty. In addition, the separation of the bands, known as the band-gap, E_{g}, is small enough that at room temperature a low, but not insignificant, number of electrons are thermally excited to the conduction band, leaving behind a vacancy known as a hole. Both the excited electron and the hole act as charge carriers in the semiconductor.

In PV, the charge carriers are generated through the *absorption* of a quantum of light, a photon. The energy of the absorbed photon is used to excite an electron across the band-gap and this creates an electric potential, or voltage. This is known as the photovoltaic effect. In LEDs the opposite result is accomplished through *recombination* of charge carriers and the emission of a photon. As a final remark before moving on to the details of absorption and recombination, the maximum of the CB and the minimum of the VB can either be aligned in momentum space, in a so-called *direct* band-gap, or misaligned, in an *indirect* band-gap. For an indirect band-gap, the absorption and recombination need to involve a quantized lattice vibration, a phonon, to correct for the difference in momentum of the two states.

2.1.1 Absorption

A measure for the amount of absorption events taking place per distance that the light travels through the semiconductor, is the absorption coefficient, α. The absorption coefficient can be understood through the Lambert-Beer law which, for a homogeneous material, relates the incoming intensity of light, I_0, with the intensity of light, $I(d)$, at any given distance, d, into the material through:

$$I(d) = I_0 \mathrm{e}^{-\alpha d}. \tag{2.1}$$

The amount of absorption events that can take place in a semiconductor, for photons with a given energy, E, is proportional to the number of empty states that are available for the electron to be excited into. In addition the photon needs to supply the energy to overcome the band-gap, E_g. The absorption coefficient for free carriers is given by:

$$\alpha_\mathrm{free}(E) \propto \sqrt{E - E_\mathrm{g}}, \quad \text{for} \quad E \geqslant E_\mathrm{g}. \tag{2.2}$$

This is a qualitative explanation and for its derivation and the magnitude of the proportionality please see a textbook such as reference [9].

Excitons

Equation 2.2 is an idealized description of the absorption in a semiconductor and, for many materials, the measured spectrum will deviate considerably. Specifically, in the MHP semiconductors, which are studied as an exemplary material in this work, the absorption coefficient is drastically different due to a non-negligible excitonic contribution [10, 11].

Excitons are electron and hole pairs that are bound in a hydrogen-like system due to the Coulomb interaction between them. The exciton will, like the hydrogen analogy, have a fundamental energy level which is termed the exciton binding energy, E_0. Due to the screening of other electrons in semiconductors, the binding energies are much lower than for a hydrogen atom as the associated radius is typically larger than the lattice spacing. This type of exciton is usually referred to as a Wannier-Mott exciton [12].

Elliott formula

The effect of the formation of Wannier-Mott excitons on the absorption in semiconductors was first published by Elliot in 1957 [13]. For simplifying the following equations the variable Δ is introduced as:

$$\Delta = (E - E_\mathrm{g})/E_0. \tag{2.3}$$

Elliot writes that the exciton will manifest itself as a set of peaks in the spectrum of the absorption coefficient at $\Delta = -1/n^2$ with intensities falling as $1/n^3$, where $n\epsilon\mathbb{N}^*$ (Equation 3.9 in [13]). This means that there will be discrete energy levels as far as E_0 below the band-gap. In addition to these discrete levels below the band-gap, there will be an enhancement of the free absorption coefficient in to the continuum states above, by $\alpha_\mathrm{cont} = \alpha_\mathrm{free} \cdot C(\omega)$. The Coulomb enhancement factor $C(\omega)$ is given by:

$$C(\omega) = \frac{\frac{\pi}{\sqrt{\Delta}} \mathrm{e}^{\pi/\sqrt{\Delta}}}{\sinh\left(\pi/\sqrt{\Delta}\right)}. \tag{2.4}$$

A complete function for the absorption coefficient is not present in the original paper by Elliot but is by now reproduced in many textbooks and here taken from equation 10.100 in reference [9] to be:

$$\alpha(E) \propto \frac{E}{E_0} \left(\sum_{n=1}^{\infty} \frac{4\pi}{n^3} \delta(\Delta + 1/n^2) + \theta(\Delta) \frac{\pi \mathrm{e}^{\pi/\sqrt{\Delta}}}{\sinh\left(\pi/\sqrt{\Delta}\right)} \right), \tag{2.5}$$

where δ is the Dirac delta function and θ the Heaviside step function.

The important takeaway from the Elliot function, when considering for example MHPs, is that there will be an absorption peak below the band-gap and a strong enhancement of the absorption above the band-gap in the the spectrum of the absorption coefficient.

Tanguy formula

The Elliot formula is crucial for representing the spectrum of the absorption coefficients in MHPs. However, in order to model the absorption to measured values, it needs to be extended with broadening of the discrete states. In his paper from 1995, Tanguy extended the Elliot formula by convoluting it with a Lorentzian broadening [14]. In addition to treating the complex part of the refractive index, Tanguy also extends the definition, through the use of the Kramers-Kronig relation, to the full complex dielectric constant, ϵ. The full expression for the dielectric constant broadened by a Lorentzian with width Γ is given by:

$$\epsilon_{\text{lorentzian}}(E) = \frac{A\sqrt{E_0}}{E + \mathrm{i}\Gamma}(g(\xi(E + \mathrm{i}\Gamma)) + g(\xi(-(E + \mathrm{i}\Gamma))) - 2g(\xi(0)), \tag{2.6}$$

where

$$g(\xi) = 2\ln\xi - 2\pi\cot(\pi\xi) - 2\psi(\xi) - 1/\xi, \quad \xi(z) = \sqrt{\frac{E_0}{E_\text{g} - z}} \tag{2.7}$$

and $\psi(z)$ is the digamma function.

Although this Lorentzian is needed for representing the natural broadening of the transitions it often needs to be extended by a Gaussian broadening to account for thermal broadening and statistical variations in band-gap. Therefore, the dielectric constant from Equation 2.6 is in this work convoluted with a Gaussian distribution with standard deviation σ:

$$\epsilon(E) = \frac{1}{\sigma\sqrt{2\pi}}\mathrm{e}^{-\frac{E^2}{2\sigma^2}} \circledast \epsilon_{\text{lorentzian}}(E). \tag{2.8}$$

The advantage of the dielectric representation by Tanguy is that it can be used directly to model the transmittance and reflectance of a thin film, as the dielectric function is easily converted to the refractive index.

The complex transmission and reflection coefficients at an interface can be calculated from the real part of the refractive indices using the Fresnel equations. However, when dealing with multiple layers the infinite reflections at the various interfaces as well as the constructive and destructive interference need to be accounted for. One way to solve the complete system, using the boundary conditions of Maxwell's equations, is to represent each layer by a matrix and multiply them together. This approach is known as the Transfer Matrix Method (TMM). The details of this approach can be found in any photonics textbook but reference [15] provides an excellent summary and was used as a starting point for the custom solution in section C.1 which is used later in section 5.2.

2.1.2 Recombination

Absorption in a semiconductor and generation of an electron-hole pair is complemented by recombination of the charge carriers. This recombination can occur in multiple ways and understanding the dominating pathways and time scales is crucial for judging the suitability of a material for use in optoelectronics. Please note that this section is not a complete description of all recombination processes but focuses on the ones important for understanding the main results of this work.

Radiative versus non-radiative recombination

The recombination pathway directly opposite to absorption is the recombination of the electron-hole pair across the band-gap and emission of a photon. This recombination is commonly referred to as a band-to-band transition and is an example of *radiative* recombination, as it radiates light. However, there are multiple ways that charge carriers can recombine without emitting a photon and these are collectively grouped as *non-radiative* recombination.

The dominating non-radiative recombination in MHPs is facilitated by defects that cause localized states in the band-gap [16, 17]. These defect states act as traps and significantly increase the probability that carriers can recombine through the emission of phonons (lattice vibrations) rather than a photon. The model for this recombination process was first described by Shockley, Read [18] and Hall [19] and this type of recombination is therefore often referred to as Shockley-Read-Hall recombination (SRH).

The key thing to note is that radiative recombination is an inevitable consequence of absorption whilst the non-radiative recombination can (at low injection) be reduced by reducing the defects in the material. It is therefore desirable to have a large portion of radiative recombination as it indicates a lack of non-radiative recombination. This concept will be reiterated for the application of Photovoltaics (PV) in the next section and is important for understanding the main results of section 5.2.

Rate equation

In order to understand the limiting pathway of recombination, it is common to study a semiconductor in non-equilibrium after, for example, a pulse of light has excited Δn carriers. These carriers are excited in addition to the majority carriers already present in the semiconductor, n_0. The radiative recombination from before requires both an electron and a hole, meaning it is a bi-molecular recombination and will, for $\Delta n \gg n_0$, be proportional to Δn^2. The SRH recombination, on the other hand, is a mono-molecular recombination and will be directly proportional to Δn. Ignoring all other recombination pathways (most notably Auger recombination), the change in excess carrier concentration, $\mathrm{d}\Delta n/\mathrm{d}t$, can then be written as:

$$\frac{\mathrm{d}\Delta n}{\mathrm{d}t} \approx -\frac{1}{\tau_{\mathrm{SRH}}} \cdot \Delta n - k_{\mathrm{rad}} \cdot \Delta n^2 = -\frac{1}{\tau_{\mathrm{eff}}} \cdot \Delta n, \tag{2.9}$$

where τ_{SRH} is the lifetime of carriers with respect to SRH recombination, k_{rad} is the rate constant for radiative recombination and the effective lifetime τ_{eff} is defined by:

$$\frac{1}{\tau_{\mathrm{eff}}} = \frac{1}{\tau_{\mathrm{SRH}}} + k_{\mathrm{rad}} \cdot \Delta n. \tag{2.10}$$

Assuming that the injection is low enough that the rate equation is limited by the SRH lifetime, the solution to the differential equation approaches:

$$\Delta n(t) \simeq \Delta n(0) \cdot \mathrm{e}^{-t/\tau_{\mathrm{eff}}}, \quad \text{for} \quad k_{\mathrm{rad}} \cdot \Delta n \ll 1/\tau_{\mathrm{SRH}}. \tag{2.11}$$

The decay time of this exponential function is often fitted to measured values of Δn or calculated from its derivative. Here, another method is proposed where the numerically more robust integral is used. Typically, the radiative recombination is measured and that is, for these specific conditions, proportional to Δn^2. By taking the integral of the measured signal and using the expression for $\Delta n(t)$ from Equation 2.11, the effective lifetime can efficiently be calculated without the need for a fitting algorithm:

$$\int_{t_0}^{t_1} \Delta n^2(t)\mathrm{d}t = \frac{\tau_{\mathrm{eff}}}{2}\left(\Delta n^2(t_0) - \Delta n^2(t_1)\right) \tag{2.12}$$

$$\Rightarrow \tau_{\mathrm{eff}} = \frac{2\int_{t_0}^{t_1} \Delta n^2(t)\mathrm{d}t}{\Delta n^2(t_0) - \Delta n^2(t_1)}. \tag{2.13}$$

This gives the effective lifetime, τ_{eff}, in the range $[t_0, t_1]$, assuming a mono-exponential decay and $\Delta n \gg n_0$. This robust approach will be used to, in a high-throughput manner, determine the effective lifetime of thousands of samples in section 5.2 of this work.

2.2 Photovoltaics

One example of a type of optoelectronic device and the one used for the materials screening in section 5.2 is Photovoltaics (PV). Photovoltaics get their name from the photovoltaic effect mentioned in the previous section when discussing the absorption of light. These devices use the built up *voltage* of the *photo*-excited charge carriers and extract them over that voltage as electric power. The light used is typically the radiation from our sun and these electrical cells are therefore more commonly known as solar cells. In this section, a brief overview is given of the key performance parameters in solar cells as well as their limits. For a rigorous account of photovoltaics, the book by Würfel [20] is recommended for further reading.

2.2.1 Solar Cells

The two basic components of an MHP solar cell are: 1. the absorbing perovskite material where the charges are generated, which is referred to as the *absorber*, and 2. the charge selective contacts used to extract and separate the holes and electrons, known as the *p-contact* and *n-contact*, respectively. The incoming light is absorbed in the absorber, generating electron-hole pairs. The carriers drift and diffuse throughout the film and are extracted once they reach their respective selective contact or recombine before that according to one of the pathways discussed in the previous section.

If the two selective contacts are isolated from each other, i.e. the cell is in open-circuit condition, the carriers cannot be extracted and instead build up the open-circuit voltage, V_{OC}. If the contacts are instead connected, i.e. the cell is in short-circuit condition, the carriers will flow from one contact to the other in a short-circuit current, I_{SC}. The magnitude of this current will depend on the area of the solar cell and, therefore, it is sometimes useful to instead talk about the short-circuit current *density*, J_{SC}, defined as the short-circuit current per unit area. When the solar cell is at a large negative bias in the dark, thermally separated carriers will be extracted and a small current, known as the saturation current, I_0, will flow through the cell. This current is once again often defined as a current density, J_0.

When the cell is at open-circuit condition, no current can flow and, hence, no work can be performed by the cell. Similarly, when the cell is in short-circuit, no voltage can be established and no work performed. The current density, J, as a function of voltage, V, varies according to a diode curve (equation 6.30 in [20]):

$$J = J_0 \left(\mathrm{e}^{qV/k_{\mathrm{B}}T} - 1 \right) - J_{\mathrm{SC}}, \tag{2.14}$$

where k_{B} is the Boltzmann constant and T is the temperature. The difference in sign compared with [20] is due to here taking both J_{SC} and J_0 positive like for example in reference [8].

The extractable power is obtained by multiplying Equation 2.14 with the voltage. The current density and voltage maximizing the power are referred to as J_{MPP} and V_{MPP} with the subscript being an acronym for Maximum Power Point (MPP). The product of $J_{\mathrm{MPP}} \cdot V_{\mathrm{MPP}}$ will be less than that of $J_{\mathrm{SC}} \cdot V_{\mathrm{OC}}$ and the factor $(J_{\mathrm{MPP}} V_{\mathrm{MPP}})/(J_{\mathrm{SC}} V_{\mathrm{OC}})$ is known as the Fill Factor (FF). This means that the maximum power can be written as $FF \cdot I_{\mathrm{SC}} V_{\mathrm{OC}}$.

The Power Conversion Efficiency (PCE) of the solar cell, often denoted by η, is then finally given by:

$$\eta = \frac{FF \cdot I_{\mathrm{SC}} V_{\mathrm{OC}}}{P_{\mathrm{in}}}, \tag{2.15}$$

where P_{in} is the power of the incoming light.

The fill factor will depend on the diode behavior of the solar cell but an approximation for an ideal diode is given by equation 4 of reference [21] to be:

$$FF \approx \frac{\frac{qV_{\mathrm{OC}}}{k_{\mathrm{B}}T} - \ln\left(\frac{qV_{\mathrm{OC}}}{k_{\mathrm{B}}T} + 0.72 \right)}{\frac{qV_{\mathrm{OC}}}{k_{\mathrm{B}}T} + 1}. \tag{2.16}$$

2.2.2 Detailed Balance Limit

As part of this work, high-throughput screening of a material library is performed to judge the suitability of each sample of material for use as a PV absorber. One way to judge such suitability is by estimating the power conversion efficiency limit of a potential cell from the material properties of the bare absorber. The first attempt of doing so was by Shockley and Queisser in 1961 [22] where they derive the detailed balance limit, which is now commonly known as the Shockley-Queisser limit. This limit is based on a single material property, the band-gap, E_g.

In the Shockley-Queisser model, the absorptance of the semiconductor is assumed to be step-like at the band-gap, i.e. 0 for photon energies below the band-gap and 1 for energies above. Furthermore, the model is applied in the limit where all recombination is radiative as discussed above. However, the model can be extended to instead use measured values of the absorptance as a function of photon energy. The fraction of incoming photons that are absorbed and extracted as current at short-circuit is called the External Quantum Efficiency (*EQE*). The *EQE* is defined as a function of the incoming photon energy and, if the diffusion length of the carriers is much longer than the thickness of the absorber, it can be approximated by the absorptance of the film. The current density at short-circuit is simply given by the *EQE* multiplied by the number of incoming photons per unit area and the elementary charge, q, integrated over all photon energies. For the incoming photon flux, Φ_sun, this is:

$$J_\mathrm{SC} = q \int_0^\infty EQE(E)\Phi_\mathrm{sun}(E)\mathrm{d}E. \tag{2.17}$$

Similarly, the radiative saturation current density, J_0^rad, is given by the thermal photoemission multiplied with the *EQE* and q, integrated over all photon energies according to the reciprocity theorem [23]. This gives the following expression [24]:

$$J_0^\mathrm{rad} = q \int_0^\infty EQE(E)\Phi_\mathrm{bb}(E)\mathrm{d}E, \tag{2.18}$$

where the thermal radiative recombination is given by the black body radiation flux:

$$\Phi_\mathrm{bb}(E) = \frac{2\pi E^2}{h^3c^2}\frac{1}{\mathrm{e}^{E/k_\mathrm{B}T}-1}. \tag{2.19}$$

The radiative limit for the open-circuit voltage can then be calculated by rearranging Equation 2.14 into:

$$V_\mathrm{OC}^\mathrm{rad} = \frac{k_\mathrm{B}T}{q}\ln\left(\frac{J_\mathrm{SC}}{J_0^\mathrm{rad}}+1\right). \tag{2.20}$$

In order to account for a drop in the open-circuit voltage due to non-radiative recombination, the fraction of absorbed photons that recombine radiatively at open-circuit conditions needs to be known. This is frequently measured by the Photoluminescence Quantum Yield (PLQY) and can be used to calculate the deviation from the radiative limit using equation 11 in reference [25]:

$$V_{\mathrm{OC}} = V_{\mathrm{OC}}^{\mathrm{rad}} - \frac{k_{\mathrm{B}}T}{q} \ln\left(\frac{1}{PLQY}\right). \tag{2.21}$$

A great summary of these equations can be found in reference [26].

The efficiency limit

The equations above are used together with the FF approximation to estimate the PCE limit of a material library of the MHP $\mathrm{Cs}_y\mathrm{Pb}_{1-y}(\mathrm{Br}_x\mathrm{I}_{1-x})_{2-y}$ in section 5.2 of this thesis. Here the theoretical result is shown in Figure 2.1, assuming a single band-gap step like absorptance, together with the different unavoidable losses as a function of band-gap. For this calculation, the reference solar spectrum AM1.5G [27], which represents the solar spectrum after traveling through 1.5 times the Earth's atmosphere, was used to calculate the incoming flux $\Phi_{\mathrm{sun}}(E)$ in Equation 2.17.

The J_{SC} was calculated from Equation 2.17 and the radiative saturation current from Equation 2.18. These two were combined in Equation 2.20 to calculate the radiative limit of the V_{OC}. This V_{OC} was used to estimate the FF using Equation 2.16 and all these quantities were combined in Equation 2.15 to calculate the efficiency limit as a function of band-gap. This limit is plotted as the blue field in Figure 2.1. The orange field is given by the total energy of all the photons with energy lower than the band-gap and the green by the total extra energy of photons with energy above the band-gap. The red field is given by the radiative loss ($J_{\mathrm{SC}} \cdot (E_{\mathrm{g}}/q - V_{\mathrm{OC}})$) and the purple field by the loss due to the FF being less than one ($J_{\mathrm{SC}}V_{\mathrm{OC}}(1-FF)$).

From Figure 2.1 it can be seen that in an ideal case only around 33 % of the incoming energy can be converted with the rest being lost to either photons with energy below the band-gap not contributing to the current, photons with energy above the band-gap quickly thermalizing to the CB minimum not contributing to the voltage, the radiative recombination lowering the voltage or simply due to the diode behavior meaning that $J_{\mathrm{MPP}}V_{\mathrm{MPP}} < J_{\mathrm{SC}}V_{\mathrm{OC}}$.

One way to increase the theoretical limit past what is shown above is to reduce the thermalization losses and the photons lost below the band-gap by using multiple absorbers with different band-gaps in so-called multi-junction devices. By using, for example, two absorbers, one of them can have a high band-gap and use the voltage potential of the high energy photons whilst the other can have a lower band-gap and collect the current generated from the photons that pass through the first absorber. With two absorbers, these multi-junction cells are typically referred to as tandem devices. In order to maximize the gain from a tandem device the band-gaps need to be matched requiring tunability of this material property, see for example reference

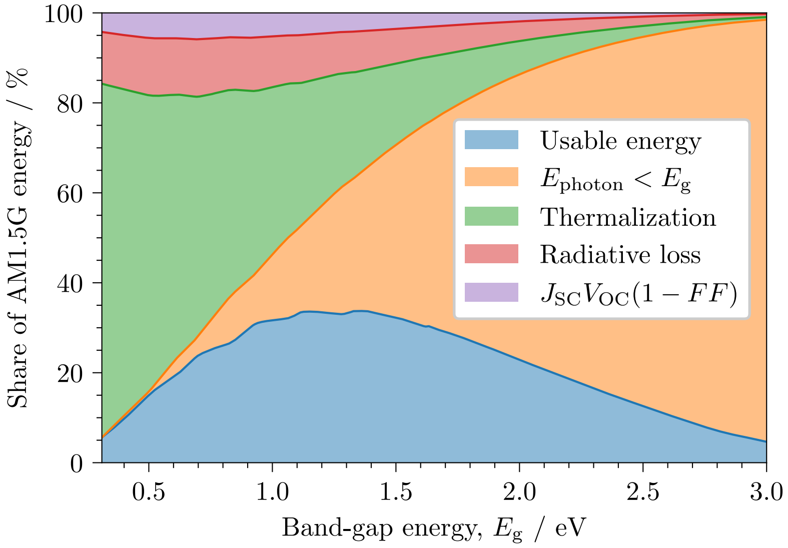

Figure 2.1: The Shockley-Queisser limit for AM1.5G illumination as a function of band-gap in blue with the losses due to thermalization in green, lost photons with energy below the band-gap in orange, unavoidable radiative recombination in red and the FF in purple.

[28] for details. This band-gap tunability is one of the important features of MHPs and will be discussed in subsection 2.3.4 below.

2.3 Metal Halide Perovskites

One example of a semiconductor material class that has been successfully employed in PV and other optoelectronics is the Metal Halide Perovskites (MHPs). Some of these materials form direct band-gap semiconductors with long charge carrier lifetimes and high absorption coefficients.

In this work, this material class is used as an example when investigating combinatorial synthesis and high-throughput analysis for optoelectronics. This section, therefore, aims to give the background needed to understand the material class as well as state some of the open scientific questions that still need answering.

2.3.1 Perovskite Definition

Metal Halide Perovskites (MHPs) get their name from the crystal structure they form, the perovskite structure. Perovskites were first discovered in the form of $CaTiO_3$ in 1840 by Rose [29] and its crystallographic structure was determined in 1926 by Goldschmidt [30]. A perovskite structure is formed by ABX_3 compounds where the B-site cation is octahedrally coordinated to the X-site anion and these octahedra are all-corner sharing in a 3D network [31]. An example of the unit cell for the cubic $Pm\bar{3}m$ perovskite structure is shown in Figure 2.2.

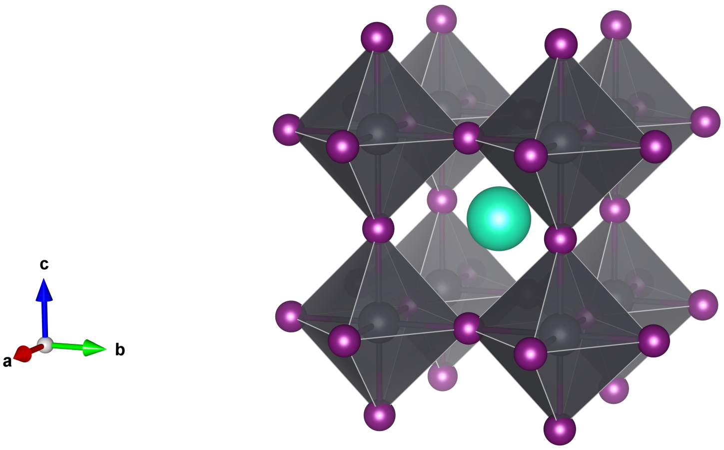

Figure 2.2: Extended unit cell of the cubic $Pm\bar{3}m$ perovskite structure ABX_3. The X-site is shown in purple spheres, the B-site in the gray spheres inside the X_6 octahedra and the A-site in the green sphere in the center of the cuboctahedral cavity formed by the BX_6 octahedra. The figure was drawn in the `VESTA 3` software [32].

In the case of MHPs, the B-site cation is a metal, typically Pb^{2+} or Sn^{2+}, and the X-site anion is a halide, typically I^{1-}, Br^{1-}, or Cl^{1-}. Typical A-site cations are Cs^{1+} or the organic compounds Methylammonium (MA), $[CH_3NH_3]^{1+}$, or Formamidinium (FA), $[CH(NH_2)_2]^{1+}$. MHPs were discovered already in 1893, in the form of $CsPbX_3$ (X = I, Br, Cl), [33] and their crystal structure confirmed as early as 1958 [34]. The hybrid $MABX_3$ (B = Sn, Pb and X = I, Br) were discovered later with their perovskite structure shown in 1978 [35, 36].

The A-site cation is in theory not constrained to a specific type but in practice, its size will be constrained by the volume of the octahedral cavity formed by 8 all-corner sharing BX_6 octahedra. This constraint was formalized in the original paper by Goldschmidt [30] where he defines the geometric tolerance factor, α, and his definition can be rewritten as:

$$\alpha = \frac{\sqrt{2}(r_\mathrm{A} + r_\mathrm{X})}{2(r_\mathrm{B} + r_\mathrm{X})}, \tag{2.22}$$

where r_A, r_B and r_X are the ionic radii of the A,B and X-site ions, respectively. This relation is simply given by the size along the diagonal, $2(r_\mathrm{A} + r_\mathrm{X})$, divided by the face diagonal of the cube, $\sqrt{2}a$, shown in Figure 2.2, over the size along a side, $2(r_\mathrm{B} + r_\mathrm{X})$, divide by the side of the cube, a. In other words, it is the lattice parameter based on the size of the A-site cation divided by the size based on the B-site metal. If α is above 1 the A-site cation is too big to fit inside the cuboctahedral cavity. Goldschmidt notes that while smaller cations, than for $\alpha = 1$, are allowed, the structure will collapse when α goes below around 0.8. The tolerance factor will be discussed further and its effects studied as part of the main results of this work in section 5.1.

2.3.2 Applications

Although MHPs were discovered already in 1893, it took until 2009 before the first optoelectronic devices made of lead halide perovskites were realized in the form of a $MAPbI_3$ solar cell [37] (not counting the layered structures from the 1990's [38]). Since then, the research field of MHPs has exploded with interest and it has been applied in various types of optoelectronic devices.

Photovoltaics

The device published in 2009 was a photovoltaic cell based on a dye-sensitized architecture and a liquid electrolyte but only a few years later in 2012, solid-state devices were shown based on $CsSnI_3$ [4] and later $MAPbI_3$ [39]. From 2012 and on-wards, photovoltaics has continued to be the main driving force for perovskite research and ten years later a search for "perovskite solar" from 2012-2021 in the BASE search engine (base-search.net) yields almost 22,000 publications.

In an effort to understand the development in such a rapidly growing field, a database was constructed in collaboration with J. Jacobsson, and numerous other co-authors, where up to 100 solar cell parameters were manually extracted from over 42,400 devices in more than 15,000 peer-reviewed articles [40]. All data is available openly and a set of interactive graphics can be accessed through the website perovskitedatabase.com. An example of such graphics, adapted from the original paper [40], is plotted in Figure 2.3. The PCE of all the devices from the database as a function of the publication year is shown in Figure 2.3a with the record efficiencies in Figure 2.3b.

From this figure it can be seen that the device efficiency has increased at a record pace and that the record devices are now on par with the industry workhorse silicon, which in contrast required almost 50 years of research to reach a record efficiency of 26.7 % [41]. The focus of MHP photovoltaics research has therefore been extended from pursuing higher PCEs to actually sustaining those efficiencies over the device's intended lifetime. One indication of this effort is the development of the fully inorganic $CsPb(Br_xI_{1-x})_3$ MHP (seen in orange, green, and red in Figure 2.3b) in an attempt to circumvent the inherent instability of the organic cations [42–44]. These devices have gone from 9 % PCE for $CsPbI_3$ in 2015 [45] (not counting failed attempt in 2014 [46]) to over 18 % for a fully inorganic mixed halide $CsPb(Br_xI_{1-x})_3$ in 2019 [47]. This approach and its challenges will be further discussed below in subsection 2.3.5 on $CsPb(Br_xI_{1-x})_3$.

In addition to the single junction devices shown here, MHP solar cells have perhaps had the biggest gains in the possibility of making tandem cells with Si. Recent tandem devices have reached almost 30 % PCE and show the advantage of the tunable band-gap in MHPs [48].

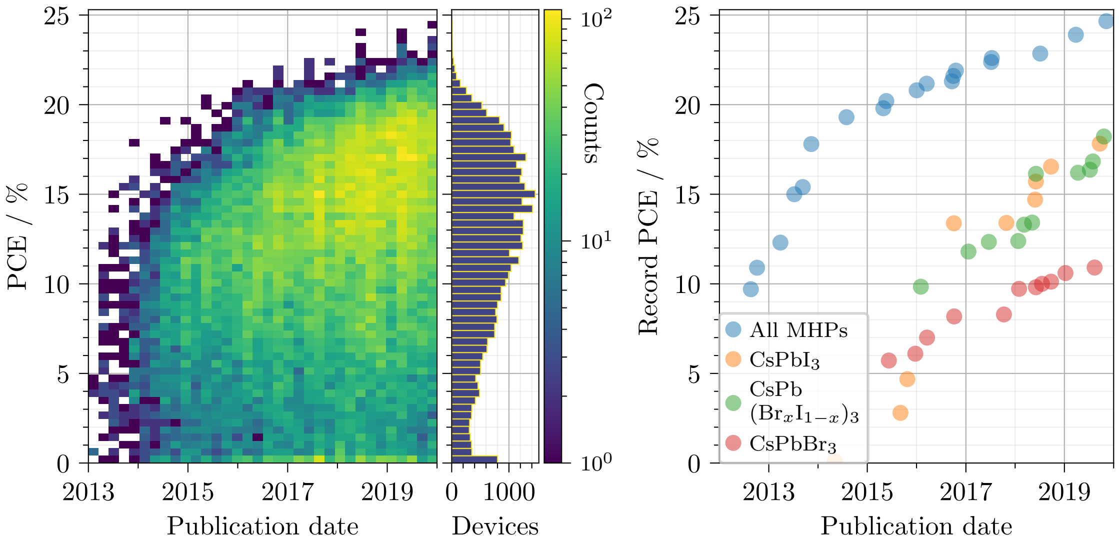

(a) All devices

(b) Record devices

Figure 2.3: Evolution of PCE for MHPs from the perovskite database [40] as reported in literature. (a) shows a 2D histogram as a function of PCE and publication date with the counts in color (blue low, yellow high). The histograms for all publication dates is plotted to the right. (b) shows the record evolution for all MHP devices in blue, $CsPbI_3$ in orange, $CsPb(Br_xI_{1-x})_3$ in green and $CsPbBr_3$ in red. Adapted from the data and Figure 3 in reference [40] under the *Creative Commons Attribution 4.0 International License* (available at creativecommons.org/licenses/by/4.0/). The data has not been changed but replotted in logarithmic scale in a new color scheme. The modified figure is available under the same licence.

Other optoelectronics

Since 2012, MHPs have been applied in a wide range of other optoelectronic devices. Most notably, perhaps, in the development of LEDs [5], where the tunable band-gap allows for bulk color tuning. Recently, MHP LEDs have even been produced by industry compatible inkjet printing [49]. In addition to the electroluminescence of LEDs, MHPs have also been used in a Light Amplification by Stimulated Emission of Radiation (LASER) [6, 50] and also here fabricated by inkjet printing [51]. Another application is in detectors where the high atomic number of Pb causes excellent absorption in X-ray detectors [52, 53] and the tunable band-gap in the visible range is ideal for photodetectors [7]. Recent work in collaboration with V. Schröder, even applied the combinatorial inkjet printing method presented in section 4.1 of this thesis to create a set of wavelength-specific photodetectors in a single deposition step [54].

2.3.3 Deposition Methods

One of the advantages of MHPs compared with other semiconductors used for optoelectronics is their low processing temperature [55, 56] and multitude of possible deposition methods. They have been processed in solid-state from ball milling [57],

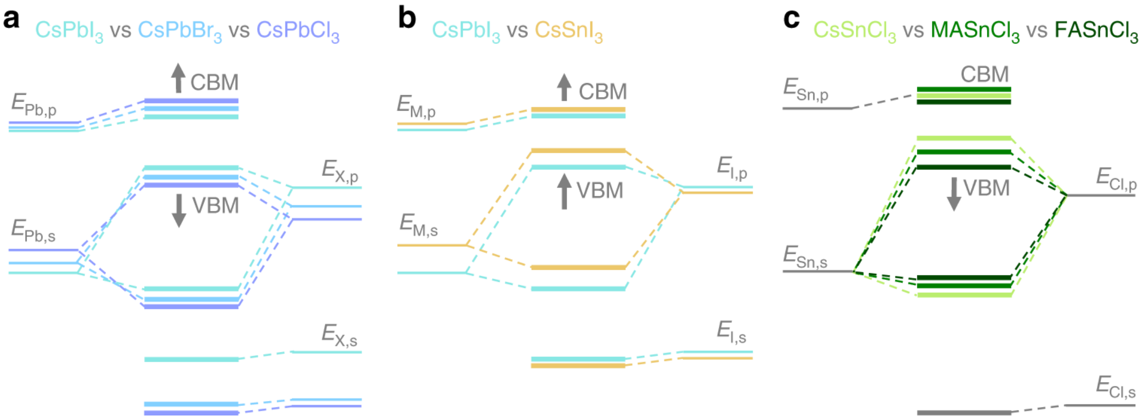

Figure 2.4: Schematic of the influence on the Valence Band (VB) and Conduction Band (CB) of changing the various ions in MHPs. Reproduced from reference [78] under the *Creative Commons Attribution 4.0 International License* (available at creativecommons.org/licenses/by/4.0/).

in vapor phase from evaporation [58–63] and perhaps most famously from solution through a myriad of different deposition techniques such as spin coating [64, 65], inkjet printing [66–75] and slot-die coating [76, 77] to mention a few. This makes this material class an excellent example material for validating and comparing different combinatorial synthesis methods as done in this work.

2.3.4 Band-Gap Tuning

Another advantage of MHPs is the tunability of one of the key parameters for an optoelectronic material, the band-gap. First, the band-gap can be changed by a complete substitution of one of the ions from 1.24 eV for FASnI$_3$ all the way to 3.55 eV for FASnCl$_3$ [78]. Secondly, many of the substitutions can be done partially and have been reported to form solid solutions. The first, and the most common, is the mixing of I and Br which was reported to change the band-gap continuously from 1.64 eV in MAPbI$_3$ to 2.39 eV in MAPbBr$_3$ [79]. In order to understand this tunability, the origin of the band-gap needs to be understood. The work by Tao et al. in 2019 [78] provides an excellent explanation from theory to experiments and a short summary will be given here.

The Valence Band (VB) in MHPs is formed by the antibonding state between the s-orbital of the B-site metal and the p-orbital of the X-site halide. The Conduction Band (CB) on the contrary, is formed by the antibonding state between the metal p-orbital and the halide s-orbital with the strongest effect from metal p-orbital. Tao et al. varied the A-site cation (Cs, MA, FA), the B-site metal (Pb, Sn), and the X-site halide (I, Br, Cl) and the resulting change is shown in the figure from their paper [78] reproduced here in Figure 2.4.

Starting from Figure 2.4c, the exchange of the A-site cation in ASnCl$_3$, from Cs to MA to FA, does not change any of the original states involved in forming the band-gap but instead influences the overlap between the metal and the halide through modulation of the lattice parameter by their size. As the small Cs ion is replaced by the large MA and finally the larger FA, the lattice expands. This causes a larger distance between the metal and the halide, which decreases the splitting of their bonding-antibonding states. This decreased splitting in turn increases the band-gap as is visible in Figure 2.4c. Interestingly, the opposite effect is shown for Pb-based MHPs and is attributed to low tolerance factor values for Cs and FA, causing tiltings of the structure leading to a reduced hybridization [78].

Figure 2.4b shows how the change in the original states of the metal influences the CB and VB differently but this is of less interest for the study in this work. Figure 2.4a, on the other hand, shows the combination of two effects and is important to understand for the discussion of the results in section 5.2 and section 5.3 of this work. As the small Cl is replaced with the large Br and the even larger I, the lattice spacing does increase, which would result in the same decrease in overlap and increase of band-gap as for the A-site cation if it were not for the strong effect of the electronegativity of the halide. This change in electronegativity is seen in the original X p-orbital and instead causes a net decrease in the band-gap when going from Cl to Br to I.

2.3.5 $\mathbf{CsPb(Br_xI_{1-x})_3}$

More specifically, than ABX_3 MHPs in general, this thesis uses fully inorganic perovskites with Cs at the A-site, Pb at the B-site, and a mixture of Br and I at the X-site. $CsPb(Br_xI_{1-x})_3$ was chosen as the example material for investigating the combinatorial synthesis and high-throughput analysis due to a number of advantageous properties. These were the main ones considered for this work:

1. The material can easily be deposited from both vapor phase and solution as opposed to for example MA-based perovskites which have hard to control evaporation rates.
2. The expected change in lattice parameter with halide ratio means that the compositional homogeneity can be investigated with X-ray diffraction techniques.
3. The band-gap changes drastically in the visible range meaning that large scale inhomogeneities are easily discernible by eye during the development process.
4. The material has been shown to be applicable for a wide range of optoelectronic applications such as PV and LEDs.
5. The band-gap is expected to be tunable in a higher range than MA or FA-based MHPs and is, therefore, especially of interest for the use in LEDs and multi-junction solar cells.

6. The inorganic nature of this MHP has gotten a lot of focus recently in an attempt to avoid the inherent instability of organic cations but many questions remain unanswered and lend themselves to a combinatorial investigation.

Here, the aim is to give the specific background on this material needed to understand the main results of this work in section 4.1 and chapter 5.

Crystal structure

Although the use of the inorganic Cs promises much better thermal and photostability than organic cations such as MA and FA, one of the main issues of $CsPbI_3$ has been its phase instability and transition to a non-perovskite phase. Additionally, when found, the perovskite phase of $CsPbI_3$ and $CsPbBr_3$ has often been missclassified as cubic due to the strong orientation of thin films. Here, an overview of the crystallographic phases is given in preparation for the investigation of the phase diagram of $CsPb(Br_xI_{1-x})_3$, which is determined as one of the main results of this thesis in section 5.1.

$CsPbI_3$ and $CsPbBr_3$ have been reported in several different crystal structures [80]. Additionally, $CsPbBr_3$ has been shown to form both Cs-rich inclusions of Cs_4PbBr_6 and Pb-rich inclusions of $CsPb_2Br_5$ [81]. A summary of all reported phases is shown in Figure 2.5 where the extended unit cell is drawn along the c direction for all the phases.

In the first crystallographic measurements of $CsPbI_3$ in 1958, Møller reported the orthorhombic *Pnma* phase seen in Figure 2.5d. From the drawing, the ratio of atoms is 1:1:3 and the octahedra are visible but they are not all corner-sharing and, therefore, fail to be a perovskite structure according to the definition in subsection 2.3.1 above. At a temperature of 587 K (314 °C), Marronnier et al. reported in 2018 that $CsPbI_3$ transitions to the cubic perovskite phase shown in Figure 2.5a [80]. This phase is the standard perovskite phase and is here referred to as the α-phase. As the sample was cooled down it was reported to transition to the tetragonal phase seen in Figure 2.5b at 554 K (281 °C) followed by the different orthorhombic structure seen in Figure 2.5c at 457 K (184 °C) [80]. These are both all-corner sharing perovskite phases and are here referred to as the β and γ-phase, respectively.

Stoumpos et al. showed in 2013 that $CsPbBr_3$ is stable in the γ-phase at room temperature and transitions to the β-phase at 361 K (88 °C) followed by the α-phase at 403 K (130 °C) [85]. There were no reports found where a δ-phase was observed for $CsPbBr_3$. All the measurements above were performed on powders and the exact transition temperature has been known to vary slightly from these values for thin films.

In addition to these phases with a 1:1:3 ratio of Cs:Pb:Br/I, there have been reports of the Pb-rich tetragonal *I4/mcm* phase, seen in Figure 2.5e, forming even in stoichiometric $CsPbBr_3$ films [81]. A Cs-rich phase was also reported in the form

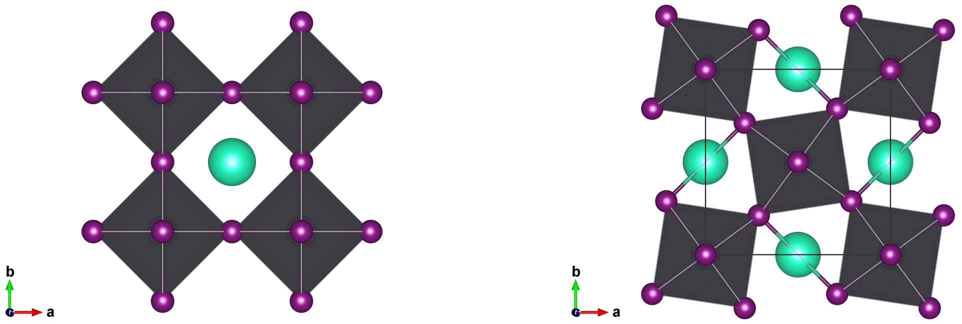

(a) Cubic perovskite $Pm\bar{3}m$ α-phase [80]

(b) Tetragonal perovskite $P4/mbm$ β-phase [80]

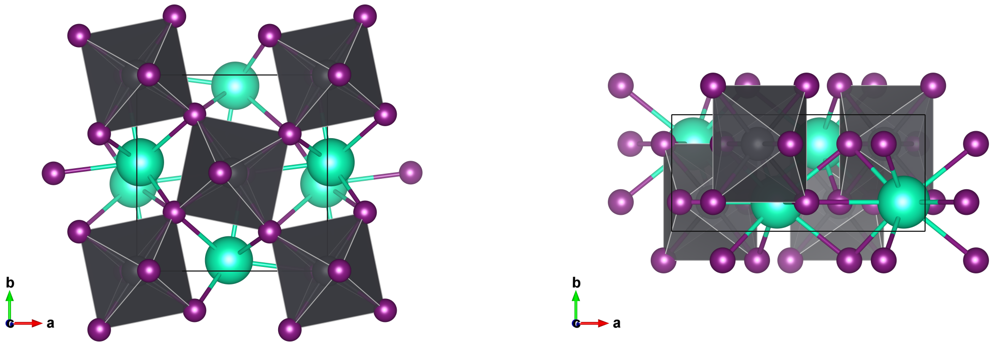

(c) Orthorhombic perovskite $Pbnm$ γ-phase [80]

(d) Orthorhombic non-perovskite $Pnma$ δ-phase [82]

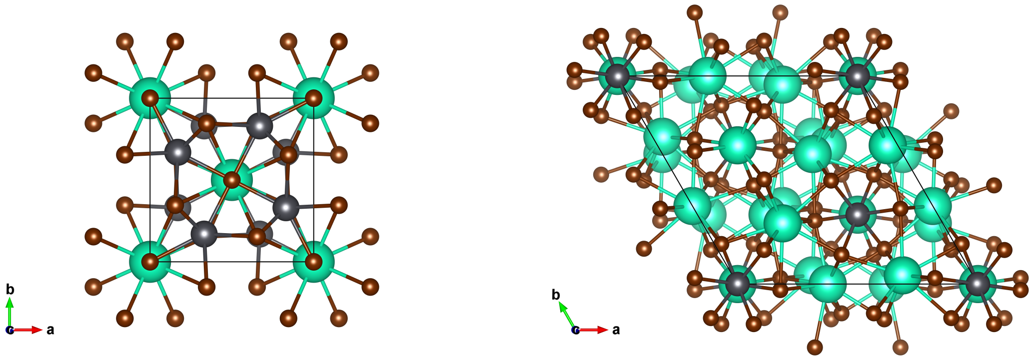

(e) Tetragonal non-perovskite $I4/mcm$ Pb-rich $CsPb_2Br_5$ phase [83]

(f) Trigonal non-perovskite $R\bar{3}cH$ Cs-rich Cs_4PbX_6 phase [84]

Figure 2.5: Extended unit cells of reported crystal structures for materials containing Cs, Pb, Br and I. (a)-(c) are found for both $CsPbI_3$ and $CsPbBr_3$, (d) for $CsPbI_3$ (e) for $CsPb_2Br_5$ and (f) for Cs_4PbBr_6 and Cs_4PbI_6. Cs is shown in green spheres, I in purple, Br in bronze and Pb in gray spheres (inside gray octahedra in (a)-(d)). All figures were drawn in the `VESTA 3` software [32].

of the trigonal $R\bar{3}cH$ phase shown in Figure 2.5f. These phases are not perovskite structures due to the deviation from the 1:1:3 atomic ratios.

One important thing to note when comparing the different polymorphs of $CsPbI_3$ and $CsPbBr_3$ is the change in the definition of the unit cell. For the α-phase the unit cell is defined with the Cs atom in the center and the corners at the four closest Pb atoms. As the symmetry is reduced in the $a-b$ plane for the β phase, the unit cell needs to be extended and is now rotated by $\pi/4$, increasing the length of the a and b parameters by $\sqrt{2}$. At a further loss of symmetry, and rotations also with respect to the c axis, in the γ-phase the unit cell is increased to include 2 "layers" of Cs atoms causing the c parameter to increase by a factor of 2. In order to compare changes in the lattice parameters across the phase transitions, the pseudocubic lattice parameters are defined as $a/\sqrt{2}, b/\sqrt{2}, c$ in the β-phase and $a/\sqrt{2}, b/\sqrt{2}, c/2$ in the γ-phase.

As Br and I are mixed together in $CsPb(Br_xI_{1-x})_3$ the mixed material has been shown to have lattice spacings that are approximately a linear combination of those for pure $CsPbI_3$ and $CsPbBr_3$ [86]. This indicates that the mixture forms a solid solution and follows Vegard's law which is an empirical law stating that the lattice parameters of a solid solution will closely resemble the linear combination of the two end species [87]. However, before this work, the crystal phases of the solid solution was largely unexplored and the measurements that had been done were on powders [88]. Additionally, the temperatures required for all the different phases had not been investigated and especially not for thin films. Determining the temperature-dependent phase diagram of the full $CsPb(Br_xI_{1-x})_3$ solid solution is one of the main results of this thesis and is presented in section 5.1.

Phase segregation

As was mentioned above, the band-gap tuning is of special interest in MHPs in general and more specifically in $CsPb(Br_xI_{1-x})_3$. The band-gap of $CsPb(Br_xI_{1-x})_3$ has been reported to vary close to linearly with the Br content from 1.77 eV for $CsPbI_3$ to 2.38 eV for $CsPbBr_3$ [86]. However, one challenge for any mixed Br-I MHP is the reported phase segregation under illumination. This effect was first reported by Hoke et al. in 2015 for $MAPb(Br_xI_{1-x})_3$ and is sometimes referred to as the Hoke effect [89]. The phase segregation of $CsPb(Br_xI_{1-x})_3$ under illumination was first observed by Beal et al. in 2016 [86].

The exact cause of the segregation is still being debated but what is clear is that for high Br compositions, under high-intensity illumination, domains of more I-rich phases tend to segregate. These I-rich domains have a lower band-gap and therefore charges are funneled there and recombine causing a shift of the observed photoluminescence. One proposed cause of the segregation is that the excited carriers tend to minimize their free energy by funneling to existing I-rich domains and causing these domains to grow by means of the mobile ions in MHPs [90]. According to this

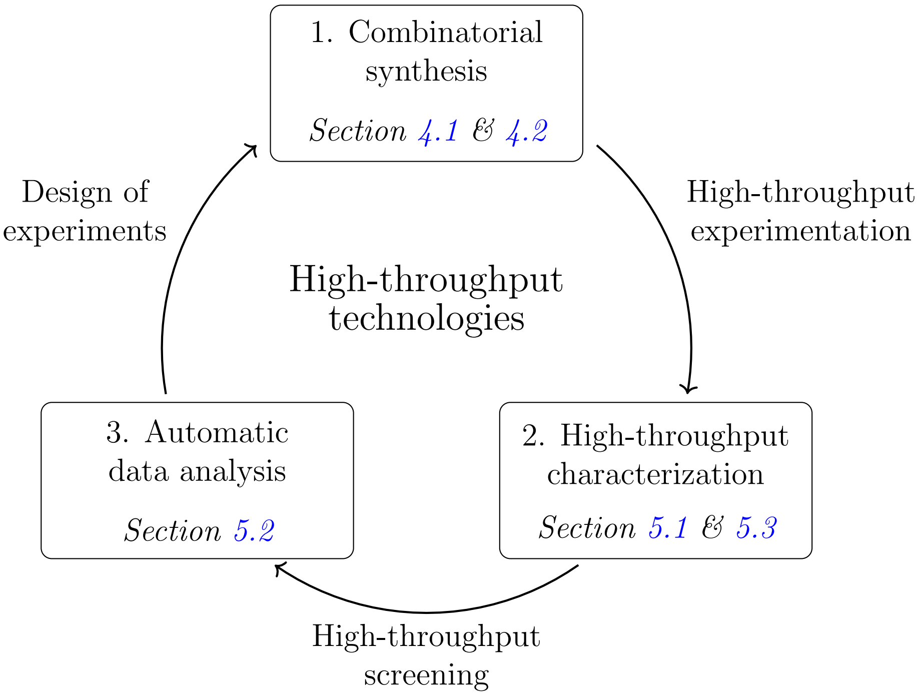

Figure 2.6: Schematic of the three components of combinatorial research.

theory, Cs-based perovskites can incorporate more Br in their structure than MA or FA based ones, and, combined with the already higher band-gap, this means that $CsPb(Br_xI_{1-x})_3$ shows the biggest potential for a tunable band-gap in the range of 1.75 to 1.95 eV.

2.4 Combinatorial & High-Throughput Research

In this final section of the fundamentals chapter, the concept of combinatorial research and high-throughput analysis is introduced and the vocabulary used throughout the thesis is defined. In addition, examples are given on the combinatorial background of the two methods of this work, inkjet printing and co-evaporation.

2.4.1 Definitions & Background

Various terms are used within the field of combinatorial and high-throughput research, often interchanged and used with slightly different meanings. Here, one interpretation of these terms is presented, with definitions of how these terms will be used in *this* work. The terms and their connection to the sections of this work are summed up in the schematic of Figure 2.6.

Combinatorial research

Combinatorial chemistry, or *combinatorial research*, was first defined in the 1990's with the International Union of Pure and Applied Chemistry (IUPAC) defining it as "Using a combinatorial process to prepare sets of compounds from sets of building blocks" [91]. This early definition was based on the work on peptides in the pharmaceutical field [92, 93] and was therefore oriented around "discrete elements belonging to finite sets". However, lately, the definition has been extended to also include continuous changes rather than just discrete [94–96].

The basic idea of combinatorial research is to create many samples at once, or in parallel, which are made up of a *combination* of different building blocks. This collection of samples, or continuous gradient, is referred to as a *combinatorial library*. The discrete elements or the investigated points in a gradient are then referred to as the *samples*. The key concept is *parallel* sample manufacturing rather than the traditional *serial* one.

As examples of parallel methods, combinatorial evaporation and combinatorial inkjet printing will be discussed further below as they are the two methods used within this work. Another example of combinatorial synthesis in the material field is the automation of traditional, serial, approaches such as drop-casting and spin coating. Specifically, this has been implemented in the field of MHPs to quickly produce sample libraries for stability studies [97].

Another concept that is closely interlinked with combinatorial research is that of *high-throughput experimentation*, where one or many parameters such as temperature, time, or pressure are varied [2]. This could either be during the deposition procedure, which in this work will be grouped under combinatorial synthesis, or during the measurements, which will here be grouped with characterization, see Figure 2.6.

High-throughput characterization

High-throughput characterization involves the rapid and often automated measurement of many samples. This can be performed in parallel using techniques like *imaging*, where the whole or large portions of the library are measured at once. It can also be performed in rapid succession by an automated movement of the library, which is typically referred to as *mapping*. The library of measured samples can either be prepared in a serial manner or combinatorially, in parallel.

One approach for achieving high-throughput characterization of optoelectronic materials is to employ *contact-less* measurements. This means that the material properties are measured without electrical contact, often optically, and therefore does not require the material to be made into a device or that a contact has to be established with every sample. This not only saves time in measurement but also in fabrication. In addition, it simplifies the system and allows to decouple absorber inherent issues from contact issues and, therefore, is generally desirable. One example of such a contact-less optical method is the use of hyper-spectral Photoluminescence (PL) imaging for the parallel measurement of PLQY, which can be used to calculate theoretical values for device parameters [98]. This and other contact-less methods for estimating device performance will be explored in section 5.2 of this work.

In addition to the parameters of interest for the performance of the device, the absolute variation in structural and compositional properties between the measured samples needs to be known [99]. This is sometimes known from the synthesis for serially produced samples, such as when accurately scaling precursors for deposition from solution. However, when using combinatorial synthesis methods it usually needs to be measured and, therefore, these measurements also need to be implemented in a high-throughput fashion.

High-throughput analysis

Once the samples have been measured, the last puzzle piece for a high-throughput workflow is the data analysis. *High-throughput data analysis* is not restricted to combinatorial libraries, or even high-throughput characterization, but is the automatic or parallel treatment of large sets of data. This is a vast field that spans most disciplines of science with increasing interest due to to the exponential increase in digital storage capacity over the last decades and the rapid development in the field of Machine Learning (ML) [100].

Here, the focus will be on its use in combination with high-throughput characterization, where one or multiple measurements are repeated over many samples and an analysis is performed to extract a parameter of interest. This search for a specific property is commonly known as *high-throughput screening*. This approach has been used in many fields, such as the pharmaceutical examples discussed above, but has also recently been employed in the field of MHPs [101].

High-throughput technologies

Finally, it is through the combination of all three of these technologies that materials research can truly be accelerated. The combination of these methods is sometimes collectively referred to as *high-throughput technologies* [2]. By using the results from the analysis of data from high-throughput experimentation to plan the *design of experiments* for the next iteration, a loop can be formed as indicated in Figure 2.6. Within optoelectronic materials research, a small scale example of such a loop has been shown for optimizing process parameters during rapid spray plasma processing of MHPs [102].

2.4.2 Co-Evaporation

Before the upswing of combinatorial research in the pharmaceutical sector, what would today be called combinatorial co-evaporation, was published already in 1965 with the work by Kennedy et al. [103]. In their paper, they show how the simultaneous evaporation from three e-beam sources onto a fixed triangular substrate directly creates a ternary diagram of compositions due to the distribution from each source. Similar studies were performed for sputtering by Miller et al. in 1967 [104] and in the more cited work by Hanak in 1970 [105]. In the work by Hanak, he defines the "multiple-sample-concept" which by some is considered the forerunner to combinatorial science [106].

Combinatorial co-evaporation is based on the fact that Physical Vapor Deposition (PVD) is a line-of-sight processes with sources that have an angular distribution in the amount of emitted material. This distribution causes a lateral gradient in the amount of material deposited on the substrate. By combining multiple sources a combinatorial library can be achieved with a gradient in composition. The PVD process will be explained in detail in section 3.1.2 and a process of thermal combinatorial co-evaporation is investigated thoroughly as part of the main results of this work in section 4.2.

Since the early works by Kennedy et al. and Hanak there have been numerous publications on combinatorial co-evaporation and a few examples will be listed here. In 2004, Mertens et al. showed the co-sputtering of Cr-Al-C and investigated the phase distributions using X-ray diffraction [95]. In 2005, Guerin and Heyden investigated a method of co-evaporation from Knudsen crucibles which is very similar to the approach taken in this work [94]. Klemm et al. presented similar work in 2010, where they also studied the distribution from the sources [96]. In general, combinatorial co-evaporation is often a natural result of the inherent distributions of the sources and the challenge of this method instead becomes to predict and control the process as well as understand the resulting library of samples. Therefore, the parameters needed for controlling the co-evaporation of $Cs_yPb_{1-y}(Br_xI_{1-x})_{2-y}$ are determined in section 4.2 of this work. Additionally, a method for high-throughput characterization of these libraries is explored in detail in section 5.2.

2.4.3 Inkjet Printing

Combinatorial inkjet printing is a solution based method for creating combinatorial libraries with a laterally controlled compositional variation throughout the printed film. This synthesis method is a less common approach than co-evaporation but has the advantage that the spatial control, inherent in inkjet printing, offers the ability to create discrete sample libraries. Combinatorial inkjet printing can be performed in multiple different ways but typically the compositional variation is achieved by the mixing of inks in a specified ratio. The method of inkjet printing, in general, will be detailed in the experimental section 3.1.1 where the setup used in this work is also presented.

One method of combinatorial inkjet printing is to simply prepare a set of inks combinatorially, i.e. mix them ex-situ before printing, through the well-established methods of the pharmaceutical sector and then load these in the printer one by one. This approach has been shown in literature, with Teichler et al. in 2010 using a pipetting robot to prepare different inks of polymer:fullerene blends for organic solar cells in a standard 96 well plate before printing them one by one [107]. This method has the advantage that it uses a well-established methodology but the material usage is typically higher than if the inks are mixed in-situ on the substrate and, fundamentally, the deposition process is still serial. Therefore, this thesis will focus on developing a method for in-situ mixing on the substrate during printing. The number of inks that can be mixed is, in theory, only limited by the number of printheads but for simplicity, this work will deal with two inks.

The controlled mixing of any number of inks can be reduced to controlling the amount printed, per unit area, of every single ink. Once that is controlled, the compositional mixing is attained by simultaneous printing at the desired ratios in any given area. There are several possible methods for controlling the amount of ink printed per unit area. Varying the printing resolution would be the most straightforward approach to this task but that becomes technically challenging when deploying more than a single printhead, as the resolution is typically controlled by the angle of the printheads and cannot be changed individually. Therefore, only methods where the printing resolution is kept constant are considered.

One such method is to vary the amount of ink in each droplet. This volume variation is known as grayscaling and requires specific printheads which can vary the drop volume in a fixed number of steps, usually not more than 16 [108]. The volume of the droplets is then varied throughout the film during the printing pass to create areas with different amounts of ink per unit area, see Figure 2.7a.

Another method for varying the amount of ink is to print multiple layers on top of each other in a multi-pass process. The variation throughout the film is then achieved by area selective printing during each pass causing different areas to have a different number of layers printed, see Figure 2.7b. A modified version of this approach has been used for creating libraries of MHPs by Chen et al. in 2019 and 2021 [109, 110] where a single-nozzle, 4-cartridge, printer was used to print $FA_yMA_{1-y}Pb(Br_xI_{1-x})_3$ mixtures in layers. This method has the advantage that the printing procedure is the same as for printing a single layer, just repeated. However, the time between passes and the inherited layering may cause inhomogeneities throughout the depth of the film.

A third method, and the one which is implemented in this thesis, is to vary the number of droplets printed throughout the film in a single printing pass. A variation in the amount of ink deposited is then achieved by locally controlling the number of droplets printed per unit area, see Figure 2.7c. This method has the advantage that no specific hardware is necessary and that the film is printed in a single layer for better homogeneity throughout the thickness of the film. However, until now there were no easy to implement methods for generating the images required for this droplet variation method. Therefore, this thesis presents a new algorithm for

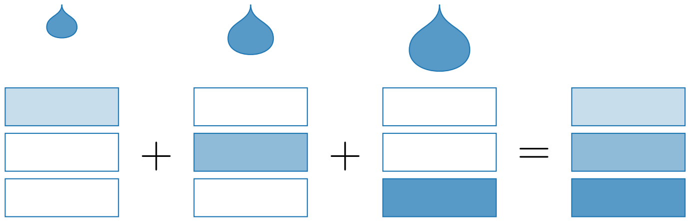

(a) Grayscaling

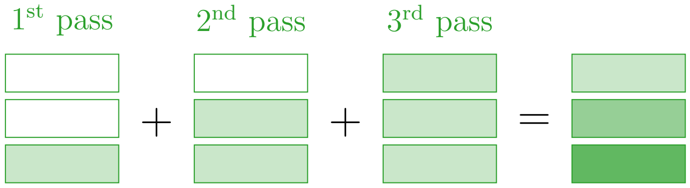

(b) Multi-pass

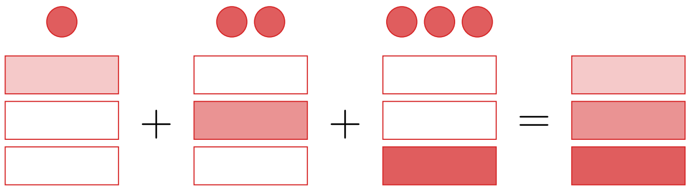

(c) Drop control

Figure 2.7: Schematic of different methods of varying the amount of ink printed per unit area. (a) Shows how printing different areas with different drop volume causes a variation, (b) how printing different number of passes causes a variation and (c) how varying the number of droplets printed in each area causes a variation.

droplet placement and the methodology, as well as validation of this, is presented in section 4.1.

Chapter 3

Experimental Methods

This chapter provides a detailed explanation of the deposition and characterization setups used for generating the results in chapter 4 and chapter 5. For each subsection, the key concepts of the method are briefly introduced and are followed by an in-depth account of the experimental setup and methodology as it is implemented in this work.

3.1 Sample Deposition

In this section, the experimental details of the two deposition methods employed in this thesis are explained. First, the deposition by inkjet printing is detailed followed by physical vapor deposition. This section is not explaining the combinatorial use of these methods as that is treated in detail in chapter 4.

3.1.1 Inkjet Printing

Inkjet printing was used in this work to prepare combinatorial libraries of $\mathrm{CsPb(Br}_x\mathrm{I}_{1-x})_3$ in various geometries. A brief introduction to inkjet printing is given here with the purpose of preparing the reader with the information needed to understand this work. This introduction is not an exhaustive description and for details, a textbook such as reference [111] is recommended.

Fundamentals

Inkjet printing is a solutions-based deposition method where a material is selectively printed on a given substrate. The precursor material in solution, that is to be deposited, is typically referred to as an ink. This ink is extruded from a small opening known as a nozzle and forms a droplet that falls onto the substrate. There are multiple types of nozzles and ejection mechanisms but this work will only concern Drop-On-Demand (DOD) types, ejecting the ink by means of a piezoelectric element.

In a DOD inkjet printer the ink is ejected from the nozzle as a droplet, when instructed to do so, i.e. on-demand. For piezoelectric nozzles, the ink is jetted out of the nozzle through the deformation of a piezoelectric element and forms a droplet as it detaches. Single nozzle printers exist but here a collection of nozzles are used in a fixed array known as printhead. This array is then moved across the substrate and the nozzles are activated where ink is to be deposited. The positions where ink is to be deposited are set by the images sent to the printing software. The time for ejecting the droplet is then calculated so that it, with its given velocity and nozzle position at ejection, ends up where instructed by the image. With an exception for the exact ejection mechanism, this is in principle how a common inkjet printer at home works when printing out, for example, one's dissertation.

One key parameter for printing is the minimum spacing between the centers of two droplets and it is typically measured by how many droplets there are per unit length, historically measured in the imperial unit inch (1 inch=25.4 mm). This measure is known as the printing resolution and given in dots per inch (dpi). The resolution in the direction of the moving printhead is set by the firing frequency of the nozzles whilst the resolution in the perpendicular direction is set by the distance between the nozzles. In a printhead, the distance between the nozzles is typically fixed but in certain printers, the printhead assembly can be rotated to decrease the projected distance.

The volume of the ejected droplets is typically fixed based on the volume of the nozzle and for the printheads used in this work, the volume amounts to 30 pl.

Experimental setup

All inkjet printing in this work was done on a Pixdro LP50 printer. The printer was placed inside a N_2-filled glovebox and all printing was performed with < 5 parts per million (ppm) of H_2O and O_2. The printer was equipped with a dual Spectra assembly with place for two Spectra printheads. For all printing, piezoelectrically activated drop-on-demand Spectra SE-128 printheads with a 30 pl drop volume were used. The controller boards for the printheads, by Pixdro called ”head personality boxes”, were placed outside the glovebox through the means of custom extension cables in order to protect the sensitive electronics from evaporated solvent. The glovebox was fitted with a laminar flow unit to minimize the risk of dust particles clogging the nozzles or ending up in the printed films.

$CsPb(Br_xI_{1-x})_3$ ink preparation

The inks were prepared by scaling and mixing in separate N_2 gloveboxes and transferred in N_2 to the printer glovebox. The two inks used for all printed samples were composed of $CsPbI_3$ and $CsPbBr_2I$, respectively. The $CsPbI_3$ ink was prepared by first scaling and dissolving 4 mmol of PbI_2, procured from TCI with a purity of $\geqslant 99.99$ %, in 3 ml of Dimethyl Sulfoxide (DMSO), from Sigma Aldrich with a purity of ⩾ 99.9 %. This solution was then used to dissolve a scaled amount of 4 mmol of CsI, from ABCR with a purity of ⩾ 99.999 %. The $CsPbBr_2I$ ink was prepared by scaling and dissolving 4 mmol of $PbBr_2$, procured from TCI with a purity of ⩾ 99.99 %, in 4 ml of DMSO and used to dissolve a scaled amount of 4 mmol of CsI. Both solutions were left in a shaker at 60 °C for 12 hours. All purities are given on trace metal basis.

After transferring to the printer glovebox with laminar flow, 1 ml of Dimethylformamide (DMF) was added to the $CsPbI_3$ ink in order to increase the evaporation rate. Both inks were filtered through 0.45 µm Polytetrafluoroethylene (PTFE) filters into the reservoirs right before printing to avoid any precipitates clogging the nozzles.

Substrate cleaning

As-purchased substrates were ultrasonicated for 15 min in a Mucasol® solution, deionized water, acetone, and isopropanol, consecutively, with a rinse of deionized water between each solvent. For the final step, the substrates were left in isopropanol until needed. Shortly before use they were taken from isopropanol and dried with pressurized N_2 gas before being placed in a UV-ozone cleaner (FHR UVOH150 LAB) for 20 s and taken directly to an adjacent, N_2-filled, glovebox.

Printing

The printheads were purged with DMSO prior to printing and the filtered inks were injected with a syringe in one inlet, through the top of the printhead, into another syringe mounted as the reservoir on the opposite port. The under-pressure in the reservoir was adjusted to the point where no ink flowed through the idle nozzles. Before printing, the nozzles were tested and, crucially for the combinatorial printing method, any clogged or miss-firing nozzles were deactivated.

All printing was performed unidirectionally with the same resolution in x and y direction set through the rotation of the assembly and the printing speed. The printing was done without heating the print-bed or the ink.

Annealing

To evaporate part of the solvent prior to annealing the printed library was moved directly from the printer into the small antechamber of the glovebox which was then evacuated to roughly 100 Pa. The library was left in the antechamber for 450 s before the antechamber was refilled with N_2 from the glovebox. Once the antechamber was at equal pressure with the glovebox, the library was returned to the glovebox and placed on a 100 °C hotplate for 60 min to crystallize the film and drive out any remaining solvent.

3.1.2 Physical Vapor Deposition

PVD is used as the other deposition method in this thesis and the key concepts of PVD and the theory of operation of a Quartz Crystal Microbalance (QCM) are here introduced. In addition, the custom evaporation chamber and method used for performing co-evaporation of $Cs_yPb_{1-y}(Br_xI_{1-x})_{2-y}$ is explained. Meanwhile, the details on combinatorial evaporation is left for section 4.2.

Fundamentals

PVD is the process by which a solid material is deposited onto a surface through evaporation, transport in the gas phase, and finally condensation. The main way that PVD differentiates itself from Chemical Vapor Deposition (CVD) is that the material to be deposited is in solid phase and that the transport is in a low-pressure environment [112].

In co-evaporation, multiple materials are evaporated at the same time inside the PVD chamber and intermix as they are co-deposited on the substrate. Typically, the substrate is rotated during deposition, to average out any distribution offsets between the sources. However, in this work, the rotation is omitted and the variation is used in a combinatorial approach which is explained in detail in section 4.2.

In this work, the material is evaporated through radiative heating of sealed ceramic crucibles with a small pinhole opening for the material to effuse from. This type of crucible is often referred to as a Knudsen cell [112]. One advantage of such a cell is that the material effusing from it typically follows a very defined cosine distribution in terms of effused material along any given direction, as a function of the angle with the source normal. This distribution will be discussed further in section 4.2 where a numerical model is constructed for estimating mixing ratios of co-evaporated materials during combinatorial co-evaporation.

Quartz crystal microbalances

In order to control the PVD process, a measurement of the rate of evaporation as well as the accumulated thickness is required. This is especially important for co-evaporation where a specific ratio of the co-evaporated materials is needed. This measurement is typically performed by employing a so-called Quartz Crystal Microbalance (QCM), which can measure very small changes in the mass of a material deposited on top of it. The QCM is placed in line-of-sight of the evaporation source so that material is deposited on it during the evaporation. The measurement is done by detecting the change in resonance frequency of an AT-cut quartz crystal and relating that frequency shift to the thickness of material deposited on top of it.

Equation 6 from reference [113] relates the mechanical resonance frequency of the deposited film, ν_f, with that of the bare quartz crystal, ν_q, and the compound resonator of the two combined, ν_c:

$$\tan\left(\frac{\pi\nu_c}{\nu_q}\right) = -\frac{\rho_f v_f}{\rho_q v_q}\tan\left(\frac{\pi\nu_c}{\nu_f}\right), \tag{3.1}$$

where ρ_f and ρ_q are the densities of the deposited film and the quartz crystal, respectively, and v_f and v_q are their shear-wave velocities. The shear wave velocity, v_f, is related to the resonance frequency and the film thickness, l_f, through [113]:

$$\nu_f = \frac{v_f}{2l_f}. \tag{3.2}$$

The shear-wave velocity of the quartz crystal, v_q, is more commonly referenced to in terms of its frequency constant, N_q, which is known, and they are related through $v_q = 2N_q$ [113]. The shear-wave velocity of the film, v_f, on the other hand is an unknown that therefore needs to be determined in order to use the measured ν_c and the known ν_q to calculate the film thickness, l_f, using Equation 3.2 and Equation 3.1. Instead of directly determining v_f the ratio of the acoustic impedance of the film and the quartz crystal is typically determined. This ratio is defined as:

$$Z = \frac{\rho_q v_q}{\rho_f v_f}. \tag{3.3}$$

As this is generally an unknown, the Z-ratio becomes an important parameter that needs to be determined for each material to correctly measure the amount being deposited. For unknown materials a Z-ratio of 1 is usually assumed.

Inserting Equation 3.2 and Equation 3.3 into Equation 3.1 and rearranging, using the trigonometric identity $\tan\theta = -\tan(\pi - \theta)$, gives:

$$\arctan\left(Z\tan\left(\frac{\pi(\nu_q - \nu_c)}{\nu_q}\right)\right) = \frac{2\pi\nu_c l_f}{v_f}. \tag{3.4}$$

In order to remove the last v_f from the equation, another Z as well as N_q is introduced and, after rearranging, this yields the following expression for the film thickness of the deposited material on the quartz crystal:

$$l_f = \frac{\rho_q N_q}{\pi\nu_c\rho_f Z}\arctan\left(Z\tan\left(\frac{\pi(\nu_q - \nu_c)}{\nu_q}\right)\right). \tag{3.5}$$

The equation above gives the thickness of the material deposited on the QCM but what is typically of interest during evaporation is the thickness of the material deposited on the *substrate*. However, these two thicknesses are directly proportional by a geometric constant, commonly referred to as the tooling factor, f_t. The tooling factor is defined as the ratio between the amount of material deposited per unit area on the substrate and that deposited on the QCM. By multiplying the QCM film thickness, l_f, with the tooling factor, f_t, the following expression for the thickness deposited on the sample, l_{sample} is finally attained:

$$l_{\text{sample}} = f_{\text{t}} \frac{\rho_q N_q}{\pi \nu_c \rho_f Z} \arctan\left(Z \tan\left(\frac{\pi(\nu_q - \nu_c)}{\nu_q} \right) \right). \tag{3.6}$$

Experimental setup

For the co-evaporation done in this thesis, a custom-built 4-source PVD chamber was used. The details of the chamber are explained in the dissertation of P. Becker [114] and was for this work extended with two additional sources and a new shutter mechanism. The chamber is built inside a N_2-filled glovebox, ensuring that the substrates can be loaded and the deposited films be extracted without exposing either of them to ambient conditions. The chamber is connected to a rotary vane pre-vacuum pump and a turbomolecular pump bringing the chamber pressure down to around $3 \cdot 10^{-6}$ Pa.

A section of the Computer Aided Design (CAD) drawing of the chamber interior is shown in Figure 3.1. The 4 heating sources in the bottom, labeled 1-4, have space for ceramic crucibles and are angled towards the center of the substrate suspended above. The substrate is mounted in a ceramic tray and pressed against a heating element for temperature control during the deposition. The temperature of the heating element is measured with a thermocouple and controlled by a Eurotherm 3054 Proportional Integral Derivative (PID) controller. The four QCMs used for detecting the rate of evaporation from each of the four sources, respectively, are mounted in the top of the chamber around the substrate. The QCMs are shielded by tubes as well as a plate between the sources to ensure that each QCM is only exposed to material from a single source. The substrate is protected by a motorized sliding shutter which can be opened once the evaporation rates are stable at their desired values.

The four QCMs are connected to two Inficon STM-2XM controllers for measuring the frequency of the quartz crystal and converting it to a film thickness, according to the equations above. The cumulative thickness during evaporation is logged in the STM-2XM controllers while the rate is outputted as a proportional DC voltage signal and read with four Eurotherm 3504 PID controllers. These PID controllers in turn control the heaters of the sources in a closed loop with the measured rate. This means that the desired evaporation rate can be set and maintained, enabling co-evaporation at specific ratios.

Source material

For evaporating $Cs_yPb_{1-y}(Br_xI_{1-x})_{2-y}$ and its binaries, the materials were loaded into Knudsen crucibles made from Macor® ceramic. CsBr beads from Sigma Aldrich

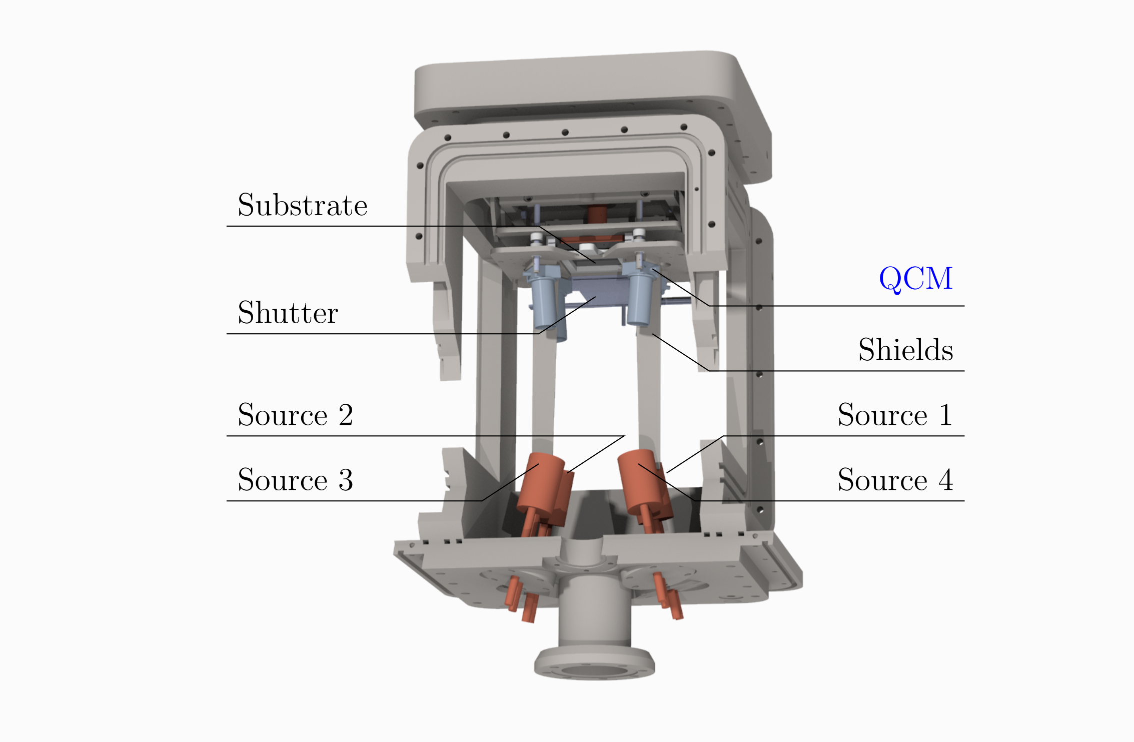

Figure 3.1: CAD drawing of the custom evaporation chamber used in this work. The orange evaporation sources in the bottom of the chamber are labeled 1-4 and they are angled at the indicated substrate position. The individual rates are measured by four QCMs, which are shielded from each other by the indicated shields. Before the rates are stabilized the sample is covered by a sliding shutter.

($\geqslant$ 99.999 %) were loaded into source 1, CsI beads from Sigma Aldrich ($\geqslant$ 99.999 %) into source 2, PbI_2 beads from Sigma Aldrich ($\geqslant$ 99.999 %) into source 3 and $PbBr_2$ beads from Alfa Aesar ($\geqslant$ 99.999 %) into source 4. All purities are given on trace metal basis. All precursors were used as purchased and the sealed glass vials they were delivered in were opened inside the N_2-filled glovebox and not exposed to ambient conditions at any time.

Substrate preparation

As purchased substrates were first labeled using a laser scriber. They were then cleaned in a Miele industrial washer IR6000 using Neod. Alka 240 and ProCoreLab 30C as process chemicals, dried, and transferred to a N_2-filled glovebox for storage. For the evaporation processes the substrates were mounted in the chamber without further treatment.

Deposition

For all depositions in this work, the substrate was heated to 50 °C. The substrate shutter was closed and the chamber pumped down to below $1 \cdot 10^{-5}$ Pa before the sources were heated to approximately 480 °C for CsBr and CsI and around 280 °C for

PbI_2 and $PbBr_2$. Once there was a consistent rate detected on the QCMs, the PID controllers were switched on and the rate left to settle to the intended value. When the rates were stable to within ±1 % of the intended value the shutter was opened and the cumulative counter started on the STM-2XM controllers. After the desired evaporation time, the shutter was closed and the heaters switched off. The sources and substrate were allowed to cool down to ambient values before the chamber was filled with N_2 and the deposited library removed.

3.2 Characterization Techniques

In this section the experimental details are provided for the various characterization setups deployed in chapter 4 and chapter 5.

3.2.1 Grazing-Incidence Wide-Angle X-Ray Scattering

Grazing-Incidence Wide-Angle X-ray Scattering (GIWAXS) is a frequently employed method in this thesis for determining the crystalline phases present in a combinatorial library. Here, a quick introduction to the method is given and the two different setups used are explained in detail.

Measurement theory

GIWAXS is an X-Ray Diffraction (XRD) method used for studying crystalline phases in materials. X-ray diffraction works on the principle that X-ray radiation traveling through a crystalline material gets partially scattered at a lattice plane and in two dimensions the diffracted beams will constructively interfere if the so-called Bragg's law [115] is fulfilled:

$$n\lambda = 2d\sin\theta, \tag{3.7}$$

where $n \epsilon \mathbb{N}^*$, λ is the wavelength of the X-rays, d is the lattice spacing and θ is the angle between the X-rays and the lattice plane. This can be understood as $2d\sin\theta$ being the extra distance that X-rays travel for each lattice plane they pass and if this is a multiple of the wavelength there will be constructive interference. This is illustrated in Figure 3.2.

By varying the angle θ and detecting the X-ray intensity a diffraction pattern will appear with peaks where Equation 3.7 is fulfilled. If there are many randomly oriented domains of lattice planes in the sample, the peaks can be used to model the crystal structure. This representation is typically enough when considering XRD of powders and scanning the X-ray source and detector in a plane. However, in GIWAXS the scattering is detected on an area detector meaning that a 3D representation is necessary.

For understanding 3D scattering it is helpful to consider the reciprocal lattice. If the incoming X-ray has the wave vector $\vec{k}_{\mathrm{i}}$ with magnitude $\|\vec{k}_{\mathrm{i}}\| = k = 2\pi/\lambda$

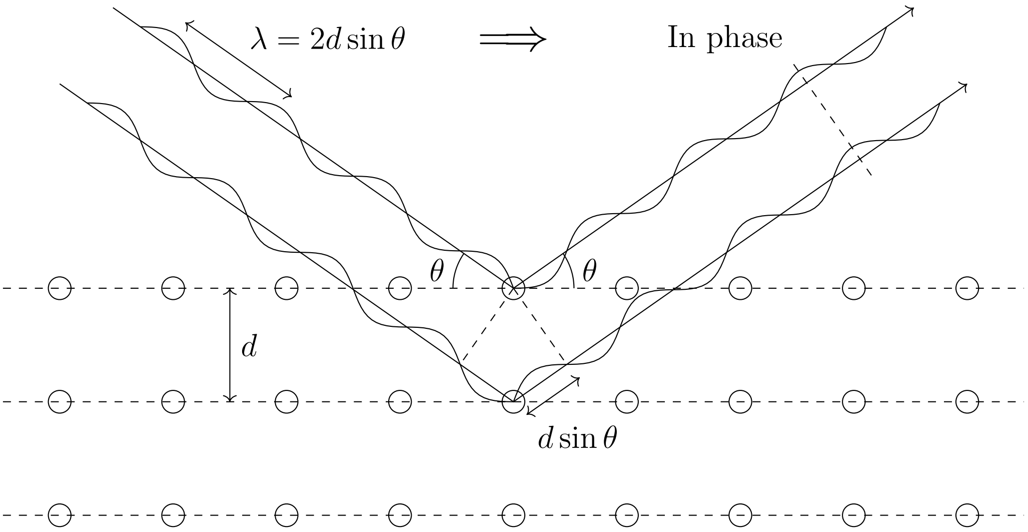

Figure 3.2: Schematic origin of Bragg's law with dashed lines indicating the lattice planes separated by a distance, d, and formed by the scattering centra drawn as circles. The X-rays are incoming at an angle, θ, to the sketched lattice plane and are drawn with a wavelength, $\lambda = 2d\sin\theta$, such that the extra path length of the wave diffracted at each lattice plane is exactly one wavelength. Note that integer multiples of the wavelength, $n\lambda$, also results in diffracted waves being in phase.

the elastically scattered X-ray wave vector $\vec{k}_\mathrm{f}$ will have the same magnitude but in a different direction. The momentum transfer is given by the scattering vector $\vec{q} = \vec{k}_\mathrm{f} - \vec{k}_\mathrm{i}$ and since the the magnitude of $\vec{k}_\mathrm{i}$ and $\vec{k}_\mathrm{f}$ are the same, $\vec{q}$ will be on a sphere known as the Ewald sphere [116]. If the origin of reciprocal space is placed at the position of the $\vec{k}_\mathrm{i}$ vector, the Bragg condition will be satisfied for any reciprocal lattice point at the surface of the sphere.

In GIWAXS, the incidence angle is fixed at a low grazing inicidence angle to increase the interaction volume of the X-rays with the sampled material and the detection is performed on an area detector over a wide range of angles of the the scattered X-rays. Each point on the area detector corresponds to a scattered wave vector $\vec{k}_\mathrm{f}$ from which the scattering vector $\vec{q}$ can be calculated. If a bright spot is seen on the detector it means that the corresponding scattering vector is coinciding with a reciprocal lattice point. If the sample is a perfect powder the direction of $\vec{q}$ will not matter and a ring will instead be seen on the detector. By performing an azimuthal integration around the axis of the incoming beam a 1D pattern as a function of $||\vec{q}|| = q$ will then be attained. Each value of q corresponds to a lattice spacing through $q = 2\pi/d$.

mySpot beamline at BESSY II

One setup used for GIWAXS was at the mySpot beamline at BESSY II, [117]. Here the source of X-ray radiation is the BESSY II synchrotron and the beam was, for the experiments shown here, monochromated to 9 keV. The beam was reduced in size by passing it through a 10 µm pinhole and the photon flux was thereby reduced to approximately $5 \cdot 10^{14}$ cm^{-2}s^{-1}.

The investigated combinatorial libraries were placed in a N_2-filled chamber with a large, domed, double Kapton window inside a glovebox. A small wire basket filled with molecular sieves was placed in the chamber to absorb any H_2O that would diffuse through the Kapton windows. The sealed chamber was then transferred to the beamline where it was placed on top of a xy-stage and goniometer. The space between the double windows in the chamber was then connected to a N_2 flow of 0.2 l/min with a 3 kPa overpressure valve on the outlet. For further details on the chamber, see reference [114].

Once the library was in place, it was aligned relative to the beam: first in the direction normal to the substrate, z, then in the direction parallel to the beam, y, and finally in the direction perpendicular to those, x. The library was also aligned along the two rotational axes around the x and y axes. The alignment of both rotational axes was needed for the mapping experiment to avoid having to do a z alignment at each measurement spot.

The aligned library was then rotated to the specific incidence angle needed and moved to the desired x, y position. The GIWAXS pattern was detected on a Dectris Eiger 9M area detector. In order to determine the exact position of the detector, in all 6 degrees of freedom, relative to the point of beam-sample intersection, a reference powder of LaB_6 was aligned and measured. From the known phase (cubic $Pm\bar{3}m$) and lattice parameters the relative position of the detector was fitted to the GIWAXS pattern using the `Python` library `PyFAI`.

Liquid metal-jet source

Another GIWAXS setup used was a high-flux lab source at the X-ray corelab facilities at Helmholtz-Zentrum Berlin. The X-ray source here is an Excillum liquid metal-jet source where the anode is a continuous jet of liquid metal. This has the advantage that the current can be increased past the point which would melt a traditional solid anode such as copper. The liquid alloy used for these experiments was a 75:25 Ga:In alloy and the acceleration voltage was set to 70 kV. The main energy used for the diffraction experiments was therefore the Ga K-L_3 line at 9.2517 keV [118].

The setup was used in two configurations, one with a Si PIN diode mounted on top for detecting X-Ray Fluorescence (XRF) and one with a fiber-coupled Charge Coupled Device (CCD) detector for detecting Ultraviolet/Visible Reflection and Transmission Spectroscopy (UV/Vis) transmittance. The details of these measurements are described below in section 3.2.2 and section 3.2.3, respectively. When the UV/Vis transmittance setup was used, a custom multi-layer focusing optics by AXO was mounted at the source. This both collimates the X-ray source and is tuned for the Ga K-L_3 energy, resulting in a monochromatic beam. Slits were placed close to the sample and the beam was cut down to have 1×1 mm^2 illuminated area on the sample. However, when mounted with the XRF detector the high-energy In contribution is needed to excite the core level electrons and the multi-layer optics could not be used. Instead, a polycapillary was used to focus the beam and a 25 µm Zn foil was placed in front of it to remove the Ga K-M$_3$ line.

The sample chamber used was a Linkam LTS420 heating stage with a modified lid fitted with a large Kapton window for X-ray transmission with a small quartz glass window just above the hotplate in the chamber. The quartz window was used together with the small hole in the hotplate for UV/Vis transmittance experiments whilst the Kapton window was large enough for GIWAXS and XRF measurements. The samples were loaded into the stage in air and, once the chamber was closed, it was flushed with N$_2$, first readily, to remove all H$_2$O and O$_2$ introduced from the air, and then at a rate of 0.2 l/min.

The hotplate temperature was controlled by a PID controller and the temperature logged. Additionally, a thermocouple was placed on top of the substrate at the edge of the hotplate. Using these two temperature readings the estimated sample temperature could be calculated using an ex-situ calibration performed through a ZnSe window using a thermal camera (Fluke TiS75, $\epsilon = 0.93$, temperature uncertainty 3 % [114]). This calibration was performed for a heating rate of 2.5 K/min and for other rates the hotplate or reference thermocouple temperature was instead used.

As the housing of the stage prevented 0° incidence, the height of the sample was aligned with a calibrated laser interferometer. There was no way to rotate the sample around the axis of the beam, so instead, the height alignment was performed for each measurement spot. Once the sample was aligned the incidence angle was set to the desired value and the GIWAXS pattern was collected on a Dectris Pilatus 1M area detector. The position of the detector relative to the sample-beam intersection was once again determined using a reference powder of LaB$_6$ and the `PyFAI` library.

3.2.2 X-Ray Fluorescence

X-Ray Fluorescence (XRF) measurements were performed on most combinatorial libraries of this thesis to determine the elemental composition of the films. Here, details of the two setups used are provided and the method is shortly explained.

Measurement theory

In an XRF measurement the elements of a material are probed through their characteristic energy levels. The sample to be investigated is irradiated with X-rays which can excite a core level electron. If that happens, another electron can fall down into the vacancy and emit a photon with the energy given by the difference in the two states. These secondary fluorescing photons are then collected and their energy analyzed, yielding the X-ray fluorescence spectrum. According to the IUPAC standard from 1991 [119], the fluorescence lines are labeled by the end and start level of the relaxing electron. For example, if an incoming X-ray excites an L_3 level electron in a Pb atom and an electron from the M_5 level relaxes down to that vacancy it will emit a photon with the characteristic energy of 10.5512 keV [118] and this fluorescence line is labeled L_3-M_5. This notation will be used predominantly in this thesis over the old Siegbahn notation where the L_3-M_5 line is known as $L\alpha_1$.

Due to these characteristic lines, the elements present in the sample can be deduced from a quantitative analysis of a calibrated spectrum. If additionally the intensity and the geometry of the XRF setup are known, the absolute amount of a material can be modeled to the measured spectra, taking attenuation and re-absorption into account.

Si PIN diode at metal-jet

One of the setups used was the setup at the metal-jet source explained above in section 3.2.1. Here the high energy contribution from the In was used to excite the core level electrons and the emission was detected by an energy dispersive Si PIN diode (Ketek AXAS-M). The Ga K-L_3 was used to calibrate the energy axis of the detector.

Bruker M4

Another setup used was a commercial ”M4 Tornado” from the company Bruker. The excitation source was a Rh tube and an electron current of 200 µA accelerated at 50 kV was used. Here the sample was placed in a vacuum chamber and the pressure was pumped down to below 100 Pa. The X-ray source was focused on the substrate by a polycapillary to a spot size of roughly 20 µm. The focus was adjusted using a camera with optics aligned to that of the X-rays. The spectrum was acquired for 100 s per spot and self-calibrated by the included software.

The spectra were modeled using the supplied ”XMethod” software by Bruker. The fitting is based on the known geometry of the setup and references measured for individual elements but Bruker does not disclose the exact fitting algorithm.

3.2.3 UV/Vis Transmission & Reflection Spectroscopy

Ultraviolet/Visible Reflection and Transmission Spectroscopy (UV/Vis) is used as one of three optical measurements in this work and here the technique is introduced followed by an explanation of the two different setups used.

Measurement theory

UV/Vis works by illuminating the sample with light in the ultraviolet to visible, and commonly also Near-Infrared (NIR), range. The transmitted and the reflected intensity are then detected and recorded. The light can either be monochromatic with a variable wavelength or polychromatic for which a dispersive spectrometer is used to detect the signal. The collection can be done either by measuring the direct transmission and specular reflection or by using an integrating sphere and also collecting the diffuse transmission and reflection. When using an integrating sphere the measurement is typically divided into measuring the reflection and transmission separately. For both measurement modes, the dark and bright references need to be collected to calculate the transmittance, T, and reflectance, R, of the sample. The transmittance and reflectance are the fractions of the transmitted and reflected power with respect to the power of the incoming light as a function of its wavelength.

For a strongly absorbing thin film on a substrate the absorption coefficient α is approximately given by:

$$\alpha \approx \frac{1}{d} \ln \left(\frac{1-R}{T} \right), \tag{3.8}$$

where d is the thickness of the film. The validity of this formula for the films studied in this work is discussed in section C.2.

Integrating sphere mapping

The first setup used was a custom-built UV/Vis mapper placed inside a N_2-filled glovebox. The setup was constructed from an integrating sphere (Avantes Ava-Sphere-50) suspended above an xy-stage, see Figure 3.3a. The sample port of the integrating sphere was reduced by a 1 mm pinhole and the sphere aligned to be approximately 1 mm above the surface of the sample. The detection port of the integrating sphere was connected by an optical fiber to a CCD spectrometer (Thorlabs CCS200/M). The illumination was provided by a stabilized halogen lamp (Thorlabs SLS201/M) which was connected to the setup via an optical fiber. For the transmission measurement, the fiber was connected to a collimating mirror and a lens under the sample, directly below the detection port of the integrating sphere. For the reflection measurement, the fiber was connected to the illumination port of the integrating sphere, which was fitted with a collimating lens and directed at the sample with an 8° angle to the sample normal. For the bright reflection reference, a silver mirror with known reflectance was measured (Thorlabs PFSQ10-03-P01) and for the bright transmittance the sphere was illuminated without a substrate or sample in the holder. The thin film sample to be measured was placed with the film side up, towards the integrating sphere.

Direct transmission

The second setup used was the GIWAXS setup at the metal-jet source explained above in section 3.2.1. Here the light from the same stabilized halogen lamp was collimated and reflected up, by a mirror, through the sample. The direct transmission was collected by suspending a split optical fiber with a double core, 25 mm above the sample, see Figure 3.3b. The light coupled into the fiber was detected

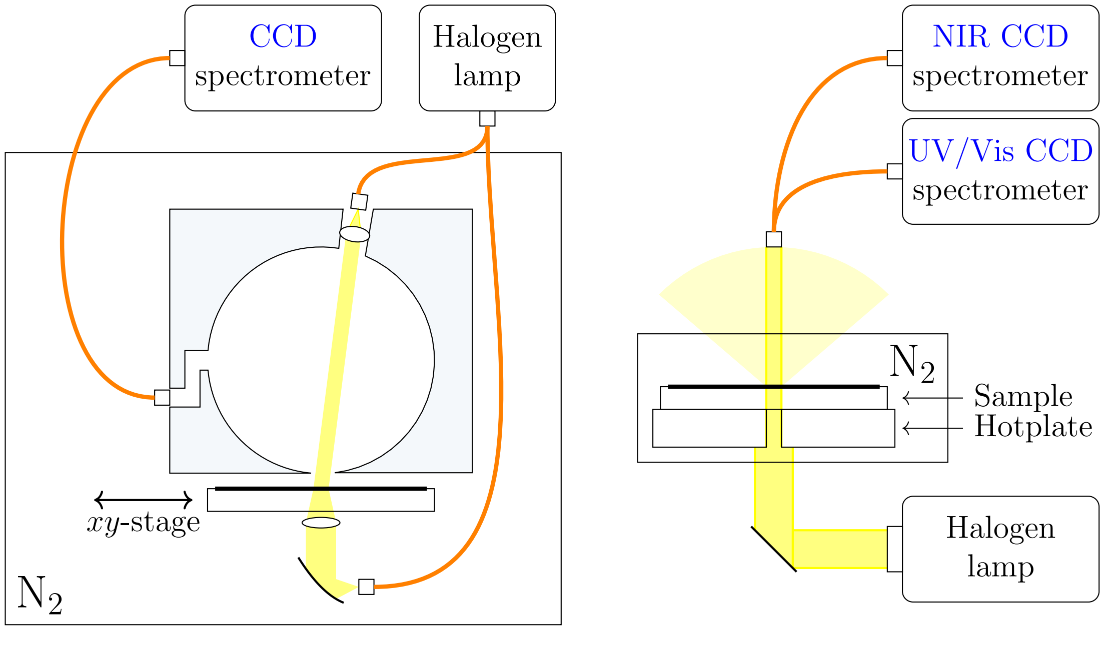

(a) Integrating sphere mapper

(b) Direct transmission at metal-jet

Figure 3.3: Schematics of the two UV/Vis setups used within this work. (a) Shows the integrating sphere mounted on top of the sample inside a N_2-filled glovebox. The sample is mounted on an xy-stage and the detection port is connected to a CCD spectrometer. In (a), only one light path is active at a time, i.e. either the fiber on the top port is connected for a reflection measurement *or* the fiber on the bottom is connected for a transmission measurement. (b) Shows the setup used at the liquid metal-jet source with the light being passed through an aperture in the hotplate and detected through a split fiber by a UV/Vis and a NIR CCD spectrometer. The sample is mounted inside a N_2-filled chamber with fused silica windows. In (b), only the light that is directly transmitted is collected by the fiber.

by a UV/Vis spectrometer (Ocean Optics Maya2000 Pro) and an NIR spectrometer (Ocean Optice NIRQuest). The two spectra were stitched together for the data analysis.

3.2.4 Steady-State Photoluminescence Spectroscopy

Photoluminescence (PL) in the steady-state, i.e. under continuous illumination, was used within this thesis to determine the energy of the radiatively recombining charge carriers as well as the fraction of carriers that do recombine radiatively. Here the theory of the measurement is introduced and the details of the two setups used in this work are provided.

Measurement theory

PL is the emission of a photon after the photo-excitation of a material. In an ideal direct band-gap semiconductor, this emission is dominated by the band-to-band transition of thermally relaxed carriers. By continuously exciting carriers with a high energy light source and monitoring the energy spectrum of the emitted photons, the difference in energy between the VB and CB can be determined. Additionally, if the number of incoming photons per unit area and time is known and the number of photons emitted is also measured, the fraction of excited carriers that recombine radiatively can be determined. This fraction is known as the Photoluminescence Quantum Yield (PLQY).

PL imaging

For measuring the PL energy and PLQY, a custom built and calibrated PL imaging setup was used. A schematic of this setup is shown in Figure 3.4a. The charge carriers in the samples were excited by a collimated high-power 445 nm LED (Thorlabs SOLIS-445C) mounted at a 45° angle to the substrate normal. The luminescence from the radiative recombination of the charge carriers was split by a dichroic mirror to allow for detection in two separate wavelength regimes by passing through two different tunable liquid crystal filters (Thorlabs KURIOS-WB1/M). In this work, only the high energy path was used and imaged onto a scientific Complementary Metal–Oxide–Semiconductor (sCMOS) camera (Thorlabs CS2100M-USB). A 500 nm short-pass filter was placed in front of the excitation source to cut off the low energy tail of the LED emission and an additional 500 nm long-pass filter was placed before the tunable filter to remove more of the excitation light.

Before measuring, the setup had previously been calibrated to measure the absolute number of photons emitted per unit area and time. This had been done by first imaging the emission of an integrating sphere, illuminated by a halogen lamp with a known spectrum, to get the spatial and spectral response. The absolute value of this response had then been scaled by collecting all emission from a fiber-coupled laser with the absolute number of photons emitted known from a measurement with a power meter. The details of this calibration procedure are explained in reference [98].

The focus was adjusted on a sample with equivalent thickness and the shutter of the LED was kept closed until the measurement was started. The sample was kept inside a sealed box with a constant flow of N_2 gas and an over-pressure of 3 kPa. The measurements were performed through a fused silica window and with a black diffusive tape (Thorlabs T205-2.0) below the sample. For measuring the hyperspectral image, the tunable filter was set to a wavelength, an image was acquired and the filter changed to the next wavelength with a short settling time before the next image was acquired.

PL microscope

For fast measurements of the complete PL spectrum, a custom-built PL microscope coupled with a fiber to a CCD spectrometer (Ocean Insight Flame) was used. A schematic of this setup is shown in Figure 3.4b. The luminescence was excited by

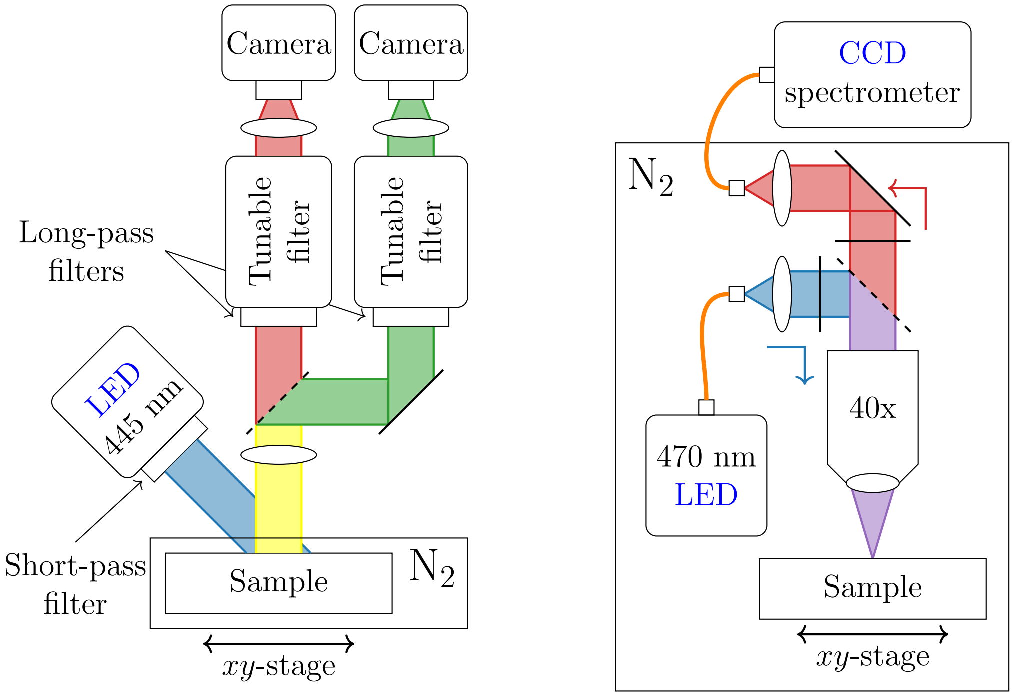

(a) Absolute PL imaging

(b) PL microscope

Figure 3.4: Schematics of the two PL setups used within this work. The dashed lines indicate a dichroic mirror which reflects short wavelength light (blue and green in schematic) and transmits long wavelengths (red in schematic). White ellipses represent lenses and orange lines are optical fibers. In (a) the sample is enclosed in a N_2 flushed chamber and in (b) the whole setup is inside a N_2-filled glovebox. For the absolute PL imaging setup in (a), only the right column was used in this work. Further details are explained in the text.

a fiber-coupled LED (Thorlabs M470F3) with a peak wavelength of 470 nm, which was driven by a current of 1 A. The out-coupled excitation was collimated, filtered by a 500 nm short-pass filter, and reflected by a dichroic mirror into a 40x objective (Nikon). The PL was detected by the same objective, passed through the dichroic mirror, and filtered by a 500 nm long-pass filter. Before being coupled into a fiber, which was connected to the CCD spectrometer, the PL was split by a beam-splitter. This was done to facilitate imaging but this feature was not used in this work. The microscope was placed inside a N_2-filled glovebox and the measurements were performed with < 5 ppm of H_2O and O_2.

3.2.5 Time-Resolved Photoluminescence Spectroscopy

Another PL method used in this work is Time-Resolved Photoluminescence (TRPL). Here the fundamentals of this method, as well as the details of the custom setup and its operation, are explained.

Fundamentals

In TRPL a pulsed excitation source is used instead of a continuous one. The pulse duration is kept shorter than the timescales that need to be investigated and is typically in the range of hundreds of picoseconds. After the excitation, the PL is detected as a function of time to investigate the decay of charge carriers. The TRPL signal, I_{TRPL}, depends on the generated carriers and doping. For a p doped semiconductor:

$$I_{\text{TRPL}} \propto \Delta n(\Delta p + p_0) \sim \begin{cases} \Delta n^2, & \text{for } p_0 \ll \Delta p \\ \Delta n \cdot p_0, & \text{for } p_0 \gg \Delta p \end{cases}, \tag{3.9}$$

where Δn and Δp are the excess charge carriers from the photo-excitation and p_0 is the doping concentration. This means that for low doping, with respect to the generated carriers, the excess carriers will depend on the measured intensity as:

$$\Delta n \propto \sqrt{I_{\text{TRPL}}}. \tag{3.10}$$

One method of measuring these fast decays is through Time-Correlated Single Photon Counting (TCSPC). In this method, no more than one photon is detected for each pulse of light. The time delay of the detection of this photon with respect to the excitation pulse can then be measured using a trigger from the excitation source. By repeating this measurement over many pulses and assigning each photon to a time bin, a histogram of the recombination time is constructed. This histogram is typically referred to as the transient and plotted as a function of the delay time.

TRPL mapper

For the TRPL measurements done in this work, a custom-built mapping setup was used and it is schematically drawn in Figure 3.5. The excitation source was a pulsed white light LASER (NKT Photonics SuperK Extreme) run at 1.2 MHz for all measurements presented here. The light was passed through a double monochromator (Spectral Products CM112) set to 500 nm. A variable Neutral Density (ND) filter was used to set the desired excitation level and the light was reflected from a beam splitter and focused onto the sample using a parabolic mirror. The PL was collected with the same parabolic mirror and the portion passing through the beam splitter was passed through a 600 nm long-pass filter, to remove any reflected excitation light. Finally, the PL was detected in a Si Photo Multiplier Tube (PMT) and the electrical signal generated for each photon was passed with the trigger from the LASER into the TCSPC electronics (PicoQuant PicoHarp 300).

The sample stage was equipped with two linear x and y motors with a travel range of 50 mm (Thorlabs MTS50/M-Z8). Before placing the sample on the stage the power and spot size was measured using a power meter (Thorlabs S130C) and by scanning over two razor blades mounted orthogonal to each-other. Defining the

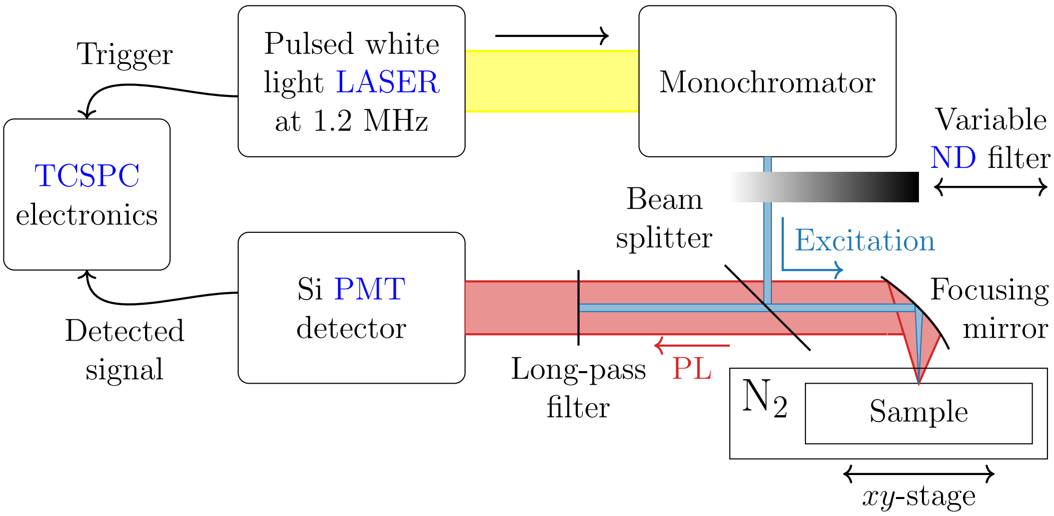

Figure 3.5: Schematic of the TCSPC TRPL mapper used in this work. The pulsed white light source is monochromized and the intensity is adjusted with a variable ND filter. The excitation is, partially, reflected of the beam splitter and focused on to the sample. The resulting luminescence is collected and detected by a PMT with any reflected excitation light filtered out by a long-pass filter. The photon counting is performed by comparing the source trigger and the detected signal for each pulse. The sample is enclosed in a chamber flushed with N_2 and fitted with a fused silica window.

beam diameter as the Full Width at Half Maximum (FWHM) of the gaussian beam profile the spot area had a typical value of 2000 μm^2. For all experiments in this dissertation, the power was adjusted to 1 µW. Assuming a film thickness of 500 nm, full absorption, and instant diffusion, this corresponds to a generated charge carrier concentration, Δn, of $2 \cdot 10^{15}$ cm^{-3}, which is well above the doping levels measured and reported for lead-based MHPs.

All measurements were performed with the sample inside a sealed box with a constant flow of N_2 gas and an over-pressure of 3 kPa. The measurements were performed through a fused silica window and with a black diffusive tape (Thorlabs T205-2.0) below the sample.

3.2.6 Additional Techniques

Here the methodology of two supplementary measurements is briefly presented.

Contact angle

The contact angle of inks on UV ozone cleaned quartz glass was measured at a DSA100E setup from Krüss. The quartz glass was cleaned directly before measuring in an Ossila E511 ozone cleaner. A drop was suspended on the surface and a spherical model was fitted to the live view of the droplet to calculate the contact angle.

Scanning electron microscopy

The Scanning Electron Microscopy (SEM) images were collected by Carola Klimm on a Hitachi S 4100 microscope using an acceleration voltage of 5 kV and 10^4 times magnification.

Chapter 4

Combinatorial Synthesis of $\mathbf{CsPb(Br}_x\mathbf{I}_{1-x})_3$

As discussed in the introduction, combinatorial synthesis has the potential for accelerating the materials discovery process through rapid manufacturing of multiple samples in a single deposition of a so-called combinatorial *library*. In this chapter, the two methods for combinatorial synthesis, developed and used in this thesis, are explained and their results validated through careful compositional and structural measurements.

In the first section, a new algorithm for droplet placement in *combinatorial inkjet printing* is explained. This algorithm is tested using the $\mathrm{CsPb(Br}_x\mathrm{I}_{1-x})_3$ solid solution and the compositional homogeneity of each sample in the printed libraries is investigated in detail.

In the second section, *combinatorial co-evaporation* is explained and a model is determined for estimating the composition throughout the library. The detailed calibration of the evaporation sources in a custom evaporation chamber is explained and the results of evaporating CsI, CsBr, PbI_2, and PbBr_2 are shown.

4.1 Combinatorial Inkjet Printing

As was discussed in subsection 2.4.3 of the fundamentals, this thesis focuses on developing a new method for varying the number of droplets per unit area, with the purpose of achieving combinatorial inkjet printing. In this section, the developed algorithm for droplet placement is presented followed by an explanation of how this can be used to perform the in-situ mixing of inks on the substrate. This method is then used to print an example library of $\mathrm{CsPb(Br}_x\mathrm{I}_{1-x})_3$ and the compositional homogeneity of each sample is thoroughly investigated as a function of printing resolution using advanced X-ray techniques. The results shown in this section were published in an article in the Journal of Materials Chemistry A [120].

4.1.1 Droplet Placing Algorithm

Here, a new method for controlling the amount of ink per unit area through optimized droplet placement is explained. In this method, an original image intended for printing is replaced by an image with a specified amount of droplets per unit area. In order to vary the number of droplets printed per unit area, each pixel of the original image is expanded into a subpixel matrix of size $n \times n$. The problem is then reduced to filling each subpixel matrix with a fraction of droplets, k/n^2, corresponding to the desired amount of the ink in that pixel. This means that for a subpixel matrix size of $n \times n$ there are $n^2 + 1$ different "levels" of filling from $k = 0$ to $k = n^2$.

The position of the droplets inside the subpixel matrix for a general number of droplets, k, is not trivial. Consider first the simplest, non-trivial, case of a 2×2 base matrix. For $k = 0$ and $k = 2^2 = 4$, the placement is trivial as it corresponds to no droplets and droplets in all the positions, respectively. Similarly, the droplet placement for $k = 1$, and its inverted counterpart $k = 2^2 - 1 = 3$, is trivial as it corresponds to placing a single droplet, or a single vacancy, anywhere and all positions are symmetric, i.e. equal after translations and/or rotations. However, for the case of half-filling, $k = 2^2/2 = 2$, there are two and only two distinct sets of positions for the two droplets in the matrix. The droplets can either be placed in a row (which is equivalent to a column after a $\pi/2$ rotation) or on the diagonal. The goal of this work is to space the droplets as far away from each other as possible, or in other words mix the droplet positions and vacancy positions as much as possible. The choice then falls on the diagonal positions which will create a checkerboard pattern as seen in Figure 4.1a. However, for a general base matrix of size $n \times n$ a definition of "spacing the droplets as far away from each other as possible" is needed.

One possible way of defining the spacing out of droplets is to maximize the minimum distance, $d_{\min}$, between two droplets up to half-filling, i.e. for $k \leqslant n^2/2$, and maximize the minimum distance between two vacancies above half-filling, i.e. for $k > n^2/2$. This definition works well while the matrix has a small number of droplets or vacancies but when the matrix starts to fill up the discrete nature of the positions presents a problem. Specifically, when there are so many droplets (or vacancies) in the matrix that two droplets need to be placed directly adjacent to each other, the definition breaks down as the minimum distance will always be $d_{\min} = 1$. The definition can then be extended to minimizing the number of droplets that would be directly adjacent to other droplets.

Using the above definition an algorithm can be constructed for creating a subpixel matrix of size $n \times n$ with a filling k. Importantly, the fact that the subpixel matrices will be tiled to fill an image needs to be considered when calculating the distance to other droplets. However, as only the minimum distances to other droplets are considered it is sufficient to tile the subpixel matrix in a 3×3 repetition and cal-

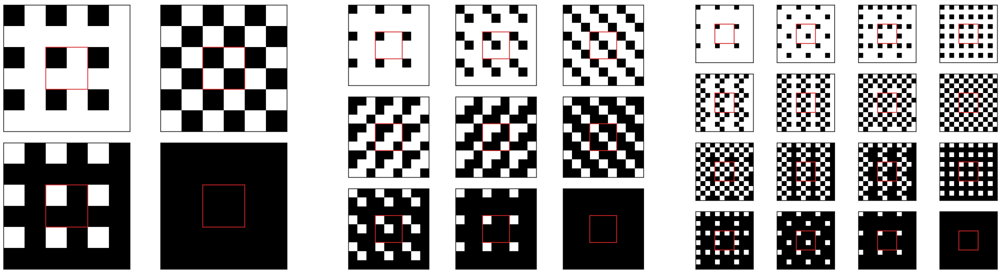

(a) 2 × 2 (b) 3 × 3 (c) 4 × 4

Figure 4.1: Subpixel matrices of different sizes generated using the code in section A.1. The black squares are where ink will be printed. The case of no filling ($k = 0$) is omitted as it would only be a white square. Note how the patterns for any filling k is the inverse of the pattern for the respective $k' = n^2 - k$.

culate the distances from the center matrix, see Figure 4.1. The following algorithm was then created:

1. If $k > n^2/2$: run the algorithm with $k_{\text{new}} = n^2 - k$ and invert the result.
2. List all possible sets of positions for k droplets in n^2 places, i.e. find all options for the subpixel matrix.
3. Tile these sets of positions in a 3 × 3 repetition.
4. For each droplet in the center matrix find the distance to the nearest neighboring droplet.
5. Find the minimum of the distances to the nearest neighbor from point 4, d_{min}, for each set of positions.
6. Find the maximum d_{min} in all sets of positions,
    - if the maximum is > 1: return the corresponding set of positions as the result of the algorithm,
    - else: return the set of positions that minimizes the number of droplets directly adjacent to other droplets.

The algorithm above was implemented in `Python` using the `NumPy` library [121] and the code can be found in section A.1. The `Python` code was used to construct the subpixel matrices for subpixels of size 2 × 2, 3 × 3, and 4 × 4 and the results are shown in Figure 4.1. For larger subpixel matrices the non-optimized code and the quick growth of the binomial coefficient of a square integer make the computational time too long.

4.1.2 Dual Ink Mixing by Drop Control

Once the subpixel matrices have been constructed the image can be rasterized by expanding each intended pixel and substituting it with the subpixel matrix. In

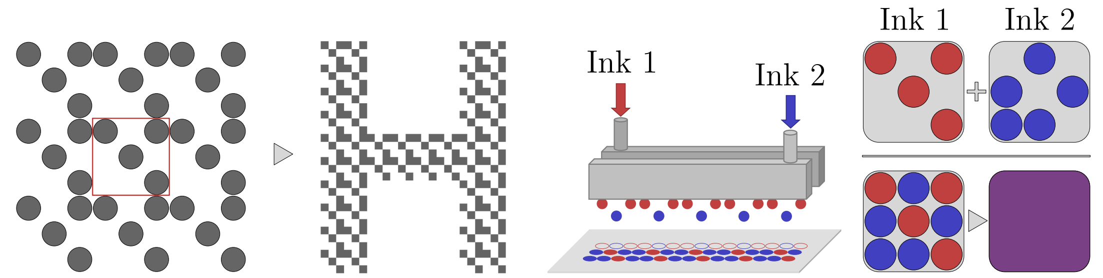

(a) 4/9 subpixel matrix (b) Tiled matrix (c) In-situ mixing (d) 4:5 of ink 1 to 2

Figure 4.2: Schematic of how combinatorial inkjet printing is achieved from the subpixel matrices defined in subsection 4.1.1. In (a), an example of a repetition of a 3×3 matrix with filling 4/9 is shown and in (b), the same matrix tiled in the shape of the letter "H" is generated. The schematic in (c) shows two printheads and how the inks from these are combined on the substrate. Finally, (d) shows the matrices sent to the two printheads for achieving a 4:5 ratio of ink 1 (red) to ink 2 (blue) and how they are intended to mix together (to purple). Reproduced from Ref. [120] with permission from the Royal Society of Chemistry.

Figure 4.2a, an area of 3×3 pixels has been replaced by 9 subpixel matrices of size 3×3 and filling 4/9, the center subpixel matrix is marked by a red square. The astute reader will notice that the subpixel matrix depicted in Figure 4.2a appears different from the one in Figure 4.1b, however, the previous matrix is equivalent and can be recovered through a translation of 1 subpixel in both vertical and horizontal direction followed by a rotation of $\pi/2$. This replacement of pixels with subpixels can be done to any shape and is shown for an image of the letter "H" in Figure 4.2b using the same 4/9 filling matrix.

The co-deposition of two inks is performed by using a dual printhead system where a different ink is fed into each printhead, see the schematic in Figure 4.2c. To get a pixel with the mixture of ink 1 and 2 in a ratio of $k : n^2 - k$ the printhead with ink 1 gets an image where the pixel is replaced with a subpixel matrix with a filling of k/n^2 and for the printhead with ink 2 the pixel is replaced with the inverse subpixel matrix, i.e. a filling of $(n^2 - k)/n^2$. For a ratio of $4 : 5$ the subpixels for ink 1 and ink 2 are shown in Figure 4.2d. In this way, ink 2 is printed in the spaces where ink 1 is not printed and if the droplets are spaced close enough to each other in space and time the inks will mix in the desired ratio, see the schematic in Figure 4.2d.

The space between the droplets will be decided by the distance between centers, and the diameter of the droplets on the substrate. The distance between the center of the droplets is controlled by the printing resolution, which is typically specified parallel and perpendicular to the printing direction in dots per inch, dpi. In this work, the same resolution is used in both directions. For a printing resolution of 350 dpi the distance between the center of the droplets will be $2.54 \cdot 10^4 \frac{\mu m}{\text{inch}} \cdot \frac{1}{350} \frac{\text{inch}}{\text{dot}} \approx 73 \frac{\mu m}{\text{dot}}$. For a given drop volume, the diameter of the droplets is decided by the wetting

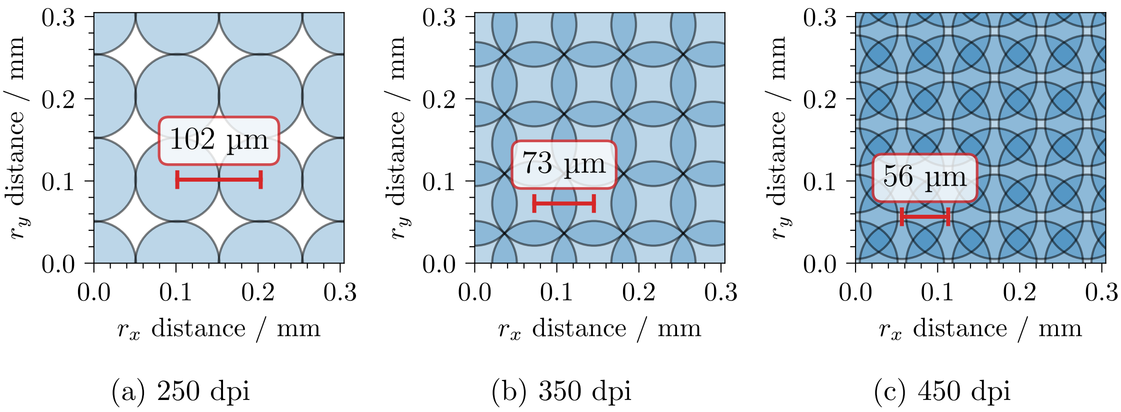

(a) 250 dpi (b) 350 dpi (c) 450 dpi

Figure 4.3: Schematic of the expected droplet overlap at different printing resolutions assuming a drop volume of 30 pl and a contact angle of 16°. The printing resolutions are 250, 350, and 450 dpi from left to right and the corresponding droplet pitch is shown as a red line. Reproduced from Ref. [120] with permission from the Royal Society of Chemistry.

of the ink on the substrate, which is a factor of the surface energy of the substrate and the viscosity and surface tension of the ink. The wetting can be measured by the contact angle of the ink on the substrate. From the contact angle, θ, and the drop volume, V, the contact diameter, D, i.e. the diameter of the circle formed at the interface of the planar substrate and the spherical section of the droplet, can be estimated according to Equation 4.1 (for derivation, see section A.2). This equation is also valid for $\theta > 90°$, however, it then no longer refers to the outer diameter of the droplet but only its intersection with the substrate.

$$D = 2\sin\theta \cdot \left(\frac{3V}{\pi(2 - 3\cos\theta + (\cos\theta)^3)}\right)^{1/3} \tag{4.1}$$

In order for the droplets printed in the subpixel to mix, they need to come in contact with each other. The printing resolution needed for this to happen can be estimated by calculating the contact diameter. For a contact angle of 16° and a drop volume of 30 pl the contact diameter would be 102.6 µm according to Equation 4.1. A droplet pitch of 102.6 µm, corresponding to a printing resolution of 248 dpi, would then bring the droplets close enough to just come into contact with their nearest neighbor, see Figure 4.3a. As seen in the schematic, this still leaves a gap to the neighbor on the diagonal. For the droplets on the diagonals to come into contact, the resolution would need to increase by a factor of $\sqrt{2}$ to 350 dpi, see Figure 4.3b. The general printing resolution for these two cases as a function of the contact angle is shown in Figure 4.4 for the case of 30 pl drop volumes. It is important to note that this is a single droplet approximation and the actual behavior of multiple droplets will differ. If the printing resolution is further increased to 450 dpi, as seen in Figure 4.3c, the droplets start to overlap with multiple droplets and the thickness

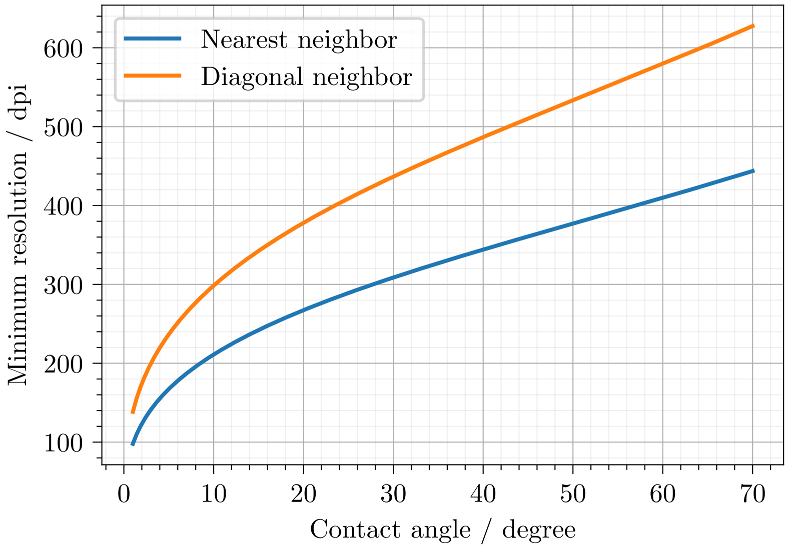

Figure 4.4: Minimum printing resolutions required for droplet overlap as a function of the contact angle and assuming a drop volume of 30 pl. The blue line is for overlap with the nearest neighboring droplet and the orange line for the nearest neighbor on the diagonal.

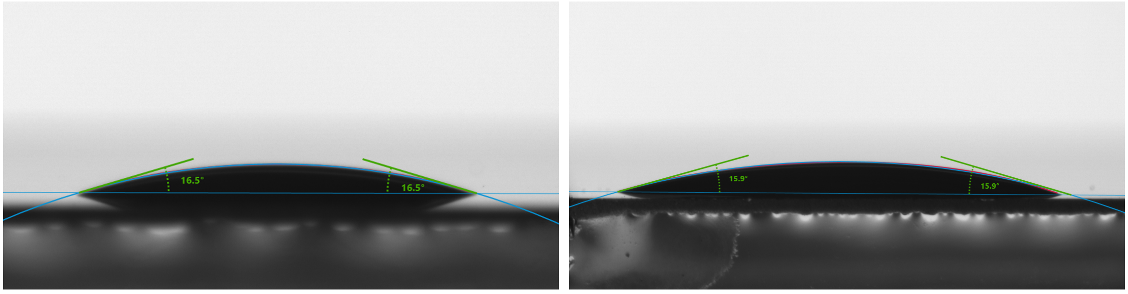

(a) Ink 1 of $CsPbI_3$ with $x = 0$: 16.5°

(b) Ink 2 of $CsPbBr_2I$ with $x = 2/3$: 15.9°

Figure 4.5: Contact angle of the two investigated inks on UV-ozone cleaned quartz glass measured according to section 3.2.6.

of the wet film formed will instead increase until the film can no longer be contained within the intended printing area.

4.1.3 Combinatorial Printing of CsPb(Br_xI_{1-x})$_3$

To assess the potential of the combinatorial printing method explained above, the CsPb(Br_xI_{1-x})$_3$ solid solution was selected as an example material. Two inks were prepared according to the details in section 3.1.1, ink 1 contained $CsPbI_3$ with $x = 0$ and ink 2 contained $CsPbBr_2I$ with $x = 2/3$. The contact angle of these inks on UV-ozone cleaned quartz glass was measured with the experimental setup detailed in section 3.2.6 and the result of one such measurement is given in Figure 4.5.

Firstly, the two inks were combined to print the logotype of the HySPRINT innovation lab on photopaper, see the scanned image of the sample in Figure 4.6a. The logotype was split up into 9 different objects (the symbol on the left and the

(a) Logotype (b) Combinatorial library

Figure 4.6: Samples of combinatorial inkjet printing combining $CsPbI_3$ ink and $CsPbBr_2I$ ink. In (a), a photograph of the logotype of the HySPRINT innovation lab combinatorially printed on photopaper (HP) with 4×4 subpixel matrices. In (b), a photograph of the combinatorial library used for investigating the compositional homogeneity of the method. This library was printed on quartz glass and the sample numbers of the library are overlayed in white text.

8 letters) and the pixels of each object were replaced by subpixel matrices of size 4×4, where every other matrix was used to create 9 levels of filling. The image with a filling of 0/16 on the left and 16/16 on the right was sent to the printhead with ink 1 ($CsPbI_3$) and the inverted image to the printhead with ink 2 ($CsPbBr_2I$) resulting in a printed image which is Br-rich on the left and I-rich on the right. This can be seen by eye in the sample which is yellow on the left, corresponding to the higher optical band-gap $CsPbBr_2I$, and transitions through orange and red to fully absorb the visible light on the right side, corresponding to the low optical band-gap of $CsPbI_3$.

In order to quantitatively investigate this shift in optical band-gap, a combinatorial library of 10 samples was printed using all the subpixel matrices of size 3×3. The samples were printed as two rows of five squares each and labeled 1-5 in the upper row and 6-10 in the bottom row, see the image of the library in Figure 4.6b. For the image sent to the printhead with $CsPbI_3$, sample 1 (upper left corner) was a square of subpixel matrices with filling 9/9 and for the rest of the samples, the filling was reduced by 1 so that finally sample 10 (bottom right) was a square with filling 0/9. The inverted image was sent to the printhead with $CsPbBr_2I$. The library was printed at 350 dpi on quartz glass which was cleaned according to the method described in section 3.1.1.

After deposition, the optical properties of the samples were first investigated. The photoluminescence and UV/Vis transmittance spectra of the samples in the library printed on quartz glass were measured with the microscope setup from section 3.2.4 and the integrating sphere setup from section 3.2.3, respectively. The measurements were performed at the center of each sample and the normalized results can be seen in the waterfall plots in Figure 4.7. A Gaussian function was fitted to the PL as well as the derivative of the transmittance, and the peak position indicates the optical band-gap, which is plotted as a function of the sample number in Figure 4.7c. The qualitative shift in optical band-gap as seen by eye

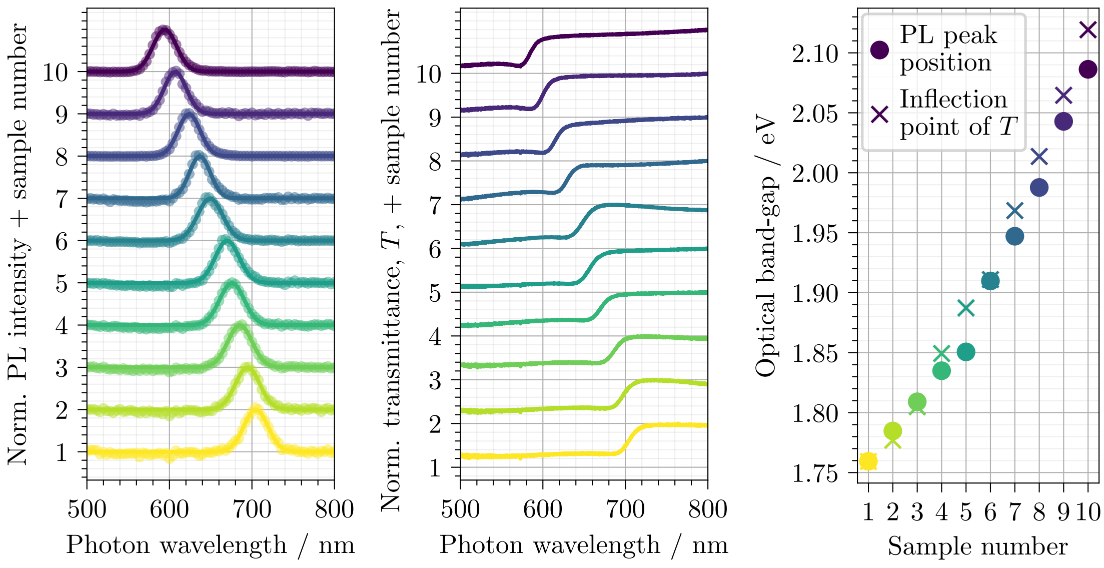

(a) PL (b) UV/vis (c) Optical band-gap

Figure 4.7: Normalized waterfall plots of the PL (a) and UV/Vis (b) spectra of the the 10 samples in the combinatorial library shown in Figure 4.6b. In (c) the inflection point of the transmittance is plotted with crosses and the peak position of the PL with circles.

for the printed logotype can now be seen quantitatively and the value shifts from 1.76 eV for the $CsPbI_3$ in sample 1 to 2.12 eV for the $CsPbBr_2I$ in sample 10. For the samples with higher Br content, the PL peak is slightly lower in energy than the transmittance inflection point due to the onset of light-induced phase segregation as published by Beal et al. in 2016 [86] and discussed in section 2.3.5. This result shows that the two inks are truly mixing on the atomic level as a single shifted band-gap is observed rather than a linear combination of two. However, it is important to note that the PL quantum yield and the absorption coefficient might differ largely between different species present in the film. Therefore, small variations in the composition could be lost in the natural broadening of the measurements as these optical measurements are averaging over a large area. In order to properly determine the compositional homogeneity of the printed samples, a set of structural and compositional measurements with a higher spatial resolution also needs to be performed.

4.1.4 Compositional Homogeneity of Printed Films

To investigate the microscopic compositional homogeneity of the combinatorial library printed using the developed algorithm, a set of mapping GIWAXS and XRF measurements was performed. The GIWAXS mapping measurements were performed at the mySpot beamline as described in section 3.2.1 and the XRF in a Bruker M4 Tornado according to section 3.2.2. The mapping was performed in a $1 \times 1\ \mathrm{mm}^2$ section in the center of each sample with a step size of 50 µm.

First, the library from Figure 4.6b above, which was printed with a resolution of 350 dpi on quartz glass, was investigated. All samples were found to be in an orthorhombic *Pbnm* phase and the azimuthally integrated GIWAXS patterns in the range of the 110 and 220 peaks, averaged over all points in each sample, are plotted in a waterfall plot in Figure 4.8a. The 110 lattice spacing was extracted using the position of the 110 and 220 peaks and the resulting spacing is shown as a collection of heat maps in Figure 4.8b.

The collected XRF spectra for the same library were first background corrected and then normalized by the area of the Pb L_3-M_5 peak to remove the effect of potential thickness variations which is possible because the Pb content is the same for both inks. The averaged spectra for each sample are plotted in Figure 4.8c in the range of the relevant fluorescence lines. The Br content, x, in the $CsPb(Br_xI_{1-x})_3$ samples were calculated by the area of the Br K-L_3 peak, assuming that the value for sample 10 is $x = 2/3$ as this corresponds to pure ink 2 which is precisely scaled. A set of heatmaps of the Br content distribution in each sample is shown in figure Figure 4.8d.

From the averaged diffraction patterns in Figure 4.8a it can be seen that there is a monotonic increase in the peak positions as iodide is replaced with bromide. This means that the lattice parameter is decreasing as the large iodide ion is being replaced with the smaller bromide ion in the solid solution. A similarly clear trend is present for the XRF spectra in Figure 4.8c where the I L_3-M_5 peak area is monotonically decreasing and the Br K-L_3 peak area is monotonically increasing with an increasing fraction of the $CsPbBr_2I$ ink. Meanwhile, the Cs L_3-M_5 peak remains constant, with the broadening being caused by overlapping I lines, indicating that all samples are stoichiometric.

The heatmaps of both the lattice parameter and the XRF determined Br content show a clear distinction between the samples, with only a small variation within each sample, demonstrating the success of the developed method. The horizontal (x direction) reproducibility of the measured position is quite high whilst the exact vertical (y direction) position in the GIWAXS measurement is hard to determine. In the horizontal direction, there is a clear correlation between the two measurements and the small compositional inhomogeneity present in the samples is on the order of the printing resolution (73 µm droplet spacing for 350 dpi). The correlation between the GIWAXS determined lattice parameter and the XRF determined Br content is further visualized in Figure 4.9 where the histograms of the distribution of both values within the samples are shown on the right and top, respectively, and the correlation of the mean values is plotted, with error bars indicating ±1 standard deviation.

Two things are of interest in the results presented in Figure 4.9. Firstly, the lattice parameter decreases monotonically with the Br content, x, in a close to linear dependence with a small bowing as previously reported in literature [86]. This indi-

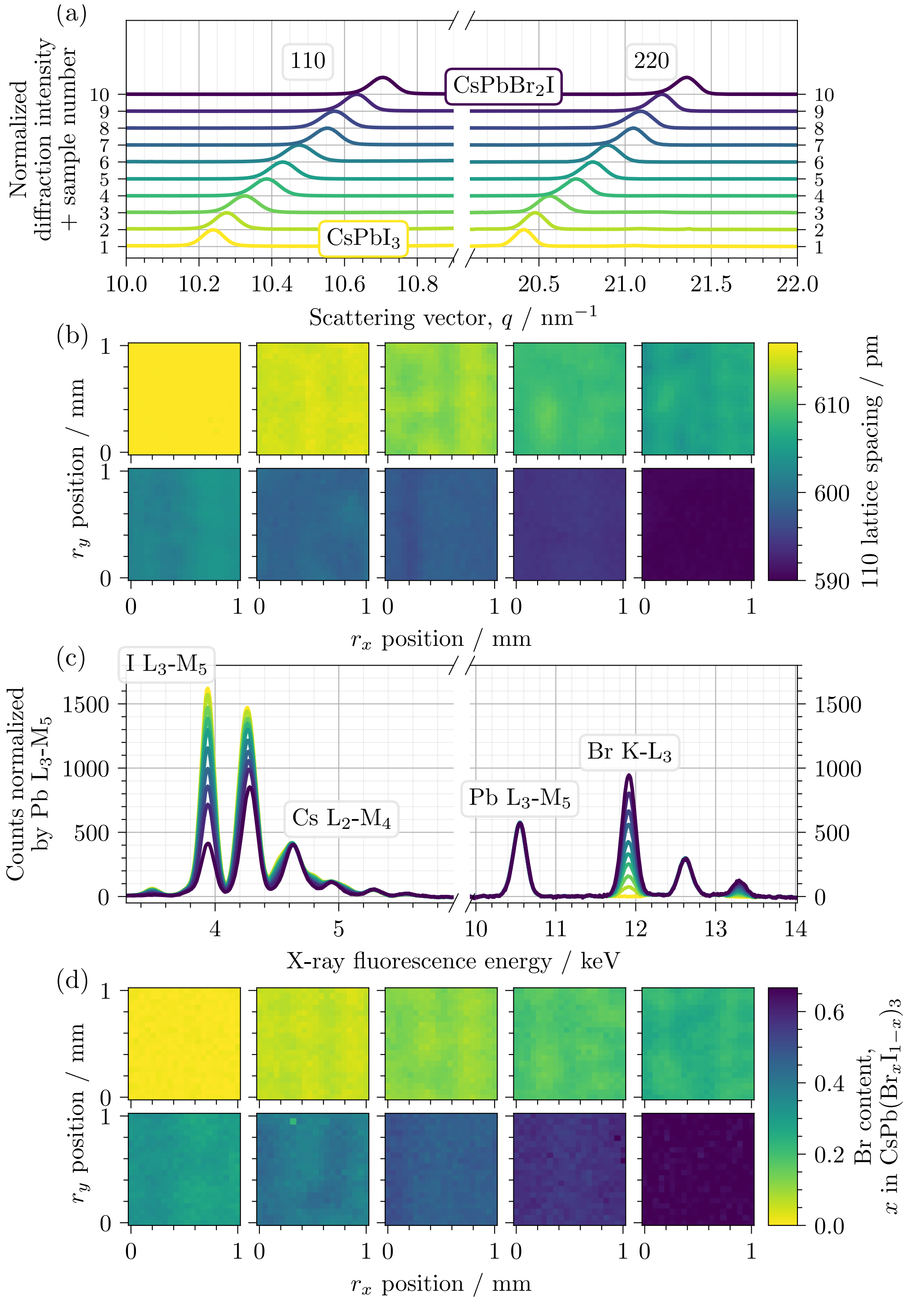

Figure 4.8: GIWAXS and XRF maps of the combinatorial library printed at 350 dpi. In (a) the azimuthally integrated GIWAXS patterns, averaged over the map, for each sample are plotted as a waterfall plot in the region of the 110 and 220 peaks of the orthorhombic perovskite phase. In (b) the 110 lattice spacings as a function of position, (r_x, r_y), for a 1×1 mm^2 area in the center of each sample are plotted in heatmaps. In (c) the averaged XRF spectra, background corrected and normalized by the Pb peak area, are plotted for each sample in the range of the fitted peaks. In (d) the Br contents, x in $CsPb(Br_xI_{1-x})_3$, for the same 1×1 mm^2 area in the center of each sample are plotted in heatmaps. Reproduced from Ref. [120] with permission from the Royal Society of Chemistry.

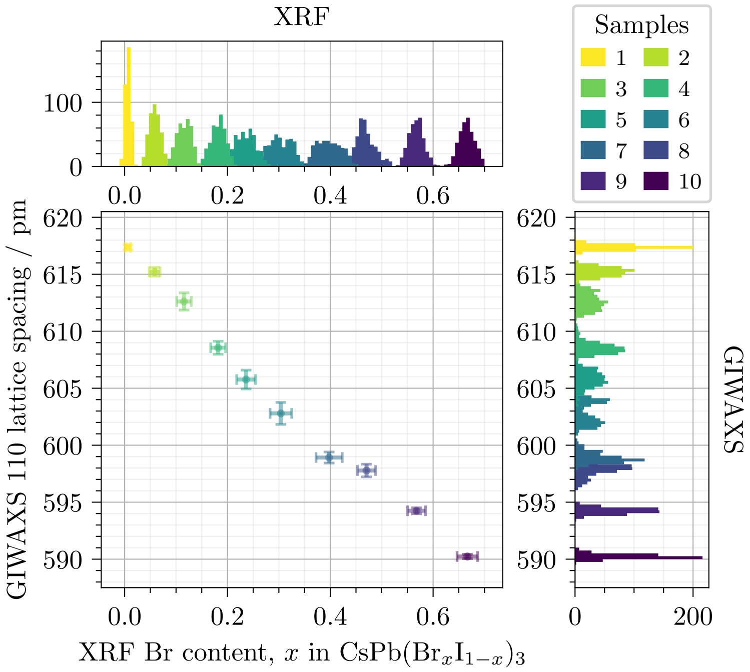

Figure 4.9: Correlation of the GIWAXS determined 110 lattice spacing and the XRF determined Br content, x in $CsPb(Br_xI_{1-x})_3$. The top pane shows the histograms of all 110 lattice spacings measured for each sample and the right pane the histograms of all the Br contents measured. The center pane shows the mean value of each histogram plotted against each other with error bars indicating ±1 standard deviation. All data is color-coded per sample according to the legend in the top right. Reproduced from Ref. [120] with permission from the Royal Society of Chemistry.

cates that the lattice parameter can be used to directly determine the Br content, x, in the film and that it can, therefore, be used to determine the degree of intermixing. Secondly, the distributions of the lattice spacing are considerably narrower than those of the XRF-determined Br content. This is especially noticeable when comparing the Br content and lattice parameter distributions for sample 10, which is printed from a pure ink of $CsPbBr_2I$. For this pure ink, the experimental uncertainty of the measurement is expected to be the main contributor to the broadening of the distributions and it is clear that, for the two experimental setups used in this work, the GIWAXS determined lattice parameter will be more sensitive to small deviations in the Br content. This difference is in part due to the difference in setups (i.e. lab source vs. synchrotron). However, it is also due to the fact that a peak shift, in the case of the determination of lattice parameter, is less sensitive to noise than a peak area, in the case of determining the Br content. The apparently sharper Br content distribution for the pure $CsPbI_3$ ink is due to the complete absence of a peak as no Br should be present in the sample.

Printing resolution dependence

In order to understand how the mixing of the inks and the compositional homogeneity of the samples in the combinatorial library is affected by the droplet spacing, two additional libraries were prepared according to the steps above but with the printing resolution set to 250 and 450 dpi, respectively. Recalling the discussion from subsection 4.1.2 these values should correspond to the droplets just about touching their nearest neighbor for a resolution of 250 dpi and an overfilling of ink for the case of 450 dpi. Once again the samples were mapped by GIWAXS and the 110 lattice spacing was determined according to the method above. The resulting map of the lattice spacing is shown in Figure 4.10 for a selection of the samples of the libraries printed at 250, 350, and 450 dpi respectively. The samples chosen were the ones where the $CsPbBr_2I$ ink was printed with the 3/9, 5/9, and 7/9 subpixel matrices. These samples were chosen as they showed the most broadening in the histogram of Figure 4.9. On top of each lattice spacing map the image as used for printing is displayed, with the color yellow for the $CsPbI_3$ ink and dark blue for the $CsPbBr_2I$ ink, scaled in such a way that this would be the theoretical image (ignoring the square shape and any droplet overlap) if no mixing occurred.

For the samples in the library printed at 250 dpi, corresponding to a droplet pitch of 102 µm, there is a noticeable inhomogeneity on the scale subpixel matrix variation, compare (a) and (d) in Figure 4.10. In addition, there are large holes in the film where no diffraction peaks were observed, which are shown as white squares in (p). This printing resolution is right at the lower boundary of values for which the droplets are expected to come in contact with each other and that explains why the mixing of the two inks is limited. As the printing resolution is increased to 350 dpi and the deposited droplets move closer to each other (73 µm center to center), the films show a much higher degree of compositional homogeneity, and the subpixel matrix pattern can no longer be observed. This corresponds roughly to the case where the diagonal droplets come in contact as discussed in subsection 4.1.2 and here the droplets overlap enough to fully intermix. If the printing resolution is further increased to 450 dpi the droplets move even closer to each other (56 µm center to center), but as they are already overlapping the main effect is an increase in the amount of material deposited and, hence, the thickness of the formed wet film. At this point, large scale deviations from the intended composition can be observed. For an example of this, compare the intended lattice spacing for the 3/9 sample of the 350 dpi library in Figure 4.10e with that of the sample from the 450 dpi library in Figure 4.10f. This large-scale inhomogeneity is consistent with previous studies showing that certain compositions of the CsPb(Br_xI_{1-x})$_3$ solid solution are formed preferentially [122] and when a thicker wet film is deposited the crystallization process is delayed and large scale diffusion of species has time to occur.

Morphology of printed films

In order to understand how the combinatorial printing affects the microscopic morphology of the printed films, a set of SEM pictures was taken of all the samples

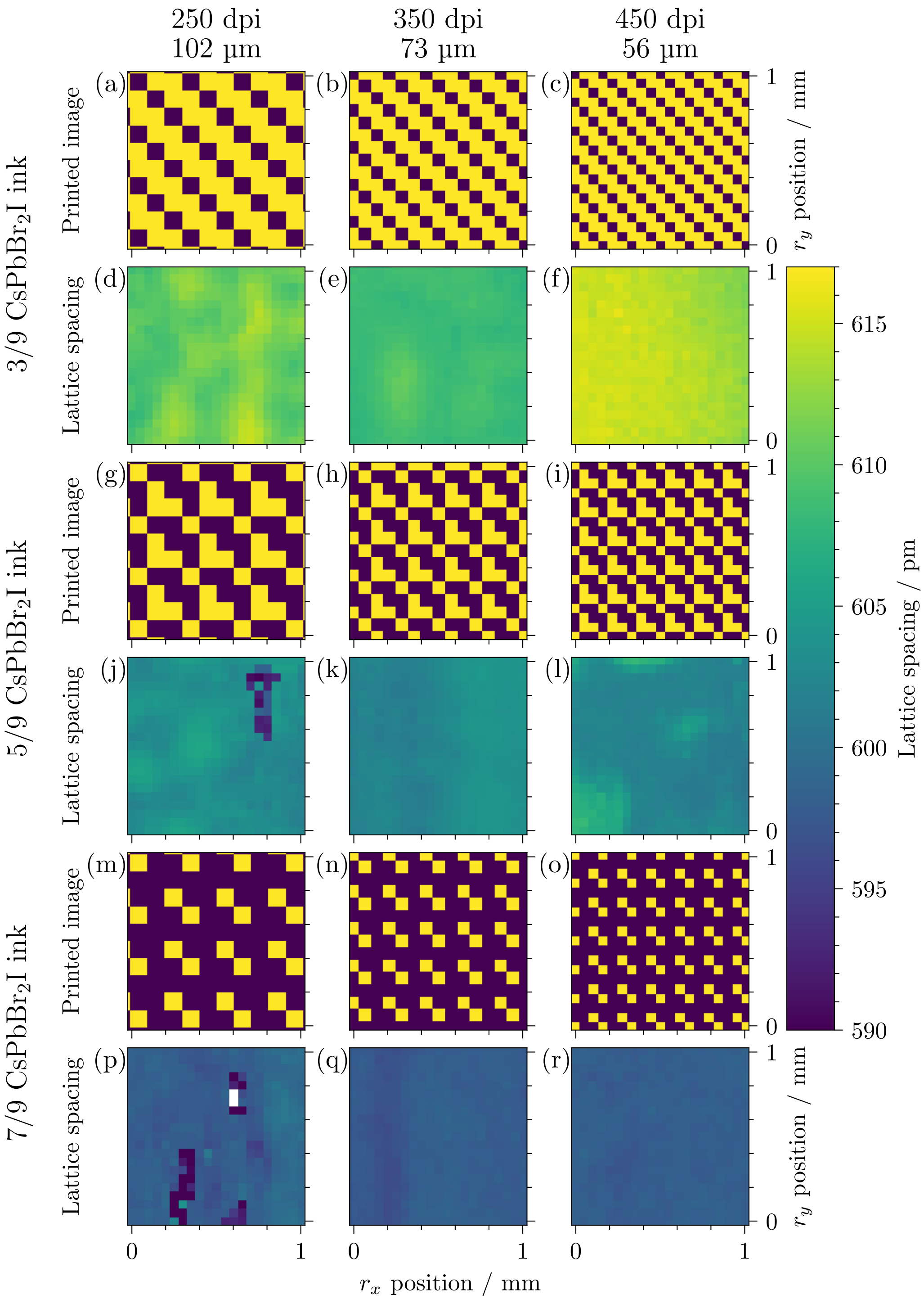

Figure 4.10: Dependence of the printing resolution on the compositional homogeneity determined by micro-spot GIWAXS maps of the 110 lattice spacing. The printing resolutions are 250, 350 and 450 dpi from left to right and the samples shown are those with filling 3/9, 5/9 and 7/9 of the CsPbBr$_2$I ink from top to bottom. (a-c), (g-i), and (m-o) show the images sent to the two printheads with the CsPbI$_3$ ink in yellow and the CsPbBr$_2$I ink in dark blue. (d-f), (j-l), and (p-r) show the corresponding maps of the 110 lattice spacing. Reproduced from Ref. [120] with permission from the Royal Society of Chemistry.

printed at the three different resolutions. The images at 10^4 times magnification for every sample of the three libraries are shown in Figure 4.11.

From the SEM images it can be seen that the mixed films in fact show a better morphology than the pure inks, with the samples of 4/9 to 6/9 filling of $CsPbBr_2I$ showing mostly compact films with only a few pinholes. In general, the *microscopic* film morphology is more dependent on the ink composition than the printing resolution. This indicates that the printing resolution optimization needed for the compositional mixing above is, to a certain extent, independent of the ink and process engineering needed to produce compact films for high-quality optoelectronics. From the SEM images of the samples printed from the pure $CsPbI_3$ ink, it is clear that the ink and drying process needs to be further optimized for applications in for example photovoltaics, where pinholes will have a detrimental effect on the device performance by short-circuiting the cell.

4.1.5 Applicability of Combinatorial Inkjet Printing

From the results above it is evident that the developed algorithm can be used to generate images for combinatorial inkjet printing that, with the right printing parameters, result in well-mixed samples. For the example above, the optimal printing resolution was found to be 350 dpi, for which the standard deviation in 110 lattice spacing was only 0.5 pm. For this solid solution, one of the key varying parameters is the optical band-gap and a 0.5 pm variation in lattice spacing translates to only an 18 meV variation in band-gap, which is less than the natural linewidth caused by thermal broadening at room temperature, $k_\mathrm{B}T = 26$ meV.

The method was used to determine the temperature-dependent phase diagram of CsPb(Br_xI_{1-x})$_3$ by printing samples using the 4×4 base matrix and characterizing them at a high-throughput GIWAXS setup. The details of this study are shown in section 5.1 of the chapter on high-throughput experiments.

The CsPb(Br_xI_{1-x})$_3$ solid solution was used as an example as it can be solution-processed and the clear shift in cell volume, and therefore band-gap, allows for precise determination of the intermixing. However, the method is generic in the sense that it is, to a certain extent, independent of the inks used as long as they are miscible and can be engineered to have similar wetting parameters on the desired substrate. With the method above, a suitable printing resolution can be estimated from the drop volume and contact angle by calculating the contact diameter (Equation 4.1) and making sure that the diagonal distance of the droplets is similar.

The combinatorial printing method outlined here has also been studied in collaboration with V. Schröder for the application in devices [54]. The approach was used by the collaborators to print photodetectors using the hybrid MAPb(Cl_yBr_{1-y})$_3$ and MAPb(Br_xI_{1-x})$_3$ perovskite solid solutions and, through the tunability of the band-gap, achieve selective detection for photon wavelengths between 410 and 790 nm.

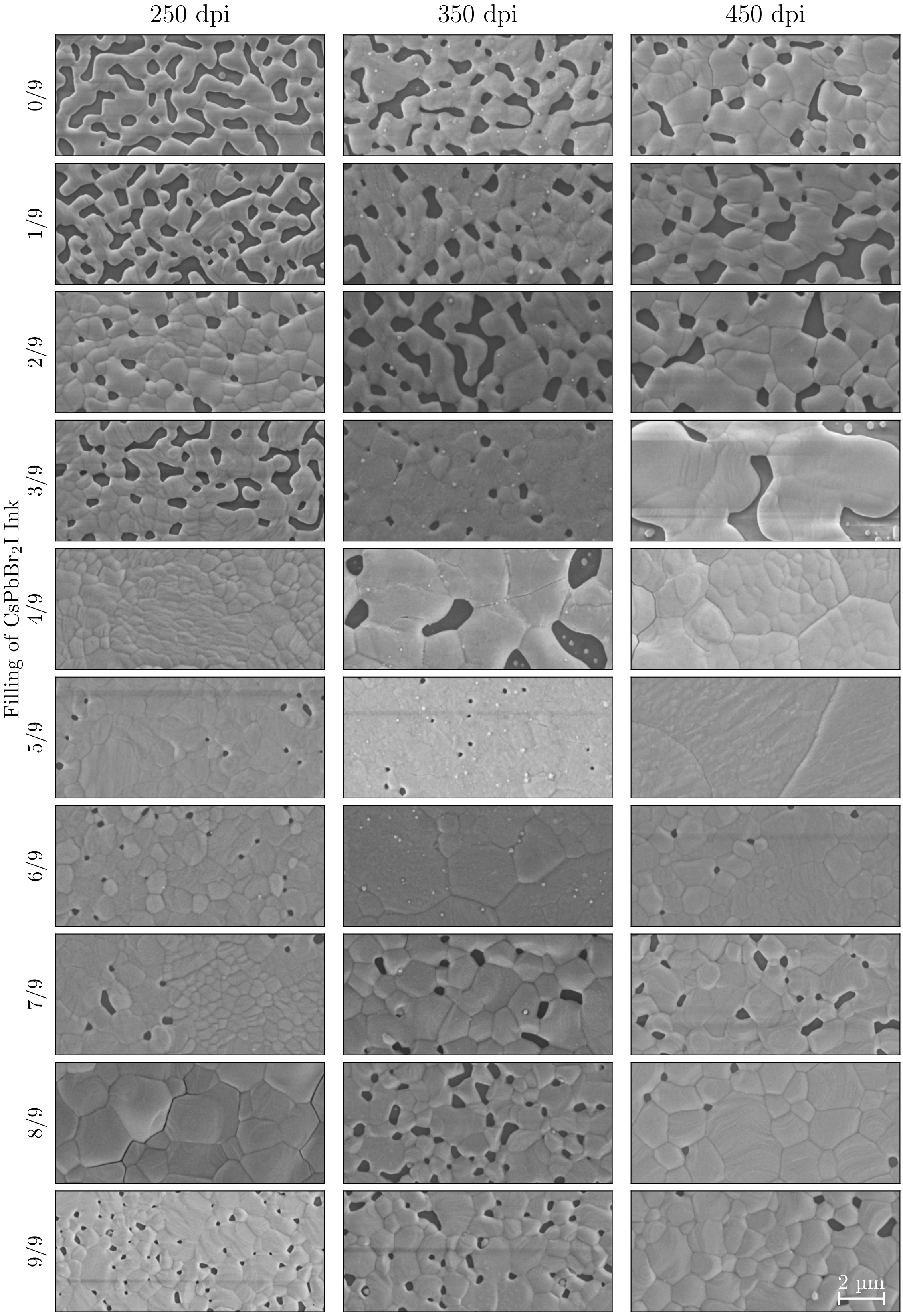

Figure 4.11: SEM images, at 10^4 times magnification, of all the samples in each of the three printed libraries. From left to right the printing resolutions are 250, 350, and 450 dpi, respectively, and from the top to bottom the samples are printed with a filling of 0/9 to 9/9 of the $CsPbBr_2I$ ink, and 9/9 to 0/9 of the $CsPbI_3$ ink. The scale is the same for all images and is given in the bottom right.

The detectors were printed with two inks at a time (first $MAPbCl_3$ and $MAPbBr_3$, then $MAPbBr_3$ and $MAPbI_3$) and a base matrix size of 2 × 2 was used.

4.2 Combinatorial Co-Evaporation

A second, more common, approach to the combinatorial synthesis of thin films is through physical vapor deposition. The process of co-evaporation and the chamber used are described in detail in subsection 3.1.2. In this section, the method of combinatorial co-evaporation through PVD will be explained and the process by which the CsPb(Br_xI_{1-x})$_3$ samples studied in section 5.2 were made will be detailed.

4.2.1 Compositional Variation

As discussed in subsection 3.1.2, the emission from a single source, in a vacuum, typically conforms to a $\cos^k \varphi$ distribution, where φ is the angle to the source normal and k accounts for deviations due to the crucible geometry [112]. This means that different points inside the evaporation chamber will be subjected to a different flux of the source material deposited from a single source. Films deposited from traditional co-evaporation are made compositionally homogeneous through the rotation of the substrate during the deposition. The most straightforward way of creating a sample with a compositional gradient is to omit the rotation of the substrate. Thereby, each point on the substrate will receive an individual ratio of the co-evaporated materials on account of the difference in the flux of evaporated material from each source at each point throughout the sample.

Distribution model

In order to plan the combinatorial experiments, it is vital that the distribution of the co-deposited materials can be modeled and the composition throughout the film estimated. Assuming point sources, the thickness of material deposited from a single source oriented in an arbitrary relation to the substrate is given by Equation 4.2, where φ is the angle between the source normal and the line between the source and the point on the substrate, θ is the angle between the same line and the substrate normal, s is the distance between the source and the point on the substrate, m is the mass of the evaporated material and ρ is the density of the material [123]. The angles θ and φ are clarified in Figure 4.12.

$$l = \frac{m \cos^k \varphi \cos \theta}{\rho \pi s^2} \tag{4.2}$$

To compute the thickness distribution efficiently Equation 4.2 is redefined in terms of vector operations. Let $\vec{n}_{\text{source}}$ be the unit length normal vector of the source, $\vec{n}_{\text{substrate}}$ be the unit length normal vector of the substrate. Let $\vec{s}$ be the vector from the source to any point (r_x, r_y) on the substrate, given by the vector

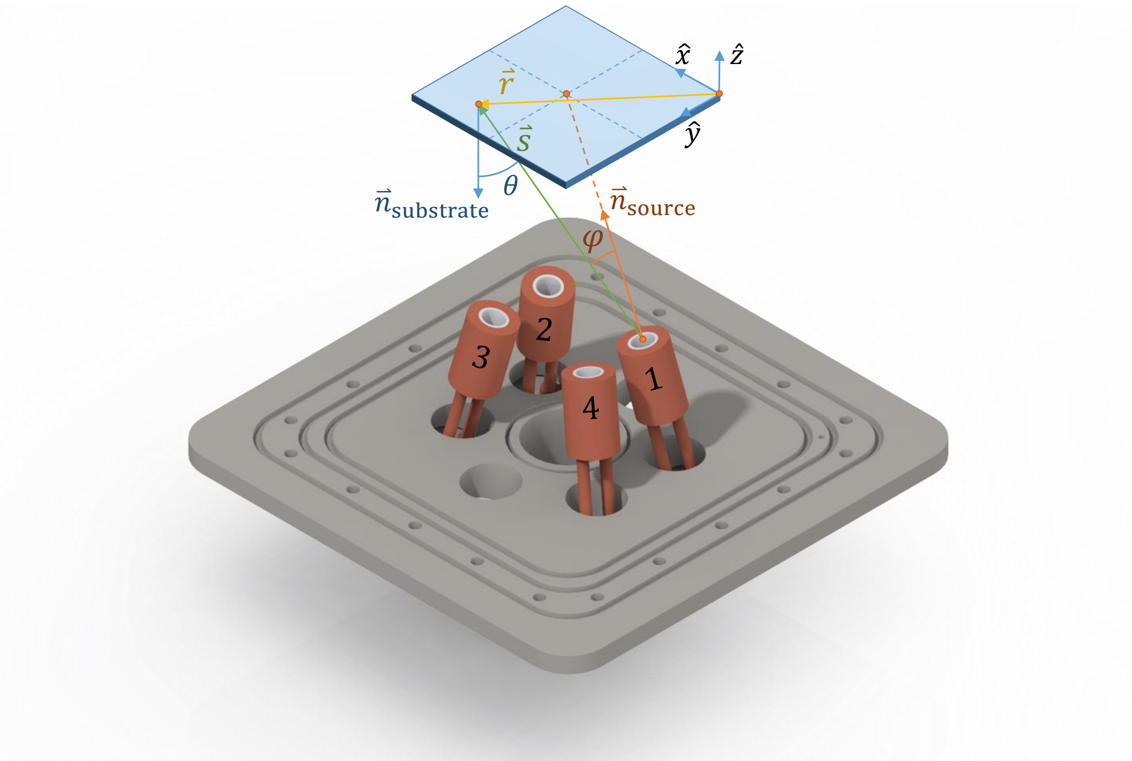

Figure 4.12: Vectors and angles defined for the distribution model shown in relation to the CAD model of the evaporation sources and substrate. The orange arrow is the normal vector of the source, $\vec{n}_{\text{source}}$ and is pointed at the center of the substrate. The green arrow is the vector, $\vec{s}$, from the source to an arbitrary point (r_x, r_y) on the substrate, given by the $\vec{r}$ vector. The blue arrow is the normal vector of the substrate, $\vec{n}_{\text{substrate}}$, and is at angle θ to the $\vec{s}$ vector. φ is the angle between the $\vec{n}_{\text{source}}$ vector and $\vec{s}$ vector.

$\vec{r}$. See Figure 4.12 for the definition of all vectors and the coordinate system. The cosine of the angles φ and θ can then be calculated from the dot products of the corresponding normal vectors with $\vec{s}$:

$$\vec{n}_{\text{source}} \cdot \vec{s} = \|\vec{s}\| \cos\varphi, \tag{4.3a}$$

$$\vec{n}_{\text{substrate}} \cdot \vec{s} = \|\vec{s}\| \cos\theta. \tag{4.3b}$$

By solving Equation 4.3 for the cosine terms and inserting these into Equation 4.2, noting that $s = \|\vec{s}\|$, the following equation is obtained for the thickness, l, at any point (r_x, r_y) on the substrate:

$$l(r_x, r_y) = \frac{m}{\rho\pi} \frac{\left(\vec{n}_{\text{source}} \cdot \vec{s}(r_x, r_y)\right)^k \left(\vec{n}_{\text{substrate}} \cdot \vec{s}(r_x, r_y)\right)}{\|\vec{s}(r_x, r_y)\|^{k+3}}. \tag{4.4}$$

For the evaporation chamber used in this work, all sources are pointed at the center of the substrate at $(r_x, r_y) = (25, 25)$ mm. The substrate is normal to the vertical $\hat{z}$-axis, and the position along the $\hat{x}$ and $\hat{y}$ direction of the four sources are mirrored along two orthogonal lines that intersect under the center of the substrate,

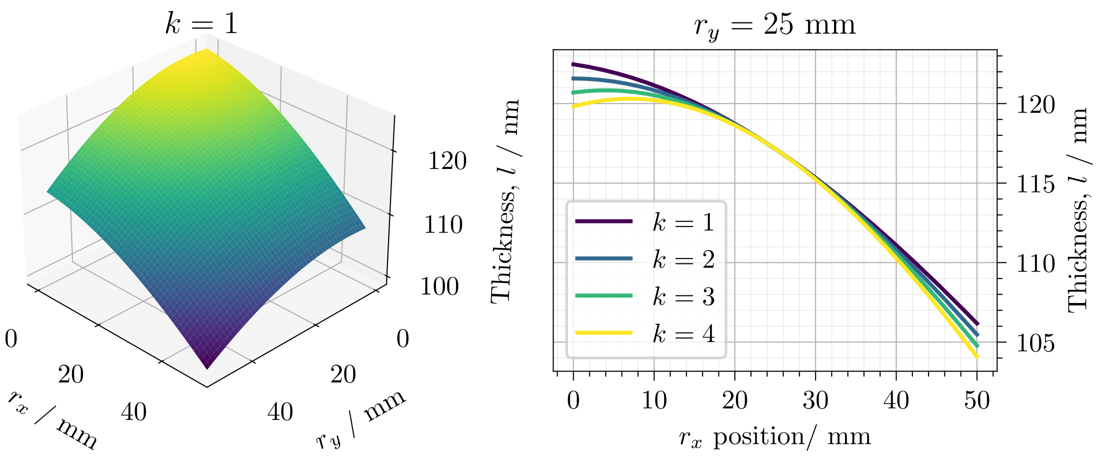

(a) Thickness surface plot for $k = 1$ (b) Thickness cross section at $r_y = 25$ mm

Figure 4.13: The modeled distribution for a material with a density of 6.16 g/cm^3 evaporated on a 50×50 mm^2 substrate, with a total of 100 mg being evaporated into the chamber. In (a), the thickness is plotted as a function of the r_x and r_y position on the substrate, for a cosine order $k = 1$. In (b), the cross section for $r_y = 25$ is plotted for cosine orders from $k = 1$ to $k = 4$.

see subsection 3.1.2 for details. For a source at a position $(25 - \Delta x, 25 - \Delta y, -\Delta z)$, the vector from the source, $\vec{s}$, to the point (r_x, r_y) is given by $\vec{s}(r_x, r_y) = (r_x - 25 + \Delta x, r_y - 25 + \Delta y, \Delta z)$. Based on this source layout, a vectorized `Python` function was implemented for Equation 4.4 using the `NumPy` library, and the code can be found in section B.1. The geometry of the chamber can then be inputted from the CAD files by simply taking the absolute distances, along the $\hat{x}$, $\hat{y}$, and $\hat{z}$ directions, from the sources to the center of the substrate. In the case of the chamber used in this work, these values were determined to be $\Delta x = 41.54$ mm, $\Delta y = 26.06$ mm, and $\Delta z = 201.12$ mm. Using these values in the `Python` function from section B.1, the simulated thickness of evaporating 100 mg of a material with a density of 6.16 g/cm^3 on a 50×50 mm^2 substrate is shown as a surface plot in Figure 4.13a with the order $k = 1$. The cross-section of this surface at $r_y = 25$ mm is plotted for $1 \leq k \leq 4$ in Figure 4.13b.

From the surface in Figure 4.13a it is clear that for a first-order distribution the maximum thickness is found in the upper left corner at $(r_x, r_y) = (0, 0)$, which is the point on the substrate closest to the source as seen in Figure 4.12. It can also be seen that the thickness is slightly higher in the corner at $(r_x, r_y) = (0, 50)$ on the same side as the source than in corner straight across at $(r_x, r_y) = (50, 0)$. This is due to the fact that the sources are located slightly more to the side of the substrate than to the top $(\Delta x > \Delta y)$. As the order of the cosine distribution, k, changes in Figure 4.13b the thickness in the center of the substrate remains largely unaffected with the biggest difference occurring close to the edges. At the edges, the thickness reduces with the order k.

Combining multiple sources

When evaporating with a single source, the only thing achieved is a gradient in thickness. This gradient in the amount of deposited material could be of interest for thickness optimizations but the real goal is to combine multiple sources to create a gradient in *composition*. To discuss the composition of a film evaporated from multiple sources, it is more convenient to discuss the number of moles of a component evaporated per unit area rather than the thickness, as the density of individual components and their sum might differ. Letting the number of moles of component i evaporated per unit area be $c_{\mathrm{A,i}}$ and the total number of moles evaporated of that component be n_i, Equation 4.2 can be rewritten as:

$$c_{\mathrm{A,i}} = \frac{n_i \cos^k \varphi \cos\theta}{\pi s^2}. \tag{4.5}$$

For $c_{\mathrm{A,tot}} = \sum_i c_{\mathrm{A,i}}$ total number of moles evaporated per unit area, the molar fraction of component i, χ_i, will then be:

$$\chi_i = \frac{c_{\mathrm{A},i}}{c_{\mathrm{A,tot}}}. \tag{4.6}$$

If a second source (2) is added to the model from above, and that source is mirrored to the first source (1) along the line through the center of the substrate parallel to the $\hat{y}$-axis, the molar fraction of each component will vary close to linearly along the $\hat{x}$-axis, assuming that the cosine order is the same for both sources. The molar percentage of component 1, from source 1, for such a combination of mirrored sources is plotted in Figure 4.14, assuming that the same number of moles of each component is evaporated from their respective sources.

From Figure 4.14a, the close to linear variation in molar percentage along the $\hat{x}$-axis is clearly visible. Along the perpendicular $\hat{y}$-axis there is no change in the molar percentage. However, the total number of moles per unit area in Figure 4.14b instead varies along the $\hat{y}$-axis with a maximum towards the side with the sources. There is also a small variation of $c_{\mathrm{A,tot}}$ along the $\hat{x}$-axis which needs to be taken into consideration when later analyzing thickness-dependent properties of actual deposited films.

The achievable variation in molar fraction at any given point from $r_x = 0$ to $r_x = 50$ will vary with the molar fraction of the total amount of evaporated material, n_i/n_{tot}. In Figure 4.15a the maximum and minimum molar fraction of component 1, χ_1, is plotted as a function of the molar fraction of the total amount evaporated from source 1, $n_1/(n_1+n_2)$ and in Figure 4.15b the difference between the two curves are plotted in molar percent units.

From Figure 4.15a it is visible that the maximum and minimum value of the molar fraction of component 1, χ_1, deviate symmetrically from the molar fraction

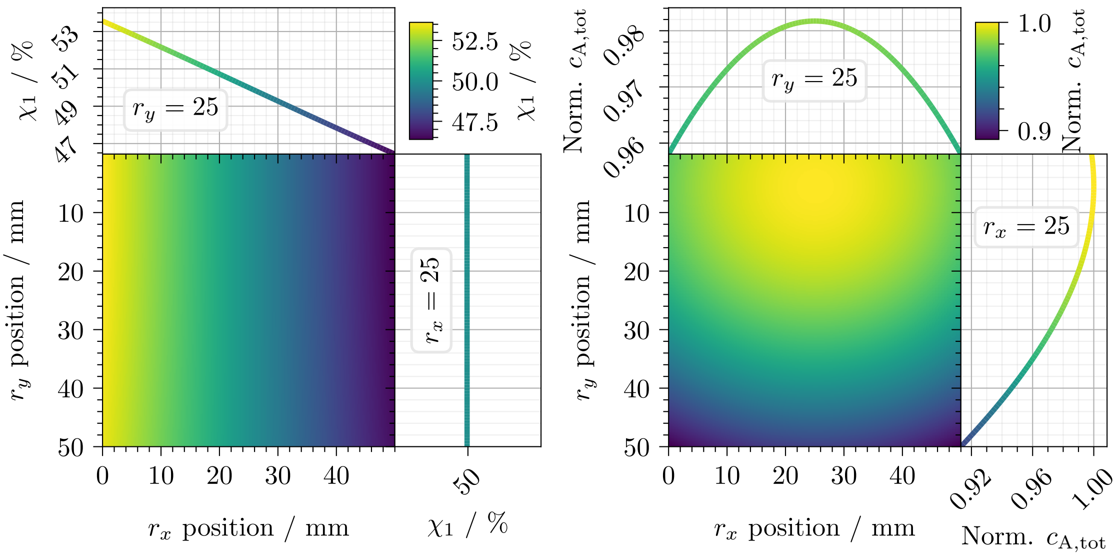

(a) Molar percentage of component 1, χ_1 (b) Normalized total moles per area, $c_{A,tot}$

Figure 4.14: Combination of *two* sources mirrored in placement about the centerline of the substrate that is parallel to the $\hat{y}$-axis, assuming the same total number of moles, n, of each component are evaporated from the respective sources. The colorscale of the plotted lines are equivalent with that for the image and can be used for reference. The molar percentage of component 1 is given by $\chi_1 = c_{A,1}/c_{A,tot}$ with the total moles per area being $c_{A,tot} = c_{A,1} + c_{A,2}$.

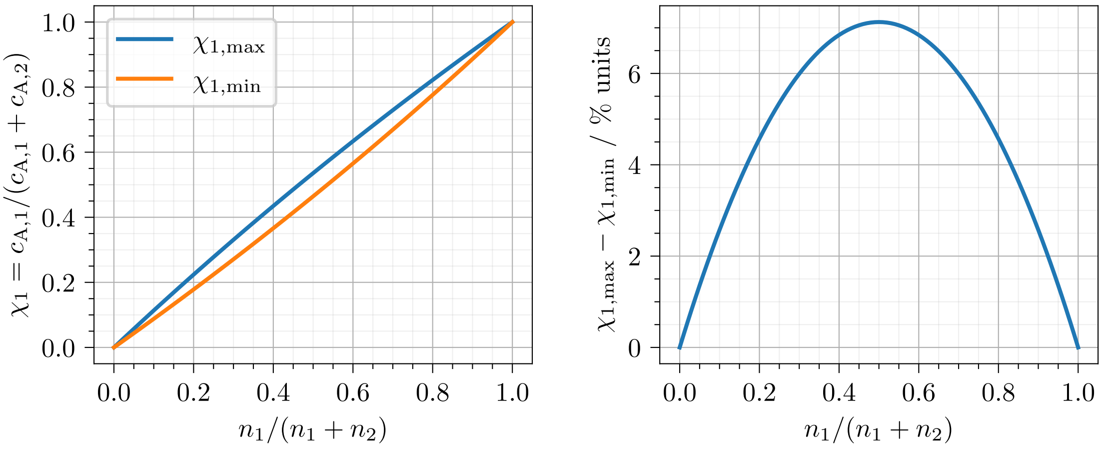

(a) Max and min molar fraction (b) Difference in molar percentage units

Figure 4.15: Variation in molar fraction of component 1, χ_1, throughout the film as a function of the total molar fraction of component 1 being evaporated for a *two* source evaporation, $n_1/(n_1 + n_2)$. The molar fraction of component 1 is given by the ratio of the evaporated moles per unit area on the substrate, $\chi_1 = c_{A,1}/c_{A,tot}$.

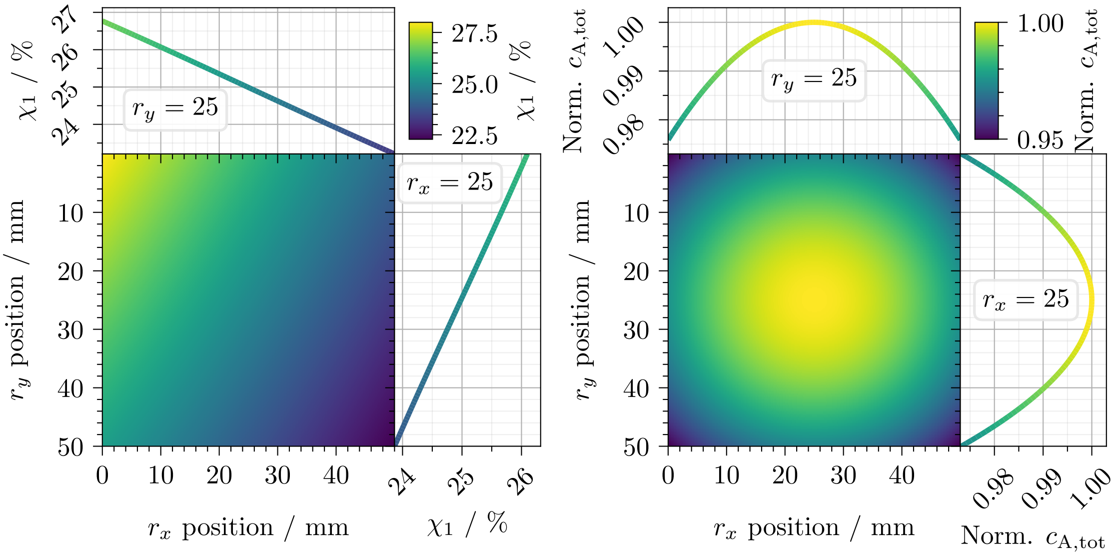

(a) Molar percentage of component 1, χ_1 (b) Normalized total moles per area, $c_{A,tot}$

Figure 4.16: Combination of *four* sources mirrored in placement about the center-lines of the substrate that are parallel to the $\hat{x}$ and $\hat{y}$-axis, assuming the same total number of moles, n, of each component are evaporated from the respective sources. The colorscale of the plotted lines are equivalent with that for the image and can be used for reference. The molar percentage of component 1 is given by $\chi_1 = c_{A,1}/c_{A,tot}$ with the total moles per area being $c_{A,tot} = \sum_{i=1}^{4} c_{A,i}$.

of total amount of evaporated component 1, $n_1/(n_1 + n_2)$. From the difference between the minimum and maximum, plotted in Figure 4.15b, it can be seen that this deviation is largest when an equal amount of components 1 and 2 are being evaporated in total and that the absolute variation in molar percentage units is then ±3.56 % units. However, when the fraction of one of the evaporated components decreases, the variation in the composition will also decrease. When the molar percentage of the total evaporated amount of component 1 is 10, or 90 %, the achieved absolute variation in molar percentage units throughout the film is only ±1.29 % units. This is one of the major limitations of this method of combinatorial PVD.

Four sources

When the model is extended to include all four sources in the evaporation chamber (see subsection 3.1.2 for details) the molar percentage of component 1 at any given point on the substrate varies according to Figure 4.16a. The total amount of material per unit area will also change its distribution and the resulting variation is shown in Figure 4.16b.

From Figure 4.16a it can be seen that the molar fraction of component 1 now forms a plane with a maximum in the upper left corner at $(r_x, r_y) = (0, 0)$, which is closest to the source, and a minimum in the opposite corner on the diagonal at $(r_x, r_y) = (50, 50)$. Furthermore, the absolute variation in molar percentage is observed to be larger along the $\hat{x}$-axis than along the $\hat{y}$-axis. This difference in absolute variation is due to the asymmetric placement of the sources which are further from the center in the $\hat{x}$ direction than in $\hat{y}$. However, the variation along each axis is still close to linear which is key for achieving an even compositional space that is not dense in samples for a particular composition.

In Figure 4.16b the combined amount of evaporated material from the four sources now show a smaller variation along the $\hat{y}$-axis than for two sources (compare with Figure 4.14b). However, there is still a variation in the total amount of deposited material of about 5 % with a minimum in each corner and this once again needs to be considered when investigating thickness-dependent parameters such as the absorption coefficient. The maximum is now in the center of the sample while the variation along the $\hat{x}$-axis remains largely similar.

4.2.2 Evaporation of PbI_2, $PbBr_2$, CsI & CsBr

To investigate combinatorial evaporation in practice, the inorganic cesium lead halide system was once again chosen as an example. In this work, the system is co-evaporated from the PbI_2, $PbBr_2$, CsI, and CsBr binaries. The main phase of interest for the co-evaporated film is the $CsPb(Br_xI_{1-x})_3$ solid solution. The off-stoichiometric variation of Cs to Pb is also interesting, as was discussed in subsection 2.3.5, but the region of interest for that variation is much smaller. Using the knowledge from the model above, the CsBr was then placed in source 1, the CsI in source 2, the PbI_2 in source 3 and the $PbBr_2$ in source 4 so that the largest gradient is achieved between the I binaries on the left and the Br binaries on the right.

Distribution

First, the distributions of the evaporated binaries were investigated individually by evaporating each one according to the methodology described in subsection 3.1.2 onto a 50×50 mm^2 quartz glass substrate. The thickness of the evaporated films was then determined using XRF mapping in a 24×24 grid according to section 3.2.2. XRF may seem as an odd choice for measuring the thickness but what is actually of interest is the number of moles of the binary per unit area and for this XRF has the advantage that it is not affected by the porosity of the deposited film or any change in density due to interaction with the atmosphere, as opposed to other conventional methods such as profilometry. In addition, the XRF method does not require the scribing of lines and can be mapped on an arbitrary grid.

The XRF spectra were modeled in the Bruker XMethod software and the thickness, normalized by the mean, of the $PbBr_2$ film evaporated from source 4 is plotted in Figure 4.17a. The thickness is calculated from the modeled atomic concentrations of Pb and Br, using the L_3-M_5 and K-L_3 lines respectively, and assuming a compact film with a density of 6.66 g/cm^3. The top and side panes in Figure 4.17a show the $\hat{x}$ and $\hat{y}$ projections, respectively, of the thickness surface in blue circles,

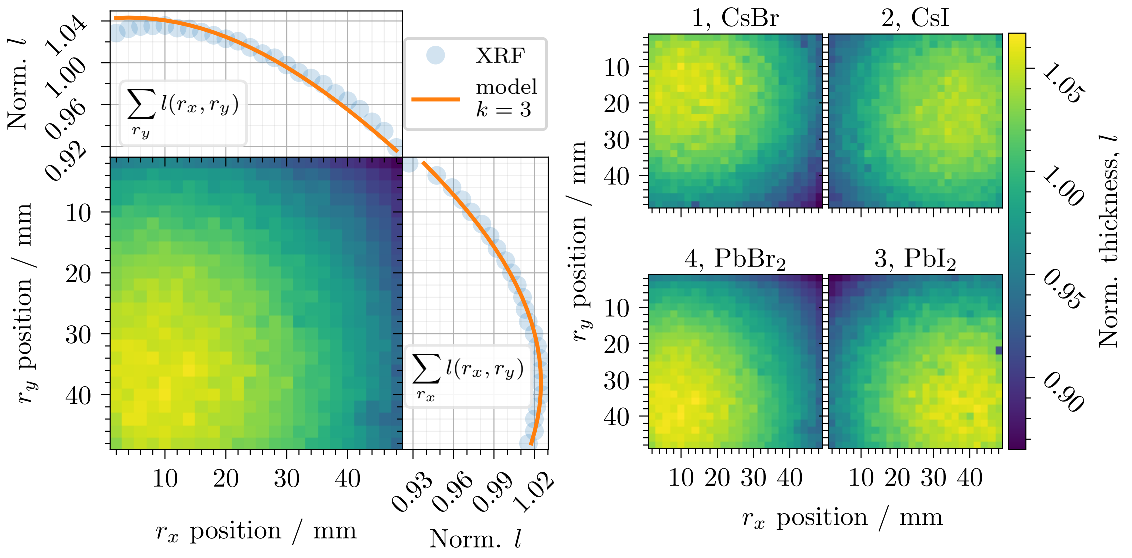

(a) Source 4 with PbBr$_2$

(b) All sources

Figure 4.17: XRF determined thickness distribution normalized by the mean thickness of each distribution in (b). For source 4 the mean projections in $\hat{x}$ and $\hat{y}$ direction are plotted together with the theoretical distribution of cosine order $k = 3$ in (a).

with the theoretical thickness from the model described in subsection 4.2.1 plotted as an orange line. The thickness is modeled using a cosine order of $k = 3$ and the total amount of material evaporated is scaled so that the model average equals the average determined from XRF. The thickness of the films from the other binaries was determined in the same way using, additionally, the L_3-M_5 I line and the L_2-M_4 Cs line. The thicknesses for all distributions, normalized by the mean, are plotted in Figure 4.17b.

From Figure 4.17a the cosine distribution of subsection 4.2.1 is clearly visible (compare with Figure 4.13a from before) and the $\hat{y}$ projections generally agree well with the modelled thickness distribution. The $\hat{y}$ projection is slightly less steep than expected but the deviation is less than ±1%. At r_x values close to the source, the thickness is lower than the theoretically expected values and this is attributed to the slight shading of the edge facing the source. In order to determine the exact cosine order of the PbBr$_2$ distribution, the thickness model from above was fitted to the thickness distribution by minimizing the sum of the square of the residuals using the Nelder-Mead method [124, 125]. The fitted cosine order was found to be $k = 3.25$.

The other sources show similar distributions with the Cs containing binaries showing slightly steeper gradients (higher cosine orders). Source 1, containing CsI, has the maximum shifted towards the center in the $\hat{y}$ direction. This is reproducible over several depositions and is possibly due to the crucible being slightly miss-aligned. In order to investigate the effect this would have on the Br content, x, and Cs content, y, in a co-evaporated $Cs_yPb_{1-y}(Br_xI_{1-x})_{2-y}$ films, the results from

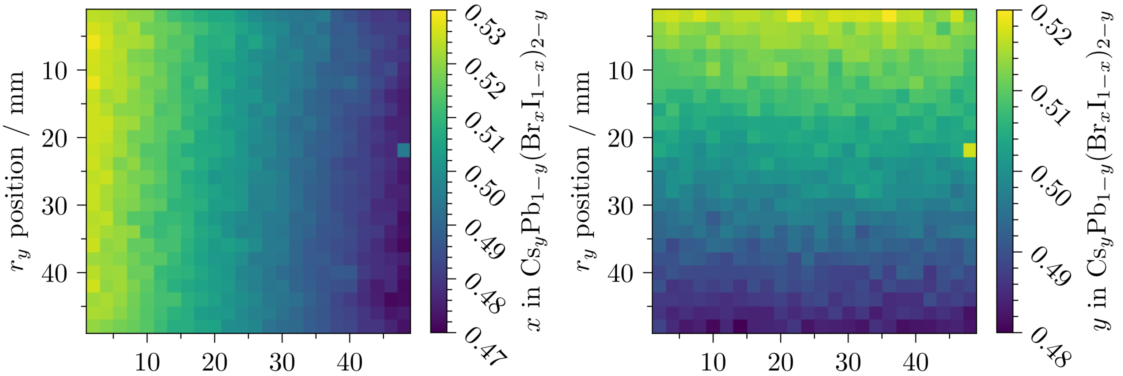

(a) Br content, x

(b) Cs content, y

Figure 4.18: Predicted Br content, x, and Cs content, y, calculated by combining the XRF determined normalized thickness distributions from Figure 4.17b.

Figure 4.17a were combined and the resulting Br content, x, and Cs content, y, are shown in Figure 4.18.

From Figure 4.18 it is evident that the slight shift in the CsI distribution has only a small effect on the gradient in the Br content, x, and Cs content, y. The distributions are slightly angled to the $\hat{x}$ and $\hat{y}$-axis but in such a way that both gradients are still close to normal in their directions, which is desirable to decouple any effects of the two gradients. The absolute variation in $\hat{x}$ is ±2.86 % units while the variation in $\hat{y}$ is slightly smaller at ±2.12 % units.

Tooling factor

In order for each of the distributions to combine in the intended ratios, shown in Figure 4.18, when later co-evaporating the binaries, it is crucial that the rate of evaporation is precisely controlled during the deposition. As described in subsection 3.1.2 the chamber employs PID feedback control of the heating elements of the sources with evaporation rate input from a QCM placed directly above each source. The QCM can accurately determine the mass of the deposited material onto the quartz crystal but in order to translate this to the amount of material on the substrate a geometrical conversion factor, commonly referred to as the tooling factor, needs to be determined.

For the purpose of determining the tooling factor, a set of depositions was performed on four 12.5 mm wide quartz glass stripes that had been scaled prior to the evaporation using a scale with µg precision. New QCM crystals were installed before the evaporation and the change in mass during the depositions was recorded. The substrates were then scaled again post-evaporation to determine the mass of the deposited film. The tooling factor was then determined from the fraction of the mass per unit area in the center of the substrates, calculated by the average of the

Table 4.1: The geometrical tooling factor determined for the four sources.

	CsI	PbI_2	CsBr	$PbBr_2$
Tooling factor	0.761	0.775	0.753	0.776

two center stripes, divided by that on the QCM. These initial tooling factors for the four sources are shown in Table 4.1.

All tooling factors are below one, meaning that more material is being deposited on the QCM than on the substrate. This agrees with the geometry of the chamber where the crystals are closer to the sources than the substrates are. Furthermore, it can be seen that all factors are similar and the slight deviations are likely due to the small differences in the distribution of the sources, see Figure 4.17b. For the determination of the tooling factor for the Pb compounds an acoustic impedance five times lower than that of quartz was assumed and a small change in the tooling factor can be expected if this value is changed.

Acoustic impedance

The QCMs measure the mass through the change in the resonant oscillation frequency of a piezoelectric quartz crystal. As discussed in section 3.1.2, the difference in acoustic impedance of the quartz crystal and the deposited material will cause a deviation of the calculated evaporation rate from the true rate when the deposited mass and frequency shift becomes large. Therefore the ratio of the acoustic impedance of quartz to that of the deposited material, the so-called Z-ratio introduced by Lu and Lewis [113], needed to be determined for all the binaries used. Note that for this work the Z-ratio is defined as the acoustic impedance of quartz divided by the acoustic impedance of the film, and not the other way around as sometimes used in literature.

For CsI and CsBr the manufacturer of the QCM measurement device, Inficon, supplied the Z-ratios to be 1.542 for CsI and 1.410 for CsBr. However, for $PbBr_2$ and PbI_2 no tabulated values could be found and the Z-ratios were instead determined experimentally. This was done once again by evaporating on scaled substrates to determine the mass per unit in the center of the substrate. This time the calibration was repeated with a new QCM and with QCMs with a substantial amount of material already deposited on them. Instead of recording the change in mass on the QCM, the raw resonance frequency of the quartz-film composite, ν_c, was recorded before, $\nu_{\mathrm{c},0}$, and after the deposition, $\nu_{\mathrm{c},1}$. Using Equation 3.6 from section 3.1.2, the tooling factor, f_t, and Z-ratio was fitted to the measurements of difference in film thickness on the QCM, l_f, before and after the depositions. The measured values and results of the fits are plotted in Figure 4.19, where the derivative of the QCM film thickness with respect to the composite frequency, ν_c, is shown. The measurement points, plotted as circles, are scaled by the fitted tolerance factor, f_t, and in

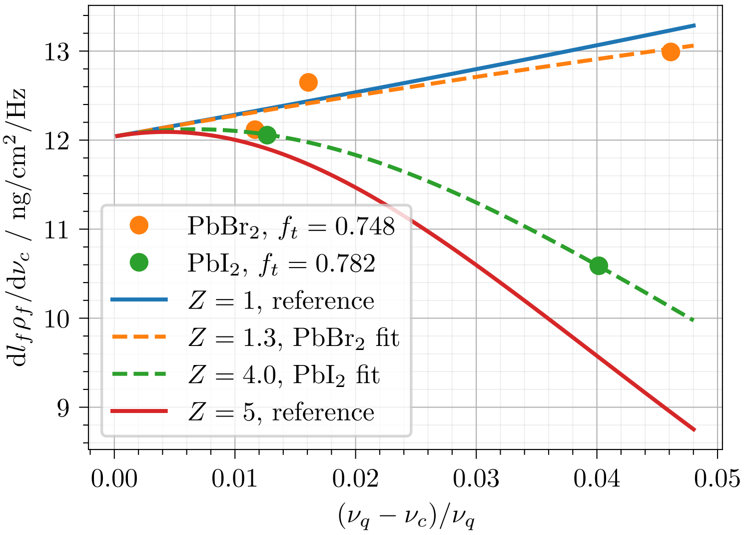

Figure 4.19: Measured values of change in film thickness divided by the fitted tooling factor over change in composite resonance frequency, ν_c, in circles for $PbBr_2$ (orange) and PbI_2 (green). The fitted derivative is plotted in dashed lines with references for $Z = 1$ and $Z = 5$ in solid blue and red lines, respectively.

addition to the fitted lines, the derivatives for a Z-ratio of 1 and 5 are plotted for reference.

The fit was performed by minimizing the square of the normalized residual of the measured difference in film thickness and the result of subtracting the value of Equation 3.6 at $\nu_{\mathrm{c},0}$ from the value at $\nu_{\mathrm{c},1}$. The minimization was once again performed using the Nelder-Mead method [124, 125]. It is important to note, that for the PbI_2 measurements, the two parameters, f_t and Z, are uniquely defined by the two measurement points. From the fit of the $PbBr_2$ measurement, there is a slight mismatch at small frequency shifts, however, the values for larger shifts have higher importance for determining the Z-ratio. From these values it is visible that the Z-ratio for $PbBr_2$ is close to but slightly above 1, here fitted to 1.3, and the PbI_2 value is clearly below 5, here fitted to 4.0.

The Z-ratio of $Z = 4$ found for PbI_2 is lower than the $Z = 9$ previously reported in literature [126]. This discrepancy could be due to the method used for determining the thickness. In the work reporting $Z = 9$, SEM was used to determine the thickness of the PbI_2 layer whilst in this work the mass per unit area was instead determined by scaling. PbI_2 is known to form porous films and it is therefore likely that the density will deviate from the bulk value of 6.16 g/cm^3. In contrast, for the method used in this work, the density factor used when converting the scaled mass per unit into thickness will cancel out in Equation 3.6 removing the uncertainty in the exact value of the density. As the goal of the careful calibration presented here is to control the number of moles deposited per unit area, and not the thickness, the value of $Z = 4$ found in this setup, by scaling, is used.

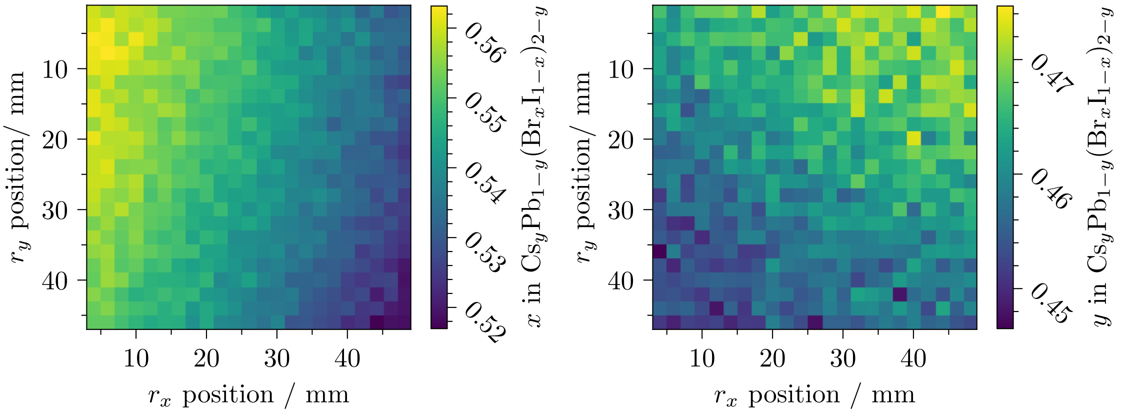

(a) Br content, x

(b) Cs content, y

Figure 4.20: The XRF determined Br content, x, and Cs content, y, as a function of the position (r_x, r_y) for a film of $Cs_yPb_{1-y}(Br_xI_{1-x})_{2-y}$, deposited with a 1:1:1:1 ratio of rates of the four sources CsBr, CsI, PbI_2, and $PbBr_2$.

4.2.3 Four Source Co-Evaporation of $Cs_yPb_{1-y}(Br_xI_{1-x})_{2-y}$

Once the careful calibration of all sources is completed, the co-evaporation of the PbI_2, $PbBr_2$, CsI, and CsBr binaries in a 1:1:1:1 ratio could be conducted to get a film of $Cs_yPb_{1-y}(Br_xI_{1-x})_{2-y}$ with a distribution of y and x around 0.5. A film was evaporated on a 50×50 mm^2 quartz substrate by controlling the rate of each source to be 0.5 nmol/cm^2/10s. After the deposition, XRF mapping was performed on the samples and the spectra were modeled in the Bruker XMethod software. The Br content, x, and Cs content, y, were determined using the L_3-M_5 I line, the L_2-M_4 Cs line, the L_3-M_5 Pb line, and the K-L_3 Br line. The contents are plotted as a function of position on the samples in Figure 4.20.

From the measured distribution in Figure 4.20 there is a clear gradient in both Br and Cs content throughout the film. As expected from the modeling, the Br content in Figure 4.20a is highest in the left part of the sample and is decreasing towards the right. As seen in the prediction in Figure 4.18a the gradient is not perfectly along the $\hat{x}$-axis and there is a slightly higher value at the top than at the bottom. For the Cs content in Figure 4.20b, the measured trend follows the predicted one shown in Figure 4.18b with the gradient being slightly off the $\hat{y}$-axis with higher values on the right-hand side. In general, both gradients are rotated in the same direction as the prediction but with a slightly larger rotation, indicating only slight errors in the calibrations. The mean value indicates that the film is overall Pb-rich and I-poor, which will be discussed further in section 5.2 where the trend for multiple libraries is studied.

The absolute range of variation in Br content, x, is ±2.3 molar % and the variation in Cs content, y, is ±1.4 molar %. These values are from a slightly smaller sample area than the theoretical values calculated above and the corresponding expected values are ±2.7 molar % and ±1.9 molar %. The measured deviation is therefore slightly smaller than expected by 0.4 and 0.5 molar %, respectively. However, the film shows a continuous material gradient as seen in the Br content and the noise in Cs content is most likely due to uncertainties in the quantification of the Cs amount caused by an overlap of the L_2-M_4 Cs line with I lines.

4.2.4 Applicability of Combinatorial Co-Evaporation

As described above combinatorial co-evaporation can create a continuous gradient in material composition throughout a film. With this method, the compositional *homogeneity* of a given sample within the combinatorial library is only limited by the probing area of the selected measurement technique. Instead, the limiting factor of this method is the compositional *range*, which for the chamber utilized here is only ±2.3 molar %. This value could be increased slightly by redesigning the evaporation chamber purposefully for combinatorial evaporation. If the sources are placed further apart and not directed at the substrate, additional deviation in composition could be achieved. However, the method is fundamentally limited at the endpoints of the mixture, as shown in Figure 4.15b, where the deviation drops to zero. Therefore, combinatorial co-evaporation is most suitable for investigating small variations in interesting regions and has proven a valuable tool for doing so [127].

In the later section 5.2, the optical properties in a region of interest within the $Cs_yPb_{1-y}(Br_xI_{1-x})_{2-y}$ compositional space are investigated using this method of combinatorial co-evaporation. This method is here uniquely suited with a very high compositional resolution compared to what is achievable in other combinatorial deposition methods like the discussed combinatorial inkjet printing. The high material quality also facilitates direct studies of individual samples of interest, such as the lattice band-gap correlation investigation in section 5.3, without having to make a stand-alone sample.

Chapter Summary

As a final remark for this chapter on combinatorial synthesis, the two methods outlined here complement each other well. The combinatorial inkjet printing has the advantage that it can span large gradients, from 0-100 molar % of multiple constituents, and it is, therefore, particularly suitable for the first investigation into a solid solution or compositional mixture. Once a region of interest has been established the combinatorial evaporation with its potentially high sample density and generally better morphology can take over. However, it is worth noting that not all materials can easily be processed from both solution and vapor but MHPs can, which makes them especially suitable for comparing these methods. In the following chapter, examples of both methods will be provided, using the MHP $CsPb(Br_xI_{1-x})_3$, and the individual strengths of the methods will be highlighted.

Chapter 5

High-Throughput Analysis of $CsPb(Br_xI_{1-x})_3$

The combinatorial deposition shown in the previous chapter is an excellent tool for speeding up sample preparation during a materials discovery process. However, it is only if combined with high-throughput measurements and analysis that it can substantially decrease the whole investigation time. In this chapter, the two methods of the previous chapter, combinatorial inkjet printing and combinatorial co-evaporation, are used to create libraries of samples that are investigated in a high-throughput manner. From these libraries and measurements the temperature-dependent phase diagram of $CsPb(Br_xI_{1-x})_3$ thin films is determined for the first time. An example of screening material libraries for PV applications is shown with $Cs_yPb_{1-y}(Br_xI_{1-x})_{2-y}$ libraries and the correlation of optical band-gap and the lattice parameters as a function of temperature is investigated for $CsPbBr_{0.9}I_{2.1}$.

5.1 Phase Diagram of $CsPb(Br_xI_{1-x})_3$

The first example of a study enabled by the high-throughput analysis of combinatorial libraries is the determination of the temperature-dependent phase diagram of $CsPb(Br_xI_{1-x})_3$ published in the Journal of Materials Chemistry A [128]. As previously discussed in section 2.3.5, $CsPbI_3$ can exist in several different, semiconducting and non-semiconducting, phases and understanding the transitions between these is key for the development of optoelectronic devices. Until this study, the dependence of the phase transition temperatures on the Br content introduced to the $CsPb(Br_xI_{1-x})_3$ solid solution thin films was not reported. In this section, the details and result of the high-throughput experiment in which the temperature-dependent phase diagram of the full solid solution of $CsPb(Br_xI_{1-x})_3$ $(0 \leq x \leq 1)$, determined from a combinatorially inkjet-printed film, is shown.

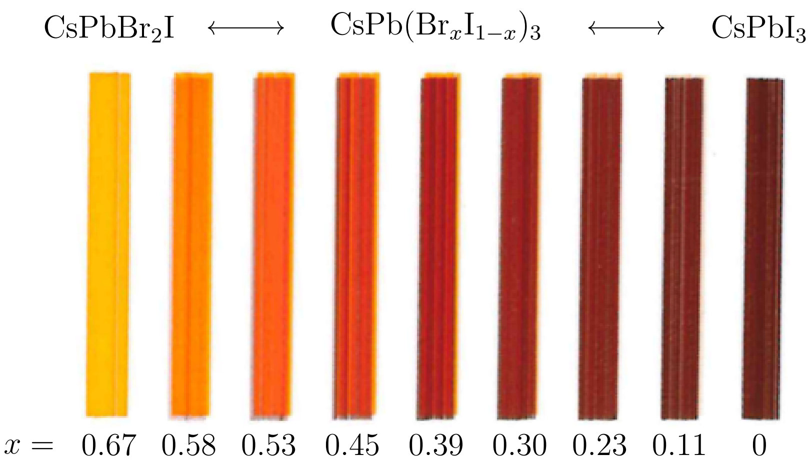

Figure 5.1: Photograph of a combinatorial sample printed on photo paper by mixing a $CsPbI_3$ ink and a $CsPbBr_2I$ one. The sample layout is identical to the combinatorial library used later for the phase diagram determination. The text overlay shows the Br content, x, measured by XRF.

5.1.1 Combinatorially Inkjet-Printed Film

To investigate the transition temperatures in $CsPb(Br_xI_{1-x})_3$ for future use in optoelectronics, a combinatorial library was printed using the method explained in great detail in section 4.1. The library was printed with 9 samples of x, linearly spaced from 0 to 2/3, and later extended by spin-coating a film with $x = 0.85$ and blade-coating one with $x = 1$. The combinatorial image was constructed using every other subpixel matrix with size 4×4 in the same way as the printed logotype in subsection 4.1.3. This time, each sample was printed as a rectangle to accommodate the elongated beam profile of grazing incidence XRD experiments. The samples were printed on quartz glass, cleaned according to section 3.1.1, and a picture of the same image printed on photo paper is shown in Figure 5.1. The stripes observable within some samples of the library printed on photo paper are due to defective nozzles and the misalignment of the two inks due to an offset between the printheads. Both of these effects were accounted for when printing the library on quartz glass.

After printing the library it was placed in the antechamber of the glovebox and the chamber pumped down according to the details in subsection 3.1.1. After being removed from the antechamber the library was annealed at 100 °C for 90 min to crystallize and drive out any remaining solvent. Upon crystallization, all samples turned dark but after the 90 min annealing, the samples with the most iodide content turned completely or partially yellow. In order for all samples to reach their thermodynamically most stable phase in ambient conditions, the library was taken out of the inert atmosphere of the glove box and left in air with ~60% relative humidity for 24 hours before measuring.

5.1.2 High-Throughput GIWAXS Measurements

Once the library printed on quartz glass had relaxed in ambient conditions it was placed on top of a heater element inside an inert sample chamber and placed in the GIWAXS setup, explained in detail in section 3.2.1. As the heating element was heated up to 400 °C, at a specific rate detailed below, the library was moved in steps in the beam so that each sample was exposed for 10 s while a GIWAXS diffractogram and a XRF spectrum were collected. Once all 9 samples had been measured the beam was moved back to the first sample and the steps were repeated throughout the heating up ramp. When the heating element reached 400 °C the temperature was held for 5 min and then cooled down at the same rate, while the samples of the library were continuously measured. The experiment was performed multiple times on equivalent libraries with a heating and cooling rate of 2.5 K/min, 5 K/min, 25 K/min, and another 5 K/min but with the library in the reverse direction to detect any heater inhomogeneity.

Temperature-dependent diffraction patterns

The Br content, x, was determined from the XRF spectra through a fit of the linear combination of the spectra corresponding to pure ink samples of $CsPbI_3$ ($x = 0$) and $CsPbBr_2I$ ($x = 2/3$) respectively. No discernible change in the XRF spectra was observed between the start and the end of the heating ramp and the loss of material from evaporation was, therefore, considered negligible. The GIWAXS patterns were integrated azimuthally and the resulting diffraction pattern for the sample with a composition of $x = 0.23$, heated at a rate of 2.5 K/min, is plotted in Figure 5.2 as a function of the scattering vector q and the sample temperature. In the right panel of the same figure, the diffractograms of the four identified phases are shown.

From the temperature-dependent diffractograms in Figure 5.2a, it can be seen that the $x = 0.23$ sample starts at room temperature in a low symmetry phase, with a multitude of reflexes, and transitions to a higher symmetry phase, with only a few visible reflexes, at a temperature of approximately 500 K. As the sample is cooled down there is a monotonic increase in the position of all reflexes indicating a contraction of the cooling lattice. At around 440 K a kink in the temperature evolution of the strongest reflex is observed together with the appearance of additional peaks, indicating a second-order phase transition. Upon further cooling, the sample exhibits another second-order transition to a lower symmetry phase at around 370 K.

Using the known phase diagram of $CsPbI_3$ [80], the same phases were identified in the Br containing sample. The initial low symmetry phase was identified as the orthorhombic $Pnma$, non-perovskite, δ-phase, which transforms to the high symmetry cubic $Pm\bar{3}m$ perovskite α-phase at a temperature of 499 K. During the cooling down the sample remains in the perovskite phase but loses symmetry as it undergoes second-order phase transitions to the tetragonal $P4/mbm$ β-phase at

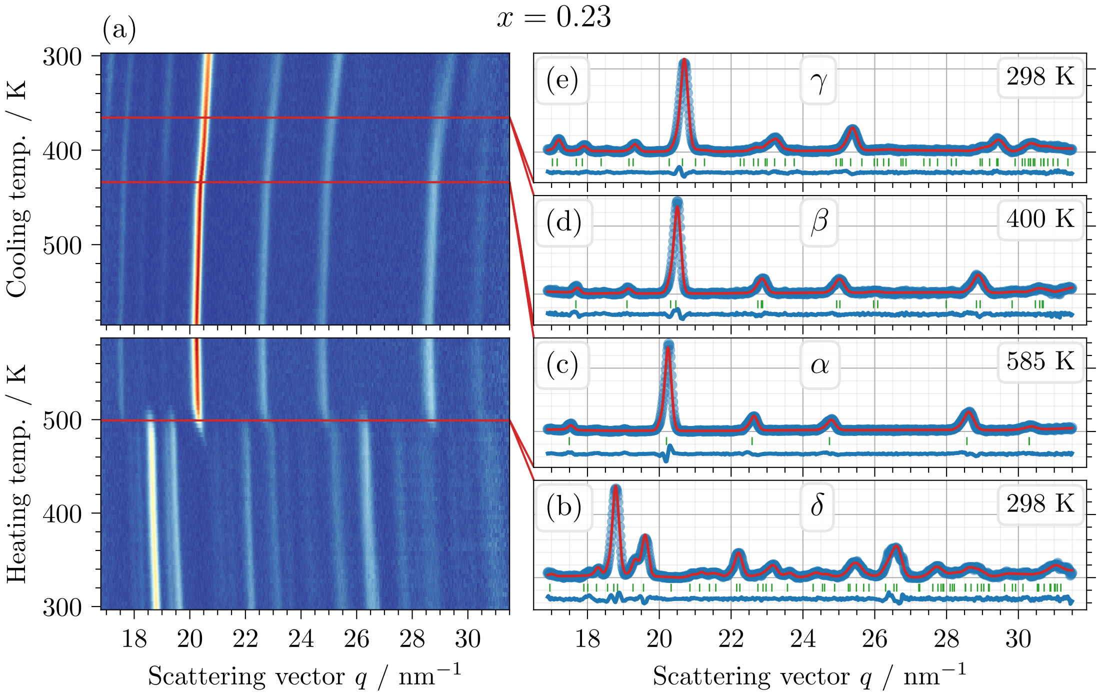

Figure 5.2: Temperature-dependent GIWAXS patterns for the sample with Br content $x = 0.23$. In (a) the heatmap of the azimuthally integrated patterns is plotted as a function of heating temperature (bottom), cooling temperature (top), and scattering vector, q. Blue through yellow to red is increasing intensity in arbitrary units. The horizontal red lines show the phase transitions and an example pattern for each of the four phases are plotted on the right in (b-e) with blue circles. The corresponding Le Bail refinement is plotted as a red line with the peaks in green vertical lines and the residual at the bottom in blue. Reproduced from Ref. [128] with permission from the Royal Society of Chemistry.

439 K and then to the orthorhombic *Pbnm* γ-phase at 370 K. In order to determine the evolution of the lattice parameters, a series of Le Bail refinements were performed on the patterns for the reducing temperatures starting from the α-phase. The refinement results for the example diffractograms in Figure 5.2b-e are plotted together with the measurements in the same plot. The resulting lattice parameters and the normalized cell volume are plotted as a function of the reducing temperature in Figure 5.3.

In the cubic α-phase all three lattice parameters are equivalent and decrease linearly with temperature in Figure 5.3a. As the three lattice parameters are equivalent, the cell volume also decreases linearly with temperature in Figure 5.3b. When the lattice continues to cool down it transitions to the tetragonal β-phase. The cell volume then continues to shrink with the same linear dependence while the equivalent a and b parameters (here normalized by dividing by $\sqrt{2}$) decrease at an increasing rate and the c parameter starts to slightly *increase* in size. As the temperature of the sample continues to decrease, the sample undergoes the phase transition to the orthorhombic γ-phase. The c parameter (now normalized by dividing by 2)

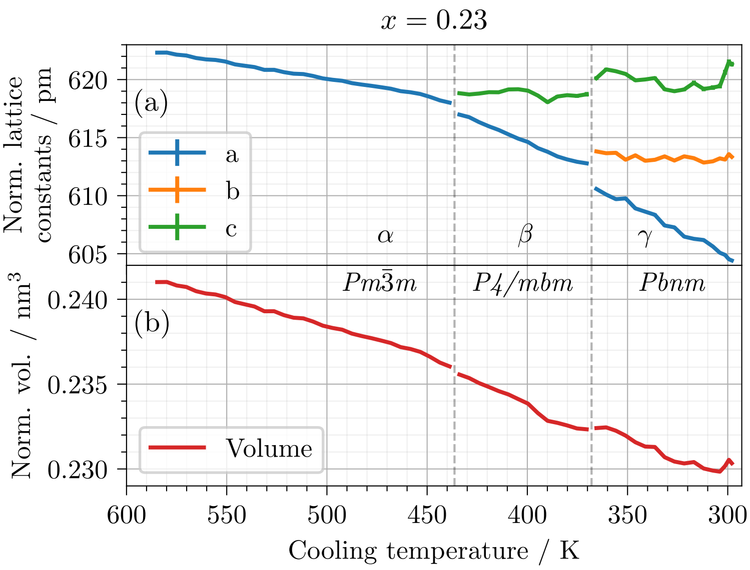

Figure 5.3: Temperature-dependent lattice parameters for the sample with Br content $x = 0.23$ during cool down. In (a) the pseudocubic lattice parameters are plotted in the three different phases with the transitions indicated by dashed gray lines. In (b) the corresponding pseudocubic cell volume is plotted. Reproduced from Ref. [128] with permission from the Royal Society of Chemistry.

and b parameter then level off while the a parameter decreases at an even steeper rate meaning that the overall decrease in cell volume remains linear with a similar slope as before. The small change in slope of the cell volume for the β and γ-phase is further investigated in section 5.3. The evolution of the lattice parameters is in agreement with the values reported for $CsPbI_3$ by Marronnier et al. in 2018 [80].

Temperature-dependent phase diagram

The temperature-dependent diffraction patterns for all samples of the library measured at a rate of 2.5 K/min are shown in section D.2, plotted in the same way as Figure 5.2. The δ to α transition temperature was determined by fitting a sigmoidal curve to the peak area of the 204 and 105 peaks of the δ-phase as well as to the 002 peak of the α-phase. The transition temperature was then extracted as the average inflection point of the two sigmoidal curves. For the cooling down of the library, a series of Le Bail refinements were once again performed and the transition temperatures were determined by the deviation from the linear decrease in normalized cell volume, caused by refining the wrong phase, and the deterioration of the fit. For the samples with $x = 0.85$ and $x = 1$, the transition temperatures to the β- and γ-phase were additionally deduced from the peak area of the 121 and 211 reflections due to the increased q range and resolution for the measurement of these samples. The transition temperatures for the heating and cooling as a function of the Br content, x, are plotted in Figure 5.4.

All samples except for the ones with $x = 0.85$ and $x = 1$ were found to be in the non-perovskite, δ-phase after being stored at ambient conditions for 24 hours. For

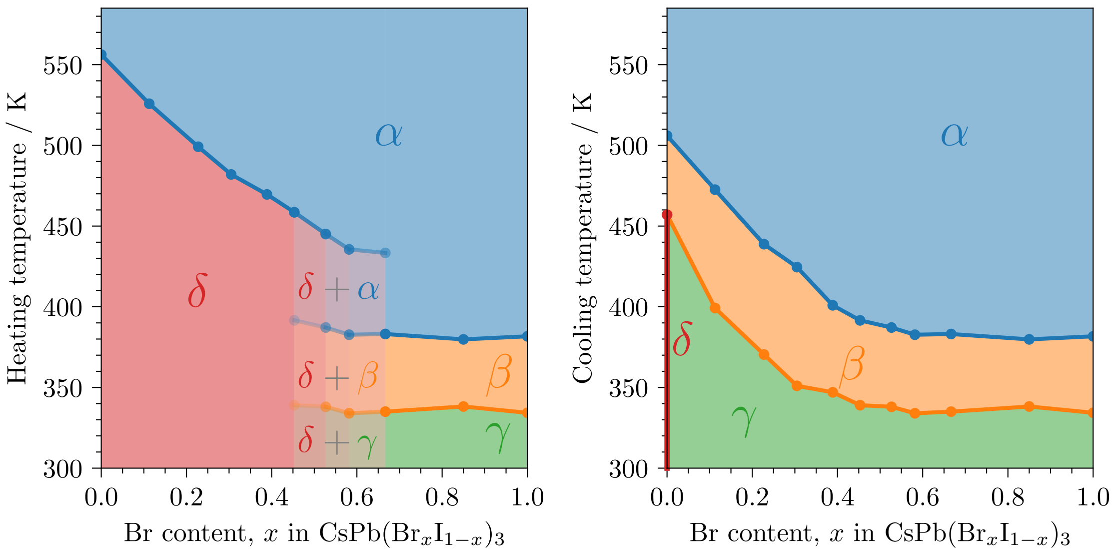

(a) Heating up (b) Cooling down

Figure 5.4: Temperature-dependent phase diagram for the $CsPb(Br_xI_{1-x})_3$ solid solution during (a) heating up and (b) cooling down. The four phases are indicated by the color: the orthorhombic non-perovskite δ-phase in red, the cubic perovskite α-phase in blue, the tetragonal perovskite β-phase in yellow and the orthorhombic perovskite γ-phase in green. Reproduced from Ref. [128] with permission from the Royal Society of Chemistry.

the higher Br content samples, an increasing amount of perovskite phase was present even after being stored in air. From the phase diagram of heating the sample in Figure 5.4a, it can be seen that all compositions transition to the cubic perovskite α-phase with a decreasing temperature needed as the Br content increases. For the samples with some residual perovskite, the initial perovskite phase is the orthorhombic γ-phase which transitions to the tetragonal β-phase followed by the cubic α-phase. During cooling down, all samples started in the cubic α-phase and transition to the tetragonal β-phase between 506 and 380 K with the transition temperature once again decreasing with the Br content. Approximately 50 K below the $\alpha \rightarrow \beta$ transition all samples, except the pure $CsPbI_3$ one, transition to the orthorhombic γ-phase. The pure $CsPbI_3$ instead degrades to the δ-phase slightly before the expected transition to the γ-phase. From the rate-dependent measurements, discussed below, it is only for a fast cooling rate of 25 K/min that the $CsPbI_3$ sample can be thermally quenched into the perovskite phase as reported in literature [129].

The lattice parameter for the cubic phase at a sample temperature of 575 K is plotted in Figure 5.5 as a function of the XRF determined Br content, x. The lattice parameter is seen to decrease linearly with the Br content, x. In the same figure, the Goldschmidt tolerance factor from subsection 2.3.5 is plotted as a function of the Br content for comparison and its effect will be discussed below.

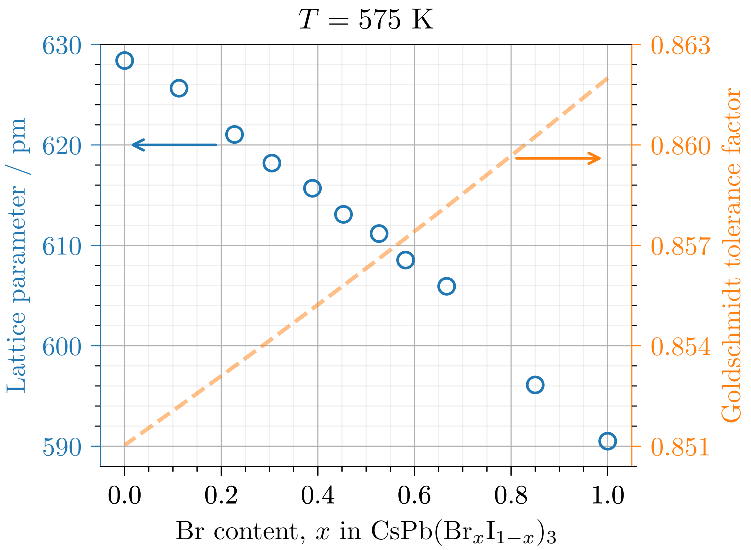

Figure 5.5: Left axis, cubic lattice parameter as a function of XRF determined Br content at 575 K. Right axis, the Goldschmidt tolerance factor as defined in subsection 2.3.5, plotted as a function of the same Br content. Reproduced from Ref. [128] with permission from the Royal Society of Chemistry.

This linear decrease in lattice parameter as a function of the substitution of one ion, I, with another, Br, follows Vegard's law [87] and shows that the CsPb(Br_xI_{1-x})$_3$ mixture is, in fact, a solid solution. This is an important result that explains why the ion ratio can be tuned continuously. Because of the difference in electronegativity between the halides, this also means that the band-gap can be tuned continuously. This effect of ion substitution on optical properties is studied in detail in section 5.2.

Rate dependence of $\delta \to \alpha$ transition

The transition temperature for the formation of perovskite, in the α-phase, from the non-perovskite, δ-phase, was determined for all heating rates using the same sigmoidal fit as explained above. The resulting transition temperatures are plotted as a function of the *intended* Br content, x, for all samples that contained the δ-phase, in Figure 5.6. As can be seen in the figure, there is no clear dependence of the transition temperature on the rate. This means that the transition is not limited by an activation energy and is rather driven by the change in lattice spacing with temperature. The experiments also show a clear dependence on the Br content, as seen in the constructed phase diagram, and show the reproducibility of the combinatorial inkjet printing method as well as the high-throughput characterization method employed. Additionally, the scan with the library in the reverse direction shows the same result meaning that the observed dependence is not an artifact of heater inhomogeneity.

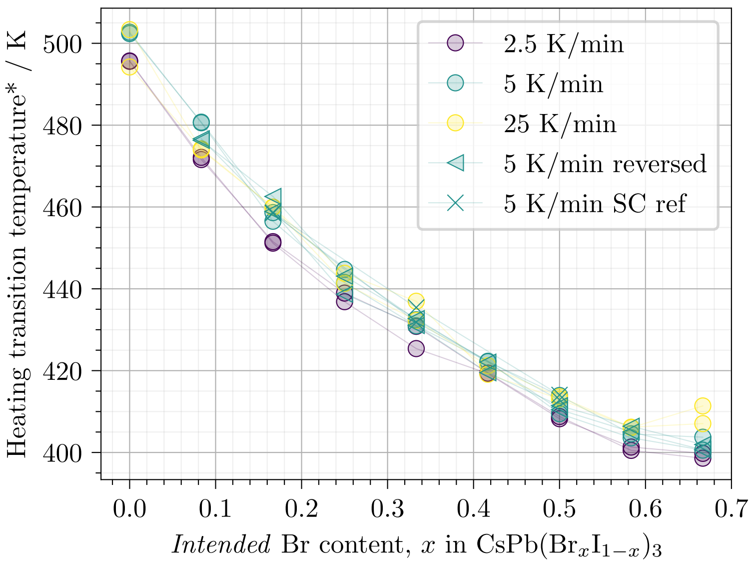

Figure 5.6: The $\delta \rightarrow \alpha$ transition temperature for all investigated heating rates, determined from a sigmoidal fit to the intensity of the 204 and 105 peaks of the δ-phase as well as to the 002 peak of the α-phase. Additionally, the transition temperature is shown in crosses for three spin-coated references (SC ref) that were prepared from inks with known composition. The transition temperatures are plotted as a function of the *intended* Br content, x. *The transition temperature is taken from a reference thermocouple inside the chamber and is, therefore, consistently lower than the calibrated temperatures but is valid for a relative comparison.

5.1.3 The Tolerance Factor of $CsPb(Br_xI_{1-x})_3$

As was concluded above, the introduction of Br ions into the $CsPbI_3$ lattice decreases the cell volume. Consider for simplicity the cubic phase for which all lattice parameters are equal and plotted as a function of the Br content, x, in Figure 5.5. The linear decrease of the lattice parameter shows that the substitution of I with Br occurs within the unit cell, as opposed to in separate domains. Recalling the cubic structure from subsection 2.3.5, this reduction in lattice parameter and, therefore, in volume causes a reduced size of the cuboctahedral cavity formed by the halides. From subsection 2.3.5 the Goldschmidt tolerance factor [30] of $CsPbI_3$ is 0.851 and means that the cuboctahedral cavity formed by the I anions (r = 220 pm) and the Pb cations (r = 119 pm) is too large to be stabilized by the small Cs cation (r = 188 pm) [130]. This means that the reduction in cell size observed when the I anions are partially replaced with the smaller Br anions (r = 196 pm) will continuously increase the tolerance factor towards the ideal value of 1, as indicated in Figure 5.5.

The change in tolerance factor when going from $CsPbI_3$ to $CsPbBr_3$, 0.851 → 0.862, may be small but recent work by Yang et al. in 2017 [131], suggests that this small change can have a large effect on the transition temperatures from the ideal cubic perovskite to the distorted tetragonal and orthorhombic perovskites. Yang et al. simulated the anharmonic potential energy of various Cs-based MHPs and show a non-linear dependence on the tolerance factor, with the largest decrease found for the low tolerance factors of $CsPbI_3$ and $CsPbBr_3$. The same non-linear decrease of energy required to overcome the octahedral tilting is observed in the transition temperatures of the $\alpha \rightarrow \beta \rightarrow \gamma$ transitions in Figure 5.4b suggesting that the same trend observed by Yang et al. can be generalized to the solid solutions between the simulated endpoints.

It is important to note that the argument of decreased anharmonic potential energy from above can only be applied to the octahedral tilting occurring in the second-order $\alpha \rightarrow \beta \rightarrow \gamma$ transitions and not to the transition to and from the non-perovskite δ-phase. However, it has been shown that the tolerance factor can also affect the thermodynamic stability of MHPs [132]. Together with the similarity in the temperature dependence between the two types of transitions, compare Figure 5.4a and b, it is probable that the small changes in tolerance factor are responsible for the trend in the $\delta \rightarrow \alpha$ transition temperature. The reverse process, i.e. the degradation of the perovskite to the δ-phase was not studied quantitatively but observations during the aging of the samples in humid air before measurements suggest that the same trend is present for this transition as well. The pure $CsPbI_3$ samples were observed to turn yellow, indicating a transition to the δ-phase, already on the hotplate with the other samples also turning yellow, one-by-one, *in order* of increasing Br content. Only the samples with the highest Br content ($x > 0.67$) remained fully in the perovskite phase. The same degradation of the pure $CsPbI_3$ sample was observed in the measurements and only with a fast cooling rate of 25 K/min the metastable perovskite phase could be obtained at room temperature. All this indicates that the increase in tolerance factor from including Br stabilizes the perovskite phase.

5.2 Material Screening for Photovoltaics

After showing in the previous section that the addition of Br stabilizes the perovskite phase of the inorganic $CsPbI_3$, the optoelectronic properties of the solid solutions are here investigated. In this section, screening for the expected performance in a PV device is performed on co-evaporated $Cs_yPb_{1-y}(Br_xI_{1-x})_{2-y}$ as a second example of high-throughput analysis implemented on combinatorial libraries. The study expands on the results of the previous section through increasing the dimensionality of the compositional distribution by introducing an off-stoichiometric variation in Cs to Pb ratio. This variation has earlier proved crucial for directly obtaining the perovskite phase of $CsPbI_3$ during low-temperature deposition [127].

The section begins with defining the combinatorially co-evaporated libraries used and is followed by explaining and presenting the results of the key composition measurement, XRF. After that, the complementary structural analysis by means of GIWAXS is presented, followed by the three contactless optical screening methods UV/Vis, TRPL, and absolute PL. In general, the full measurement result from a single sample within the library is presented, followed by a dimensional reduction to a 0D property. These properties are then plotted versus the XRF determined Br content, x, and Cs content, y, to investigate any compositional correlations. Finally, the results are combined to estimate the potential power conversion efficiency of PV devices made from any of the sample compositions.

5.2.1 Combinatorially Co-Evaporated Libraries

Six combinatorial libraries of $Cs_yPb_{1-y}(Br_xI_{1-x})_{2-y}$, labeled 1-6, were deposited by combinatorial co-evaporation of CsI, PbI_2, CsBr, and $PbBr_2$ according to the method described in detail in section 4.2. For all libraries, the reported evaporation rates from the QCMs were kept at a constant value throughout the evaporation and controlled so that the number of moles, of the binaries containing Pb and Cs, deposited at the center of the substrate, per unit area and time, was kept at a 1:1 ratio. In other words, all libraries were evaporated with an intended Cs content, y in $Cs_yPb_{1-y}(Br_xI_{1-x})_{2-y}$, of 0.5 at the center of the substrate. The ratio of the rates between the Br and I binaries was varied to achieve a variation in intended Br content, x, of 0.303 to 0.5. Additionally, two reference libraries of $Cs_yPb_{1-y}I_3$ and $Cs_yPb_{1-y}Br_3$, corresponding to $x = 0$ and $x = 1$ respectively, were prepared. The evaporation time of each library was scaled according to the relative densities, reported in Figure 5.5 of the previous section, to achieve the same mean thickness for all libraries. The rate of all the four binaries and the evaporation times used for the $6 + 2$ libraries are shown in Table 5.1.

The libraries were evaporated on 50×50 mm^2 quartz glass in vacuum with a substrate temperature of 50 °C. After deposition, the libraries were annealed inside a N_2-filled glovebox by placing them on a 275 °C hotplate for 30 s before removing

Table 5.1: The different evaporation rates and times used for the manufacturing of the combinatorial libraries studied in this section.

Library number	Rate in nmol/cm^2/10 s CsBr	$PbBr_2$	CsI	PbI_2	Evaporation time in s
1	0.303	0.303	0.697	0.697	3667
2	0.37	0.37	0.63	0.63	3712
3	0.452	0.452	0.548	0.548	3768
4	0.5	0.5	0.5	0.5	3801
5	0.409	0.409	0.591	0.591	3738
6	0.335	0.335	0.665	0.665	3688
10	1	1	0	0	4189
11	0	0	1	1	3479

them and directly placing them on a metal heatsink to quench them back down to room temperature.

5.2.2 XRF

The compositional XRF characterization was performed last as the libraries needed to be briefly transported in the air before being loaded into the vacuum chamber of the XRF. However, the results are here presented first as the composition is key to understanding the results of the other measurements.

The XRF was mapped on a 24 × 24 grid on the library and the same grid was used for all other mappings. The starting point, relative to the top left, was at $(r_x, r_y) = (2.5, 2.5)$ mm with the points spaced 2 mm apart from each other.

Single XRF spectrum

As an example, the background-corrected XRF spectrum for the sample at the position $(r_x, r_y) = (26.5, 26.5)$ mm of library 6 is plotted in the region of the fluorescence peaks used for the compositional analysis in Figure 5.7. The spectrum was modeled with the Bruker XMethod software and the modeled contribution of each of the spectral lines for each of the four elements I, Cs, Pb, and Br are shown as vertical lines placed at the theoretical energy of fluorescence with the height scaled by their contribution to the complete spectrum.

From Figure 5.7 it is clear that the film contains the four intended elements I, Cs, Pb, and Br. The strongest contribution comes as expected from the L_3-M_5 and L_2-M_4 fluorescence lines which for I is at 3.94 keV and 4.22 keV, for Cs at 3.29 keV and 4.62 keV, and for Pb at 10.55 keV and 12.61 keV. For Br, the L-lines overlap with the K-lines of the Si in the substrate and the K-L_3 line at 11.92 keV is therefore used instead. With the exception of the I L_2-M_4 and Cs L_3-M_5 line, the lines are well-separated meaning that robust modeling of the atomic concentrations can be performed.

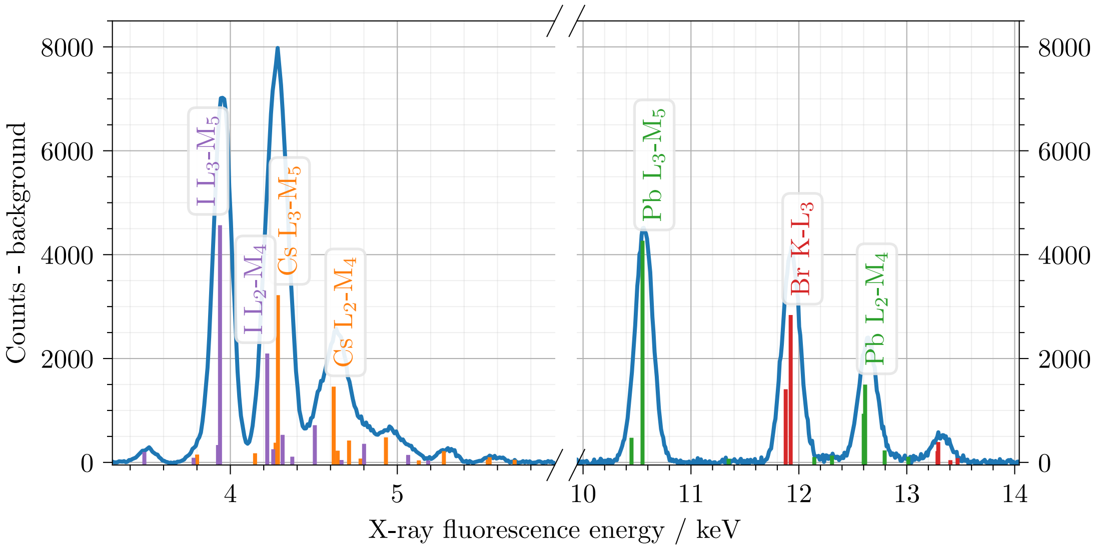

Figure 5.7: Background subtracted XRF spectrum for the sample at the position $(r_x, r_y) = (26.5, 26.5)$ mm in library 6. The spectrum is plotted in two regions, first the region around the I and Cs L-lines (3-6 keV) and, secondly, the region around the Pb L-lines and the Br K-lines (10-14 keV). The fluorescence lines for the four elements are plotted as vertical lines with each individual height scaled by the modeled intensity of that line. From the modelling the $Cs_yPb_{1-y}(Br_xI_{1-x})_{2-y}$ sample was found to have a Br content of $x = 0.36$ and a Cs content of $y = 0.50$.

Br and Cs content

For each of the 576 samples in each of the 6 libraries, the XRF spectrum was modeled using the Bruker XMethod software with the lines discussed above used for determining the atomic concentrations. This is a quite time-consuming task but it is necessary as both the Pb to Cs ratio as well as the Br to I ratio varies throughout the film. Because of this variation, an absolute determination is necessary rather than normalization by the Pb peak as was used in the previous section. The result of the modeling is shown in Figure 5.8 as a scatter plot of the Cs content, y, versus the Br content, x, of the $Cs_yPb_{1-y}(Br_xI_{1-x})_{2-y}$ mixture. The library of each sample is indicated by its color and goes from purple, through green, to yellow in the order in which the libraries were deposited.

There are multiple important results that can be found in Figure 5.8. The first thing to note is that all six libraries show a variation in Br content around a different point as intended. However, recalling that the most I-rich library, 1, was evaporated with an intended ratio of Br sources to I sources of 0.303:0.697 and the most Br-rich library, 4, with a ratio of 0.5:0.5, all libraries seem to be shifted towards a more Br-rich composition by roughly 4 % units. Instead of the expected variation of around 0.3, library 1 shows a variation of around 0.34, and for library 4 the variation is around 0.54 instead of the expected 0.5.

The second thing to note is that instead of the intended variation of Cs content around the stoichiometry point ($y = 0.5$) for all libraries, there is an offset that

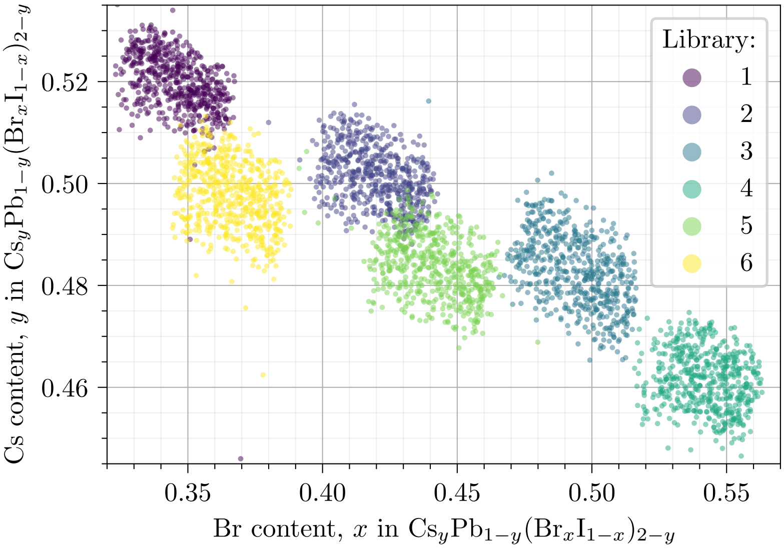

Figure 5.8: Scatter plot of the XRF determined Cs content, y, versus Br content, x, in $Cs_yPb_{1-y}(Br_xI_{1-x})_{2-y}$ for the the 24×24 samples in each of the 6 evaporated libraries, color coded in order of evaporation.

depends both on Br content, x, and order of evaporation. This indicates that the calibration of one or several sources is off slightly. Specifically, the dependence on the order of evaporation indicates that the Z-ratio, of one or multiple sources, is wrong as a drift with the amount of material on the QCM is observed.

These results underscore the importance of careful calibrations of the Z-ratio and tooling factor but more importantly that a compositional evaluation is necessary for investigating libraries fabricated by combinatorial co-evaporation. Without the results from Figure 5.8 a dependence on the Cs content could easily have been confused for dependence on Br content.

Thickness

An advantage of modeling the XRF spectra quantitatively is that the absolute atomic concentrations can be used to calculate the film thickness. The film thickness determined by the model for all samples in all libraries is plotted as a function of the Br content, x, in Figure 5.9a and Cs content, y, in Figure 5.9b.

From Figure 5.9 it is clear that the deviation from the intended Cs content, previously observed, also causes the thickness to deviate from the intended 500 nm. From Figure 5.9b it can be seen that the thickness correlates with the Cs content and the deviation from the trend, i.e. the spread of thickness value for any given Cs content, is explained by expected variation throughout the film as discussed in subsection 4.2.1 of the previous chapter. This spread is also clear in Figure 5.9a where the variation within each library takes on the shape of an arch as expected from the distribution model in the aforementioned section. This observed variation

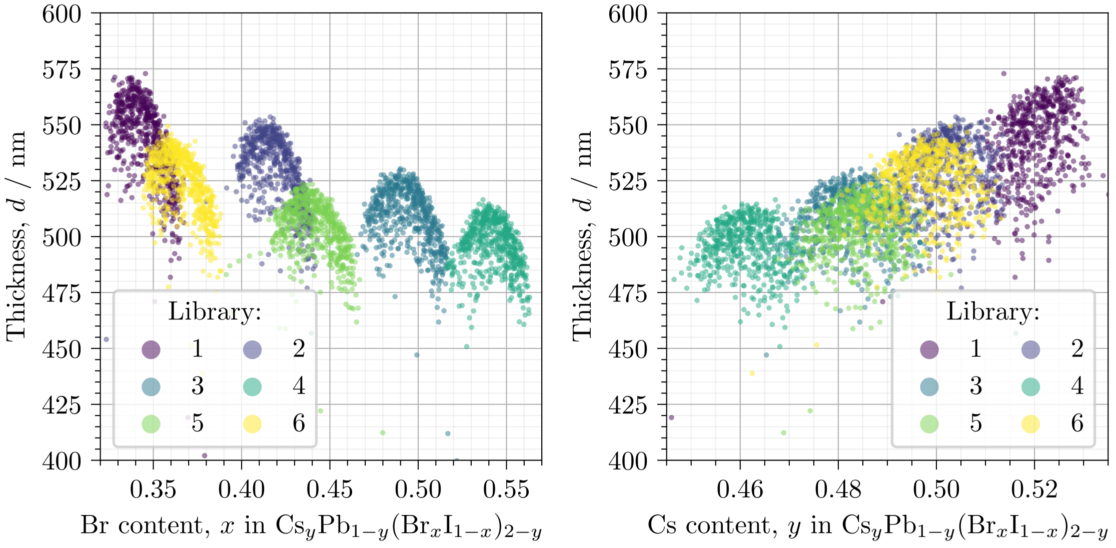

(a) Thickness, d, versus Br content, x

(b) Thickness, d, versus Cs content, y

Figure 5.9: Scatter plot of the XRF determined film thickness, d, versus Br content, x, and Cs content, y, in $Cs_yPb_{1-y}(Br_xI_{1-x})_{2-y}$ for the the 24×24 samples in each of the 6 evaporated libraries, color-coded in order of evaporation.

in thickness is important to keep in mind when later interpreting results such as UV/Vis absorptance, which has a direct dependence on the thickness of the film.

5.2.3 GIWAXS

In addition to the compositional analysis by XRF, the structural properties of the libraries are investigated through mapping GIWAXS measurements at the mySpot beamline of the BESSY II synchrotron. These measurements are performed to investigate the crystallographic phases present in the film. As the main perovskite phase consists of Cs and Pb in a 1:1 ratio ($x = 0.5$) it is of interest to investigate whether the excess Cs or Pb forms crystalline secondary phases or not. The measurements were performed in a nitrogen environment and the full experimental details are explained in section 3.2.1.

3D diffractogram

GIWAXS is especially complex to plot as a function of Br and Cs content as the measurement at each point in 2D space is the scattering intensity measured on a 3-dimensional sphere in reciprocal space. As an example, the scattering intensity for a sample with Br content $x = 0.5$ and Cs content $y = 0.48$, at position $(r_x, r_y) = (26.5, 26.5)$ in library 3, is plotted in a heatmap as a function of the in-plane and out-of-plane scattering vector in Figure 5.10. In this figure, the sphere from the reciprocal space, $I(q_x, q_y, q_z)$, has been distorted onto a 2D plane, in a similar way to how certain maps of the spherical earth are created, and the in-plane scattering

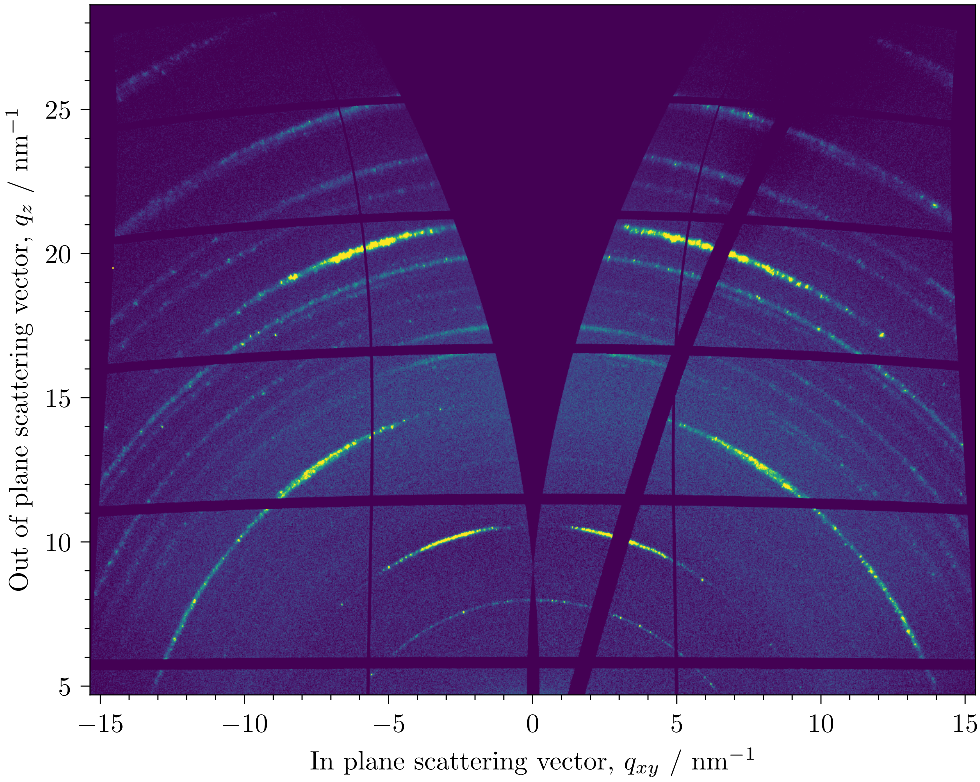

Figure 5.10: 3D GIWAXS pattern for a sample with Br content $x = 0.5$ and Cs content $y = 0.48$, plotted in a heat-map as a function of the out-of-plane scattering vector, q_z, and the in-plane scattering vector, q_{xy}. The points are sampled on a sphere and in order to display it here in 2D the in plane scattering vectors, q_x and q_y, are assumed to be equal and the total in plane scattering vector, q_{xy}, is defined as $q_x\sqrt{1 + q_y^2/q_x^2}$.

vector $\vec{q}_{xy}$ taken as the sum of the $\vec{q}_x$ and $\vec{q}_y$ vectors. The sign of q_{xy} is taken to be the same as that of q_x.

From Figure 5.10 it can be seen that there is an out-of-plane oriented crystalline phase present. The missing wedge along the q_z axis is observed because the true q_z axis is only probed at two points (think of a line through a sphere), the first is along the direction of the beam (below what was here measured) and the second is in the Bragg-Brentano geometry where the angle of the diffracted beam is exactly twice the angle of incidence ($\omega = \theta$), seen here at around $q_z = 9$.

In a first step to reduce the dimensionality of this data, the 3D GIWAXS diffractogram is integrated azimuthally around the propagation axis of the incident beam. In order to perform this integration, the position of the detector needs to be known in relation to the point of beam-sample intersection for all 6 degrees of freedom. This position was determined by measuring a LaB_6 reference powder with known lattice parameters through the use of the `Python` library `PyFAI`. The same library was used to perform the azimuthal integrations. This reduces the 3D diffractogram from Figure 5.10 to the 1D diffractogram plotted in red circles in Figure 5.11.

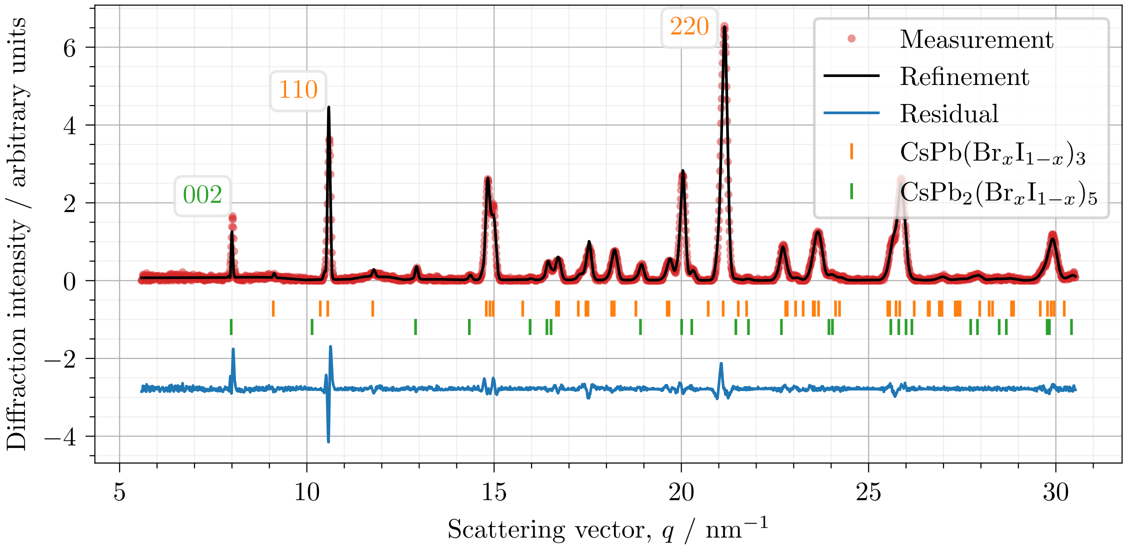

Figure 5.11: Azimuthally integrated pattern from the 3D GIWAXS pattern in Figure 5.10. The pattern is plotted in red with the refinement of the orthorhombic perovskite phase and the Pb-rich tetragonal phase in black. The peak positions of the refined phases are plotted as vertical lines and the residual in blue at the bottom.

The 1D diffractogram can then be used to identify the phases present in the film. First of all, the expected orthorhombic perovskite phase is identified by for example the strong 110 peak at around 10.5 nm^{-1} and the 220 peak at around 21 nm^{-1}. However, the peak at 8 nm^{-1} is not from the perovskite phase and together with the peak at 20 nm^{-1}, as well as the fact that the sample was determined to be Pb-rich from the XRF measurement, a secondary tetragonal $I4/mcm$ phase of the Pb-rich CsPb$_2$(Br_xI_{1-x})$_5$ was identified. Using these two phases a Le Bail refinement was performed using the software `Fullprof`. The result of the refinement is plotted with a black line in Figure 5.11 and the residual at the bottom in blue. The peaks of the main perovskite phase are indicated with vertical orange lines whilst those of the Pb-rich phase are shown in green.

The refinement shows good agreement with the measured values and it is concluded that no other crystalline phases are present in any large amounts. The assignment of the phases is further supported by the fact that the peaks identified as the Pb-rich phase show no orientation in the 3D diffractogram of Figure 5.10 whilst the peaks assigned to the main perovskite phase do. Compare for example the 002 peak of the Pb-rich phase at 8 nm^{-1} with the 110 peak of the orthorhombic perovskite phase at 10.5 nm^{-1} or the peaks at 20 and 21 nm^{-1}.

110 lattice spacing

The refinement from above is an excellent tool for determining the phases present in a diffractogram and indexing the individual peaks. However, the refinement is a very manual process and, although it could potentially be automized, it is still very time-consuming. For the high-throughput analysis, the phases are instead assumed

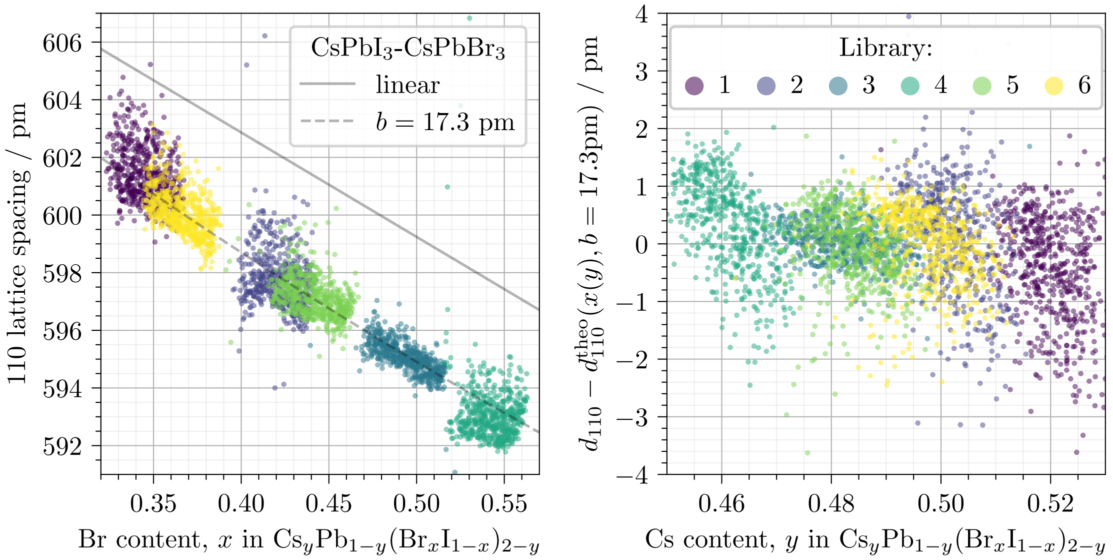

(a) d_{110} versus Br content x

(b) Δd_{110} versus Cs content y

Figure 5.12: The 110 lattice spacing of the orthorhombic perovskite phase as a function of Br content, x, and Cs content, y, in $Cs_yPb_{1-y}(Br_xI_{1-x})_{2-y}$ for all the samples in the 6 libraries. The solid gray line in (a) shows the linear combination of the 110 lattice spacings for pure $CsPbI_3$ at $x = 0$ and for pure $CsPbBr_3$ at $x = 1$. The dashed line shows the same linear combination, corrected by a quadratic term, $x(1-x)$, with coefficient b according to Equation 5.1. The fitted quadratic trend as a function Br content, $d_{110}^{\text{theo}}(x)$, is used for calculating the Br decoupled deviation, Δd_{110}, in (b).

to be those found through the refinement of the sample with Br content $x = 0.5$ and Cs content $y = 0.48$ shown in Figure 5.11. As a first step, the lattice parameters of the main perovskite phase are studied. This in theory also requires a refinement and, therefore, the analysis is here restricted to the 110 lattice spacing, which is directly dependent on the a and b lattice parameters. The 110 spacing is chosen due to the strong diffraction observed from these planes. Another advantage of choosing the 110 spacing is that both the 110 and the doubled 220 peak are observed. This means that any deviation in the 220 peak, from exactly twice the value of the 110 peak, is a zero offset, most likely due to a small misalignment of the sample. Finding the position of the peak maximum of two peaks is considerably faster than a full refinement and through this method, the 110 lattice spacing of the orthorhombic perovskite phase was determined for all samples in all libraries. The resulting values of the lattice spacing are plotted as a function of Br content, x, in Figure 5.12a.

In Figure 5.12a there is a clear formation of a solid solution between $CsPbI_3$ and $CsPbBr_3$, as was shown for the stoichiometric case in the previous section. The lattice spacing is strongly correlated with the Br content, x, but there is a considerable spreading compared to the case of the combinatorial inkjet-printed films.

The 110 lattice spacing for pure $\mathrm{CsPbI_3}$ and $\mathrm{CsPbBr_3}$ can be calculated from reported values of the a and b parameters [133, 134] to be 617 and 581 pm respectively. According to Vegard's law [87], the solid solution would be expected to have a and b parameters, and, therefore, 110 lattice spacing, that approximately follows a linear combination of these endpoints. This linear combination is plotted as a solid gray line in Figure 5.12a and it can be seen that the measured values deviate systematically from this line. This fact was already mentioned in subsection 4.1.4 where a slight bowing of the lattice spacing was seen and has also been reported previously in literature [86]. In order to characterize the bowing a quadratic term was added to the linear combination above according to the following equation:

$$d_{110}^{\mathrm{theo}}(x) = x d_{110}^{\mathrm{CsPbBr_3}} + (1-x) d_{110}^{\mathrm{CsPbI_3}} - bx(1-x), \tag{5.1}$$

with the parameter b introduced as the bowing parameter in the same units as d (pm). This method is commonly employed to characterize deviations in band-gaps of solid solution semiconductors, see equation 4.1 in [135].

Equation 5.1 was fitted to the measured values and the bowing parameter was determined to be $b = 17.3$ pm, the result is plotted with a dashed gray line in Figure 5.12a. Using this modelled lattice spacing, the dependence on Br content can be decoupled from the Cs one. This is done by subtracting the modelled lattice spacing as a function of Br content, $d_{110}^{\mathrm{theo}}(x)$, from the experimentally determined one for each point. These values are plotted as a function of Cs content, y, in Figure 5.12b.

There is no clear correlation between the lattice parameter and Cs content in Figure 5.12b and the spread of values for a given Br content does therefore not seem to correlate with the Cs content. One possible explanation for the spreading is local inhomogeneity. The GIWAXS was used to determine the lattice spacing and the XRF used to determine the Br content were measured in different setups using small approximately 20 µm spot sizes. The points were selected relative to the edge of the substrate and although this alignment is precise on the order of the grid size (2 mm) it is not guaranteed that the small spot XRF and GIWAXS measurements probed the same volume. This means that for a given composition there is an uncertainty in the lattice spacing and vice versa.

Secondary phases

In order to investigate the secondary Pb-rich phase, without a quantitative refinement for each sample, the area of the 100 peak of the Pb-rich phase was compared to the area of the 110 peak of the main perovskite phase. The area fraction of the 100 peak is plotted as a function of the Pb content, $1 - y$, for each sample of each library in Figure 5.13. It is here worth noting that this is not a quantitative measure of the amount of one phase. However, this method gives a qualitative idea of the variation in the amount of the Pb-rich phase throughout the libraries.

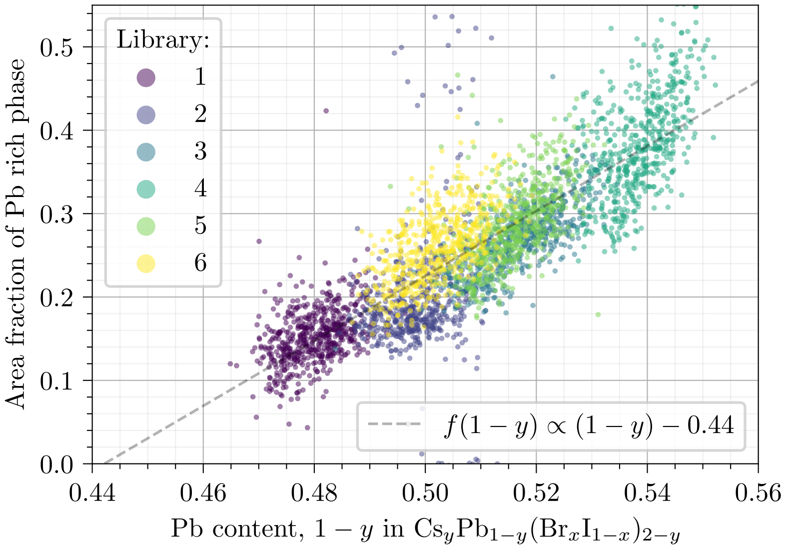

Figure 5.13: Area fraction of the 002 peak area of the Pb-rich $CsPb_2(Br_xI_{1-x})_5$ phase over the 110 peak area of the $CsPb(Br_xI_{1-x})_3$ phase for all the samples of the 6 libraries. The fitted trend line shows and the intersection with the x-axis is at $1-y = 0.44$.

As could be expected, there is a clear correlation between the amount of the Pb-rich phase and the Pb content, $1-y$, seen in Figure 5.13. Although there is no physical reason to assume a linear dependence, linear regression is performed as a first approximation and can be seen as a dashed gray line in Figure 5.13 with a zero-crossing at $1-y = 0.44$. Although the absolute value might vary slightly from this, it is clear that there is a substantial amount of the Pb-rich phase present even for Pb-poor samples. The preferential formation of this phase has been shown previously for pure $CsPbBr_3$ [81] but is far less studied for pure $CsPbI_3$ or mixed halide materials.

5.2.4 UV/Vis

An essential parameter of materials for photovoltaic applications is their optical band-gap and absorption coefficient, both of which can be determined from a UV/Vis measurement. The libraries were therefore mapped using a custom setup consisting of a fiber-coupled halogen lamp, an integrating sphere, and a fiber-coupled CCD spectrometer, see section 3.2.3 for details. Using this setup the reflectance and the transmittance spectra of all samples were collected.

Reflectance and transmittance spectra

The reflectance spectrum, $R(\lambda)$, and transmittance spectrum, $T(\lambda)$, for a sample with Br content $x = 0.5$ and Cs content $y = 0.48$, at position $(r_x, r_y) = (26.5, 26.5)$ in library 3, is plotted as a function of the photon wavelength with blue and orange circles respectively in Figure 5.14. In order to prevent secondary reflections from different library areas to be detected by the integrating sphere, the opening of the

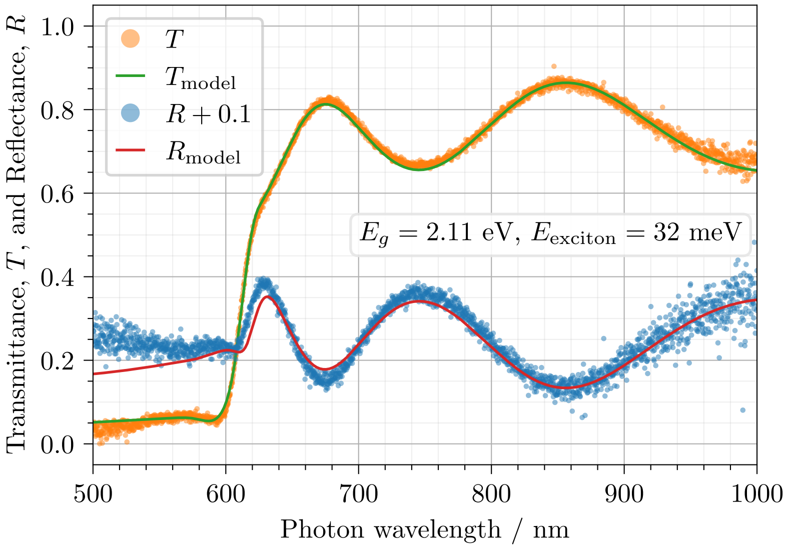

Figure 5.14: Calculated reflectance, R, and transmittance, T, from the UV/Vis measurement in orange and blue dots with the values modeled using the Elliot-Tanguy formula and TMM in green and red lines for a sample with Br content $x = 0.5$ and Cs content $y = 0.48$. The measured reflectance was too low due to a calibration offset and the values are shifted under the assumption that there is no absorption for photon wavelengths of 850 nm.

sphere was reduced with an aperture and, together with the distance between the sample and the sphere needed to map the library, this makes the setup sensitive to changes in roughness between the sample and the references. This caused a consistent offset in the measured reflectance and the values presented are therefore shifted so that the absorptance $(1 - R - T)$ at 850 nm is zero.

From both the sharp decrease in transmittance and the change in reflectance at around 600 nm in Figure 5.14 it is clear that there is a strong absorbing feature, which agrees with the expected position of the optical band-gap. There is a local minimum in the transmittance for wavelengths just below this value indicating the presence of a non-negligible excitonic contribution to the absorption in the film. For longer wavelengths, there is little to no absorption occurring and instead, the interference fringes of the thin film are observed.

As explained in subsection 2.1.1, the reflectance and transmittance of the thin film on top of the quartz glass substrate can be modeled using TMM. For this model, the thickness and the complex refractive index of the thin film are taken as variables. However, in order to make sure that the result is consistent with the Kramers-Kronig relationship, the complex refractive index is in turn modeled by assuming any given absorption model and calculating the corresponding dispersive part. As there is a considerable excitonic contribution, the Elliott formula [13] is used for modeling the attenuation coefficient. However, instead of performing the numerically heavy convolution required for calculating the dispersive part, the analytical solution for the complex permeability derived by Tanguy was used [14].

Please see subsection 2.1.1 for details on TMM, the Elliot formula and the Tanguy solution.

For this analysis, the TMM model was solved analytically for the case of a thick non-absorbing incoherent substrate, with a thin absorber on top, all surrounded by air. A numerical model for this analytical solution was implemented in Python and is detailed in section C.1. Through the simulation, it became apparent that the measured interference fringes, for photon energies below the band-gap, had a smaller amplitude than theoretically expected. In order to account for this, the transmittance was simulated for a range of thicknesses around the mean value. The mean transmittance was calculated weighted by a normal distribution centered at the mean thickness and with a standard deviation, σ. Using published values for the coefficients of the dispersion function for fused silica [136] and the thickness determined from XRF, the measured transmittance in Figure 5.14 was fitted by a global minimization of the square of the residuals using the differential evolution method of the `Python` library `Scipy` which is based on an algorithm by Storn and Price [137]. The resulting transmittance and reflectance curves are plotted in solid green and solid red, respectively, in Figure 5.14.

The modeled band-gap was found to be $E_\mathrm{g} = 2.11$ eV and the exciton binding energy was determined to be $E_\mathrm{exciton} = 32$ meV. From the amplitude of the sub-band-gap interference fringes, the film roughness was determined, through the modeled normal distribution of thicknesses, to be $\sigma = 25.2$ nm and the background dielectric permittivity as $\varepsilon = 1.47$. The model agrees well with the measured spectra below and just above the band-gap. The deviations seen for shorter wavelengths (higher energies) are most likely due to a combination of measurement noise, because of the strong absorption, and deviations from the ideal square root dependence in the contribution from the continuum states.

Determining optical band-gap

Although the most correct method for determining the optical band-gap for a semiconductor with such a strong exciton binding energy is through a model like the one described above, this method is once again very resource and time-consuming. The modeling approach is especially time-consuming due to a large number of variables and local minima meaning that a global optimization tool needs to be applied. Together with the computationally heavy convolution needed to be performed to broaden the Tanguy function, the minimization of the error for a single spectrum can take up to an hour on current personal computer hardware. This rules out the use of this method for high-throughput analysis and instead a simplified approach is proposed.

For determining the trend in the optical band-gap throughout the libraries, the wavelength-dependent absorption coefficient was instead estimated through the use of Equation 3.8, $\alpha \approx \ln\left((1-R)/T\right)/d$, using the measured reflectance, R, and trans-

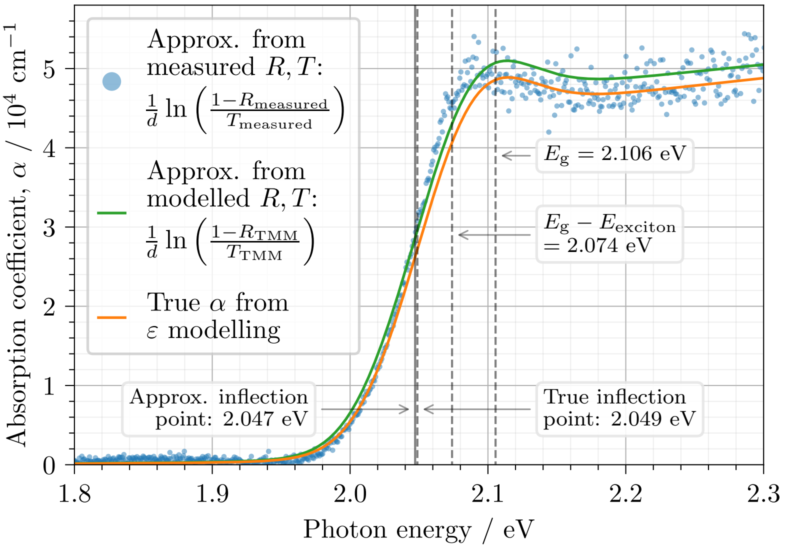

Figure 5.15: True and approximated absorption coefficient, α, as a function of the photon energy. The true α from the modeled ϵ in Figure 5.14 is plotted as an orange line and the approximated one from the calculated R and T in green. The approximated α from the measured values of R and T are plotted in blue circles. The band-gap (E_g), exciton binding energy (E_{exciton}), and the inflection point of the true model are plotted in dashed gray lines. The inflection point for the approximated α from the measured R and T is plotted in a solid gray line.

mittance, T, spectra as well as the XRF determined thickness, d. It is important to note that this is only an approximation of the absorption coefficient and the validity of this assumption is discussed in section C.2. As an example, the true absorption coefficient calculated from the modeled dielectric constant, ϵ, in Figure 5.14 is plotted as a function of photon energy in Figure 5.15. In addition, the approximated absorption coefficient from both the modeled R and T as well as the measured ones are plotted.

In Figure 5.15, the approximated absorption coefficient is slightly higher and marginally shifted towards lower energy than the true value. Additionally, the absorption onset is well below both the band-gap and the position of exciton ground-state transition ($E_g - E_{\text{exciton}}$). What is of interest later in this chapter when modeling the absorption in a PV device is the actual onset of absorption and not necessarily the true band-gap. Therefore, the inflection point of the absorption coefficient spectrum is instead studied as the metric of interest. The inflection point for both the true absorption coefficient as well as the approximated one is plotted as a dashed and solid vertical line, respectively, in Figure 5.15. These two values only differ by 2 meV and this approximation is therefore considered sufficiently accurate for the screening performed here.

The 1D absorption coefficient spectrum is then reduced to a 0D measure of the onset of absorption by extracting the inflection points in all samples. This can efficiently be performed by finding the zero-crossing of the second derivative and

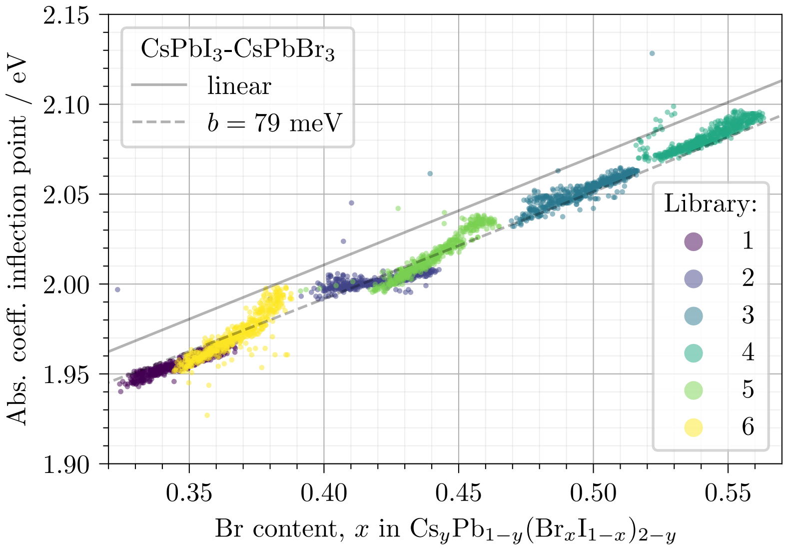

Figure 5.16: Scatter plot of the absorption coefficient inflection point versus Br content, x in $Cs_yPb_{1-y}(Br_xI_{1-x})_{2-y}$, for the 24×24 samples in each of the 6 evaporated libraries, color-coded in order of evaporation. The solid gray line shows the linear combination of the inflection points for pure $CsPbI_3$ at $x = 0$ and for pure $CsPbBr_3$ at $x = 1$. The dashed line shows the same linear combination, corrected by a quadratic term, $x(1-x)$, with coefficient b according to Equation 5.2.

the `Python` implementation used for this is shown in section C.1. The absorption coefficient inflection point in photon energy, $E_{\alpha,\text{infl}}$, is plotted as a function of the Br content, x, for all samples of all libraries in Figure 5.16.

From the data in Figure 5.16 the shift in optical band-gap with Br content is clear. This is in agreement with the results from the inkjet-printed films in the previous chapter but is here shown for thousands of samples. The inflection point of the absorption coefficient point was also determined, using the exact same numerical method, for the reference libraries of $CsPbI_3$ and $CsPbBr_3$ to be 1.77 eV and 2.37 eV respectively. If a linear combination of the two endpoints is assumed the resulting inflection point as a function of Br content would be the solid gray line in Figure 5.16. As was the case for the GIWAXS determined lattice spacing, there is a deviation of the measured points from the linear approximation. If a quadratic term with the bowing parameter, b, is introduced the following equation is obtained [135]:

$$E^{\text{theo}}_{\alpha,\text{infl}}(x) = xE^{\text{CsPbBr}_3}_{\alpha,\text{infl}} + (1-x)E^{\text{CsPbI}_3}_{\alpha,\text{infl}} - bx(1-x). \tag{5.2}$$

By fitting Equation 5.2 to the measured inflection points, the bowing parameter $b = 79$ meV is obtained and the result is plotted with a dashed gray line in Figure 5.16. The fitted curve goes through the measured points but there is a small symmetric deviation from low x values to high. This could either be explained by Equation 5.2 not being a good approximation or by a non-linear change in the exciton binding energy which would shift the inflection point.

At first glance, this shift in band-gap, and even the bowing of this shift, seems reasonable considering the same shift in lattice spacing observed in Figure 5.12a. However, upon closer inspection, it is clear that the bowing of the lattice spacing and the bowing of the absorption coefficient inflection point are in opposite directions. For the lattice spacing, the measured values are shifted to the *left* of the linear combination and for the absorption coefficient inflection point the values are shifted to the *right*. This underscores the fact, discussed in subsection 2.3.4, that the band-gap of MHPs is primarily affected by the electronegativity of the halide and only slightly (in the opposite direction) by the lattice spacing. The decoupled effect of the lattice spacing on the band-gap will be further studied using temperature-dependent measurements in section 5.3.

Absorption coefficient

In addition to the inflection point in the absorption coefficient spectrum, the magnitude of the absorption coefficient is also of great interest for PV applications. The higher the absorption coefficient is above the band-gap, the thinner the absorber layer can be made without a loss in absorbed photons, or equivalently the number of separated charge carriers. Making the absorber thinner not only helps with material consumption but more crucially means that the separated charge carriers have to diffuse a shorter distance and, therefore, are less likely to recombine before they can be extracted as current.

Therefore, the calculated approximation of the absorption coefficient from above was averaged in the range of photon energies from 100 meV to 200 meV above the inflection point. The resulting absorption coefficients are plotted as a function of Br content, x, in Figure 5.17a and as a function of Cs content, y, in Figure 5.17b.

From Figure 5.17 a high absorption coefficient of around $4.5{\cdot}10^4$ cm^{-1} is observed for all samples which is similar to other values reported for direct band-gap metal-halide perovskites [89]. This means that the absorber layer only needs to be around 511 nm thick to absorb 99 % of the photons in two passes through the absorber. For Si with an indirect band-gap, the corresponding value is 450 times larger at over 230 µm, assuming an absorption coefficient of around 10^2 cm^{-1}, 150 meV above the band-gap.

There is a small variation in the absorption coefficient throughout the samples which seems to be to an extent correlated with the Cs content, as is visible in Figure 5.17b. One possible reason for this perceived lowering of absorption coefficient with lower Cs content, and higher Pb content, is the change in the fraction of the Pb-rich phase. As shown in Figure 5.13, the fraction of the tetragonal Pb-rich phase increases with the Pb content. The band-gap of this mixed halide Pb-rich phase, $CsPb_2(Br_xI_{1-x})_5$, is not yet studied but for the pure Br case, $CsPb_2Br_5$, it is reported to be both higher than the perovskite phase, 3.0 vs 2.3 eV, as well as indirect [138]. Assuming that this holds for the mixed halide phase as well, the absorption of this

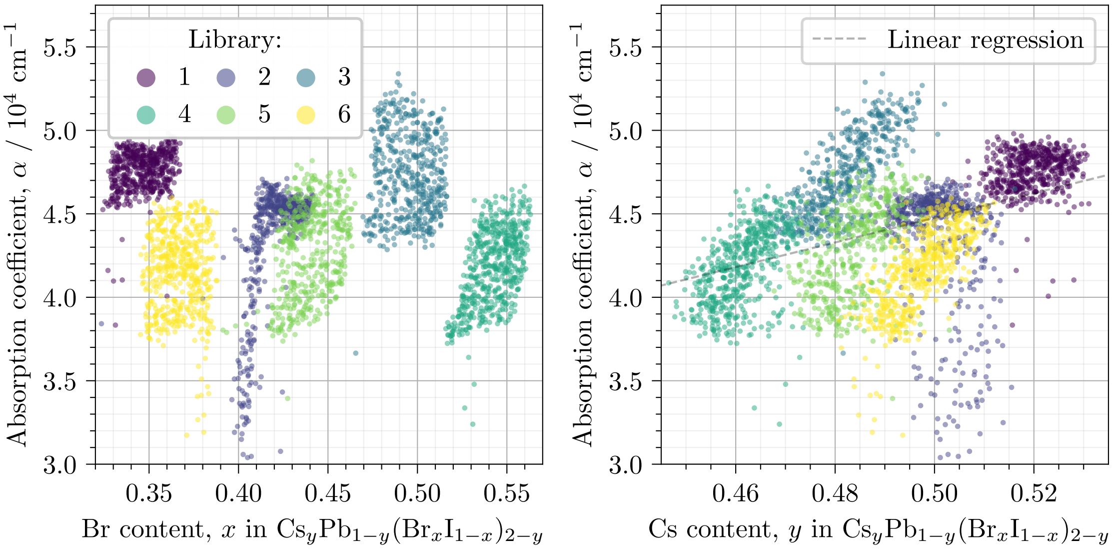

(a) α versus Br content x

(b) α versus Cs content y

Figure 5.17: The average absorption coefficient in a 100 meV wide range, 150 meV above the inflection point of its spectrum, as a function of Br content, x, and Cs content, y, in $Cs_yPb_{1-y}(Br_xI_{1-x})_{2-y}$. In (b), the linear regression is shown as a dashed grey line.

phase 150 meV above the band-gap of the perovskite phase will be negligible. This means that the fraction of material that is in this phase will not contribute to the overall absorption coefficient and an increase of this fraction can be observed as a decrease in the effective absorber thickness, explaining the apparent decrease of absorption coefficient with Cs content in Figure 5.17b.

5.2.5 TRPL

The second method applied for assessing the suitability of a given sample for use in optoelectronics is TRPL. This method allows the measurement of the dynamics of the separated charge carriers through the measurement of their radiative recombination over time. This allows for the estimation of the charge carrier lifetime which is a key parameter in photovoltaics as it gives an indication of how many carriers will be lost through recombination before they can be separated at the contacts.

The libraries 1-6 were mapped in a custom-built TRPL setup, the details of which are explained in subsection 3.2.5. Assuming that all the incident photons, with a wavelength of 500 nm, were absorbed, the injection level was approximately $2 \cdot 10^{15}$ cm^{-3}. The repetition rate of the laser was set to 1.2 MHz and the counts in each of the delay bins counted for 60 s per sample. The libraries were transferred from the N_2 glovebox as well as measured in a sealed box with a 3 kPa over-pressure through a constant flow of N_2 gas and a fused silica window.

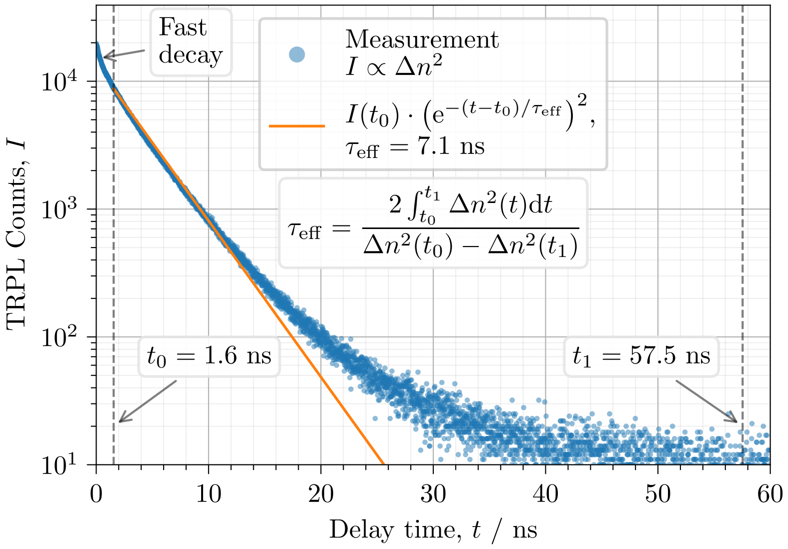

Figure 5.18: The TRPL decay for a sample with Br content $x = 0.36$ and Cs content $y = 0.50$. The corresponding mono-exponential decay for the calculated effective charge carrier lifetime, τ_{eff}, is plotted as an orange line. The effective lifetime is calculated by integrating the measured data from $t_0 = 1.6$ ns to $t_1 = 57.5$ ns according to the equation in the figure (Equation 2.13).

Carrier decay

The direct counts, minus the dark background, in each of the time bins are plotted in Figure 5.18 for a sample with Br content $x = 0.36$ and Cs content $y = 0.50$, at position $(r_x, r_y) = (26.5, 26.5)$ in library 6.

As expected, there is an exponential decay of charge carriers observed in Figure 5.18. There is a fast component during the first nanosecond followed by a close to mono-exponential decay of the carriers for the next 20 ns. At longer times the decay levels out before being masked by the noise floor.

The most elaborate approach would be to model the decay using the rate equation (Equation 2.9) and diffusion but this is a time-consuming process. Instead, the effective lifetime, τ_{eff}, is calculated by integrating the decay from 1.6 ns until the noise floor, according to Equation 2.13. This integral approach has the advantage that it is less sensitive to noise than a differential approach and that no iterative fitting algorithm needs to be deployed making it uniquely suited for a fast analysis of high-throughput data. The result of such an integration is plotted as an orange line in Figure 5.18 and yields a value of $\tau_{\mathrm{eff}} = 7.1$ ns, assuming high injection. High injection is here referred to as a doping concentration well below the injection level and the counts are therefore proportional to the square of the excess charge carrier concentration.

The mono-exponential decay of the integral approach shown in Figure 5.18 follows the measured decay for the majority of the carriers. This approach will not fit the data exactly, like a fit of a stretched multi-exponential function, but it has the advantage that it yields a single effective lifetime for the carriers, which can be used to compare different samples in one or multiple combinatorial libraries. The initial faster decay observed here has been shown to not relate to carrier recombination in comparison studies with Time-Resolved Microwave Conductivity (TRMC) [139]. Instead, it is likely due to the initial diffusion of the carriers from the surface causing a change in the carrier concentration, without recombination, which is observed as a faster decay due to the square dependence of the PL intensity on carrier concentration for high injection levels.

The slower decay just before the background level is reached could be due to different reasons. One possible reason is a distribution of lifetimes throughout the film, with the few domains having the longest lifetime being observed after the majority of the carriers in the other domains have already recombined. This would then be seen as an increase in the instantaneous lifetime over time. Another possible explanation is trapping of charge carriers, either at defects or through charge separation due to band bending at the surfaces. As these charges are de-trapped over time they would recombine and show a decay with a different time constant. However, these effects do not influence the decay of the vast majority of the carriers and, for screening purposes, it is therefore decided to study a single effective lifetime.

Carrier lifetimes

Using the previously mentioned integral approach under the assumption of high injection, the effective lifetime is calculated for all samples of all libraries and the results are plotted as a function of Br content, x, in Figure 5.19a and as a function of Cs content, y, in Figure 5.19b.

From Figure 5.19 it can be seen that the effective lifetimes of all samples are relatively low compared to state-of-the-art lead-halide perovskites at only 4 to 10 ns. There is also a weak trend visible as a function of the Cs content where any deviation from the stoichiometric case, $y = 0.5$, results in a decrease in the lifetime. For the samples with the highest Cs content there are a few data points which exhibit a longer effective lifetime but due to the large spread and limited number of measurement points the spread in values is also increased substantially. This compositional area should, therefore, be studied further in future work.

5.2.6 Absolute PL

Another method for determining the suitability of a material for use in optoelectronics is measuring the absolute PL and calculating the Photoluminescence Quantum Yield (PLQY). The PLQY is simply the fraction of absorbed photons that get re-emitted through radiative recombination. The ideal optoelectronic material, be it for PV or in LEDs, has a PLQY of 1, meaning that all recombination is radiative and no carriers are lost through non-radiative recombination.

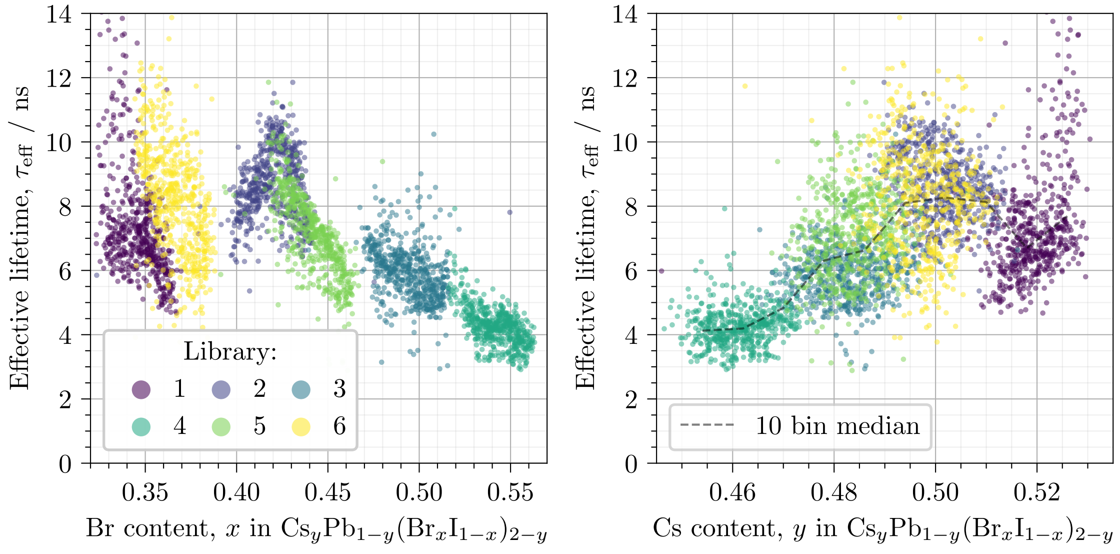

(a) τ_{eff} versus Br content x

(b) τ_{eff} versus Cs content y

Figure 5.19: Effective carrier lifetimes, τ_{eff}, as a function of Br content, x, and Cs content, y, in $Cs_yPb_{1-y}(Br_xI_{1-x})_{2-y}$. In (b), the 10 bin median is plotted in a dashed grey line.

A custom PL imaging setup was used to measure the absolute PL of all the libraries. The details of the calibrated setup are explained in section 3.2.4. Using the band-gap values of 1.74 and 2.40 eV for $CsPbI_3$ and $CsPbBr_3$ respectively, the average band-gap of each library was estimated from the linear combination of the endpoints and the intended Br content, x. The photon flux of the collimated LED excitation source, with a peak wavelength of 445 nm, was adjusted to correspond to the injection of carriers by 1 sun (AM1.5G) for each of the estimated band-gaps of the libraries. This was done by integrating the AM1.5G spectrum in photons/eV multiplied with a step function at the band-gap, assuming full absorption above the band-gap and none below, to get the total number of carriers generated per unit area and then matching the flux of the LED to this value.

The limited field of view for the imaging setup meant that the libraries had to be measured in 9 hyperspectral images starting in the upper left corner and then going row by row from left to right in a 3 × 3 grid. The hyperspectral stack was collected starting with the variable detection filter set to 500 nm and scanned with a 2 nm step size up to 730 nm with an acquisition time of 1 s per image. Between each of the 9 spots, the light was turned off and the sample was left in dark for 200 s. Once again, the libraries were transferred from the N_2 glovebox as well as measured in a sealed box with a 3 kPa over-pressure through a constant flow of N_2 gas and a fused silica window.

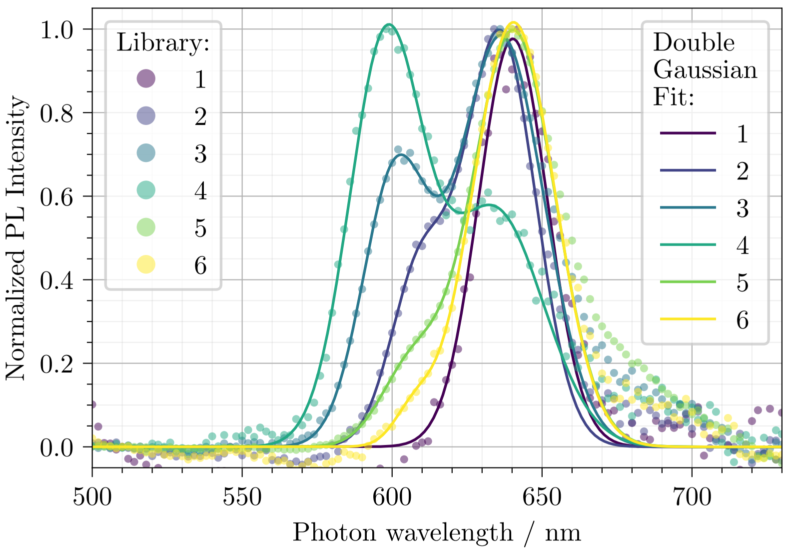

Figure 5.20: Normalized averaged PL spectra in the first measured spot of each library in circles and a double gaussian fit for each of the spectra in lines. The Br content of the libraries are increasing in the order 1, 6, 2, 5, 3, 4 and the dependence is further clarified in Figure 5.21 below.

PL spectra

Measuring the PL of mixed halide perovskites with Br content above 1/3 is not straightforward due to the light-induced phase segregation, which is sometimes referred to as the Hoke-effect [89]. As this phase segregation is dependent on illumination time [86], the 9 different spots imaged per library might show different degrees of segregation due to the difference in illumination time. Therefore, the normalized averaged spectra of only the first image, corresponding to the upper left corner, of each library is plotted first in Figure 5.20.

The previously mentioned phase segregation is clearly visible in Figure 5.20 where most libraries display a double peak corresponding to the initially mixed phase and the segregated state. The spectra were, therefore, fitted with a double Gaussian function and the result is plotted as solid lines together with the measurement in Figure 5.20. In general, there is a good agreement between measured values and the fitted curves with the exception of the broadening for wavelengths above 650 nm. This broadening is likely due to increased segregation during the measurement. Since the detection is scanned from low to high wavelength any increase in the intensity of the peak at 640 nm during the measurement will cause an asymmetric broadening for longer wavelengths. The peak positions of the two Gaussian functions are plotted for each library as a function of the Br content, x, in Figure 5.21. The peak is omitted if the fitted area is less than 10 % of that of the other peak. The fitted curve for the absorption coefficient inflection point from Figure 5.16 is plotted in a gray dashed line with the peak positions for reference.

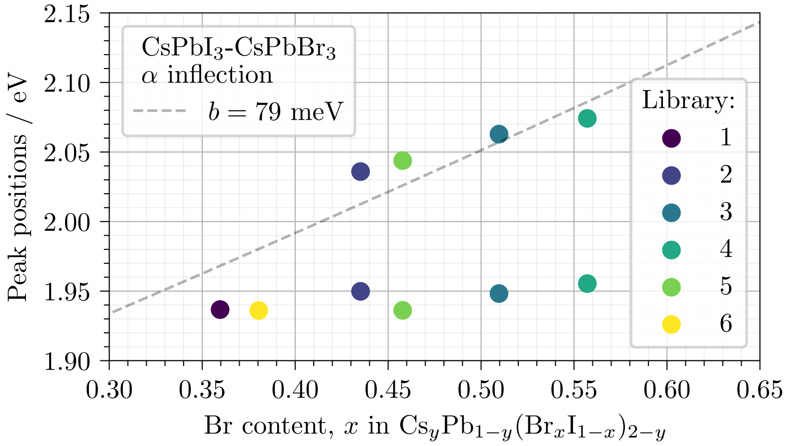

Figure 5.21: The peak position of the the two Gaussians fitted to each PL curve in Figure 5.20 as a function of the average Br content, x, in the upper left corner of each library. The absorption coefficient inflection point model from the UV/Vis measurement is plotted in a gray dashed line for reference.

From the fitted peak positions in Figure 5.21 the phase segregation is even clearer. Here the segregated peak is at energy of around 1.95 eV, which approximately corresponds to the absorption coefficient inflection point for a Br content of $x = 1/3$. The mixed phase peak has some uncertainty in its position for lower Br contents due to the difficulty in uniquely fitting the shoulder of a peak but, in general, the position can be seen to increase with Br content and roughly follows the optical band-gap of the mixed phase.

This phase segregation presents one of the main challenges for mixed Br-I lead halide perovskites and effectively limits the range within which they can be used. The original goal with the series of libraries was to closely investigate the area between $x = 0.3$ and $x = 0.4$ to determine how far the Br content could be integrated stably. Unfortunately, the unintended composition shift during deposition meant that the lowest Br content achieved was $x = 0.36$. However, the unintended shift did present an opportunity for studying the effect of larger-scale variation in Cs content which will be investigated next for the PLQY.

PLQY

The pixels of the PL images were binned together into samples on the same 24×24 grid as for the rest of the characterizations to facilitate a quick correlation analysis. The spectrum for each sample was integrated and divided by the incoming flux to determine the PLQY. The PLQY is plotted as a function of the Br content, x, in Figure 5.22a and as a function of the Cs content, y, in Figure 5.22b.

In general, the observed PLQY is below $5 \cdot 10^{-6}$ meaning that less than 0.0005 % of the separated carriers recombine radiatively. This is a low value but does agree with the observed carrier lifetimes of less than 10 ns. This will severely limit the

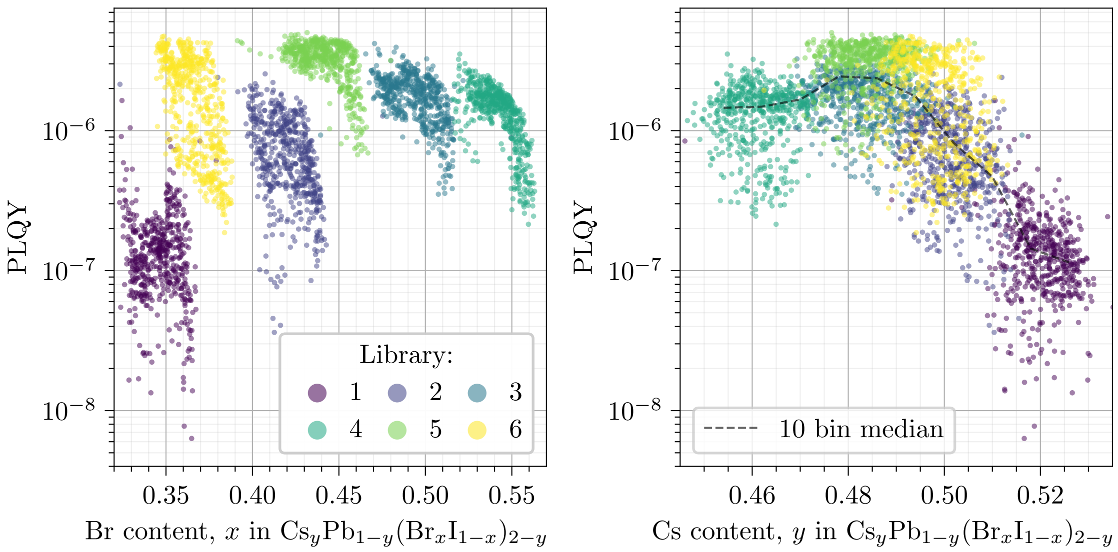

(a) PLQY versus Br content x

(b) PLQY versus Cs content y

Figure 5.22: PLQY as a function of Br content, x, and Cs content, y, in $Cs_yPb_{1-y}(Br_xI_{1-x})_{2-y}$. In (b), the 10 bin median is plotted in a dashed grey line.

V_{OC} of a PV device even if there would not be any phase segregation and any LEDs would obviously be very inefficient.

From Figure 5.22 it can be seen that the PLQY correlates with the Cs content, similarly to the previous TRPL results in Figure 5.19b. There is a clear decrease in the PLQY for Cs-rich compositions with a less clear trend for Cs-poor ones. This agrees with the result of the TRPL where a decrease in the effective carrier lifetime was observed for off-stoichiometric compositions. These two separate results strongly indicate that there is an increase in non-radiative recombination for samples with excess Cs or Pb.

5.2.7 Estimated PV Parameters

In the following section the results from the UV/Vis, TRPL and PLQY high-throughput analysis will be used to estimate the performance of each sample in a potential PV device. This estimation will be the upper limit for the performance of the material as a solar cell, assuming perfect contacts and interfaces.

Diffusion length

The first step in constructing such a potential device is to decide on the thickness of the absorber layer. As previously discussed in connection with the absorption coefficient results, the absorber needs to be thick enough to absorb the incoming photons and excite charge carriers but thin enough to allow the excited carriers to travel across to their respective contacts without recombining non-radiatively.

There are two main transport methods for charge carriers, drift and diffusion. For the following estimation, it is assumed that the transport is diffusion-limited. A good measure of the distance that carriers can diffuse before recombining is the diffusion length, L_D, which is the mean length that carriers diffuse within their lifetime, τ. The diffusion length is calculated as $L_\mathrm{D} = \sqrt{\tau \mu k_\mathrm{B} T}$ where μ is the mobility of one of the carriers. The mobility is typically modelled from a measurement such as optical-pump THz-probe spectroscopy or TRMC. This has previously been done for pure $\mathrm{CsPbI_3}$ films, manufactured in the very same chamber as the libraries here, and values for sum mobility of more than 60 $\mathrm{cm^2/Vs}$ were determined using optical-pump THz-probe spectroscopy [127]. For this estimation, a conservative sum mobility of 30 $\mathrm{cm^2/Vs}$ will be assumed, which was measured for a hybrid mixed Br-I triple cation perovskite [139]. The actual mobility of the carriers will likely vary but this value should provide a relative measure of the diffusion length based on the measured lifetimes. Assuming a mobility of $\mu = 15\ \mathrm{cm^2/Vs}$ (half of the sum mobility) and a temperature of $T = 298$ K the estimated diffusion lengths of all samples were calculated from the effective lifetimes, τ_eff, shown in Figure 5.19. As μ and T were kept constant, these values follow the same trends as the effective lifetimes. The measured lifetimes between 4 and 10 ns results in diffusion lengths between 393 and 621 nm. For reference, all estimated diffusion lengths are plotted as a function of Br and Cs content in Figure D.1 of the appendix section D.1.

In state-of-the-art perovskite solar cells with lifetimes of microseconds, the diffusion length is not a limiting factor but with the lifetimes measured here of only 5-10 ns the short diffusion length could have an impact on the collection probability of carriers. Calculating the actual collection probability as a function of depth in the device is quite complicated and will depend on the electric field in the absorber, requiring a drift-diffusion simulation. For the high-throughput analysis of 3456 samples here, the absorber thickness is instead taken to be half of the diffusion length and all absorbed carriers are then considered to be extracted at short-circuit conditions.

Short-circuit current

Once the theoretical absorber thickness has been set to half the estimated diffusion length, the absorptance can be calculated using the pseudo absorption coefficients from Figure 5.17 and the Lambert-Beer law, Equation 2.1. For the calculation, it is assumed that there is a perfect mirror on the back surface yielding an effective thickness of twice that of the absorber. Furthermore, the reflections at the air/superstrate and superstrate/absorber interfaces are neglected.

Since all generated carriers are assumed to be extracted at short-circuit conditions, the calculated absorptance is then used as the *EQE* when calculating the short-circuit current density, J_SC. The expected short-circuit current density was calculated as $J_\mathrm{SC} = q\int_0^\infty EQE(E)\Phi_\mathrm{sun}(E)\mathrm{d}E$ (Equation 2.17), where the AM1.5G spectrum was used as $\Phi_\mathrm{sun}(E)$. The resulting values are plotted in Figure 5.23a as a

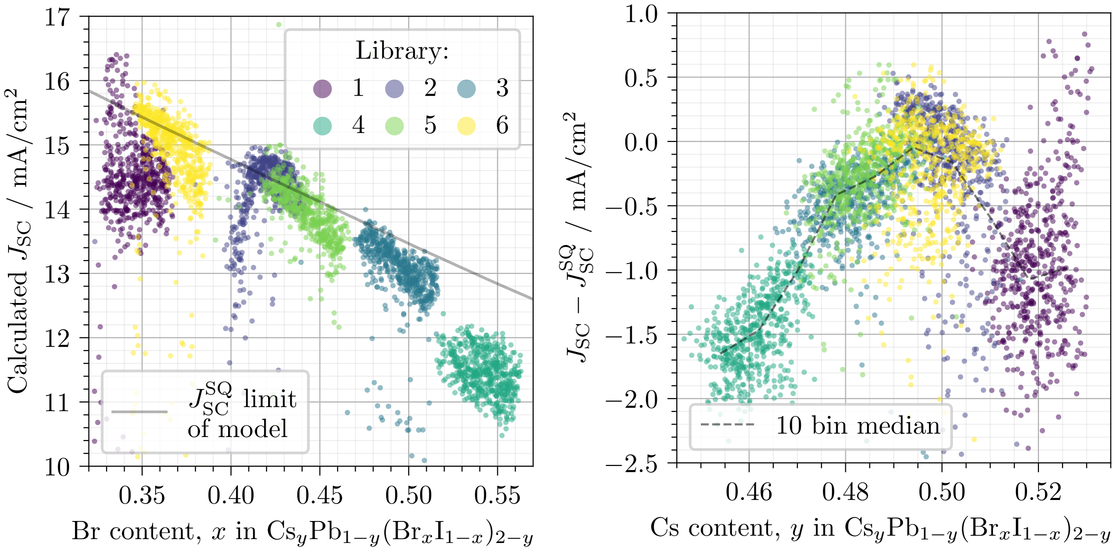

(a) Calculated J_{SC} versus Br content x

(b) $J_{SC} - J_{SC}^{SQ}$ versus Cs content y

Figure 5.23: Calculated J_{SC} as a function of Br content, x, and Cs content, y, in $Cs_yPb_{1-y}(Br_xI_{1-x})_{2-y}$. The color of each sample indicates which library it belongs to. The gray line in (a) shows the J_{SC} for step-like absorptance at band-gap, which is taken as a function of Br content from the bowing model in Figure 5.16. The values in (b) are plotted relative to this model J_{SC}. In (b), the 10 bin median is plotted in a dashed grey line.

function of the XRF determined Br content, x. In addition, the short-circuit current density in the limit of step-like absorptance (i.e. 0 below band-gap and 1 above), J_{SC}^{SQ}, is plotted with the band-gap taken to be the absorption coefficient inflection point as a function of Br content from the bowing model in Figure 5.17a.

In order to also investigate the dependence on the Cs content, y, the band-gap dependence is decoupled through subtraction of the step-like limit, J_{SC}^{SQ}. The resulting values are plotted as a function of the Cs content, y, in Figure 5.23b.

From Figure 5.23a the dependence of the short-circuit current density on the band-gap, and in turn the Br content, is clear. Most values fall along or below the limit for step-like absorptance and the few values above are due to deviations from the band-gap predicted by the bowing model. In addition to the dependence on Br content, there is a clear decrease in the current density observed for libraries 1 and 4. This decrease is instead explained by the Cs content, y, as shown in Figure 5.23b. Here, the deviation from the J_{SC}^{SQ} shows a clear dependence on the Cs content with both Cs-poor ($x < 0.5$) and Cs-rich ($x > 0.5$) compositions exhibiting a decrease in the current density.

The cause of the deviations from the J_{SC}^{SQ} is two-fold. Firstly, there is a decreased absorption coefficient with decreased Cs content due to the formation of the Pb-rich $CsPb_2(Br_xI_{1-x})_3$ phase as discussed in section 5.2.4. Secondly, there is a decreased diffusion length for off-stoichiometric compositions due to the decreased lifetime observed in Figure 5.19b, which in turn reduces the maximum thickness for charge extraction and therefore the number of absorbed photons.

Open-circuit voltage

From the J_{SC}, the theoretical open-circuit voltage, V_{OC} is calculated using both the absorption coefficient inflection point and the PLQY. This is done by first calculating the saturation current density in the device as $J_0^{\mathrm{rad}} = q\int_0^\infty EQE(E)\Phi_{\mathrm{bb}}(E)\mathrm{d}E$ (Equation 2.18).

For this calculation, a step-like absorptance at the *measured* inflection point of the absorption coefficient is used rather than the spectral measurement used above for calculating J_{SC}. This has to be done since the black body radiation spectrum, $\Phi_{\mathrm{bb}}(E)$ (Equation 2.19), which is multiplied by the absorptance, decreases drastically with wavelength. Because of this drastic decrease, any noise in the absorptance below the band-gap will have a dramatic influence on J_0.

Once the saturation current density is calculated for each sample, the result can be combined with the previously calculated J_{SC} to calculate the radiative limit for the open-circuit voltage as $V_{\mathrm{OC}}^{\mathrm{rad}} = \frac{k_{\mathrm{B}}T}{q}\ln\left(\frac{J_{\mathrm{SC}}}{J_0^{\mathrm{rad}}}+1\right)$ (Equation 2.20). Finally, the implied open-circuit voltage, V_{OC}, is calculated by subtracting the non-radiative losses, calculated from the PLQY, from the radiative limit as $V_{\mathrm{OC}} = V_{\mathrm{OC}}^{\mathrm{rad}} - \frac{k_{\mathrm{B}}T}{q}\ln\left(\frac{1}{PLQY}\right)$ (Equation 2.21). The result is plotted as a function of the Br content in Figure 5.24a.

The same modeled dependence of band-gap on Br content as used above for the $J_{\mathrm{SC}}^{\mathrm{SQ}}$, is used to calculate the radiative limit of the open-circuit voltage, $V_{\mathrm{OC}}^{\mathrm{SQ}}$, as a function of Br content, assuming a step-like absorptance for both $J_{\mathrm{SC}}^{\mathrm{SQ}}$ and J_0^{rad}. The result is plotted in Figure 5.24a. Once again the band-gap dependence of the V_{OC} is decoupled by subtracting this radiative limit, $V_{\mathrm{OC}}^{\mathrm{SQ}}$, and the result is plotted as a function of the Cs content in Figure 5.24b.

From Figure 5.24a the increase of the calculated V_{OC} with Br content, due to the increase in band-gap, can be seen. However, the absolute values are far below the radiative limit due to the non-radiative losses seen as the low PLQY in Figure 5.22 and the short lifetimes in Figure 5.19. Similarly to the J_{SC}, there is a deviation from the trend which is explained by the Cs content in Figure 5.24b. Here the deviation from the radiative limit drops by an additional 80 mV when going from the stoichiometric, $x = 0.5$, to the most Cs-rich composition, $x = 0.52$. In contrast to the J_{SC}, there is a less dramatic decrease in voltage for the Cs-poor compositions.

Power conversion efficiency

The last step before calculating the expected PCE, η, using Equation 2.15, is to estimate the fill factor, FF. This is simply done here by using the analytical approximation for an ideal diode curve, $FF \approx \left(\frac{qV_{\mathrm{OC}}}{k_{\mathrm{B}}T} - \ln\left(\frac{qV_{\mathrm{OC}}}{k_{\mathrm{B}}T}+0.72\right)\right) / \left(\frac{qV_{\mathrm{OC}}}{k_{\mathrm{B}}T}+1\right)$ (Equation 2.16), using the V_{OC} calculated above (Figure 5.24). For the radiative

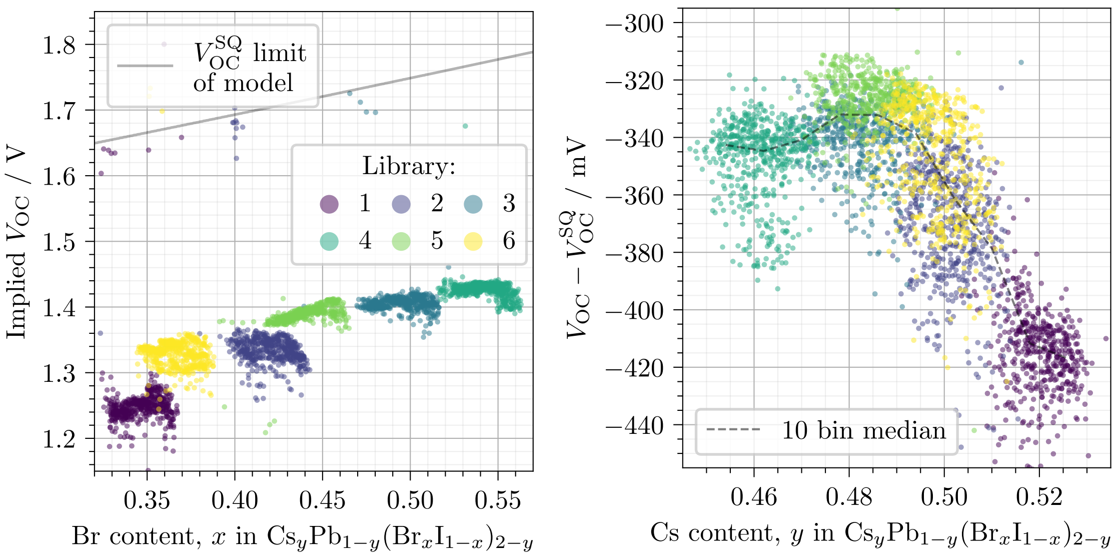

(a) Implied V_{OC} versus Br content x

(b) $V_{\mathrm{OC}} - V_{\mathrm{OC}}^{\mathrm{SQ}}$ versus Cs content y

Figure 5.24: Implied V_{OC} as a function of Br content, x, and Cs content, y, in $\mathrm{Cs}_y\mathrm{Pb}_{1-y}(\mathrm{Br}_x\mathrm{I}_{1-x})_{2-y}$. The color of each sample indicates which library it belongs to. The gray line in (a) shows the radiative limit of the V_{OC} assuming step-like absorptance at the band-gap from the bowing model in Figure 5.16. The values in (b) are plotted relative to this radiative limit. In (b), the 10 bin median is plotted in a dashed grey line.

limit, the $FF^{\mathrm{SQ}}(x)$ is calculated using the $V_{\mathrm{OC}}^{\mathrm{SQ}}(x)$ curve in Figure 5.24a. As the FF approximation only depends on the V_{OC}, the dependence on Br and Cs will be largely the same. The calculated FF values are plotted as a function of the Br and Cs content in Figure D.2 in the appendix section D.1 and are between 0.9 and 0.91.

Once the J_{SC}, V_{OC} and FF have been calculated, the results can be combined to calculate the expected PCE in the limit of perfect contacts. The PCE is given by $\eta = FF \cdot I_{\mathrm{SC}} V_{\mathrm{OC}} / P_{\mathrm{in}}$ (Equation 2.15) and the resulting PCE is plotted as a function of the Br content, x, in Figure 5.25a. In addition, the short-circuit current density, $J_{\mathrm{SC}}^{\mathrm{SQ}}(x)$, the radiative limit for the open-circuit voltage, $V_{\mathrm{OC}}^{\mathrm{SQ}}(x)$, and the ideal fill factor, $FF^{\mathrm{SQ}}(x)$, for step-like absorptance at the inflection point of the absorption coefficient, are combined into the PCE limit, $\eta^{\mathrm{SQ}}(x)$. The resulting curve is plotted in Figure 5.25a.

Finally, the calculated efficiency is decoupled from the band-gap variation by subtracting the radiative limit, $\eta^{\mathrm{SQ}}(x)$, and the results plotted as a function of the Cs content, y, in Figure 5.25b.

As expected, there is a decrease in the PCE with increasing Br content due to an increasing band-gap, which causes larger losses in current than the gain in voltage. In addition, the estimated efficiencies are lowered by about 6 absolute % units with respect to the SQ limit, due to the non-radiative losses in V_{OC}. In the plot of the deviation from η^{SQ} over Cs content in Figure 5.25b, there is a larger loss observed

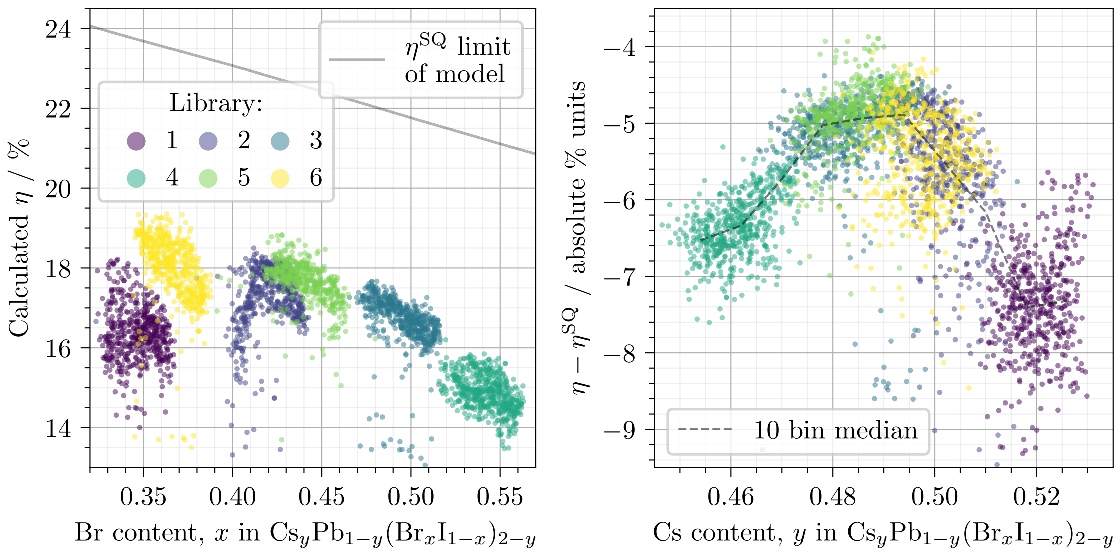

(a) Calculated PCE versus Br content x

(b) $\eta - \eta^{SQ}$ versus Cs content y

Figure 5.25: Calculated PCE as a function of Br content, x, and Cs content, y, in $Cs_yPb_{1-y}(Br_xI_{1-x})_{2-y}$ for all libraries using the J_{SC} values from Figure 5.23 and the V_{OC} values from Figure 5.24 while assuming an ideal diode behavior. The color of each sample indicates which library it belongs to. The gray line in (a) shows the efficiency limit for the radiative V_{OC} and step-like absoptance according to the band-gap model as a function of Br content. The values in (b) are subtracted by this limit to decouple the band-gap dependence. In (b), the 10 bin median is plotted in a dashed grey line.

for off-stoichiometric compositions with a minimum loss close to the stoichiometric point. This is a combined effect of the losses of J_{SC}, seen in Figure 5.23b, and V_{OC}, seen in Figure 5.24b.

In general, the trend in both J_{SC} and V_{OC}, as a function of Br content, follows the Shockley-Queisser limit for the expected band-gap values. More interestingly, the combined results, taking into consideration the measured UV/Vis, TRPL and PLQY, show that the maximum efficiency can be reached for stoichiometric films and that any excess Pb or Cs is detrimental for the PCE due to increased non-radiative losses. This agrees with earlier studies on individual Br to I ratios, which show reduced efficiencies for large Cs or Pb excess [61].

The method above shows how, through contactless optical measurements, the potential of a material library for use in PV devices can be screened in a high-throughput capacity. Specifically, these results provide information on a large compositional range of $CsPb(Br_xI_{1-x})_3$ between $x = 1/3$ and $x = 2/3$ where only 7 individual devices are reported in the perovskite database as of this moment [40]. Furthermore, the whole methodology, from characterization to analysis, is automized and can be applied to any new combinatorial libraries that are manufactured in a high-throughput screening workflow.

5.3 Correlation of Lattice Parameters & Band-Gap for $CsPbBr_{0.9}I_{2.1}$

Following the wide-range structural analysis of the full solid solution of $CsPb(Br_xI_{1-x})_3$ as well as the detailed optical investigation of a portion of the $Cs_yPb_{1-y}(Br_xI_{1-x})_{2-y}$ compositional space, a single sample of $CsPbBr_{0.9}I_{2.1}$ is here investigated in detail. Specifically, the correlation between the structural parameters as a function of sample temperature discussed in section 5.1 and the optical band-gap discussed in section 5.2 is here studied. The chosen composition contains an amount of Br which is below the limit for the phase segregation shown in section 5.2 whilst still being more stable in the perovskite phase than more I-rich compositions as shown in section 5.1.

5.3.1 Sample Preparation

The sample was prepared by combinatorial evaporation of a $Cs_yPb_{1-y}(Br_xI_{1-x})_{2-y}$ library on fused silica using the three sources: CsI, CsBr, and PbI_2. The details of the deposition method are explained in subsection 3.1.2 and section 4.2. The sample studied within the library was selected in the center of the substrate where the Cs to Pb ratio is expected to be stoichiometric and the Br content to be $x = 0.3$. The library was evaporated at 50 °C and was *not* further annealed post-deposition.

5.3.2 GIWAXS and UV/Vis Transmittance

The library was transferred in a sealed container from the N_2 glovebox to the metal-jet experimental setup detailed in section 3.2.1. Once at the setup, the sample was loaded into the sample chamber under a constant flow of N_2 gas. The library is estimated to have been outside of a pure N_2 environment for less than 5 s. Once in the chamber, the substrate was aligned to the X-ray source as explained in section 3.2.1.

In addition to the detection of the GIWAXS from the Metal-jet X-ray source, similarly to section 5.1, the small hole in the hotplate was used to simultaneously detect the direct transmittance of light in the visible range. This was done by the use of a halogen lamp reflected up from underneath the library and then collected by an optical fiber suspended above the fused silica window of the chamber, see section 3.2.3 for details on the setup. The fiber was connected to a dispersive CCD spectrometer.

The acquisition of the GIWAXS diffractogram was started and let run continuously, saving the result every 12 s. Similarly, the direct transmittance was collected continuously with an integration time of 100 ms but averaged and saved every 2 s. The hotplate was kept at 298 K (25 °C) for 3 min and then ramped down to 113 K (-160 °C) at a rate of 25 K/min using liquid N_2. The substrate was then cycled between 113 K (-160 °C) and 573 K (300 °C) twice with the same heating and cooling rate of 25 K/min before finally being returned to 298 K (25 °C). The measured temperature of the hotplate as a function of the processing time is plotted in Figure 5.26a.

The sample position relative to the detector was once again calibrated using a LaB_6 powder and the 3D GIWAXS pattern integrated azimuthally to attain the 1D diffraction patterns as a function of the scattering vector, q. The resulting patterns are plotted as a heatmap over the process time in Figure 5.26b.

The transmittance was calculated using bright and dark reference measurements. Unfortunately, there was a buildup of ice on the outside window of the chamber for low temperatures causing a considerable portion of the directly transmitted light to be scattered away. Therefore, the spectra were normalized so that they could be compared with each other. The normalized transmittance spectra are plotted as a heatmap over the process time in Figure 5.26c.

The process times in Figure 5.26 are all correlated. From Figure 5.26b it can be seen that the as-deposited sample is in the orthorhombic perovskite phase. As the sample is cooled down it remains in the perovskite phase and a change in cell parameters can be observed in the shift of the peaks. Upon heating the sample has an opposite shift of the parameters which continues up to 400 K (127 °C) where the sample undergoes a first order transition to the non-perovskite δ-phase, see section 5.1 for details. However, after further heating the sample re-crystallizes back to a perovskite phase in the form of the cubic α-phase as expected from the phase diagram determined in section 5.1. In addition to the perovskite phase, there is the formation of the Pb-rich $CsPb_2(Br_xI_{1-x})_3$ phase discussed in section 5.2. This can be seen from the appearance of the peaks at around 19.5 and 22.5 nm^{-1}, which is indicated by a * in the figure.

At first glance, comparing the peak positions before and after the re-crystallization seems to indicate a change in the lattice spacing. However, after indexing the peaks it is evident that this is merely a result of a lattice reorganization. Where before the 004 peak was oriented out-of-plane it is now the 220 peak that is oriented out-of-plane and, due to the geometry of the detection, gives a stronger contribution to the integrated pattern. In addition to the change in orientation, the peaks are considerably sharper after re-crystallization indicating either a change in grain size or a relaxation of the strain, both of which are plausible.

During the second cycle from 113 K (-160 °C) to 573 K (300 °C) there are noticeable differences from the first cycle during heating up. First and foremost, there is no degradation to the δ-phase. Instead, the sample undergoes the same changes previously observed on cool-down but in the reverse order, i.e. the sample starts in the orthorhombic γ-phase and transitions to the tetragonal β-phase followed by the cubic α-phase. Additionally, and more subtly, there is a hysteresis observed in the position of the main peak between cool-down and heat-up, mostly noticeable

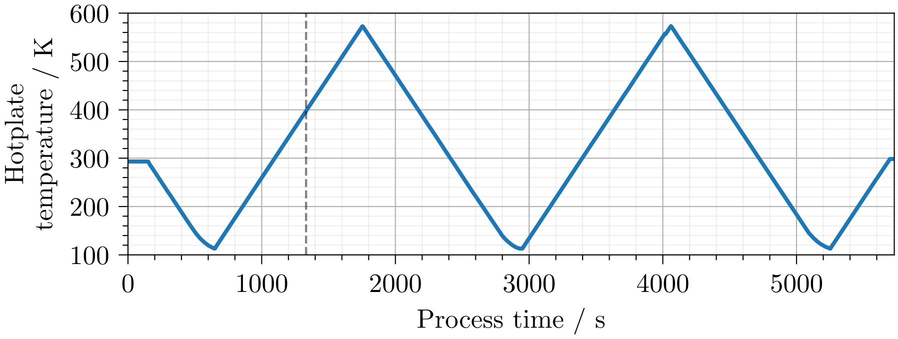

(a) Heating profile

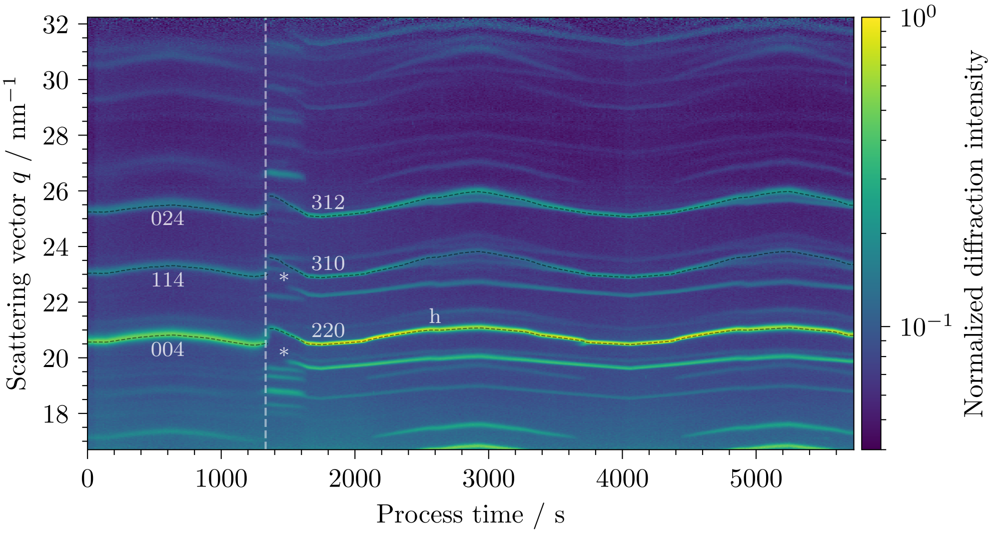

(b) Integrated GIWAXS

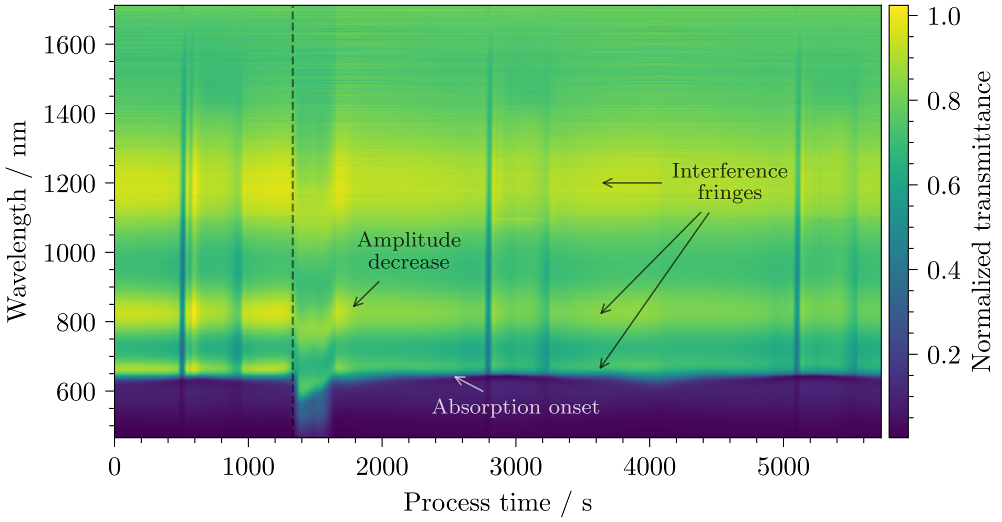

(c) UV/Vis transmittance

Figure 5.26: Correlated GIWAXS and UV/Vis transmittance measurements as a function of the hotplate temperature shown in (a). All measurements use the same process time. The azimuthally integarated GIWAXS patterns are plotted as a heatmap in (b) with a logarithmic colorscale and the indexed peaks are labeled. The * indicates the Pb-rich phase and "h" a point of hysteresis. The normalized transmittance spectra are plotted as a heatmap in (c), with dark color indicating low transmittance.

in the main peak around 21 nm^{-1} at the process time of approximately 2600 s, indicated by an ”h” in the figure.

In the transmittance spectra of Figure 5.26c, there is a clear absorption onset at around 650 nm which is attributed to the direct optical band-gap of the main perovskite phase. There are also clear thin-film interference fringes below the band-gap at 650, 810, and 1200 nm. The amplitude of the fringes decreases after the re-crystallization indicating an increase in thickness variations of the film, i.e. the roughness. This correlates with a decreased width of the GIWAXS peaks.

The transmittance spectra in Figure 5.26c also clearly show the degradation to the δ-phase shortly before the process time 1200 s. The δ-phase is there seen as a shift of the absorption onset from the 650 nm of the perovskite phase to less than 500 nm. The interference fringes of the thin film are also shifted due to coupled changes in the dispersive part of the refractive index. The vertical lines at 500, 2800, and 5100 s are artifacts of the normalization during ice formation on the chamber and will not be discussed further.

5.3.3 Lattice Parameters & Optical Band-Gap

To quantify the changes observed above and further correlate temperature, lattice parameters, and band-gap, the perovskite peaks of the GIWAXS patterns were indexed and a selection fitted with a gaussian peak shape. Before crystallization, the 004, 114, and 024 peaks were fitted and afterward the 220, 310, and 312 peaks were instead fitted, as these now show higher intensity due to the re-orientation mentioned above. From these peaks, with Miller indices hkl, the lattice parameters a, b, and c can be calculated by solving the set of equations generated by the following formula for a single peak at q_{hkl}:

$$\frac{1}{d_{hkl}^2} = \frac{q_{hkl}^2}{4\pi^2} = \frac{h^2}{a^2} + \frac{k^2}{b^2} + \frac{l^2}{c^2}. \tag{5.3}$$

The set of equations and a `Python` script for solving these are shown in section C.3.

The resulting pseudo cubic lattice parameters as well as the geometric mean, $\sqrt[3]{abc}$, are plotted as a function of the process time in the top pane of Figure 5.27. In the bottom pane of the same figure, the hotplate temperature is plotted again for ease of comparison, together with the inflection point of the measured transmittance spectra. The inflection point is used as an estimate for the optical band-gap. If the exciton binding energy remains the same as a function of temperature, the inflection point should provide an accurate relative measure for the optical band-gap.

From the lattice parameters in Figure 5.27 the three perovskite phases are visible as the cubic α-phase where all parameters overlap, the tetragonal β-phase where the a and b parameters overlap and the orthorhombic γ-phase where all three parameters are distinct. As previously shown in section 5.1, there is an anisotropic evolution of

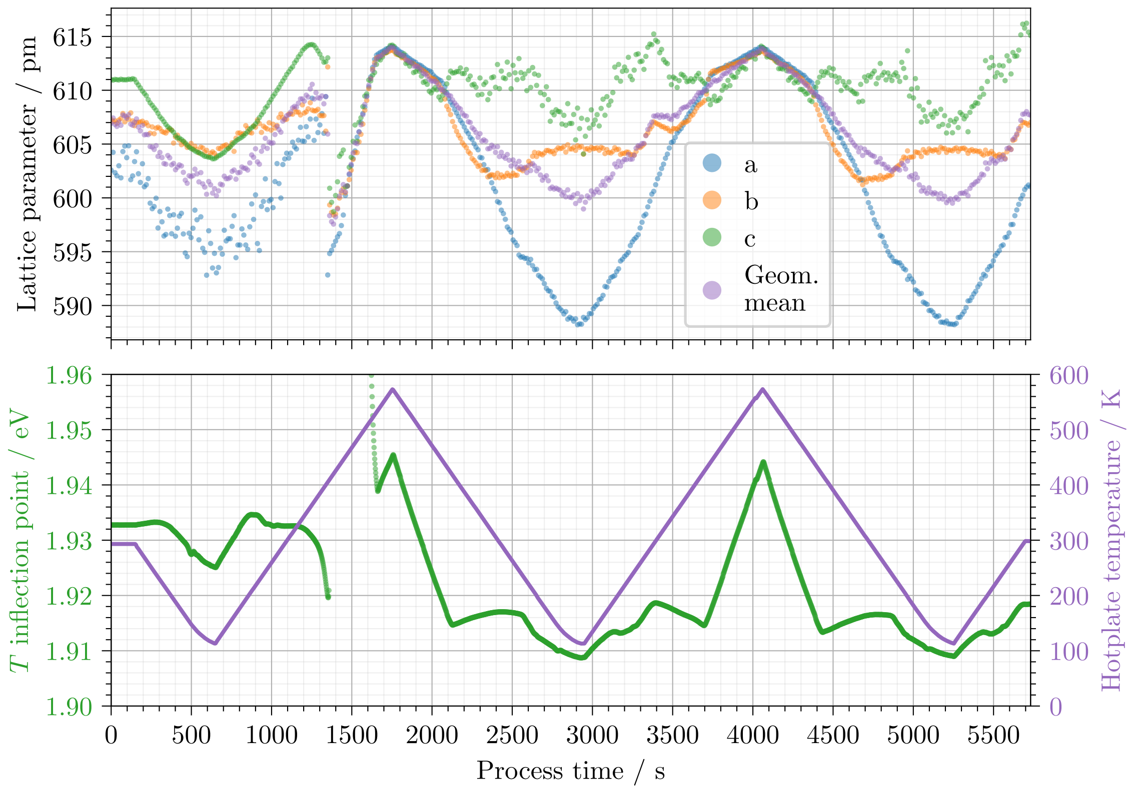

Figure 5.27: Top pane shows the calculated pseudocubic lattice parameters and their geometric mean as a function of the process time. Bottom pane shows the inflection point of the transmittance spectra on the left axis and the hotplate temperature on the right axis as a function of the same process time.

the lattice parameters in the tetragonal and orthorhombic phase whilst the geometric mean of the parameters shows a close to direct correlation with temperature.

Starting from the highest hotplate temperature at a process time of 1750 s and 4070 s, the inflection point of the transmittance shows a linear reduction with the temperature in the α-phase but shows a complete change of trend at the moment of transition to the β-phase. Upon the transition to the β-phase, the inflection point instead starts to increase in value and it is not until the c parameter starts to decrease, at process time 2600 and 4900 s, that a decrease in the transmittance inflection point is observed again. Upon heating up there is a hysteresis observed in comparison with the cooling down, as was the case for the lattice parameter. This hysteresis is most noticeable in the peak at a process time of 3400 s.

In general, the transmittance inflection point, and therefore the band-gap, seems to correlate most closely with the c parameter and not with the cell volume. The proportionality constant changes between the cubic α-phase and the tilted β and γ-phases but, with an exception of the region before the phase transition and the small dip in c parameter observed at 2300 and 4650 s, otherwise follows the parameter closely.

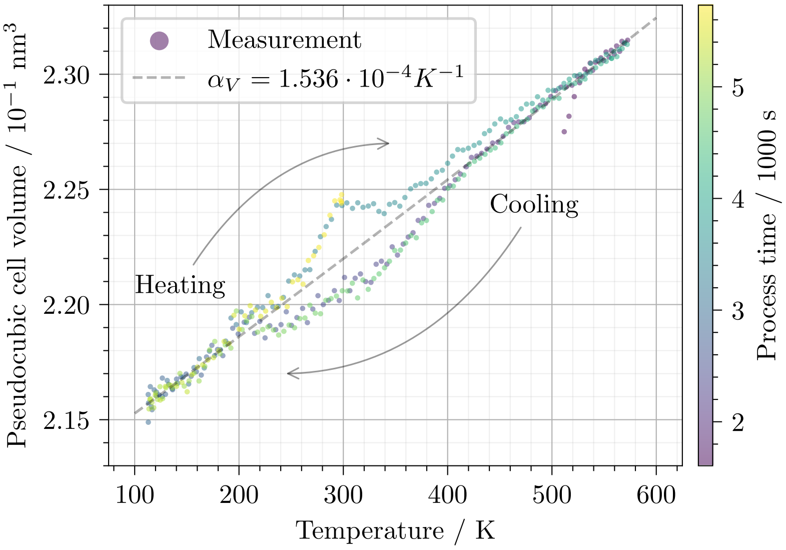

Figure 5.28: The pseudocubic cell volume, calculated from the lattice parameters in Figure 5.27 for process times after the recrystallization, are plotted in circles as a function of the hotplate temperature. The color of the circles corresponds to the process time with dark blue being short time and bright yellow long times. The fitted thermal expansion, α_V, according to equation Equation 5.4 is plotted as a dashed grey line.

In order to further investigate the correlation between the cell parameters and the temperature, the cell volume is plotted as a function of the hotplate temperature in Figure 5.28.

From Figure 5.28, the previously discussed hysteresis is clearly seen between the cooling and heating curves with a peak deviation at 300 K. This hysteresis starts upon cool down with a downwards deviation from the linear trend at the temperature of the $\alpha \to \beta$ transition of around 400 K. The value continues to bow down with a maximum deviation of -0.015 nm^3 around 320 K and does not meet the heating curve until 200 K. From that point, the heating and cooling overlap and the heating curve continues to follow the linear trend up to a temperature of 260 K. From there the heating curve displays a sharp increase compared to the linear trend with a maximum deviation of +0.025 nm^3 at 300 K followed by a sharp decrease before getting close to the linear trend at the $\gamma \to \beta$ transition temperature of around 350 K. From the process time, which is plotted as the color of the scatter points, it can be seen that there is a clear overlap between the two heating cycles and that the hysteresis is not due to measurement noise.

In order to quantify the temperature dependence of the cell volume, the volumetric thermal expansion coefficient is calculated. The thermal expansion coefficient is defined as:

$$\alpha_V = \frac{1}{V}\frac{\partial V}{\partial T} \quad \Rightarrow \quad V(T) \propto \mathrm{e}^{T\alpha_V}. \tag{5.4}$$

The linear trend of the data is fitted with Equation 5.4 and a thermal expansion coefficient of $\alpha_V = 1.536 \cdot 10^{-4}$ K^{-1} is determined. The resulting cell volume as a function of temperature is plotted as a line in Figure 5.28.

The determined value of $1.536 \cdot 10^{-4}$ K^{-1} agrees well with values reported for other lead halide perovskites such as $1.53 \cdot 10^{-4}$ K^{-1} reported for $CsPbI_3$ [80], $1.57 \cdot 10^{-4}$ K^{-1} reported for $MAPbI_3$ [140] and the somewhat lower $1.2 \cdot 10^{-4}$ K^{-1} reported for $CsPbBr_3$ [85]. As noted by others, this value is considerably larger than that of most substrates used and is a key to understanding the stress in films during annealing. This is especially the case for pure Cs perovskites which, as shown in section 5.1, require much higher annealing temperatures than their organic or hybrid counterparts.

In order to investigate the apparent correlation between the transmittance inflection point and the pseudocubic c parameter, observed in Figure 5.27, the two values are plotted against each other in a scatter plot in Figure 5.29 for process times after the recrystallization through the δ-phase. The scattered points are separated by their respective crystal phase and for each group a linear regression is performed. The points belonging to the γ-phase are split into points for hotplate temperatures above 200 K, γ_1, and below 200 K, γ_2. This temperature point was chosen as discontinuities were observed in the lattice parameters and inflection point of Figure 5.27 at this temperature. In addition, the hysteresis in Figure 5.28 is only observed above 200 K.

The previously observed correlation between optical band-gap and the c parameter is evident in Figure 5.29. However, the crystallographic phases show distinct correlations. From the linear regression, it is clear that both the cubic α-phase and the orthorhombic γ-phase show a direct correlation whilst the tetragonal β-phase shows an indirect correlation. Furthermore, the regression slope of the α-phase is the steepest with an increase in optical band-gap of 5.5 meV for every pm of the c parameter. The two regions of the γ-phase show similar regression slopes but with an offset in the zero-crossing meaning that band-gap values below 200 K are consistently lower than those above. The β-phase shows a slight negative regression slope of about -0.5 meV/pm.

At first, the positive correlation between the lattice parameter and the optical band-gap might seem counter-intuitive as most semiconductors show a negative correlation, where decreasing size, and increased overlap of electronic states, causes larger splittings and higher band-gaps [141]. This can be understood by analogy with the classical particle in a box example from quantum mechanics where a smaller box causes a larger splitting of the energy levels due to quantum confinement. In addition to the quantum confinement argument, the band-gap of $CsPb(Br_xI_{1-x})_3$ was in section 4.1 observed to increase with Br content and, hence, decreasing lattice parameter.

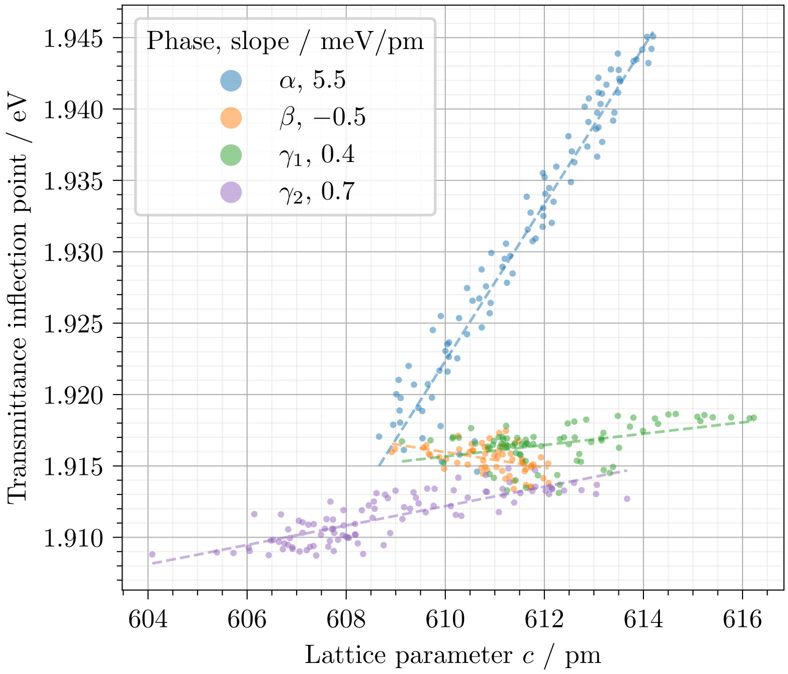

Figure 5.29: Scatter plot of the transmittance inflection point versus the c lattice parameter. The scatter points are colored after the respective phase that they correspond to with the orthorhombic γ-phase being split into γ_1 and γ_2 for the two regions discussed in the text. The linear regression for the points of each phase is plotted as dashed lines with the slopes noted in the legend.

In order to explain this, the levels forming the band-gap in lead halide perovskites need to be recalled. As explained in subsection 2.3.4, the band-gap is established between the conduction band formed by the Pb p atomic level and the valence band formed by the antibonding state of the Pb s and halide p overlap. As the lattice spacing is decreased there is indeed a confinement effect that increases the splitting of the bonding-antibonding states between the Pb p-orbital and the halide s-orbital due to increased overlap. However, this will *increase* the valence band maximum causing a *decrease* in the band-gap. There is a small increase also in the conduction band minimum but measurements on the effect of cation exchange, which is mainly effecting band-gap through size modulation, have shown that this is less than the increase of the valence band [78]. The net result is, therefore, an overall decrease in the band-gap. Similarly, the exchange of a large halide ion, such as I, for a smaller one, such as Br, will cause a shift upwards of the levels but this is counteracted by the stronger effect of the electronegativity of the halide which will shift the level in the opposite direction. As there is no change in the halide here, but only a change in the lattice spacing due to temperature, the result is a decrease in band-gap with decreasing lattice spacing.

The effect of the lattice parameter decrease on the optical band-gap is strongest in the cubic α-phase where all three parameters decrease and there is no tilting. As the perovskite transitions to the tetragonal β-phase, a tilting of the lead-halide octahedra occurs in the $a - b$ plane and the band-gap stops decreasing with cell volume. Shortly thereafter, the material transitions to the orthorhombic γ-phase and tilting in the c direction also occurs. From this point, any further decrease in the band-gap seems to be limited by the largest lead-halide distance in the c-direction. For a more quantitative analysis, the results should be compared with theoretical simulations.

The jump in both lattice parameters and optical band-gap at 200 K seems to suggest that this is a real effect on the parameters rather than some systematic error of any one of the characterization methods. The point coincides with the density maximum of the fused silica substrate [142] but the three orders of magnitude lower expansion coefficient of the substrate makes this change unlikely to have a significant effect on the rapidly contracting perovskite. This phenomenon remains unexplained and is left for future work to study.

Chapter 6

Summary & Conclusion

In this final chapter, a summary of the main results of this thesis is given followed by the conclusions that can be drawn from combining these findings. In the end, an outlook on the next steps of combinatorial synthesis and high-throughput analysis is provided.

6.1 Summary

In summary, the implementation of two combinatorial thin-film synthesis methods, one vapor-based and one solution-based, has been shown. These methods have been combined with high-throughput analysis to illustrate how materials research for optoelectronics can be parallelized and accelerated.

The combinatorial method of DOD inkjet printing was through this work extended with an algorithm for droplet placement to optimize the mixing of the combined inks. Using this method, combinatorial libraries of $CsPb(Br_xI_{1-x})_3$ were printed with sample compositions varying from completely one ink to the other in discrete steps. The compositional homogeneity within each sample was validated through micro spot mapping with GIWAXS and XRF. The homogeneity was observed to depend on the printing resolution and an optimum value was found for which the samples were homogeneous to the required degree.

Using the developed droplet placement algorithm, a combinatorial library of $CsPb(Br_xI_{1-x})_3$ was made for the purpose of determining the previously unknown temperature-dependent phase diagram as a function of the Br content. The material was chosen for its promised thermal and photo-stability over organic cations in MHP photovoltaic applications. Through a single high-throughput GIWAXS experiment the complete temperature-dependent phase diagram of the combinatorial library was obtained.

The $CsPb(Br_xI_{1-x})_3$ mixture was found to form a solid solution. All samples except for the most Br-rich started out in the non-perovskite δ-phase and transitioned to the cubic α-phase at high temperature. Upon cooling down the samples transitioned to the distorted β and γ phases with all but the pure $CsPbI_3$ sample being metastable in a semiconducting perovskite phase at room temperature. All transition temperatures were found to decrease with Br content. The result showed that an increasing Br content stabilized the semiconducting perovskite phase due to an increasing tolerance factor.

As a complementary example of combinatorial deposition from vapor phase, a custom evaporation chamber was extended with four sources to facilitate the co-evaporation of combinatorial $Cs_yPb_{1-y}(Br_xI_{1-x})_{2-y}$ libraries. The necessary calibration was explained in detail and a model was created for the source distributions. The model was tested through evaporation of the CsI, CsBr, $PbBr_2$, and PbI_2 binaries.

By utilizing the model of the distributions a set of combinatorial libraries were evaporated with a small continuous gradient of Cs to Pb and, in the perpendicular direction on the substrate, Br to I. These libraries were characterized by contact-less measurements in an effort to determine the photovoltaic potential of each sample. Previously established methods were optimized for high-throughput screening and the dimensionality of the data was reduced to facilitate correlation analysis. By measuring UV/Vis, TRPL and absolute PL, the limit for the photovoltaic parameters J_{SC}, V_{OC} and PCE was directly calculated for 3,456 samples of varying composition.

From these results, it was concluded that Pb-rich compositions show a lower absorption coefficient due to the formation of a secondary, non-semiconducting, phase. Additionally, both Cs-rich and Cs-poor compositions exhibited short carrier lifetimes and lower PLQY due to increased non-radiative recombination. By combining these results the PCE limit was calculated to decrease, with respect to the radiative limit, for any off-stoichiometric compositions.

Finally, the structural and optical analyses were combined in a correlative high-throughput experiment. The temperature-dependent optical transmittance and GIWAXS were recorded for a sample of interest, with Br content $x = 0.3$, during a continuous temperature ramp. The thermal expansion coefficient was determined and the optical band-gap was found to correlate with the largest pseudocubic lattice parameter, c.

6.2 Conclusion

In conclusion, this thesis has demonstrated the development, implementation, and validation of combinatorial inkjet printing and co-evaporation combined with high-throughput characterization techniques. These methods have been employed for the investigation of the structural and optical properties of the $Cs_yPb_{1-y}(Br_xI_{1-x})_{2-y}$ metal halide perovskite, for the use of this material in thin-film optoelectronic devices.

Specifically, the new algorithm for optimized droplet placement in combinatorial inkjet printing, developed and validated here, provides a method for fast investigation of thin-film materials. The inkjet printing method has the advantage that it can span the full range of the compositions of the individual inks and creates locally homogeneous samples. However, the ink printability and mixing on the substrate need to be optimized and there could also be additional optimization needed to generate compact films from this method. Combinatorial co-evaporation, on the other hand, only requires precise calibration of the rate measurement but the compositional range of this method is limited and it is, therefore, more suited when small variations are to be studied.

Combinatorial synthesis alone is not enough to speed up the material investigation process. Without high-throughput experiments, such as the temperature-dependent GIWAXS measurement or the contact-less optical investigation shown here, the characterization time will instead be the bottleneck. In the same way, dimensional reduction of the data and automatic analysis, such as the ones performed here for estimating the photovoltaic performance of $Cs_yPb_{1-y}(Br_xI_{1-x})_{2-y}$, is needed to reduce the total investigation time from synthesis to characterization to analysis.

Using both combinatorial synthesis methods, high-throughput experiments, and automized data reduction, new insight on the influence of $Cs_yPb_{1-y}(Br_xI_{1-x})_{2-y}$ composition on phase stability and optical properties was here found for applications in thin-film optoelectronics. For the first time, the heating and cooling thin-film phase diagram of the full solid solution was determined, which is crucial for understanding the material during thin-film fabrication. It was found that the addition of Br to the thermally stable but phase unstable $CsPbI_3$ stabilizes the perovskite phase and has the implications of improved device stability and that reduced annealing temperatures can be used for film preparation. For these films, any off-stoichiometry, with respect to Cs and Pb, was found to limit performance due to non-radiative recombination and this provides important information for optimizing these stabilized compositions in solar cells and LEDs. Finally, this work shows that by speeding up all three components of combinatorial research a leap in sample throughput can be achieved and the materials research can be greatly accelerated.

6.3 Outlook

Taking into consideration the findings and methodology developed within this thesis, the natural next step is to apply these methods on new materials of interest. As an example, current work is underway to partially or fully replace the Pb sources of the co-evaporation chamber with Sn-based compounds. By employing the synthesis, characterization, and analysis methods developed in this thesis, the hope is to quickly find an answer to how compositional variations affect the photovoltaic potential of $Cs_y(Pb_zSn_{1-z})_{1-y}(Br_xI_{1-x})_{2-y}$.

Additionally, the use of these combinatorial methods should be expanded beyond single films for fundamental research to the direct manufacturing of devices. This work has already been started by V. Schröder in his study on directly printing wavelength selective photodetectors [54]. The main problem identified for complex optoelectronic devices is the film quality of the combinatorially printed films. One proposed approach is to identify device architectures that are less sensitive to variations in ink properties.

Beyond these suggestions, additional parameters of variation should be identified to further increase the dimensionality of the combinatorial library and thereby the potential speedup. As an example, the effect of additives or variation of process parameters such as substrate temperature could be changed throughout a single library substrate.

Finally, the three components of combinatorial research, synthesis, characterization, and analysis should be brought to a full circle by allowing the results of the analysis to dictate the next synthesis. This is by no means an original idea and has long been envisioned by others. However, both the printing and co-evaporation here would with some minor modifications lend themselves well to this task. By allowing for the process parameters to vary as suggested above and evaluating a figure of merit, such as the PCE limit calculated in this work, an iterative process of library creations and characterization could be started. With automatic sample changers or even rolls of flexible substrates, an almost continuous library of samples could be made in a fully automized search for the optoelectronic thin-film materials of tomorrow.

Appendix A

Combinatorial Inkjet Printing

In this appendix some additional information on the developed method for combinatorial inkjet printing is shown. Firstly, the `Python` implementation of the algorithm explained in section 4.1 is given. Secondly, the derivation of the expression for contact diameter used in the same section is shown.

A.1 Droplet Placement Algorithm

Here an implementation of the droplet algorithm from subsection 4.1.1 is shown in the high-level programming language `Python`. This algorithm was published in reference [120].

```python
import sys
from typing import Tuple, List

import numpy as np
from itertools import combinations
from scipy.special import comb
from PIL import Image

"""
Code for generating base matrices to use for combinatorial inkjet printing.
Please cite http://dx.doi.org/10.1039/d1ta08841f if used.
"""


def combs(a: np.ndarray, r: int) -> np.ndarray:
    """
    Return successive r-length combinations of elements in the array a.
    Should produce the same output as array(list(combinations(a, r))), but
    faster.
    From:
    https://stackoverflow.com/questions/16003217/n-d-version-of-itertools-combinations-in-numpy

    :param a: Array with elements to make combinations from
    :type a: numpy.ndarray
    :param r: Number of elements to combine
    :type r: int
    :return: 2d array of all combinations
    :rtype: numpy.ndarray
```

```python
    """
    a = np.asarray(a)
    dt = np.dtype([('', a.dtype)] * r)
    b = np.fromiter(combinations(a, r), dt)
    return b.view(a.dtype).reshape(-1, r)


def droplet_position_optimization(n: int, k: int) -> Tuple[List[int], List[int]]:
    """
    Function for generating a base matrix with side n and filling k.

    :param n: Side length of base matrix
    :type n: int
    :param k: Filling of the base matrix
    :type k: int
    :return: Tuple of two lists of the optimal droplet positions,
             one for the x position and one for the corresponding y positions
    :rtype: Tuple[List[int], List[int]]
    """
    x, y = np.indices((n, n))
    pos = combs(np.arange(n ** 2), k)
    x_base_pos = x.flatten()[pos]
    y_base_pos = y.flatten()[pos]
    points = comb(n ** 2, k, exact=True)
    x_pos = np.zeros((points, k * 9))
    y_pos = np.zeros((points, k * 9))
    count = 0
    for y_rep in [-1, 0, 1]:
        for x_rep in [-1, 0, 1]:
            roi = slice(k * count, k * (count + 1))
            x_pos[:, roi] = x_base_pos + (x_rep * n)
            y_pos[:, roi] = y_base_pos + (y_rep * n)
            count += 1
    x_pos = np.tile(x_pos, (k, 1, 1))
    y_pos = np.tile(y_pos, (k, 1, 1))
    distances = np.sqrt(
        np.power(x_pos - np.broadcast_to(x_base_pos, (k * 9, points, k)).T, 2)
        + np.power(y_pos - np.broadcast_to(y_base_pos, (k * 9, points, k)).T, 2)
    )
    distances[np.where(distances < 1)] = (2 * n) ** 2
    min_dist = np.min(distances, axis=2)
    worst_point = np.argmin(min_dist, axis=0)
    if np.max(min_dist[worst_point, np.arange(points)]) > 1:
        best_option_index = np.argmax(min_dist[worst_point, np.arange(points)])
    else:
        worst_min_dist = np.min(min_dist, axis=0)
        min_dist_copy = min_dist
        min_dist_copy[np.where(min_dist != worst_min_dist)] = 0
        best_option_index = np.argmin(np.sum(min_dist_copy, axis=0))
    return x_base_pos[best_option_index], y_base_pos[best_option_index]


def generate_bases(size: int) -> List[np.ndarray]:
    """
    Function for generating all base matrices for a certain size.

    :param size: Side length of the base matrix
    :type size: int
    :return: A list of the base matrices as size*size numpy arrays
    :rtype: List[numpy.ndarray]
    """
    if size > 5:
        print('For size above 4 the algorithm takes a long time.')
    high = int(np.ceil((size ** 2 + 1) / 2)) - 1
    bases = [np.zeros((size, size), dtype=bool)]
```

```
    for fill in range(high):
        best_x, best_y = droplet_position_optimization(size, fill + 1)
        base = np.zeros((size, size), dtype=bool)
        for idx in range(len(best_x)):
            base[best_y[idx], best_x[idx]] = True
        bases.append(base)
    remaining = size ** 2 + 1 - len(bases)
    for idx in range(remaining):
        bases.append(np.invert(bases[remaining - idx - 1]))
    return bases
```

A.2 Contact Diameter

Here follows the derivation of the expression for contact diameter, D, as a function of drop volume, V, and contact angle, θ, as used in subsection 4.1.2 of the main text.

Let the radius of curvature for the droplet with volume V and contact angle θ be r, and its maximum height above the substrate be h as seen in the illustration of Figure A.1.

From the Figure A.1 it can be seen that:

$$\frac{D/2}{r} = \sin\theta \quad \Rightarrow \quad D = 2r\sin\theta, \tag{A.1}$$

and that:

$$\frac{r-h}{r} = \cos\theta \quad \Rightarrow \quad h = r(1-\cos\theta). \tag{A.2}$$

The volume can be obtained by the disc method:

$$V = \pi \int_{r-h}^{r} f(x)^2 \mathrm{d}x, \tag{A.3}$$

where $f(x)$ is the function of the circular drop as seen in Figure A.1 and therefore given by $f(x)^2 = r^2 - x^2$. The three equations above are valid for $0 \leqslant \theta \leqslant \pi$. Solving the integral gives the following expression for the volume:

$$V = \pi\left(r^2 h - \frac{r^3 - (r-h)^3}{3}\right). \tag{A.4}$$

Inserting the expression of h from Equation A.2 and solving for r yields:

$$r = \left(\frac{3V}{\pi(2 - 3\cos\theta + (\cos\theta)^3)}\right)^{1/3}. \tag{A.5}$$

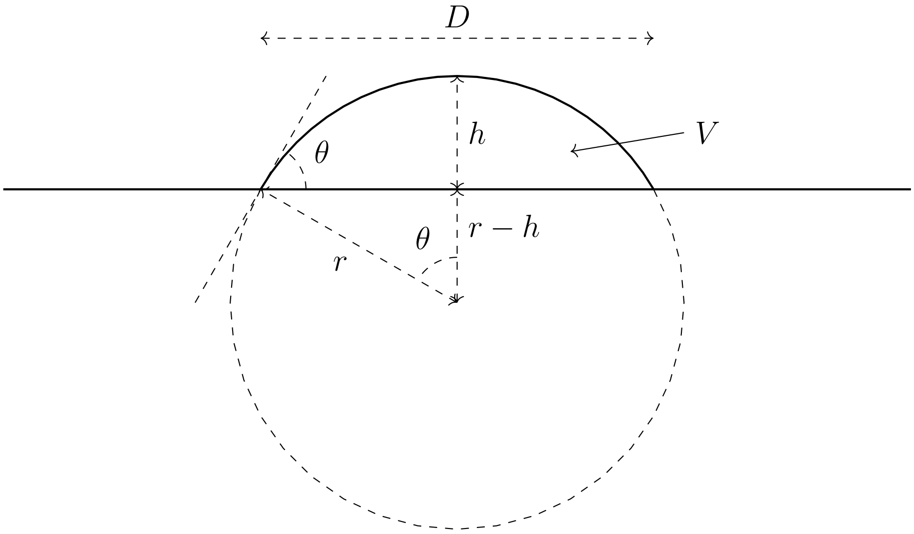

Figure A.1: Illustration of spherical droplet with volume V, contact angle θ, radius of curvature r and height h.

By inserting this expression into Equation A.1 from above the contact diameter is finally given by:

$$D(\theta, V) = 2\sin\theta \cdot \left(\frac{3V}{\pi(2 - 3\cos\theta + (\cos\theta)^3)}\right)^{1/3} \tag{A.6}$$

Appendix B

Combinatorial Evaporation

In this appendix the code for the distribution model from section 4.1 is shown.

B.1 Distribution Model

Here the function for calculating the thickness distribution, according to the model from subsection 4.2.1, from one of the 4 sources in the setup explained in subsection 3.1.2, is shown. The default parameters for the offset are those of the specific PVD chamber used in this work but can be exchanged for the values of any other evaporator *if* the sources are angled towards the center of a 50×50 mm^2 substrate. Otherwise the model will have to be slightly modified.

```python
import numpy as np
from numpy.linalg import norm


def pvd_thickness(x, y, source, v=1e6, order=1.0, offset=np.array([41.54, 26.06, 201.12])):
    """
    Function for calculating the thickness on a xy grid of a 50x50 mm2 substrate from four PVD
    sources placed symmetrically around it.

    :param x: Array for x positions for which to calculate the thickness.
    :type x: np.array
    :param y: Array for y positions for which to calculate the thickness.
    :type y: np.array
    :param source: Which one of the four sources that is evaporating in the substrate coordinate
    system: 1-upper left, 2-upper right, 3-bottom right and 4-bottom left.
    :type source: int
    :param v: Volume of evaporated material
    :type v: float
    :param order: Cosine order of the distribution.
    :type order: float
    :param offset: x,y,z offset of the source relative to the substrate center.
    :type offset: np.array
    :return: 2D array of thicknesses for the grid spanned by the supplied x and y values in units of
    the specified volume.
    :rtype: np.ndarray
    """
    if source == 1:
        source_loc = np.array([1, 1, 1])
```

```
    elif source == 2:
        source_loc = np.array([-1, 1, 1])
    elif source == 3:
        source_loc = np.array([-1, -1, 1])
    elif source == 4:
        source_loc = np.array([1, -1, 1])
    else:
        raise ValueError('Not valid source')
    # Vector from source to middle of substrate
    o = offset * source_loc
    # Unit vector for substrate plane
    n = np.array([0, 0, 1])
    # Repeat x and y vectors to form a matrix
    xv, yv = np.meshgrid(x, y)
    # Vector from source to each x and y point (r0,r1,r2)
    r0 = o[0] - 25 + xv
    r1 = o[1] - 25 + yv
    r2 = np.ones(xv.shape) * o[2]
    # Length of r vector
    r_norm = np.sqrt(np.power(r0, 2) + np.power(r1, 2) + np.power(r2, 2))
    # Dot product of o and r
    o_dot_r = o[0] * r0 + o[1] * r1 + o[2] * r2
    # Dot product of n and r
    n_dot_r = n[0] * r0 + n[1] * r1 + n[2] * r2
    # Cosine of angle between o and r
    cos_phi = o_dot_r / norm(o) / r_norm
    # Cosine of angle between n and r
    cos_theta = n_dot_r / norm(n) / r_norm
    # Thickness according to doi:10.3390/coatings8090325
    thickness = v * np.power(cos_phi, order) * cos_theta / np.power(r_norm, 2) / np.pi
    return thickness
```

Appendix C

Python Models & Calculations

In this appendix a collection of calculations implemented in the high-level programming language `Python` is shown. The code was developed using `Python` version 3.9. The appendix starts by explaining the implementation of the numerical optical model used in section 5.2, followed by the method for determining the inflection point in absorption coefficient from the same section and ends with the solution for finding the lattice parameters from a set of indexed peaks which is used in section 5.3.

C.1 Numerical Optical Model

The excitonic absorption in semiconductors is frequently included in literature by simply citing the original paper by Elliot [13]. However, the implementation of this formula is *not* straight forward and therefore a considerable section of this appendix is dedicated to providing the full code needed to calculate the reflectance and transmittance.

Below follows the `Python` implementation of the transfer matrix method and Tanguy formula [14] for a thin absorber on a thick substrate. The functions are explained in their respective `docstring`.

For the final function, `elliot_tmm`, the dielectric constant is calculated from the gaussian broadened Tanguy function from Equation 2.8 of the fundamentals and used to calculate the wavelength dependent refractive index. Using this refractive index the reflectance and transmittance is calculated by a transfer matrix model. The values are calculated for a normal distribution of thicknesses to account for sample roughness.

```python
from typing import Union, Tuple, Callable

import numpy as np

from scipy.special import digamma
from scipy.interpolate import interp1d
```

```python
# Constants:
h_bar = 6.582119569e-16  # eV*s
h = 4.135667696e-15  # eV*s
c = 299792458.0  # m/s
k = 8.617333262145e-5
std_to_hwhm = np.sqrt(2 * np.log(2))
fused_silica_sellmeier = [
    [0.6961663, 0.4079426, 0.8974794],
    [0.0684043 ** 2, 0.1162414 ** 2, 9.896161 ** 2]
]


# General functions:
def gaussian(x: Union[int, float, np.ndarray], hwhm: float) -> Union[int, float, np.ndarray]:
    """
    Calculate the Gaussian profile at value(s) x.

    :param x: Value(s) for which to evaluate the profile
    :type x: Union[int, float, np.ndarray]
    :param hwhm: Half width at half maximum of the profile
    :type hwhm: float
    :return: Evaluation of the profile at the x values
    :rtype: Union[int, float, np.ndarray]
    """
    return np.sqrt(np.log(2) / np.pi) / hwhm * np.exp(-1 * np.power((x / hwhm), 2) * np.log(2))


def sellmeier(wavelengths: np.ndarray, b_constants: Union[list, np.ndarray],
              c_constants: Union[list, np.ndarray]) -> np.ndarray:
    """
    Calculates real part of refractive index from the sellmeier coefficients.

    :param wavelengths: The wavelengths for which to calculate the refractive index, unit should
    match coefficients
    :type wavelengths: np.ndarray
    :param b_constants: Array of sellmeier B coefficients
    :type b_constants:Union[list, np.ndarray]
    :param c_constants: Array of sellmeier C coefficients
    :type c_constants:Union[list, np.ndarray]
    :return: Array of the real refractive index at the specified wavelengths
    :rtype: Union[list, np.ndarray]
    """
    if len(b_constants) != len(c_constants):
        raise ValueError
    n_squared = 1
    wave_squared = np.power(wavelengths, 2)
    for idx, bi in enumerate(b_constants):
        n_squared += bi * wave_squared / (wave_squared - c_constants[idx])
    return np.sqrt(n_squared)


# Elliot functions:
def tanguy(energy: np.ndarray, exciton_energy: float, bandgap_energy: float, broadening: float,
           scale_factor: float) -> np.ndarray:
    """
    Function for calculating complex dielectric constant for a direct band-gap semiconductor
    considering the exciton binding energy and lorentzian broadening.
    Implemented from equation in article from Tanguy with doi: 10.1103/physrevlett.75.4090

    :param energy: The photon energies for which to calculated the dielectric constant
    :type energy: np.ndarray
    :param exciton_energy: The exciton binding energy in units of the energy array
    :type exciton_energy: float
    :param bandgap_energy: The band-gap in units of the energy array
    :type bandgap_energy: float
```

```
    :param broadening: The lorentzian broadening in units of the energy array
    :type broadening: float
    :param scale_factor: The scale factor
    :type scale_factor: float
    :return: The complex dielectric constant
    :rtype: np.ndarray
    """

    def eta(z):
        return np.sqrt(exciton_energy / (bandgap_energy - z))

    def g(z):
        eta_val = eta(z)
        return (2 * np.log(eta_val) - 2 * np.pi / np.tan(np.pi * eta_val) - 2 * digamma(eta_val)
                - 1 / eta_val)

    arg = energy + 1j * broadening
    return scale_factor * np.sqrt(exciton_energy) * (g(arg) + g(-arg) - 2 * g(0)) / np.power(arg, 2)


def refractive_index(epsilon: np.ndarray) -> np.ndarray:
    """
    Function for calculating the real refractive index from the complex dielectric constant.

    :param epsilon: The complex dielectric constant
    :type epsilon: np.ndarray
    :return: The real refractive index
    :rtype: np.ndarray
    """
    return np.sqrt((epsilon.real + np.sqrt(np.power(epsilon.real, 2) + np.power(epsilon.imag, 2))))


# Transfer matrix method functions:
def incoherent_tmm(n_absorber: np.ndarray, n_substrate: np.ndarray, wavelengths: np.ndarray,
                   d_absorber: float, superstrate: bool = False) -> Tuple[np.ndarray, np.ndarray]:
    """
    Function for calculating the reflectance and transmittance of an absorbing thin film on a thick
    (in relation to the wavelength) non-absorbing substrate. Assumes incoherence in the substrate.
    Implementation is based on solution to the transfer matrix model.

    :param n_absorber: Complex refractive index of absorber as a function of wavelength
    :type n_absorber: np.ndarray
    :param n_substrate: Real refractive index of substrate as a function of wavelength
    :type n_substrate: np.ndarray
    :param wavelengths: Wavelengths for which to calculate reflectance and transmittance
    :type wavelengths: np.ndarray
    :param d_absorber: Thickness of absorber in units of the wavelength
    :type d_absorber: float
    :param superstrate: Whether the reflectance is measured from the substrate side or not
    :type superstrate: bool
    :return: The reflectance, the transmittance
    :rtype: Tuple[np.ndarray, np.ndarray]
    """
    n_array = np.array([np.ones(n_absorber.shape), n_absorber, n_substrate])
    r01, t01 = tmm_reflectance_transmittance(n_array, wavelengths, d_absorber)
    r10, t10 = tmm_reflectance_transmittance(np.flip(n_array, axis=0), wavelengths, d_absorber)
    r12 = np.power((n_substrate - 1) / (n_substrate + 1), 2)
    t12 = 1 - r12
    p1 = 1
    if superstrate:
        r21 = np.power((1 - n_substrate) / (n_substrate + 1), 2)
        t21 = np.power(2 * 1 / (n_substrate + 1), 2) * n_substrate / 1
        l00 = ((1 / p1) - (r12 * p1 * r10)) / (t21 * t10)
        l10 = ((r21 / p1) + (((t12 * t21) - (r12 * r21)) * p1 * r10)) / (t21 * t10)
    else:
```

```python
        l00 = ((1 / p1) - (r10 * p1 * r12)) / (t01 * t12)
        l10 = ((r01 / p1) + (((t10 * t01) - (r10 * r01)) * p1 * r12)) / (t01 * t12)
    return l10 / l00, 1 / l00


def tmm_reflectance_transmittance(n: np.ndarray, wavelengths: np.ndarray,
                                  d: float) -> Tuple[np.ndarray, np.ndarray]:
    """
    Function for calculating the reflectance and transmittance for an absorbing thin film surrounded
    by two infinitely thick non absorbing media.
    Implementation is based on solution to the transfer matrix model.

    :param n: 3 by len(wavelengths) array with each row being the refractive index as a function of
    wavelength for the starting medium, the absorber and the ending medium.
    :type n: np.ndarray
    :param wavelengths: The wavelengths for the specified refractive indices.
    :type wavelengths: np.ndarray
    :param d: The thickness of the absorber in units of the wavelength
    :type d: float
    :return: The reflectance, the transmittance
    :rtype: Tuple[np.ndarray, np.ndarray]
    """
    n_sum = n[:-1] + n[1:]
    r = (n[1:] - n[:-1]) / n_sum
    t = 2 * n[:-1] / n_sum
    delta = d * 2 * np.pi * n[1:-1] / wavelengths

    transmittance = (
            np.power(
                np.abs(
                    t[0] * t[1] / (np.exp(-1j * delta[0]) + r[0] * r[1] * np.exp(1j * delta[0]))),
                2
            ) * n[-1].real / n[0].real
    )
    reflectance = (np.power(
        np.abs(((r[0] * np.exp(-1j * delta[0]) + r[1] * np.exp(1j * delta[0])) /
                (np.exp(-1j * delta[0]) + r[0] * r[1] * np.exp(1j * delta[0])))), 2
    ))
    return reflectance, transmittance


# Combined functions:
def get_elliot_tmm_function(
        thickness: float, temperature: float = 298, wavelength_low: float = 500,
        wavelength_high: float = 1000, energy_0: float = 0.1, energy_1: float = 10,
        points: int = 20001
) -> Tuple[
    Callable[[float, float, float, float, float, float, float], Tuple[np.ndarray, np.ndarray]],
    np.ndarray
]:
    """
    Function for generating a function and wavelengths for calculating the reflectance and
    transmittance of a direct band-gap thin film absorber on a thick fused silica substrate for
    those wavelengths. This function is used to save memory when evaluating multiple times in a
    fitting routine.

    :param thickness: The thickness of the absorber
    :type thickness: float
    :param temperature: The temperature of the absorber in kelvin
    :type temperature: float
    :param wavelength_low: The lowest wavelength of interest in units of absorber thickness
    :type wavelength_low: float
    :param wavelength_high: The highest wavelength of interest in units of absorber thickness
    :type wavelength_high: float
    :param energy_0: The lowest energy for the convolution should be kept as low as possible
```

```
    :type energy_0: float
    :param energy_1: The highest energy for the convolution should be kept as high as possible
    :type energy_1: float
    :param points: Number of energy points used for the convolution, will determined the resolution
    of the calculated values
    :type points: int
    :return: Function for calculating reflectance and transmittance (see docstring of returned
    function for details), the wavelengths for which the reflectance and transmittance is
    calculated.
    :rtype: Tuple[
        Callable[[float, float, float, float, float, float, float], Tuple[np.ndarray, np.ndarray]],
        np.ndarray
    ]
    """
    energy_ev = np.linspace(energy_0, energy_1, points)
    energy_relative = energy_ev - energy_ev[int(points / 2)]
    d_energy = energy_ev[1] - energy_ev[0]
    wavelengths_um = 1e6 * h * c / energy_ev
    wavelengths_nm = 1e3 * wavelengths_um

    roi = np.where((wavelength_low < wavelengths_nm) & (wavelengths_nm < wavelength_high))

    n_fused_silica = sellmeier(wavelengths_um[roi], *fused_silica_sellmeier)

    def elliot_tmm(epsilon_inf: float, gaussian_broadening: float, exciton_binding_energy: float,
                   bandgap: float, lorentzian_denominator: float, scaling_factor: float,
                   thickness_sigma: float) -> Tuple[np.ndarray, np.ndarray]:
        """
        Function for calculating the reflectance and transmittance of a direct band-gap thin film
        absorber on a thick fused silica substrate for the wavelengths returned with this function.
        The thickness of the absorber is modelled with a normal distribution of thicknesses.
        The dielectric function is calculate by the Tanguy formula and broadened by a gaussian.

        :param epsilon_inf: Background dielectric constant
        :type epsilon_inf: float
        :param gaussian_broadening: The HWHM of the gaussian broadening in eV
        :type gaussian_broadening: float
        :param exciton_binding_energy:  The exciton binding energy in eV
        :type exciton_binding_energy: float
        :param bandgap: The band-gap in eV
        :type bandgap: float
        :param lorentzian_denominator: The lorentzian broadening in parts of kT
        :type lorentzian_denominator: float
        :param scaling_factor: The scaling factor
        :type scaling_factor: float
        :param thickness_sigma: The standard deviation in the thickness variation
        :type thickness_sigma: float
        :return: The reflectance, the transmittance
        :rtype: Tuple[np.ndarray, np.ndarray]
        """
        epsilon = epsilon_inf ** 2 + np.convolve(
            gaussian(energy_relative, gaussian_broadening),
            tanguy(energy_ev, exciton_binding_energy, bandgap,
                   temperature * k / lorentzian_denominator, scaling_factor),
            mode='same'
        ) * d_energy
        n_real = refractive_index(epsilon)
        n = n_real + 1j * (epsilon.imag / (2 * n_real))
        n_sigma = 3
        thicknesses = np.linspace(thickness - n_sigma * thickness_sigma,
                                  thickness + n_sigma * thickness_sigma, 11)
        rs = []
        ts = []
        for d in thicknesses:
            r, t = incoherent_tmm(n[roi], n_fused_silica, wavelengths_um[roi], d)
```

```
            rs.append(r)
            ts.append(t)
        weights = gaussian(thicknesses - thickness, std_to_hwhm * thickness_sigma)
        r_model = np.average(np.array(rs), weights=weights, axis=0)
        t_model = np.average(np.array(ts), weights=weights, axis=0)
        return r_model, t_model

    return elliot_tmm, wavelengths_nm[roi]
```

C.2 Absorption Coefficient Inflection

Here the code used to find the inflection point in the absorption coefficient is shown. However, before this the validity of the approximation used for calculating the absorption coefficient will be discussed.

Absorption coefficient approximation

For a thin film the Lambert-Beer law, Equation 2.1, *cannot* be used to calculate the absorption coefficient from the measured reflectance, R, and transmittance, T. This is due to the fact that multiple reflections and interference of waves are not taken into consideration. If one considers a "floating" film suspended in air an approximation could be that the transmittance is the ratio of light that is transmitted from a single pass through the film I/I_0 multiplied with what passes the first air-film interface and the second. If the measured reflectance is assumed to only be the result of a single interface this approximation can be written as $T \approx (1-R)^2 \cdot I/I_0$. Rearranging and plugging into the Lambert-Beer law, Equation 2.1, then gives $\alpha \approx \ln\left((1-R)^2/T\right)/d$.

The validity of this approximation for the thin films studied in this work can be investigated using the combined Tanguy and TMM model descibed in the previous section. If the model is used to calculate first the complex dielectric constant, given the fit results from the main text, this can easily be converted to the absorption coefficient. This absorption coefficient is plotted in Figure C.1 as the ground truth. The dielectric constant can then be used to calculate the reflectance and transmittance by TMM and taking all reflections and interferences into consideration. Finally, these values can be used with the approximation from above to calculate an estimate for α, this is also plotted in Figure C.1.

Another approximation would be to consider a film on a thick substrate with refractive index closer to that of the film. In this approximation, only the reflectance at the air-film interface is considered and the expression for the absorption coefficient becomes $\alpha \approx \ln\left((1-R)/T\right)/d$. This second approximation is also plotted in Figure C.1.

From Figure C.1 it is clear that the approximation of a film floating in space (green line) is not a good one for the thin film on a substrate as the approximation consistently underestimates the absorption coefficient and even yields negative values below the band-gap. The single reflection approximation (orange line) is much closer

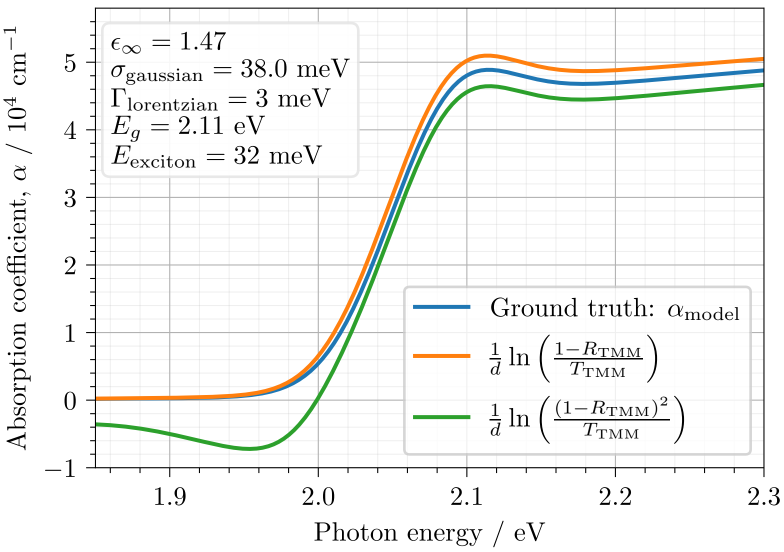

Figure C.1: Calculated absorption coefficient from the fit of the data in Figure 5.14 of the main text compared with the values given by two approximations from the R and T calculated using TMM.

to the ground truth and goes to zero below the band-gap although it slightly overestimates the absorption coefficient above the band-gap. For the analysis performed in this work the single reflection approximation was therefore chosen.

Inflection point determination

Once the pseudo absorption coefficient is calculated the inflection point can be found without the need for iterative fitting using the code below. Here a Savitzky–Golay filter is applied twice, first to get an estimate of the inflection point from the extrema of the first derivative and a second time to accurately determine the zero crossing of the second derivative. For the implementation of the Savitzky–Golay filter the `scipy.signal` library was used.

```
import numpy as np
from scipy.signal import savgol_filter

# Absorption coefficient data is stored in xarray called 'abs_coeff'
# ndarray of wavelengths
wave = abs_coeff.wavelength
# Shape of absorption coefficient data
nx = 24
ny = 24
n_wave = len(wave)
# Set any NaN values to 0
abs_coeff.values[np.isnan(abs_coeff.values)] = 0
# Get an estimate by the minium of the first derivative
max_guess = np.argmin(savgol_filter(abs_coeff.values, 243, 3, deriv=1, axis=2, mode='mirror'), axis=2)
# Calculate second derivative
abs_double_prime = savgol_filter(abs_coeff.values, 101, 3, deriv=2, axis=2, mode='mirror')
# Remove data that is not within 10 units of the max guess
filtered_data = abs_double_prime.copy().reshape(-1, n_wave)
filtered_data[np.logical_not(
    np.logical_and(
```

```
        (max_guess.reshape(-1) - 10)[:, np.newaxis] <= np.arange(n_wave),
        (max_guess.reshape(-1) + 10)[:, np.newaxis] > np.arange(n_wave)
    )
)] = 0
# Find all index where the second derivative changes sign
zero_crossings = np.where(np.abs(np.diff(np.sign(filtered_data), axis=1)) > 1)
# If there are multiple crossings, take the first one only
true_crossings, true_crossings_ind = np.unique(zero_crossings[0], return_index=True)
# Create array of NaNs to store the zero crossings
crossing_value = np.full(filtered_data.shape[0], np.nan)
# Store the value of the zero crossing
crossing_value[true_crossings] = wave[zero_crossings[1][true_crossings_ind]]
# Reshape back to original shape
abs_coeff_inflection = crossing_value.reshape(nx, ny)
```

C.3 Lattice Parameters

Here the calculation of the lattice parameters from three indexed peaks for a orthorombic lattice system is described.

For an orthorombic lattice system the lattice spacing d_{hkl} between hkl planes and corresponding scattering vector q_{hkl} is given by:

$$\frac{1}{d_{hkl}^2} = \frac{q_{hkl}^2}{4\pi^2} = \frac{h^2}{a^2} + \frac{k^2}{b^2} + \frac{l^2}{c^2}. \tag{C.1}$$

Let the inverse of the squares of the unknown lattice parameters be the column vector $X = [1/a^2, 1/b^2, 1/c^2]^T$. Using a set of three peaks with index $h_1k_1l_1$, $h_2k_2l_2$ and $h_3k_3l_3$ the set of equation formed using Equation C.1 can be written as a matrix multiplication $AX = Y$ where the element i of the column vector Y is $q_{h_ik_il_i}^2/4\pi^2$ and the row j of the matrix A is $[h_j^2, k_j^2, l_j^2]$. By multiplying with the inverse of A from the left the lattice parameter vector is given by $X = A^{-1}Y$. This has been implemented in the `Python` code below using the library `numpy`:

```
import numpy as np

def lattice_from_hkl(hkl: np.array, q: np.array) -> np.ndarray:
    """
    Function for calculating the lattice parameters a,b and c for a orthorombic lattice system
    from the positions of 3 indexed peaks.
    :param hkl: A 3 by 3 array with rows being the h,k an l of the peak
    :type hkl: np.ndarray
    :param q: A length 3 array of the scattering vector value for the specified peaks
    :type q: np.ndarray
    :return: An array of the a, b and c parameters in inverse q units
    :rtype: np.ndarray
    """
    if hkl.shape != (3, 3):
        raise ValueError('Shape of hkl matrix needs to be 3x3')
    elif len(q) != 3:
        raise ValueError('q needs to be length 3')
    q = q.reshape((3, 1))
    y = np.power(q / 2 / np.pi, 2)
    return 1 / np.sqrt(np.matmul(np.linalg.inv(np.power(hkl, 2)), y))
```

Appendix D

Additional Results

In this appendix, additional results on the temperature-dependent GIWAXS patterns used for determining the phase diagram in section 5.1 are shown as well as the estimated diffusion lengths and FF from subsection 5.2.7.

D.1 Estimated Diffusion Length & Fill Factor

Here the estimated values for the diffusion lengths, L_D, and fill factor, FF, are plotted as a function of Br content, x, and Cs content, y, $Cs_yPb_{1-y}(Br_xI_{1-x})_{2-y}$. The calculations behind the figures are explained in the main text in subsection 5.2.7.

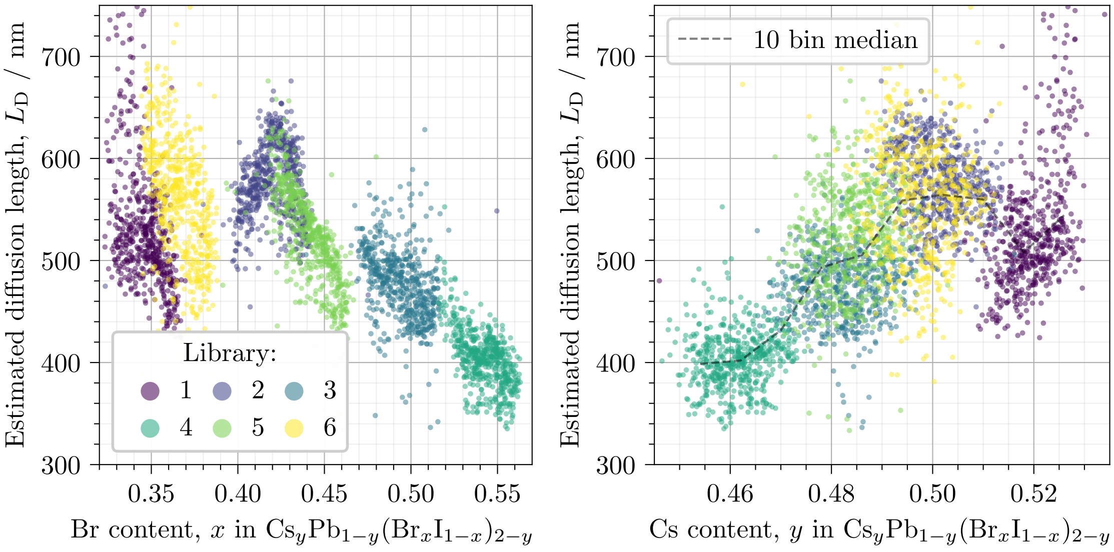

(a) Estimated L_D versus Br content x

(b) Estimated L_D versus Cs content y

Figure D.1: Estimated diffusion lengths, L_D, as a function of Br content, x, and Cs content, y, in $Cs_yPb_{1-y}(Br_xI_{1-x})_{2-y}$. The color of each sample indicates which library it belongs to. The estimate is based on a mobility of $\mu = 15$ cm^2/Vs and the effective lifetimes from Figure 5.19.

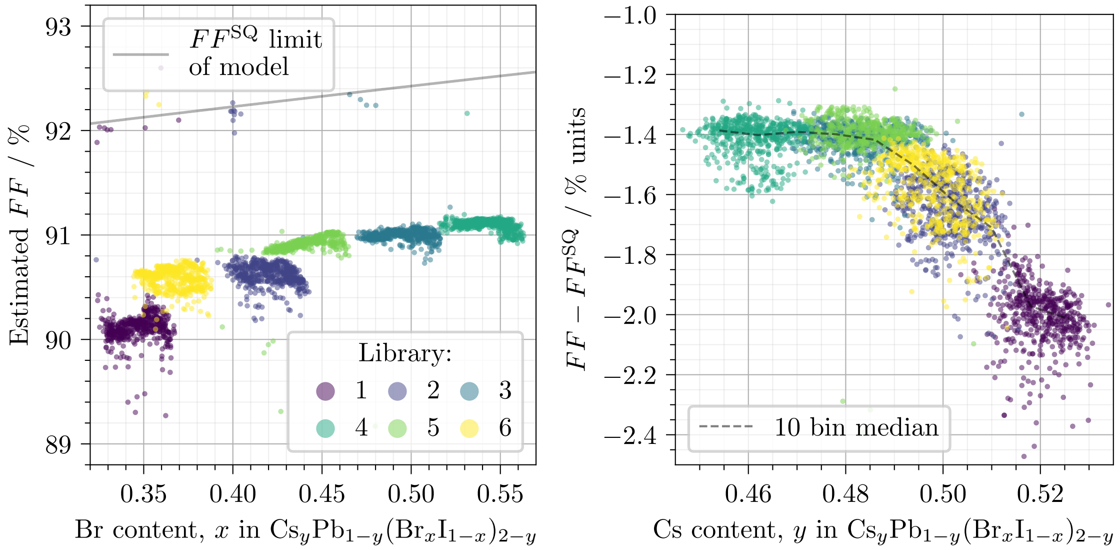

(a) Estimated FF versus Br content x (b) Estimated FF versus Cs content y

Figure D.2: Estimated FF as a function of Br content, x, and Cs content, y, in $\mathrm{Cs}_y\mathrm{Pb}_{1-y}(\mathrm{Br}_x\mathrm{I}_{1-x})_{2-y}$. The color of each sample indicates which library it belongs to. The gray line in (a) shows the limit of the FF assuming step-like absorptance at the band-gap from the bowing model in Figure 5.16. The values in (b) are plotted relative to this limit.

D.2 Temperature-dependent GIWAXS Patterns

Here, the temperature-dependent GIWAXS patterns of all samples in the combinatorially inkjet-printed library of $\mathrm{CsPb}(\mathrm{Br}_x\mathrm{I}_{1-x})_3$ are plotted as a function of the scattering vector, q, and the heating as well as cooling temperature in Figure D.3 to Figure D.11. Additionally, the patterns for the spin-coated sample with $x = 0.85$ and the blade-coated one with $x = 1$ are plotted in Figure D.12 and Figure D.13, respectively. In all figures the phase transitions are indicated by horizontal red lines and an example pattern of each phase at the indicated temperature is plotted in the right panes.

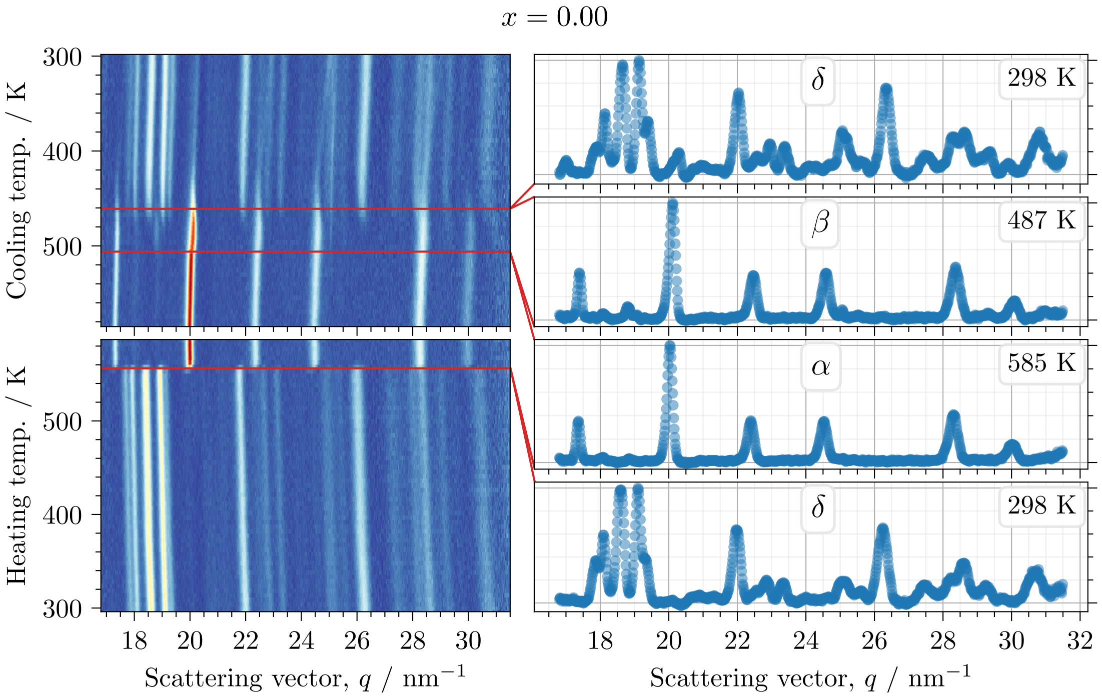

Figure D.3: Temperature-dependent GIWAXS patterns for $x = 0.00$.

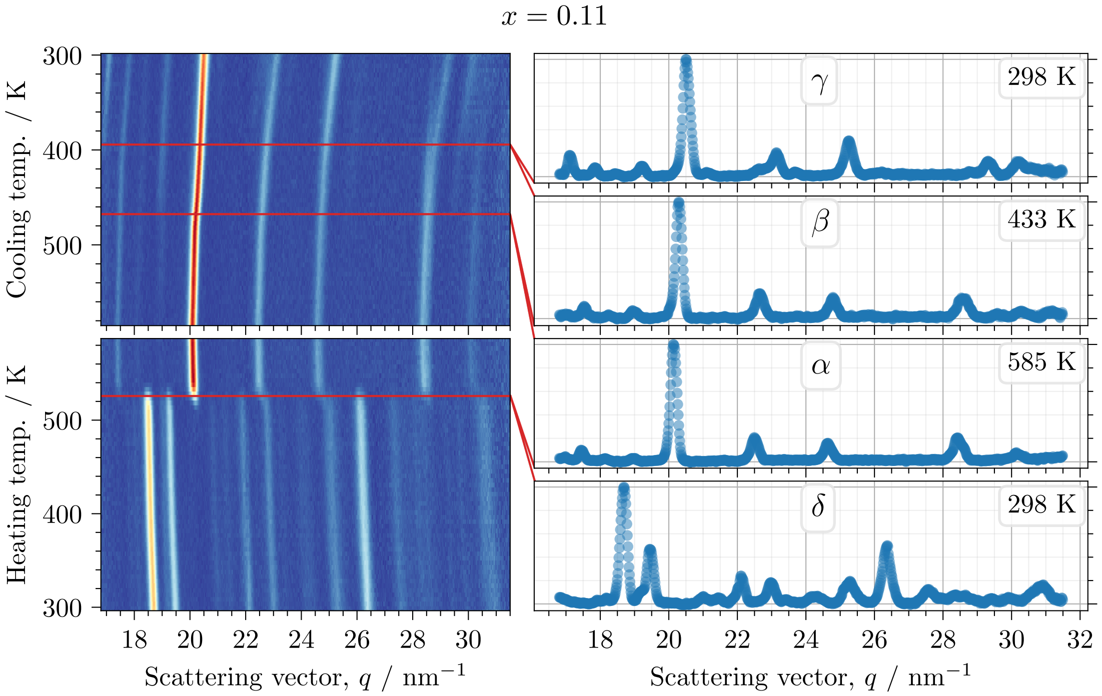

Figure D.4: Temperature-dependent GIWAXS patterns for $x = 0.11$.

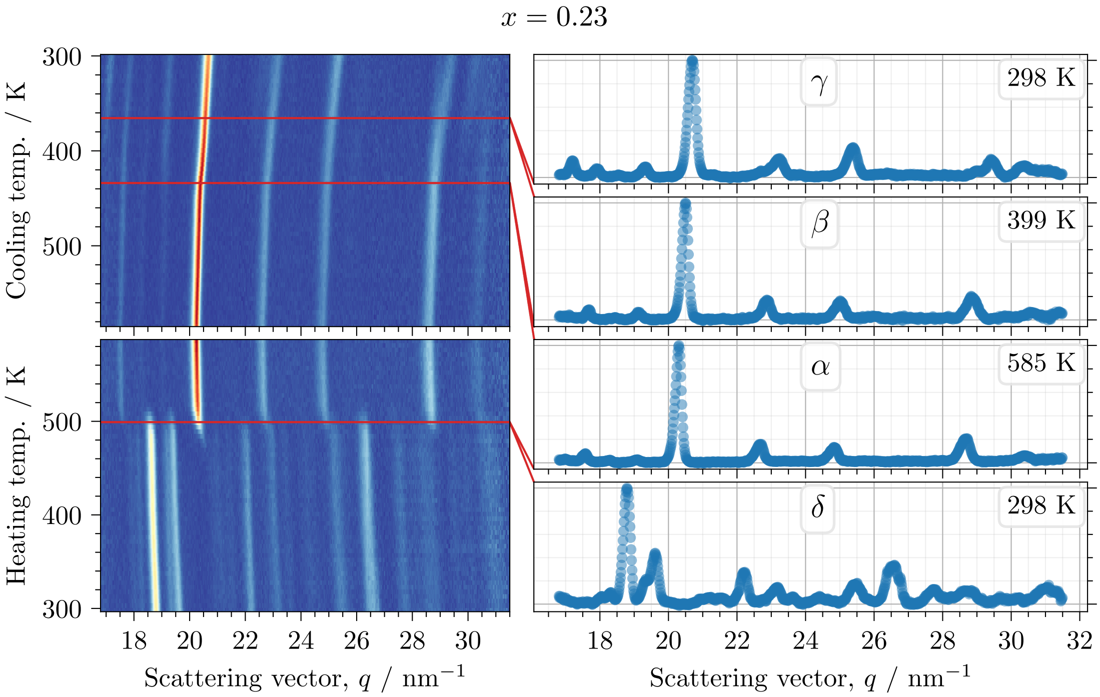

Figure D.5: Temperature-dependent GIWAXS patterns for $x = 0.23$.

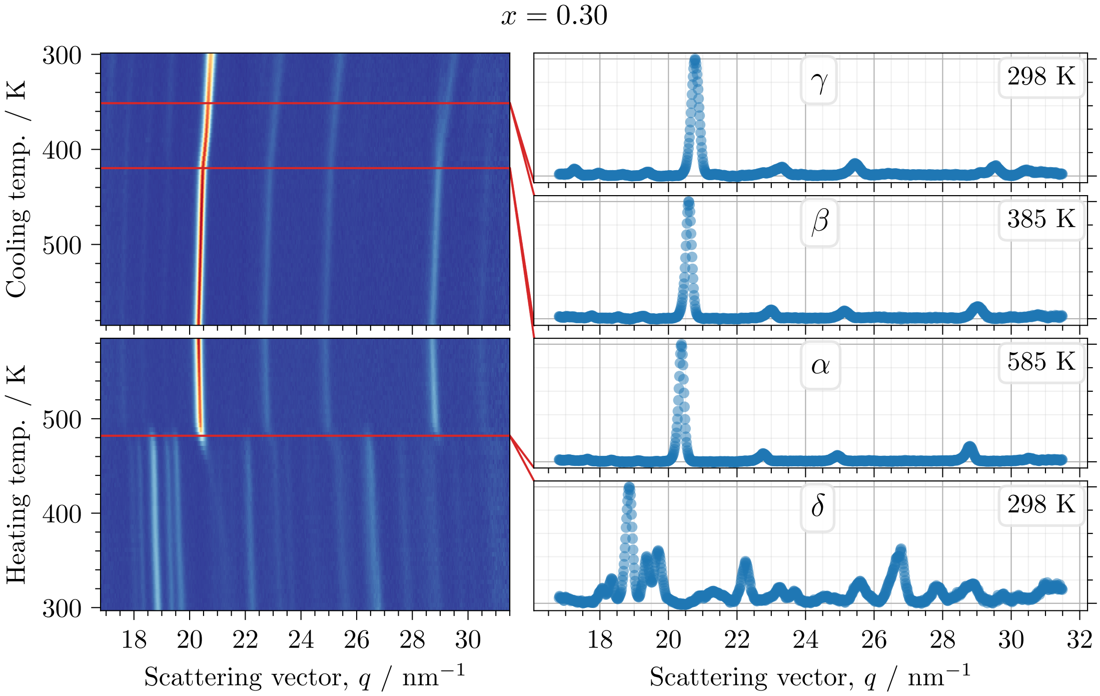

Figure D.6: Temperature-dependent GIWAXS patterns for $x = 0.30$.

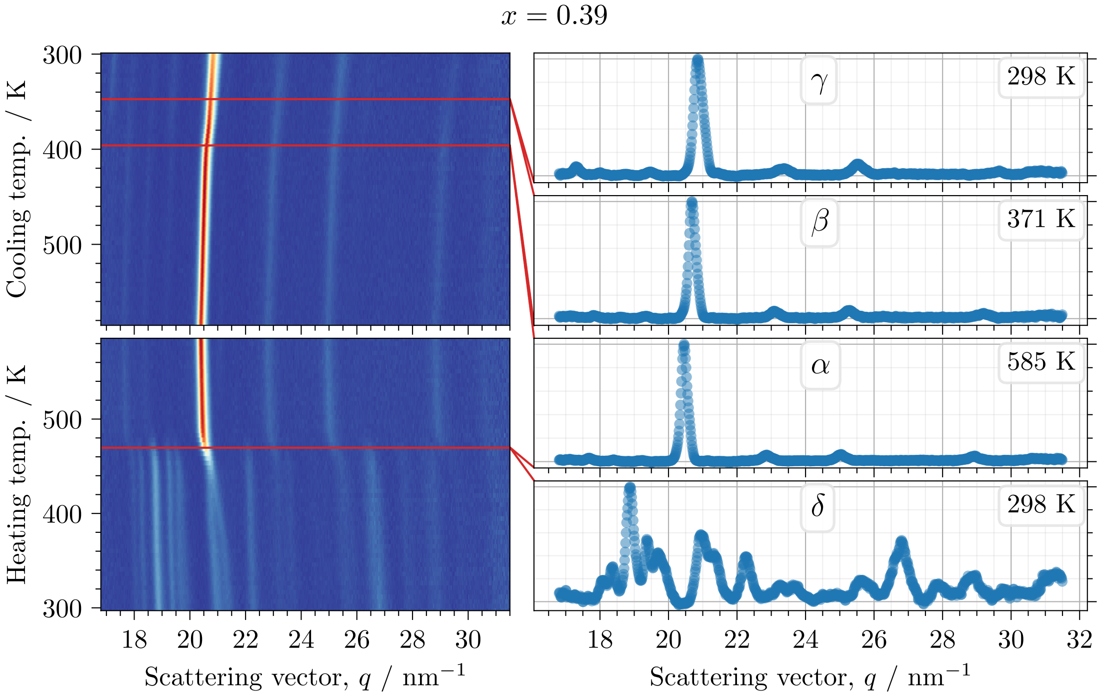

Figure D.7: Temperature-dependent GIWAXS patterns for $x = 0.39$.

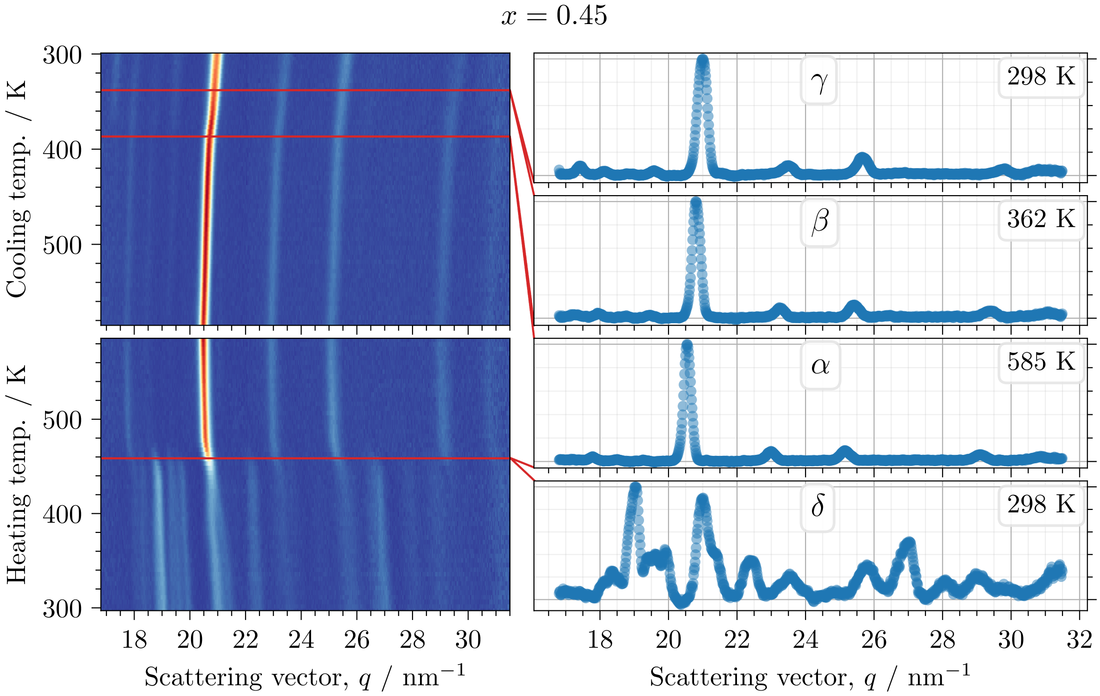

Figure D.8: Temperature-dependent GIWAXS patterns for $x = 0.45$.

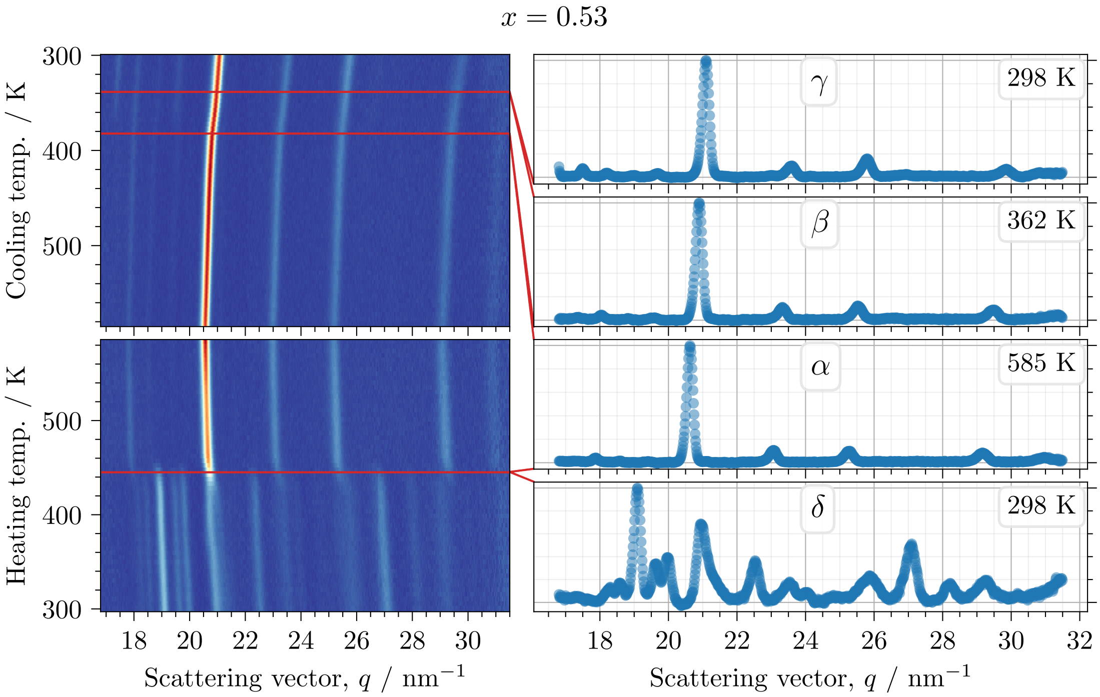

Figure D.9: Temperature-dependent GIWAXS patterns for $x = 0.53$.

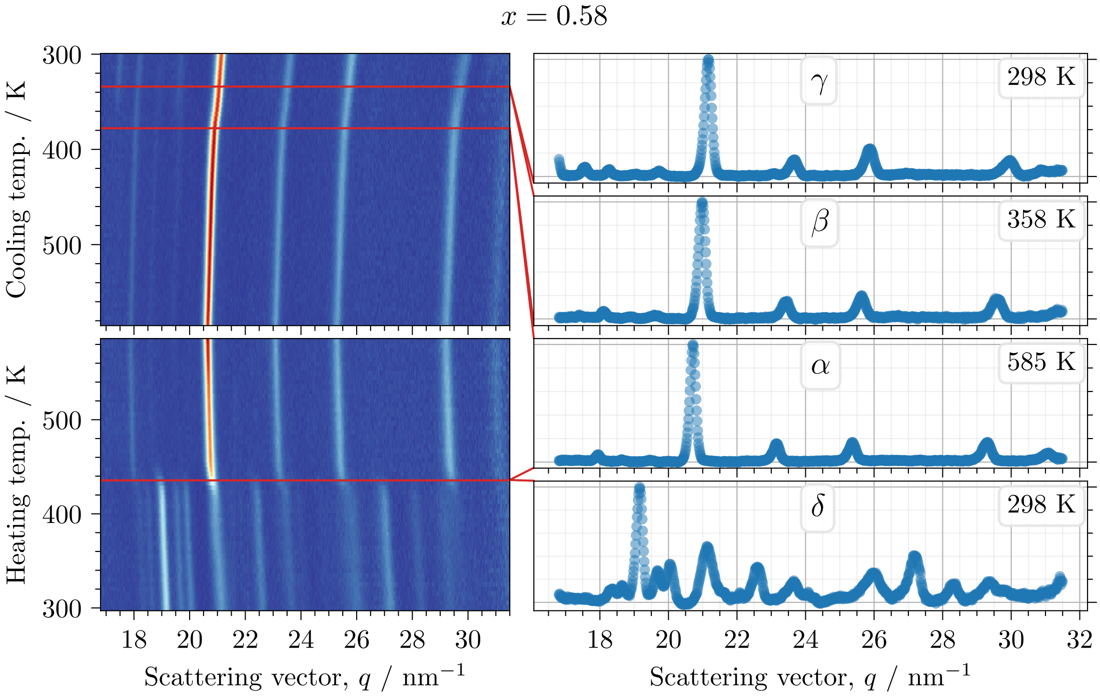

Figure D.10: Temperature-dependent GIWAXS patterns for $x = 0.58$.

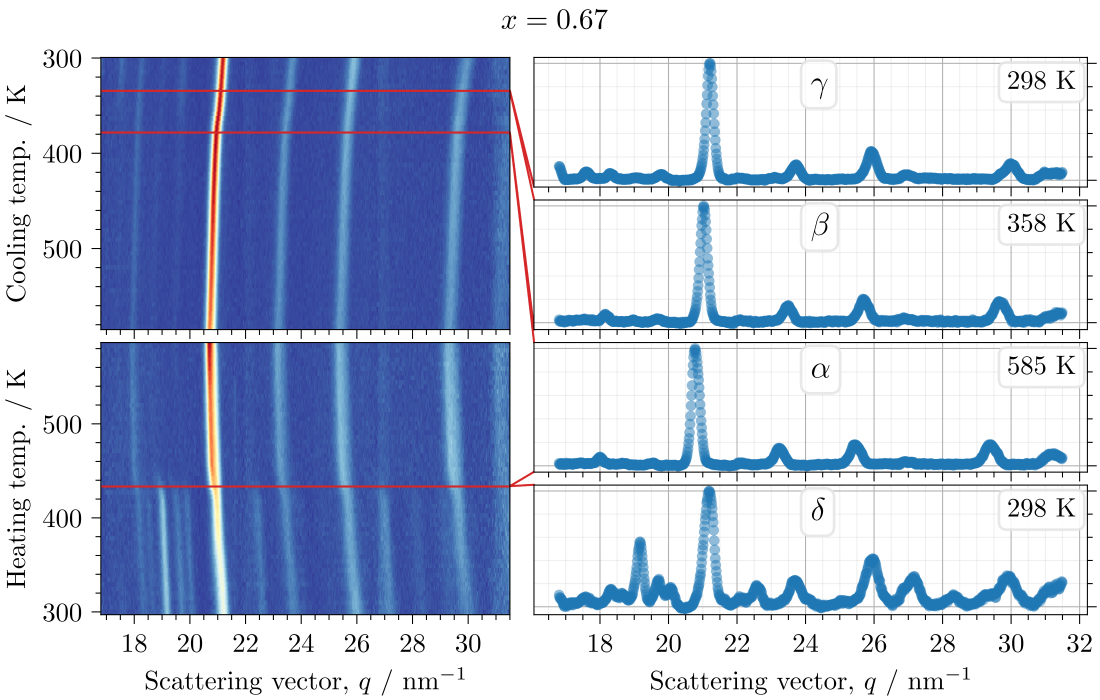

Figure D.11: Temperature-dependent GIWAXS patterns for $x = 0.67$.

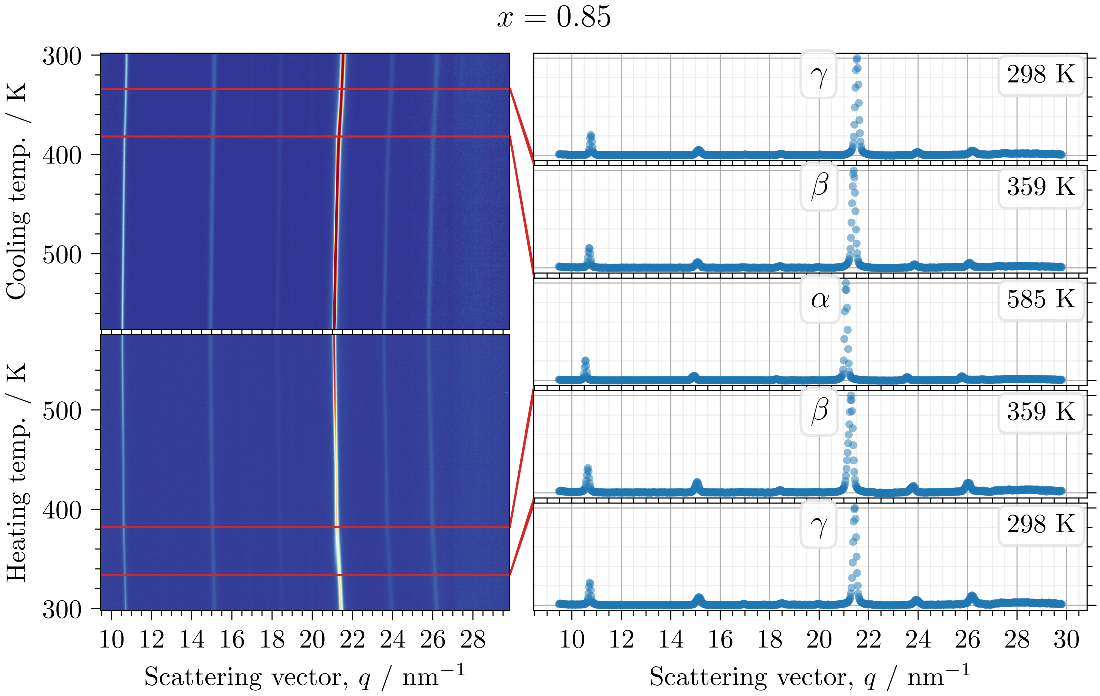

Figure D.12: Temperature-dependent GIWAXS patterns for $x = 0.85$.

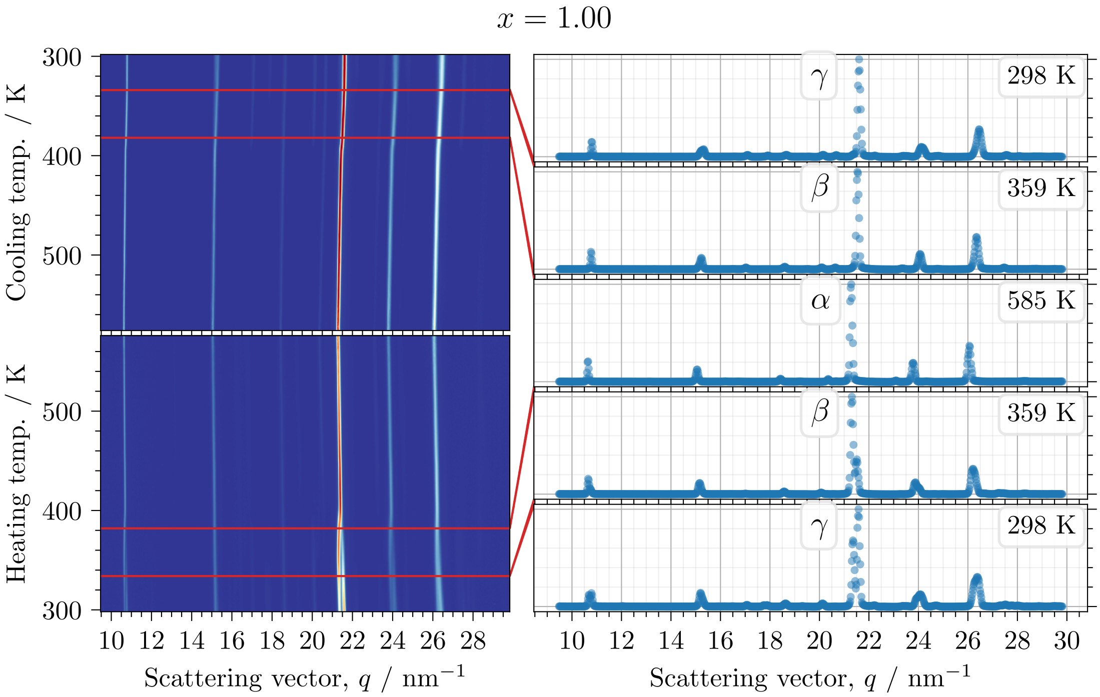

Figure D.13: Temperature-dependent GIWAXS patterns for $x = 1.00$.

Declaration of Independent Work

I declare that I have completed the thesis independently using only the aids and tools specified. I have not applied for a doctor's degree in the doctoral subject elsewhere and do not hold a corresponding doctor's degree. I have taken due note of the Faculty of Mathematics and Natural Sciences PhD Regulations, published in the Official Gazette of Humboldt-Universität zu Berlin no. 42/2018 on July 11th 2018.

Berlin, April 29th 2022

Hampus Näsström

Publications

First Author Publications

120. **Näsström**, **H.**, Shargaieva, O., Becker, P., Mathies, F., Zizak, I., Schröder, V. R. F., List-Kratochvil, E. J. W., Unold, T. & Unger, E. Combinatorial inkjet printing for compositional tuning of metal-halide perovskite thin films. *Journal of Materials Chemistry A* **10,** 4906–4914. doi:`10.1039/d1ta08841f` (Jan. 2022).
128. **Näsström**, **H.**, Becker, P., Márquez, J. A., Shargaieva, O., Mainz, R., Unger, E. & Unold, T. Dependence of phase transitions on halide ratio in inorganic $\mathrm{CsPb(Br}_x\mathrm{I}_{1-x})_3$ perovskite thin films obtained from high-throughput experimentation. *Journal of Materials Chemistry A* **8,** 22626–22631. doi:`10.1039/d0ta08067e` (Oct. 2020).

Co-Author Publications Cited in This Work

40. Jacobsson, T. J., Hultqvist, A., García-Fernández, A., Anand, A., Al-Ashouri, A., Hagfeldt, A., Crovetto, A., Abate, A., Ricciardulli, A. G., Vijayan, A., Kulkarni, A., Anderson, A. Y., Darwich, B. P., Yang, B., Coles, B. L., Perini, C. A. R., Rehermann, C., Ramirez, D., Fairen-Jimenez, D., Girolamo, D. D., Jia, D., Avila, E., Juarez-Perez, E. J., Baumann, F., Mathies, F., González, G. S. A., Boschloo, G., Nasti, G., Paramasivam, G., Martínez-Denegri, G., **Näsström**, **H.**, Michaels, H., Köbler, H., Wu, H., Benesperi, I., Dar, M. I., Pehlivan, I. B., Gould, I. E., Vagott, J. N., Dagar, J., Kettle, J., Yang, J., Li, J., Smith, J. A., Pascual, J., Jerónimo-Rendón, J. J., Montoya, J. F., Correa-Baena, J.-P., Qiu, J., Wang, J., Sveinbjörnsson, K., Hirselandt, K., Dey, K., Frohna, K., Mathies, L., Castriotta, L. A., Aldamasy, M. H., Vasquez-Montoya, M., Ruiz-Preciado, M. A., Flatken, M. A., Khenkin, M. V., Grischek, M., Kedia, M., Saliba, M., Anaya, M., Veldhoen, M., Arora, N., Shargaieva, O., Maus, O., Game, O. S., Yudilevich, O., Fassl, P., Zhou, Q., Betancur, R., Munir, R., Patidar, R., Stranks, S. D., Alam, S., Kar, S., Unold, T., Abzieher, T., Edvinsson, T., David, T. W., Paetzold, U. W., Zia, W., Fu, W., Zuo, W., Schröder, V. R. F., Tress, W., Zhang, X., Chiang, Y.-H., Iqbal, Z., Xie, Z. & Unger, E. An open-access database and analysis tool for perovskite solar cells

based on the FAIR data principles. *Nature Energy* **7,** 107–115. doi:10.1038/s41560-021-00941-3 (Dec. 2021).

54. Schröder, V. R. F., Hermerschmidt, F., Helper, S., Rehermann, C., Ligorio, G., **Näsström**, **H.**, Unger, E. L. & List-Kratochvil, E. J. W. Using Combinatorial Inkjet Printing for Synthesis and Deposition of Metal Halide Perovskites in Wavelength-Selective Photodetectors. *Advanced Engineering Materials,* 2101111. doi:10.1002/adem.202101111 (Dec. 2021).
55. Shargaieva, O., **Näsström**, **H.**, Li, J., Többens, D. M. & Unger, E. L. Temperature-Dependent Crystallization Mechanisms of Methylammonium Lead Iodide Perovskite From Different Solvents. *Frontiers in Energy Research* **9.** doi:10.3389/fenrg.2021.749604 (Nov. 2021).
64. Dagar, J., Fenske, M., Al-Ashouri, A., Schultz, C., Li, B., Köbler, H., Munir, R., Parmasivam, G., Li, J., Levine, I., Merdasa, A., Kegelmann, L., **Näsström**, **H.**, Marquez, J. A., Unold, T., Többens, D. M., Schlatmann, R., Stegemann, B., Abate, A., Albrecht, S. & Unger, E. Compositional and Interfacial Engineering Yield High-Performance and Stable p-i-n Perovskite Solar Cells and Mini-Modules. *ACS Applied Materials & Interfaces* **13,** 13022–13033. doi:10.1021/acsami.0c17893 (Mar. 2021).

Co-Author Publications Not Cited in This Work

143. Shargaieva, O., **Näsström**, **H.**, Smith, J. A., Többens, D., Munir, R. & Unger, E. Hybrid perovskite crystallization from binary solvent mixtures: interplay of evaporation rate and binding strength of solvents. *Materials Advances* **1,** 3314–3321. doi:10.1039/d0ma00815j (Nov. 2020).

Bibliography

1. Aspuru-Guzik, A. & Persson, K. *Materials Acceleration Platform: Accelerating Advanced Energy Materials Discovery by Integrating High-Throughput Methods and Artificial Intelligence. Mission Innovation: Innovation Challenge 6.* Report (Jan. 2018). `http://nrs.harvard.edu/urn-3:HUL.InstRepos:35164974`.
2. Maier, W. F. Early Years of High-Throughput Experimentation and Combinatorial Approaches in Catalysis and Materials Science. *ACS Combinatorial Science* **21,** 437–444. doi:`10.1021/acscombsci.8b00189` (Apr. 2019).
3. Macarron, R., Banks, M. N., Bojanic, D., Burns, D. J., Cirovic, D. A., Garyantes, T., Green, D. V. S., Hertzberg, R. P., Janzen, W. P., Paslay, J. W., Schopfer, U. & Sittampalam, G. S. Impact of high-throughput screening in biomedical research. *Nature Reviews Drug Discovery* **10,** 188–195. doi:`10.1038/nrd3368` (Mar. 2011).
4. Chung, I., Lee, B., He, J., Chang, R. P. H. & Kanatzidis, M. G. All-solid-state dye-sensitized solar cells with high efficiency. *Nature* **485,** 486–489. doi:`10.1038/nature11067` (May 2012).
5. Tan, Z.-K., Moghaddam, R. S., Lai, M. L., Docampo, P., Higler, R., Deschler, F., Price, M., Sadhanala, A., Pazos, L. M., Credgington, D., Hanusch, F., Bein, T., Snaith, H. J. & Friend, R. H. Bright light-emitting diodes based on organometal halide perovskite. *Nature Nanotechnology* **9,** 687–692. doi:`10.1038/nnano.2014.149` (Aug. 2014).
6. Xing, G., Mathews, N., Lim, S. S., Yantara, N., Liu, X., Sabba, D., Grätzel, M., Mhaisalkar, S. & Sum, T. C. Low-temperature solution-processed wavelength-tunable perovskites for lasing. *Nature Materials* **13,** 476–480. doi:`10.1038/nmat3911` (Mar. 2014).
7. Dou, L., Yang, Y. (, You, J., Hong, Z., Chang, W.-H., Li, G. & Yang, Y. Solution-processed hybrid perovskite photodetectors with high detectivity. *Nature Communications* **5.** doi:`10.1038/ncomms6404` (Nov. 2014).
8. Sze, S. M. & Lee, M.-K. *Semiconductor Devices: Physics and Technology* 3rd. International Student Version. ISBN: 978-0-470-87367-0 (John Wiley & Sons Singapore Pte. Ltd, Singapore, 2013).

9. Haug, H. & Koch, S. W. *Quantum Theory of the Optical and Electronic Properties of Semiconductors* doi:10.1142/7184 (WORLD SCIENTIFIC, Jan. 2009).
10. Soufiani, A. M., Huang, F., Reece, P., Sheng, R., Ho-Baillie, A. & Green, M. A. Polaronic exciton binding energy in iodide and bromide organic-inorganic lead halide perovskites. *Applied Physics Letters* **107,** 231902. doi:10.1063/1.4936418 (Dec. 2015).
11. Davies, C. L., Filip, M. R., Patel, J. B., Crothers, T. W., Verdi, C., Wright, A. D., Milot, R. L., Giustino, F., Johnston, M. B. & Herz, L. M. Bimolecular recombination in methylammonium lead triiodide perovskite is an inverse absorption process. *Nature Communications* **9.** doi:10.1038/s41467-017-02670-2 (Jan. 2018).
12. Wannier, G. H. The Structure of Electronic Excitation Levels in Insulating Crystals. *Physical Review* **52,** 191–197. doi:10.1103/physrev.52.191 (Aug. 1937).
13. Elliott, R. J. Intensity of Optical Absorption by Excitons. *Physical Review* **108,** 1384–1389. doi:10.1103/physrev.108.1384 (Dec. 1957).
14. Tanguy, C. Optical Dispersion by Wannier Excitons. *Physical Review Letters* **75,** 4090–4093. doi:10.1103/physrevlett.75.4090 (Nov. 1995).
15. Byrnes, S. J. *Multilayer optical calculations* 2016. doi:10.48550/ARXIV.1603.02720.
16. Sha, W. E. I., Zhang, H., Wang, Z. S., Zhu, H. L., Ren, X., Lin, F., Jen, A. K.-Y. & Choy, W. C. H. Quantifying Efficiency Loss of Perovskite Solar Cells by a Modified Detailed Balance Model. *Advanced Energy Materials* **8,** 1701586. doi:10.1002/aenm.201701586 (Dec. 2017).
17. Chen, J. & Park, N.-G. Causes and Solutions of Recombination in Perovskite Solar Cells. *Advanced Materials* **31,** 1803019. doi:10.1002/adma.201803019 (Sept. 2018).
18. Shockley, W. & Read, W. T. Statistics of the Recombinations of Holes and Electrons. *Physical Review* **87,** 835–842. doi:10.1103/physrev.87.835 (Sept. 1952).
19. Hall, R. N. Electron-Hole Recombination in Germanium. *Physical Review* **87,** 387–387. doi:10.1103/physrev.87.387 (July 1952).
20. Würfel, P. *Physics of Solar Cells: From Principles to New Concepts* doi:10.1002/9783527618545 (Wiley, Jan. 2005).
21. Green, M. A. Solar cell fill factors: General graph and empirical expressions. *Solid-State Electronics* **24,** 788–789. doi:10.1016/0038-1101(81)90062-9 (Aug. 1981).
22. Shockley, W. & Queisser, H. J. Detailed Balance Limit of Efficiency of p-n Junction Solar Cells. *Journal of Applied Physics* **32,** 510–519. doi:10.1063/1.1736034 (Mar. 1961).

23. Rau, U. Reciprocity relation between photovoltaic quantum efficiency and electroluminescent emission of solar cells. *Physical Review B* **76,** 085303. doi:`10.1103/physrevb.76.085303` (Aug. 2007).
24. Kirchartz, T., Rau, U., Kurth, M., Mattheis, J. & Werner, J. Comparative study of electroluminescence from Cu(In,Ga)Se2 and Si solar cells. *Thin Solid Films* **515,** 6238–6242. doi:`10.1016/j.tsf.2006.12.105` (May 2007).
25. Ross, R. T. Some Thermodynamics of Photochemical Systems. *The Journal of Chemical Physics* **46,** 4590–4593. doi:`10.1063/1.1840606` (June 1967).
26. Krückemeier, L., Rau, U., Stolterfoht, M. & Kirchartz, T. How to Report Record Open-Circuit Voltages in Lead-Halide Perovskite Solar Cells. *Advanced Energy Materials* **10,** 1902573. doi:`10.1002/aenm.201902573` (Nov. 2019).
27. NREL. *Reference Air Mass 1.5 Spectra* `https://www.nrel.gov/grid/solar-resource/spectra-am1.5.html` (2022).
28. Hörantner, M. T., Leijtens, T., Ziffer, M. E., Eperon, G. E., Christoforo, M. G., McGehee, M. D. & Snaith, H. J. The Potential of Multijunction Perovskite Solar Cells. *ACS Energy Letters* **2,** 2506–2513. doi:`10.1021/acsenergylett.7b00647` (Oct. 2017).
29. Rose, G. Über einige neue Mineralien des Urals. *Journal für Praktische Chemie* **19,** 459–468. doi:`10.1002/prac.18400190179` (1840).
30. Goldschmidt, V. M. Die Gesetze der Krystallochemie. *Naturwissenschaften* **14,** 477–485. doi:`10.1007/bf01507527` (May 1926).
31. Breternitz, J. & Schorr, S. What Defines a Perovskite? *Advanced Energy Materials* **8,** 1802366. doi:`10.1002/aenm.201802366` (Oct. 2018).
32. Momma, K. & Izumi, F. VESTA 3 for three-dimensional visualization of crystal, volumetric and morphology data. *Journal of Applied Crystallography* **44,** 1272–1276. doi:`10.1107/s0021889811038970` (Oct. 2011).
33. Wells, H. L. On the caesium- and the potassium-lead halides. *American Journal of Science* **s3-45,** 121–134. doi:`10.2475/ajs.s3-45.266.121` (Feb. 1893).
34. Møller, C. K. Crystal Structure and Photoconductivity of Cæsium Plumbohalides. *Nature* **182,** 1436–1436. doi:`10.1038/1821436a0` (Nov. 1958).
35. Weber, D. $CH_3NH_3SnBr_xI_{3-x}$ ($x = 0 - 3$), ein Sn(II)-System mit kubischer Perowskitstruktur / $CH_3NH_3SnBr_xI_{3-x}$ ($x = 0 - 3$), a Sn(II)-System with Cubic Perovskite Structure. *Zeitschrift für Naturforschung B* **33,** 862–865. doi:`10.1515/znb-1978-0809` (Aug. 1978).
36. Weber, D. $CH_3NH_3PbX_3$, ein Pb(II)-System mit kubischer Perowskitstruktur / $CH_3NH_3PbX_3$, a Pb(II)-System with Cubic Perovskite Structure. *Zeitschrift für Naturforschung B* **33,** 1443–1445. doi:`10.1515/znb-1978-1214` (Dec. 1978).
37. Kojima, A., Teshima, K., Shirai, Y. & Miyasaka, T. Organometal Halide Perovskites as Visible-Light Sensitizers for Photovoltaic Cells. *Journal of the*

American Chemical Society **131,** 6050–6051. doi:10.1021/ja809598r (Apr. 2009).

38. Mitzi, D. B., Wang, S., Feild, C. A., Chess, C. A. & Guloy, A. M. Conducting Layered Organic-inorganic Halides Containing 110-Oriented Perovskite Sheets. *Science* **267,** 1473–1476. doi:10.1126/science.267.5203.1473 (Mar. 1995).
39. Kim, H.-S., Lee, C.-R., Im, J.-H., Lee, K.-B., Moehl, T., Marchioro, A., Moon, S.-J., Humphry-Baker, R., Yum, J.-H., Moser, J. E., Grätzel, M. & Park, N.-G. Lead Iodide Perovskite Sensitized All-Solid-State Submicron Thin Film Mesoscopic Solar Cell with Efficiency Exceeding 9%. *Scientific Reports* **2.** doi:10.1038/srep00591 (Aug. 2012).
40. Jacobsson, T. J., Hultqvist, A., García-Fernández, A., Anand, A., Al-Ashouri, A., Hagfeldt, A., Crovetto, A., Abate, A., Ricciardulli, A. G., Vijayan, A., Kulkarni, A., Anderson, A. Y., Darwich, B. P., Yang, B., Coles, B. L., Perini, C. A. R., Rehermann, C., Ramirez, D., Fairen-Jimenez, D., Girolamo, D. D., Jia, D., Avila, E., Juarez-Perez, E. J., Baumann, F., Mathies, F., González, G. S. A., Boschloo, G., Nasti, G., Paramasivam, G., Martínez-Denegri, G., **Näsström, H.**, Michaels, H., Köbler, H., Wu, H., Benesperi, I., Dar, M. I., Pehlivan, I. B., Gould, I. E., Vagott, J. N., Dagar, J., Kettle, J., Yang, J., Li, J., Smith, J. A., Pascual, J., Jerónimo-Rendón, J. J., Montoya, J. F., Correa-Baena, J.-P., Qiu, J., Wang, J., Sveinbjörnsson, K., Hirselandt, K., Dey, K., Frohna, K., Mathies, L., Castriotta, L. A., Aldamasy, M. H., Vasquez-Montoya, M., Ruiz-Preciado, M. A., Flatken, M. A., Khenkin, M. V., Grischek, M., Kedia, M., Saliba, M., Anaya, M., Veldhoen, M., Arora, N., Shargaieva, O., Maus, O., Game, O. S., Yudilevich, O., Fassl, P., Zhou, Q., Betancur, R., Munir, R., Patidar, R., Stranks, S. D., Alam, S., Kar, S., Unold, T., Abzieher, T., Edvinsson, T., David, T. W., Paetzold, U. W., Zia, W., Fu, W., Zuo, W., Schröder, V. R. F., Tress, W., Zhang, X., Chiang, Y.-H., Iqbal, Z., Xie, Z. & Unger, E. An open-access database and analysis tool for perovskite solar cells based on the FAIR data principles. *Nature Energy* **7,** 107–115. doi:10.1038/s41560-021-00941-3 (Dec. 2021).
41. NREL. *Best Research-Cell Efficiency Chart* `https://www.nrel.gov/pv/cell-efficiency.html` (2022).
42. Song, Z., Watthage, S. C., Phillips, A. B., Tompkins, B. L., Ellingson, R. J. & Heben, M. J. Impact of Processing Temperature and Composition on the Formation of Methylammonium Lead Iodide Perovskites. *Chemistry of Materials* **27,** 4612–4619. doi:10.1021/acs.chemmater.5b01017 (June 2015).
43. Nickel, N. H., Lang, F., Brus, V. V., Shargaieva, O. & Rappich, J. Unraveling the Light-Induced Degradation Mechanisms of CH3NH3PbI3Perovskite Films. *Advanced Electronic Materials* **3,** 1700158. doi:10.1002/aelm.201700158 (Nov. 2017).
44. Juarez-Perez, E. J., Ono, L. K., Maeda, M., Jiang, Y., Hawash, Z. & Qi, Y. Photodecomposition and thermal decomposition in methylammonium halide

lead perovskites and inferred design principles to increase photovoltaic device stability. *Journal of Materials Chemistry A* **6,** 9604–9612. doi:10.1039/c8ta03501f (Apr. 2018).

45. Eperon, G. E., Paternò, G. M., Sutton, R. J., Zampetti, A., Haghighirad, A. A., Cacialli, F. & Snaith, H. J. Inorganic caesium lead iodide perovskite solar cells. *Journal of Materials Chemistry A* **3,** 19688–19695. doi:10.1039/c5ta06398a (Sept. 2015).
46. Choi, H., Jeong, J., Kim, H.-B., Kim, S., Walker, B., Kim, G.-H. & Kim, J. Y. Cesium-doped methylammonium lead iodide perovskite light absorber for hybrid solar cells. *Nano Energy* **7,** 80–85. doi:10.1016/j.nanoen.2014.04.017 (July 2014).
47. Ye, Q., Zhao, Y., Mu, S., Ma, F., Gao, F., Chu, Z., Yin, Z., Gao, P., Zhang, X. & You, J. Cesium Lead Inorganic Solar Cell with Efficiency beyond 18% via Reduced Charge Recombination. *Advanced Materials* **31,** 1905143. doi:10.1002/adma.201905143 (Oct. 2019).
48. Al-Ashouri, A., Köhnen, E., Li, B., Magomedov, A., Hempel, H., Caprioglio, P., Márquez, J. A., Vilches, A. B. M., Kasparavicius, E., Smith, J. A., Phung, N., Menzel, D., Grischek, M., Kegelmann, L., Skroblin, D., Gollwitzer, C., Malinauskas, T., Jošt, M., Matič, G., Rech, B., Schlatmann, R., Topič, M., Korte, L., Abate, A., Stannowski, B., Neher, D., Stolterfoht, M., Unold, T., Getautis, V. & Albrecht, S. Monolithic perovskite/silicon tandem solar cell with $> 29\,\%$ efficiency by enhanced hole extraction. *Science* **370,** 1300–1309. doi:10.1126/science.abd4016 (Dec. 2020).
49. Hermerschmidt, F., Mathies, F., Schröder, V. R. F., Rehermann, C., Morales, N. Z., Unger, E. L. & List-Kratochvil, E. J. W. Finally, inkjet-printed metal halide perovskite LEDs – utilizing seed crystal templating of salty PEDOT:PSS. *Materials Horizons* **7,** 1773–1781. doi:10.1039/d0mh00512f (May 2020).
50. Deschler, F., Price, M., Pathak, S., Klintberg, L. E., Jarausch, D.-D., Higler, R., Hüttner, S., Leijtens, T., Stranks, S. D., Snaith, H. J., Atatüre, M., Phillips, R. T. & Friend, R. H. High Photoluminescence Efficiency and Optically Pumped Lasing in Solution-Processed Mixed Halide Perovskite Semiconductors. *The Journal of Physical Chemistry Letters* **5,** 1421–1426. doi:10.1021/jz5005285 (Apr. 2014).
51. Mathies, F., Brenner, P., Hernandez-Sosa, G., Howard, I. A., Paetzold, U. W. & Lemmer, U. Inkjet-printed perovskite distributed feedback lasers. *Optics Express* **26,** A144. doi:10.1364/oe.26.00a144 (Jan. 2018).
52. Wei, H., Fang, Y., Mulligan, P., Chuirazzi, W., Fang, H.-H., Wang, C., Ecker, B. R., Gao, Y., Loi, M. A., Cao, L. & Huang, J. Sensitive X-ray detectors made of methylammonium lead tribromide perovskite single crystals. *Nature Photonics* **10,** 333–339. doi:10.1038/nphoton.2016.41 (Mar. 2016).
53. Basiricò, L., Ciavatti, A. & Fraboni, B. Solution-Grown Organic and Perovskite X-Ray Detectors: A New Paradigm for the Direct Detection of Ioniz-

ing Radiation. *Advanced Materials Technologies* **6,** 2000475. doi:10.1002/admt.202000475 (Aug. 2020).

54. Schröder, V. R. F., Hermerschmidt, F., Helper, S., Rehermann, C., Ligorio, G., **Näsström, H.**, Unger, E. L. & List-Kratochvil, E. J. W. Using Combinatorial Inkjet Printing for Synthesis and Deposition of Metal Halide Perovskites in Wavelength-Selective Photodetectors. *Advanced Engineering Materials,* 2101111. doi:10.1002/adem.202101111 (Dec. 2021).
55. Shargaieva, O., **Näsström, H.**, Li, J., Többens, D. M. & Unger, E. L. Temperature-Dependent Crystallization Mechanisms of Methylammonium Lead Iodide Perovskite From Different Solvents. *Frontiers in Energy Research* **9.** doi:10.3389/fenrg.2021.749604 (Nov. 2021).
56. Unger, E. L., Shargaieva, O., Braunger, S. & Docampo, P. in *Solar Energy Capture Materials* 153–192 (The Royal Society of Chemistry, 2019). ISBN: 978-1-78801-107-5. doi:10.1039/9781788013512-00153.
57. Prochowicz, D., Franckevičius, M., Cieślak, A. M., Zakeeruddin, S. M., Grätzel, M. & Lewiński, J. Mechanosynthesis of the hybrid perovskite $CH_3NH_3PbI_3$: characterization and the corresponding solar cell efficiency. *Journal of Materials Chemistry A* **3,** 20772–20777. doi:10.1039/c5ta04904k (Aug. 2015).
58. Liu, M., Johnston, M. B. & Snaith, H. J. Efficient planar heterojunction perovskite solar cells by vapour deposition. *Nature* **501,** 395–398. doi:10.1038/nature12509 (Sept. 2013).
59. Lin, Q., Armin, A., Nagiri, R. C. R., Burn, P. L. & Meredith, P. Electro-optics of perovskite solar cells. *Nature Photonics* **9,** 106–112. doi:10.1038/nphoton.2014.284 (Dec. 2014).
60. Momblona, C., Gil-Escrig, L., Bandiello, E., Hutter, E. M., Sessolo, M., Lederer, K., Blochwitz-Nimoth, J. & Bolink, H. J. Efficient vacuum deposited p-i-n and n-i-p perovskite solar cells employing doped charge transport layers. *Energy & Environmental Science* **9,** 3456–3463. doi:10.1039/c6ee02100j (Sept. 2016).
61. Chen, C.-Y., Lin, H.-Y., Chiang, K.-M., Tsai, W.-L., Huang, Y.-C., Tsao, C.-S. & Lin, H.-W. All-Vacuum-Deposited Stoichiometrically Balanced Inorganic Cesium Lead Halide Perovskite Solar Cells with Stabilized Efficiency Exceeding 11%. *Advanced Materials* **29,** 1605290. doi:10.1002/adma.201605290 (Jan. 2017).
62. Pérez-del-Rey, D., Boix, P. P., Sessolo, M., Hadipour, A. & Bolink, H. J. Interfacial Modification for High-Efficiency Vapor-Phase-Deposited Perovskite Solar Cells Based on a Metal Oxide Buffer Layer. *The Journal of Physical Chemistry Letters* **9,** 1041–1046. doi:10.1021/acs.jpclett.7b03361 (Feb. 2018).
63. Lin, H.-Y., Chen, C.-Y., Hsu, B.-W., Cheng, Y.-L., Tsai, W.-L., Huang, Y.-C., Tsao, C.-S. & Lin, H.-W. Efficient Cesium Lead Halide Perovskite Solar Cells through Alternative Thousand-Layer Rapid Deposition. *Advanced Functional Materials* **29,** 1905163. doi:10.1002/adfm.201905163 (Aug. 2019).

64. Dagar, J., Fenske, M., Al-Ashouri, A., Schultz, C., Li, B., Köbler, H., Munir, R., Parmasivam, G., Li, J., Levine, I., Merdasa, A., Kegelmann, L., **Näsström, H.**, Marquez, J. A., Unold, T., Többens, D. M., Schlatmann, R., Stegemann, B., Abate, A., Albrecht, S. & Unger, E. Compositional and Interfacial Engineering Yield High-Performance and Stable p-i-n Perovskite Solar Cells and Mini-Modules. *ACS Applied Materials & Interfaces* **13,** 13022–13033. doi:`10.1021/acsami.0c17893` (Mar. 2021).
65. Yoo, J. J., Seo, G., Chua, M. R., Park, T. G., Lu, Y., Rotermund, F., Kim, Y.-K., Moon, C. S., Jeon, N. J., Correa-Baena, J.-P., Bulović, V., Shin, S. S., Bawendi, M. G. & Seo, J. Efficient perovskite solar cells via improved carrier management. *Nature* **590,** 587–593. doi:`10.1038/s41586-021-03285-w` (Feb. 2021).
66. Li, S.-G., Jiang, K.-J., Su, M.-J., Cui, X.-P., Huang, J.-H., Zhang, Q.-Q., Zhou, X.-Q., Yang, L.-M. & Song, Y.-L. Inkjet printing of $CH_3NH_3PbI_3$ on a mesoscopic TiO_2 film for highly efficient perovskite solar cells. *Journal of Materials Chemistry A* **3,** 9092–9097. doi:`10.1039/c4ta05675b` (Dec. 2015).
67. Mathies, F., Abzieher, T., Hochstuhl, A., Glaser, K., Colsmann, A., Paetzold, U. W., Hernandez-Sosa, G., Lemmer, U. & Quintilla, A. Multipass inkjet printed planar methylammonium lead iodide perovskite solar cells. *Journal of Materials Chemistry A* **4,** 19207–19213. doi:`10.1039/c6ta07972e` (Nov. 2016).
68. Hashmi, S. G., Martineau, D., Li, X., Ozkan, M., Tiihonen, A., Dar, M. I., Sarikka, T., Zakeeruddin, S. M., Paltakari, J., Lund, P. D. & Grätzel, M. Air Processed Inkjet Infiltrated Carbon Based Printed Perovskite Solar Cells with High Stability and Reproducibility. *Advanced Materials Technologies* **2,** 1600183. doi:`10.1002/admt.201600183` (Nov. 2016).
69. Mathies, F., Eggers, H., Richards, B. S., Hernandez-Sosa, G., Lemmer, U. & Paetzold, U. W. Inkjet-Printed Triple Cation Perovskite Solar Cells. *ACS Applied Energy Materials* **1,** 1834–1839. doi:`10.1021/acsaem.8b00222` (Apr. 2018).
70. Li, P., Liang, C., Bao, B., Li, Y., Hu, X., Wang, Y., Zhang, Y., Li, F., Shao, G. & Song, Y. Inkjet manipulated homogeneous large size perovskite grains for efficient and large-area perovskite solar cells. *Nano Energy* **46,** 203–211. doi:`10.1016/j.nanoen.2018.01.049` (Apr. 2018).
71. Gheno, A., Huang, Y., Bouclé, J., Ratier, B., Rolland, A., Even, J. & Vedraine, S. Toward Highly Efficient Inkjet-Printed Perovskite Solar Cells Fully Processed Under Ambient Conditions and at Low Temperature. *Solar RRL* **2,** 1800191. doi:`10.1002/solr.201800191` (Oct. 2018).
72. Liang, C., Li, P., Gu, H., Zhang, Y., Li, F., Song, Y., Shao, G., Mathews, N. & Xing, G. One-Step Inkjet Printed Perovskite in Air for Efficient Light Harvesting. *Solar RRL* **2,** 1700217. doi:`10.1002/solr.201700217` (Jan. 2018).
73. Prajongtat, P., Sriprachuabwong, C., Wongkanya, R., Dechtrirat, D., Sudchanham, J., Srisamran, N., Sangthong, W., Chuysinuan, P., Tuantranont,

A., Hannongbua, S. & Chattham, N. Moisture-Resistant Electrospun Polymer Membranes for Efficient and Stable Fully Printable Perovskite Solar Cells Prepared in Humid Air. *ACS Applied Materials & Interfaces* **11,** 27677–27685. doi:10.1021/acsami.9b05032 (July 2019).

74. Eggers, H., Schackmar, F., Abzieher, T., Sun, Q., Lemmer, U., Vaynzof, Y., Richards, B. S., Hernandez-Sosa, G. & Paetzold, U. W. Inkjet-Printed Micrometer-Thick Perovskite Solar Cells with Large Columnar Grains. *Advanced Energy Materials* **10,** 1903184. doi:10.1002/aenm.201903184 (Dec. 2019).
75. Li, Z., Li, P., Chen, G., Cheng, Y., Pi, X., Yu, X., Yang, D., Han, L., Zhang, Y. & Song, Y. Ink Engineering of Inkjet Printing Perovskite. *ACS Applied Materials & Interfaces* **12,** 39082–39091. doi:10.1021/acsami.0c09485 (Aug. 2020).
76. Li, J., Dagar, J., Shargaieva, O., Flatken, M. A., Köbler, H., Fenske, M., Schultz, C., Stegemann, B., Just, J., Többens, D. M., Abate, A., Munir, R. & Unger, E. 20.8% Slot-Die Coated $MAPbI_3$ Perovskite Solar Cells by Optimal DMSO-Content and Age of 2-ME Based Precursor Inks. *Advanced Energy Materials* **11,** 2003460. doi:10.1002/aenm.202003460 (Jan. 2021).
77. Du, M., Zhu, X., Wang, L., Wang, H., Feng, J., Jiang, X., Cao, Y., Sun, Y., Duan, L., Jiao, Y., Wang, K., Ren, X., Yan, Z., Pang, S. & Liu, S. F. High-Pressure Nitrogen-Extraction and Effective Passivation to Attain Highest Large-Area Perovskite Solar Module Efficiency. *Advanced Materials* **32,** 2004979. doi:10.1002/adma.202004979 (Oct. 2020).
78. Tao, S., Schmidt, I., Brocks, G., Jiang, J., Tranca, I., Meerholz, K. & Olthof, S. Absolute energy level positions in tin- and lead-based halide perovskites. *Nature Communications* **10.** doi:10.1038/s41467-019-10468-7 (June 2019).
79. Yang, Y., Yang, M., Li, Z., Crisp, R., Zhu, K. & Beard, M. C. Comparison of Recombination Dynamics in $CH_3NH_3PbBr_3$ and $CH_3NH_3PbI_3$ Perovskite Films: Influence of Exciton Binding Energy. *The Journal of Physical Chemistry Letters* **6,** 4688–4692. doi:10.1021/acs.jpclett.5b02290 (Nov. 2015).
80. Marronnier, A., Roma, G., Boyer-Richard, S., Pedesseau, L., Jancu, J.-M., Bonnassieux, Y., Katan, C., Stoumpos, C. C., Kanatzidis, M. G. & Even, J. Anharmonicity and Disorder in the Black Phases of Cesium Lead Iodide Used for Stable Inorganic Perovskite Solar Cells. *ACS Nano* **12,** 3477–3486. doi:10.1021/acsnano.8b00267 (Mar. 2018).
81. Caicedo-Dávila, S., Funk, H., Lovrinčić, R., Müller, C., Sendner, M., Cojocaru-Mirédin, O., Lehmann, F., Gunder, R., Franz, A., Levcenco, S., Cohen, A. V., Kronik, L., Haas, B., Koch, C. T. & Abou-Ras, D. Spatial Phase Distributions in Solution-Based and Evaporated Cs–Pb–Br Thin Films. *The Journal of Physical Chemistry C* **123,** 17666–17677. doi:10.1021/acs.jpcc.9b02567 (July 2019).
82. Stoumpos, C. C., Malliakas, C. D. & Kanatzidis, M. G. Semiconducting Tin and Lead Iodide Perovskites with Organic Cations: Phase Transitions, High

Mobilities, and Near-Infrared Photoluminescent Properties. *Inorganic Chemistry* **52,** 9019–9038. doi:10.1021/ic401215x (July 2013).

83. Nazarenko, O., Kotyrba, M. R., Wörle, M., Cuervo-Reyes, E., Yakunin, S. & Kovalenko, M. V. Luminescent and Photoconductive Layered Lead Halide Perovskite Compounds Comprising Mixtures of Cesium and Guanidinium Cations. *Inorganic Chemistry* **56,** 11552–11564. doi:10.1021/acs.inorgchem.7b01204 (Sept. 2017).
84. Cha, J.-H., Lee, H.-J., Kim, S. H., Ko, K. C., Suh, B. J., Han, O. H. & Jung, D.-Y. Superparamagnetism of Green Emissive Cs_4PbBr_6 Zero-Dimensional Perovskite Crystals. *ACS Energy Letters* **5,** 2208–2216. doi:10.1021/acsenergylett.0c00964 (June 2020).
85. Stoumpos, C. C., Malliakas, C. D., Peters, J. A., Liu, Z., Sebastian, M., Im, J., Chasapis, T. C., Wibowo, A. C., Chung, D. Y., Freeman, A. J., Wessels, B. W. & Kanatzidis, M. G. Crystal Growth of the Perovskite Semiconductor $CsPbBr_3$: A New Material for High-Energy Radiation Detection. *Crystal Growth & Design* **13,** 2722–2727. doi:10.1021/cg400645t (June 2013).
86. Beal, R. E., Slotcavage, D. J., Leijtens, T., Bowring, A. R., Belisle, R. A., Nguyen, W. H., Burkhard, G. F., Hoke, E. T. & McGehee, M. D. Cesium Lead Halide Perovskites with Improved Stability for Tandem Solar Cells. *The Journal of Physical Chemistry Letters* **7,** 746–751. doi:10.1021/acs.jpclett.6b00002 (Feb. 2016).
87. Vegard, L. Die Konstitution der Mischkristalle und die Raumfüllung der Atome. *Zeitschrift für Physik* **5,** 17–26. doi:10.1007/bf01349680 (Jan. 1921).
88. Sharma, S., Weiden, N. & Weiss, A. Phase Diagrams of Quasibinary Systems of the Type: ABX_3-$A'BX_3$; ABX_3-$AB'X_3$, and ABX_3-ABX'_3; X = Halogen. *Zeitschrift für Physikalische Chemie* **175,** 63–80. doi:10.1524/zpch.1992.175.part_1.063 (Jan. 1992).
89. Hoke, E. T., Slotcavage, D. J., Dohner, E. R., Bowring, A. R., Karunadasa, H. I. & McGehee, M. D. Reversible photo-induced trap formation in mixed-halide hybrid perovskites for photovoltaics. *Chemical Science* **6,** 613–617. doi:10.1039/c4sc03141e (Jan. 2015).
90. Chen, Z., Brocks, G., Tao, S. & Bobbert, P. A. Unified theory for light-induced halide segregation in mixed halide perovskites. *Nature Communications* **12.** doi:10.1038/s41467-021-23008-z (May 2021).
91. Maclean, D., Baldwin, J. J., Ivanov, V. T., Kato, Y., Shaw, A., Schneider, P. & Gordon, E. M. Glossary of Terms Used in Combinatorial Chemistry. *Pure and Applied Chemistry* **71,** 2349–2365. doi:10.1351/pac199971122349 (Jan. 1999).
92. Geysen, H. M., Meloen, R. H. & Barteling, S. J. Use of peptide synthesis to probe viral antigens for epitopes to a resolution of a single amino acid. *Proceedings of the National Academy of Sciences* **81,** 3998–4002. doi:10.1073/pnas.81.13.3998 (July 1984).

93. Houghten, R. A. General method for the rapid solid-phase synthesis of large numbers of peptides: specificity of antigen-antibody interaction at the level of individual amino acids. *Proceedings of the National Academy of Sciences* **82,** 5131–5135. doi:`10.1073/pnas.82.15.5131` (Aug. 1985).
94. Guerin, S. & Hayden, B. E. Physical Vapor Deposition Method for the High-Throughput Synthesis of Solid-State Material Libraries. *Journal of Combinatorial Chemistry* **8,** 66–73. doi:`10.1021/cc050117p` (Dec. 2005).
95. Mertens, R., Sun, Z., Music, D. & Schneider, J. Effect of the Composition on the Structure of Cr-Al-C Investigated by Combinatorial Thin Film Synthesis and ab Initio Calculations. *Advanced Engineering Materials* **6,** 903–907. doi:`10.1002/adem.200400096` (Nov. 2004).
96. Klemm, S. O., Martin, A. G., Lengsfeld, J., Schauer, J.-C., Schuhmacher, B. & Hassel, A. W. Theoretical simulation and preparation of binary and ternary combinatorial libraries by thermal PVD. *physica status solidi (a)* **207,** 801–806. doi:`10.1002/pssa.200983302` (Mar. 2010).
97. Zhao, Y., Zhang, J., Xu, Z., Sun, S., Langner, S., Hartono, N. T. P., Heumueller, T., Hou, Y., Elia, J., Li, N., Matt, G. J., Du, X., Meng, W., Osvet, A., Zhang, K., Stubhan, T., Feng, Y., Hauch, J., Sargent, E. H., Buonassisi, T. & Brabec, C. J. Discovery of temperature-induced stability reversal in perovskites using high-throughput robotic learning. *Nature Communications* **12.** doi:`10.1038/s41467-021-22472-x` (Apr. 2021).
98. Delamarre, A., Lombez, L. & Guillemoles, J.-F. Contactless mapping of saturation currents of solar cells by photoluminescence. *Applied Physics Letters* **100,** 131108. doi:`10.1063/1.3697704` (Mar. 2012).
99. Ludwig, A. Discovery of new materials using combinatorial synthesis and high-throughput characterization of thin-film materials libraries combined with computational methods. *npj Computational Materials* **5.** doi:`10.1038/s41524-019-0205-0` (July 2019).
100. Eyke, N. S., Koscher, B. A. & Jensen, K. F. Toward Machine Learning-Enhanced High-Throughput Experimentation. *Trends in Chemistry* **3,** 120–132. doi:`10.1016/j.trechm.2020.12.001` (Feb. 2021).
101. Sun, S., Hartono, N. T., Ren, Z. D., Oviedo, F., Buscemi, A. M., Layurova, M., Chen, D. X., Ogunfunmi, T., Thapa, J., Ramasamy, S., Settens, C., DeCost, B. L., Kusne, A. G., Liu, Z., Tian, S. I., Peters, I. M., Correa-Baena, J.-P. & Buonassisi, T. Accelerated Development of Perovskite-Inspired Materials via High-Throughput Synthesis and Machine-Learning Diagnosis. *Joule* **3,** 1437–1451. doi:`10.1016/j.joule.2019.05.014` (June 2019).
102. Liu, Z., Rolston, N., Flick, A. C., Colburn, T. W., Ren, Z., Dauskardt, R. H. & Buonassisi, T. *Machine Learning with Knowledge Constraints for Process Optimization of Open-Air Perovskite Solar Cell Manufacturing* 2021. doi:`10.48550/ARXIV.2110.01387`.

103. Kennedy, K., Stefansky, T., Davy, G., Zackay, V. F. & Parker, E. R. Rapid Method for Determining Ternary-Alloy Phase Diagrams. *Journal of Applied Physics* **36,** 3808–3810. doi:10.1063/1.1713952 (Dec. 1965).

104. Miller, N. C. & Shirn, G. A. CO-SPUTTERED Au-SiO_2 CERMET FILMS. *Applied Physics Letters* **10,** 86–88. doi:10.1063/1.1754863 (Feb. 1967).

105. Hanak, J. J. The "multiple-sample concept" in materials research: Synthesis, compositional analysis and testing of entire multicomponent systems. *Journal of Materials Science* **5,** 964–971. doi:10.1007/bf00558177 (Nov. 1970).

106. Hanak, J. J. A quantum leap in the development of new materials and devices. *Applied Surface Science* **223,** 1–8. doi:10.1016/s0169-4332(03)00902-4 (Feb. 2004).

107. Teichler, A., Eckardt, R., Hoeppener, S., Friebe, C., Perelaer, J., Senes, A., Morana, M., Brabec, C. J. & Schubert, U. S. Combinatorial Screening of Polymer:Fullerene Blends for Organic Solar Cells by Inkjet Printing. *Advanced Energy Materials* **1,** 105–114. doi:10.1002/aenm.201000027 (Dec. 2010).

108. Jayakumar, O. D. & Tyagi, A. K. in *Handbook on Synthesis Strategies for Advanced Materials* (ed Tyagi A. K.and Ningthoujam, R. S.) 119–132 (Springer Singapore, 2022). doi:10.1007/978-981-16-1803-1_4.

109. Chen, S., Zhang, L., Yan, L., Xiang, X., Zhao, X., Yang, S. & Xu, B. Accelerating the Screening of Perovskite Compositions for Photovoltaic Applications through High-Throughput Inkjet Printing. *Advanced Functional Materials* **29,** 1905487. doi:10.1002/adfm.201905487 (Oct. 2019).

110. Chen, S., Zhang, L., Liu, Y., Zhang, Z., Li, Y., Cai, W., Lv, H., Qin, Y., Liao, Q., Zhou, B., Yan, T., Ren, J., Chen, S., Xiang, X., Dai, S., So, S. K., Wang, X., Yang, S. & Xu, B. High throughput screening of novel tribromide perovskite materials for high-photovoltage solar cells. *Journal of Materials Chemistry A* **9,** 25502–25512. doi:10.1039/d1ta06594g (Oct. 2021).

111. *Fundamentals of Inkjet Printing* (ed Hoath, S. D.) doi:10.1002/9783527684724 (Wiley-VCH Verlag GmbH & Co. KGaA, Jan. 2016).

112. Ohring, M. in *Materials Science of Thin Films* (ed Ohring, M.) Second Edition, 95–144 (Academic Press, San Diego, 2002). ISBN: 978-0-12-524975-1. doi:10.1016/B978-012524975-1/50006-9.

113. Lu, C.-S. & Lewis, O. Investigation of film-thickness determination by oscillating quartz resonators with large mass load. *Journal of Applied Physics* **43,** 4385–4390. doi:10.1063/1.1660931 (Nov. 1972).

114. Becker, P. *Structural and Optoelectronic Properties, Phase Transitions, and Degradation of Semiconducting $CsPbI_3$-Perovskite Thin-Films for Photovoltaics* en. PhD thesis (2020). doi:10.25926/0088-S132.

115. Bragg, W. H. & Bragg, W. L. The reflection of X-rays by crystals. *Proceedings of the Royal Society of London. Series A, Containing Papers of a Mathematical and Physical Character* **88,** 428–438. doi:10.1098/rspa.1913.0040 (July 1913).

116. Ewald, P. P. Die Berechnung optischer und elektrostatischer Gitterpotentiale. *Annalen der Physik* **369,** 253–287. doi:10.1002/andp.19213690304 (1921).

117. Zizak, I. mySpot: a versatile microfocussing station for scanning methods at BESSY II. *Journal of large-scale research facilities* **2,** 101. doi:10.17815/jlsrf-2-115 (Dec. 2016).

118. Schoonjans, T., Brunetti, A., Golosio, B., del Rio, M. S., Solé, V. A., Ferrero, C. & Vincze, L. The xraylib library for X-ray–matter interactions. Recent developments. *Spectrochimica Acta Part B: Atomic Spectroscopy* **66,** 776–784. doi:10.1016/j.sab.2011.09.011 (Nov. 2011).

119. Jenkins, R., Manne, R., Robin, R. & Senemaud, C. IUPAC—nomenclature system for x-ray spectroscopy. *X-Ray Spectrometry* **20,** 149–155. doi:10.1002/xrs.1300200308 (June 1991).

120. **Näsström, H.**, Shargaieva, O., Becker, P., Mathies, F., Zizak, I., Schröder, V. R. F., List-Kratochvil, E. J. W., Unold, T. & Unger, E. Combinatorial inkjet printing for compositional tuning of metal-halide perovskite thin films. *Journal of Materials Chemistry A* **10,** 4906–4914. doi:10.1039/d1ta08841f (Jan. 2022).

121. Harris, C. R., Millman, K. J., van der Walt, S. J., Gommers, R., Virtanen, P., Cournapeau, D., Wieser, E., Taylor, J., Berg, S., Smith, N. J., Kern, R., Picus, M., Hoyer, S., van Kerkwijk, M. H., Brett, M., Haldane, A., del Río, J. F., Wiebe, M., Peterson, P., Gérard-Marchant, P., Sheppard, K., Reddy, T., Weckesser, W., Abbasi, H., Gohlke, C. & Oliphant, T. E. Array programming with NumPy. *Nature* **585,** 357–362. doi:10.1038/s41586-020-2649-2 (Sept. 2020).

122. Funk, H., Shargaieva, O., Eljarrat, A., Unger, E. L., Koch, C. T. & Abou-Ras, D. In Situ TEM Monitoring of Phase-Segregation in Inorganic Mixed Halide Perovskite. *The Journal of Physical Chemistry Letters* **11,** 4945–4950. doi:10.1021/acs.jpclett.0c01296 (June 2020).

123. Wang, B., Fu, X., Song, S., Chu, H., Gibson, D., Li, C., Shi, Y. & Wu, Z. Simulation and Optimization of Film Thickness Uniformity in Physical Vapor Deposition. *Coatings* **8,** 325. doi:10.3390/coatings8090325 (Sept. 2018).

124. Nelder, J. A. & Mead, R. A Simplex Method for Function Minimization. *The Computer Journal* **7,** 308–313. doi:10.1093/comjnl/7.4.308 (Jan. 1965).

125. Gao, F. & Han, L. Implementing the Nelder-Mead simplex algorithm with adaptive parameters. *Computational Optimization and Applications* **51,** 259–277. doi:10.1007/s10589-010-9329-3 (May 2010).

126. Wolter, S. J., Steckenreiter, V., Tatarzyn, M. C., Wietler, T., Niepelt, R. & Kajari-Schröder, S. Determination and influence evaluation of the acoustic impedance ratio for thermal co-evaporation. *Applied Physics Letters* **113,** 013301. doi:10.1063/1.5037403 (July 2018).

127. Becker, P., Márquez, J. A., Just, J., Al-Ashouri, A., Hages, C., Hempel, H., Jošt, M., Albrecht, S., Frahm, R. & Unold, T. Low Temperature Synthesis of Stable γ-CsPbI$_3$ Perovskite Layers for Solar Cells Obtained by High Through-

put Experimentation. *Advanced Energy Materials* **9,** 1900555. doi:10.1002/aenm.201900555 (Apr. 2019).

128. **Näsström, H.**, Becker, P., Márquez, J. A., Shargaieva, O., Mainz, R., Unger, E. & Unold, T. Dependence of phase transitions on halide ratio in inorganic $CsPb(Br_xI_{1-x})_3$ perovskite thin films obtained from high-throughput experimentation. *Journal of Materials Chemistry A* **8,** 22626–22631. doi:10.1039/d0ta08067e (Oct. 2020).
129. Steele, J. A., Jin, H., Dovgaliuk, I., Berger, R. F., Braeckevelt, T., Yuan, H., Martin, C., Solano, E., Lejaeghere, K., Rogge, S. M. J., Notebaert, C., Vandezande, W., Janssen, K. P. F., Goderis, B., Debroye, E., Wang, Y.-K., Dong, Y., Ma, D., Saidaminov, M., Tan, H., Lu, Z., Dyadkin, V., Chernyshov, D., Speybroeck, V. V., Sargent, E. H., Hofkens, J. & Roeffaers, M. B. J. Thermal unequilibrium of strained black $CsPbI_3$ thin films. *Science* **365,** 679–684. doi:10.1126/science.aax3878 (Aug. 2019).
130. Shannon, R. D. Revised effective ionic radii and systematic studies of interatomic distances in halides and chalcogenides. *Acta Crystallographica Section A* **32,** 751–767. doi:10.1107/s0567739476001551 (Sept. 1976).
131. Yang, R. X., Skelton, J. M., da Silva, E. L., Frost, J. M. & Walsh, A. Spontaneous Octahedral Tilting in the Cubic Inorganic Cesium Halide Perovskites $CsSnX_3$ and $CsPbX_3$ (X = F, Cl, Br, I). *The Journal of Physical Chemistry Letters* **8,** 4720–4726. doi:10.1021/acs.jpclett.7b02423 (Sept. 2017).
132. Burger, S., Ehrenreich, M. G. & Kieslich, G. Tolerance factors of hybrid organic–inorganic perovskites: recent improvements and current state of research. *Journal of Materials Chemistry A* **6,** 21785–21793. doi:10.1039/c8ta05794j (Nov. 2018).
133. Zhao, B., Jin, S.-F., Huang, S., Liu, N., Ma, J.-Y., Xue, D.-J., Han, Q., Ding, J., Ge, Q.-Q., Feng, Y. & Hu, J.-S. Thermodynamically Stable Orthorhombic γ-$CsPbI_3$ Thin Films for High-Performance Photovoltaics. *Journal of the American Chemical Society* **140,** 11716–11725. doi:10.1021/jacs.8b06050 (Aug. 2018).
134. López, C. A., Abia, C., Alvarez-Galván, M. C., Hong, B.-K., Martínez-Huerta, M. V., Serrano-Sánchez, F., Carrascoso, F., Castellanos-Gómez, A., Fernández-Díaz, M. T. & Alonso, J. A. Crystal Structure Features of $CsPbBr_3$ Perovskite Prepared by Mechanochemical Synthesis. *ACS Omega* **5,** 5931–5938. doi:10.1021/acsomega.9b04248 (Mar. 2020).
135. Vurgaftman, I., Meyer, J. R. & Ram-Mohan, L. R. Band parameters for III–V compound semiconductors and their alloys. *Journal of Applied Physics* **89,** 5815–5875. doi:10.1063/1.1368156 (June 2001).
136. Malitson, I. H. Interspecimen Comparison of the Refractive Index of Fused Silica. *Journal of the Optical Society of America* **55,** 1205. doi:10.1364/josa.55.001205 (Oct. 1965).
137. Storn, R. & Price, K. *Journal of Global Optimization* **11,** 341–359. doi:10.1023/a:1008202821328 (Dec. 1997).

138. Li, G., Wang, H., Zhu, Z., Chang, Y., Zhang, T., Song, Z. & Jiang, Y. Shape and phase evolution from $CsPbBr_3$ perovskite nanocubes to tetragonal $CsPb_2Br_5$ nanosheets with an indirect bandgap. *Chemical Communications* **52,** 11296–11299. doi:10.1039/c6cc05877a (Aug. 2016).

139. Hempel, H., Savenjie, T. J., Stolterfoht, M., Neu, J., Failla, M., Paingad, V. C., Kužel, P., Heilweil, E. J., Spies, J. A., Schleuning, M., Zhao, J., Friedrich, D., Schwarzburg, K., Siebbeles, L. D., Dörflinger, P., Dyakonov, V., Katoh, R., Hong, M. J., Labram, J. G., Monti, M., Butler-Caddle, E., Lloyd-Hughes, J., Taheri, M. M., Baxter, J. B., Magnanelli, T. J., Luo, S., Cardon, J. M., Ardo, S. & Unold, T. Predicting Solar Cell Performance from Terahertz and Microwave Spectroscopy. *Advanced Energy Materials,* 2102776. doi:10.1002/aenm.202102776 (Feb. 2022).

140. Jacobsson, T. J., Schwan, L. J., Ottosson, M., Hagfeldt, A. & Edvinsson, T. Determination of Thermal Expansion Coefficients and Locating the Temperature-Induced Phase Transition in Methylammonium Lead Perovskites Using X-ray Diffraction. *Inorganic Chemistry* **54,** 10678–10685. doi:10.1021/acs.inorgchem.5b01481 (Oct. 2015).

141. Dalven, R. Empirical Relation between Energy Gap and Lattice Constant in Cubic Semiconductors. *Physical Review B* **8,** 6033–6034. doi:10.1103/physrevb.8.6033 (Dec. 1973).

142. Souder, W. H. & Hidnert, P. *Measurements on the Thermal Expansion of Fused Silica* tech. rep. Scientific Paper 524 (United States. National Bureau of Standards., Apr. 1926). https://digital.library.unt.edu/ark:/67531/metadc66490/.